UMONS
Université de Mons

Faculté
des Sciences

Electronic structure methods and electrostatic models: A promising marriage in the modelling of charge-transfer excitations in organic semiconductors

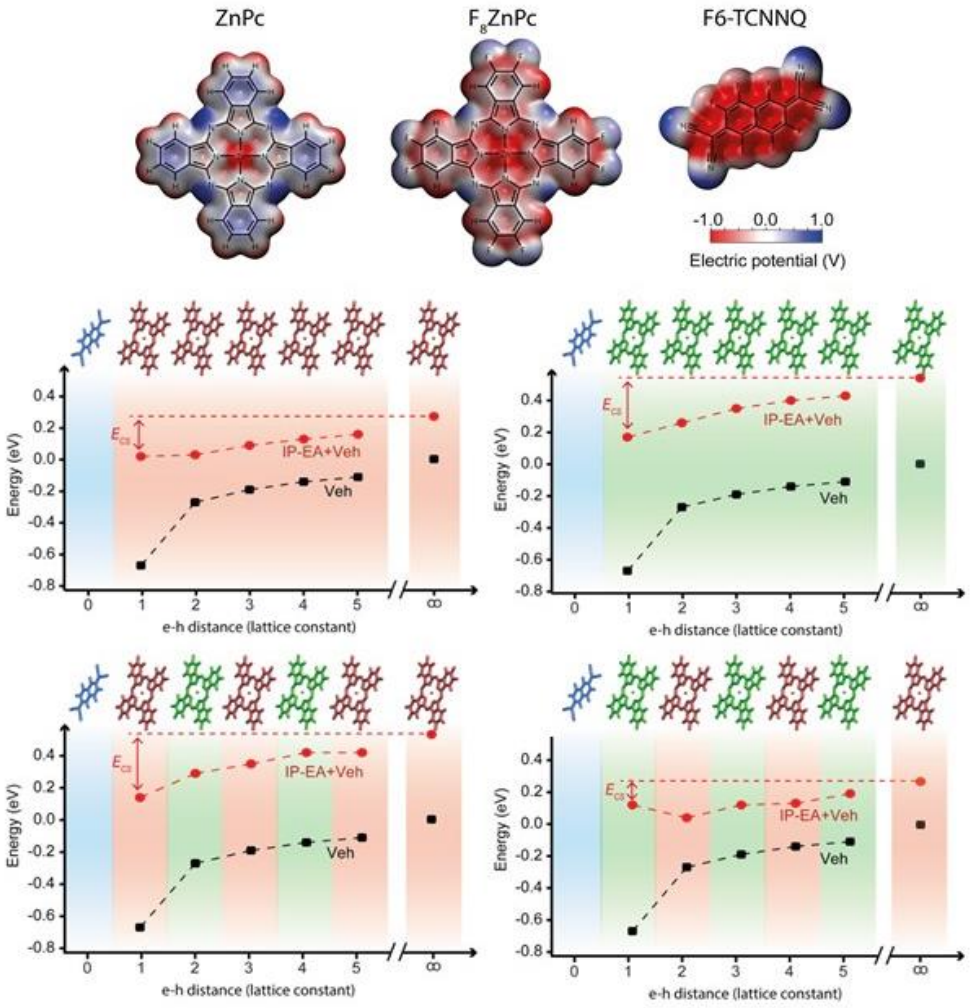

Giacomo Londi

Dissertation pour l'obtention du grade académique de

Docteur en Sciences

Service de Chimie des Matériaux Nouveaux

Université de Mons, Faculté des Sciences

Mons, Belgique, 29th Janvier 2021

devant le jury composé de:

Prof. David Beljonne (Université de Mons), Promoteur

Prof. Pascal Gerbaux (Université de Mons), Président

Prof. Jérôme Cornil (Université de Mons), Secrétaire

Prof. Colin Van Dyck (Université de Mons)

Prof. Jean-Luc Brédas (University of Arizona, USA)

Prof. Koen Vandewal (University of Hasselt, Belgium)

To my parents

Abstract

In the quest for new routes towards the replacement of fossil-based energy sources, the last 40 years witnessed an increased interest in renewable energies, such as the production of electricity directly from sunlight. In particular, much attention was paid to the use of organic π-conjugated molecules, the building blocks in active layers of emerging photovoltaic thin film technologies, as organic solar cells (OSCs). Yet, OSCs have not largely penetrated the market nowadays, since they still suffer from lower power conversion efficiencies (PCEs) with respect to those of inorganic silicon-based technologies. Nevertheless, despite their lower PCEs, OSCs offer multiple advantages: flexibility, lightness, cheapness, semi-transparency and suitability for large-scale production. Over the years, molecular engineering with the use of small molecule non-fullerene acceptors, local morphology control and optimization of the operating conditions have led to PCEs over 18%, still far away from the limit set by the Shockley-Queisser law of 33%. However, the bar has been raised and the current challenge is the achievement of PCEs larger than 20%, provided that all the superfluous loss pathways would be identified and removed.

In a bulk heterojunction (BHJ) donor:acceptor OSC, a paramount role is carried out by intermolecular charge-transfer (CT) states, which control the key photophysical phenomena occurring at the heterointerface. Indeed, CT states are intermediates of exciton dissociation, charge separation and recombination process and directly affect the performances of a working device. In addition, several other factors such as local morphology at the interface, environmental electrostatic interactions, energetic disorder, delocalization and hybridization affect dramatically the energetic landscape of CT states, the fate of free charge carriers and their transport properties. Therefore, a fundamental, thorough understanding of such effects, both from an experimental and a theoretical point of view, is essential in order to design new organic materials or architectures leading to higher performances. In this respect, modelling plays a major role in the complete rationalization of all the above-mentioned processes which take place at different length- and timescale. Setting up a proper multilevel computational approach combining several techniques, like atomistic molecular dynamics (MD) simulations, density functional theory (DFT) and its time-dependent (TD) version calculations, microelectrostatic (ME) models, is of utmost importance.

The *leitmotif* of this thesis is the application of electronic structure calculations in conjunction with a ME model, specifically designed to take into account solid-state environmental effects, in the modelling of different topics in the organic semiconductors' community. In this work, we resort to MD/TDDFT/ME methods in order to provide a fully atomistic modelling study of the broad energetic landscape and dynamics of singlet electronic excitations in amorphous thin films of two small organic π-conjugated donor-bridge-acceptor (*push-pull*) molecules, slightly different in their chemical structures, but largely different in the transport of singlet excitons. The latter is modelled by performing kinetic Monte Carlo simulations, which yield the macroscopic properties of interest, such

as the diffusion coefficients and the exciton diffusion lengths of the two materials. Then, we discuss the existence of multiple electronic CT states in amorphous donor:acceptor blends with large frontier orbital energy offset and their contributions to the photocurrent. We also focus on the energetic and dynamics of interfacial low-lying electronic CT states, by unravelling with a combined MD/(TD)DFT/ME computational protocol the different role exerted by static and dynamic disorder to the density of states of the CT states manifold. Finally, we deal with the role of local environmental interactions on the generation of free charge carriers in doped binary and ternary blends. In these systems, both the ionization and the charge dissociation step are controlled by molecular quadrupoles of host and dopant molecules, as found out by our theoretical approach based on DFT/ME calculations.

Résumé

En quête de nouvelles voies de remplacement des sources d'énergie fossiles, les quarante dernières années ont vu un intérêt accru pour les énergies renouvelables comme la production d'électricité solaire. En particulier, une grande attention a été accordée à l'utilisation de molécules organiques π-conjuguées, les éléments constitutifs des couches actives des technologies photovoltaïques à couche mince, au sein de cellules solaires organiques (OSC). Pourtant, les OSC n'ont pas encore actuellement largement pénétré le marché car elles souffrent toujours de rendements (PCE) inférieurs à ceux des technologies à base de silicium inorganique. Néanmoins, malgré leurs rendements inférieurs, les OSC offrent de multiples avantages: flexibilité, légèreté, faible coût de fabrication, semi-transparence et possibilité de production à grande échelle. Au fil des années, l'ingénierie moléculaire via l'utilisation de petites molécules non fulléréniques comme accepteurs, le contrôle de la morphologie locale et l'optimisation des conditions opératoires ont conduit à des PCE de plus de 18%, encore loin cependant de la limite fixée par la loi Shockley-Queisser à 33%. Néanmoins, cette belle percée ouvre la voie à des rendements supérieurs à 20%, à condition que toutes les voies de perte soient identifiées et supprimées.

Dans les cellules solaires organiques de type donneur:accepteur à hétérojonction en masse, un rôle primordial est joué par les états à transfert de charge intermoléculaires (CT) qui contrôlent les phénomènes photophysiques clés se produisant à l'hétéro-interface. En effet, les états CT sont des intermédiaires de dissociation des excitons, de séparation de charges et de processus de recombinaison et affectent directement les performances des dispositifs. En outre, plusieurs autres facteurs tels que la morphologie locale à l'interface, les interactions électrostatiques du milieu environnant, le désordre énergétique, la délocalisation et l'hybridation affectent considérablement le paysage énergétique des états CT, le sort des porteurs de charge libres et leurs propriétés de transport. Par conséquent, une compréhension fondamentale et approfondie de ces effets, tant d'un point de vue expérimental que théorique, est essentielle pour concevoir de nouveaux matériaux organiques ou des architectures menant à des performances plus élevées. À cet égard, la modélisation joue un rôle majeur dans la rationalisation complète de tous les processus susmentionnés qui se déroulent à des durées et étendues spatiales différentes. La mise en place d'une approche informatique multiniveau combinant plusieurs techniques comme les simulations de dynamique moléculaire atomistique (MD), la théorie de la fonctionnelle de la densité (DFT) ainsi que sa version dépendante du temps (TD) et les modèles microélectrostatiques (ME) est de la plus haute importance.

Le leitmotiv de cette thèse est l'application de calculs de structure électronique combinés avec un modèle ME spécifiquement conçu pour prendre en compte les effets environnementaux de l'état solide dans la modélisation de différentes thématiques liées aux semi-conducteurs organiques. Dans ce travail, nous recourons aux méthodes MD/TDDFT/ME afin de fournir une étude de modélisation entièrement atomistique du vaste paysage énergétique et de la dynamique des excitations

électroniques singulets dans des couches minces amorphes de deux petits systèmes organiques π-conjugués de type donneur-pont-accepteur (*push-pull*) qui ont la particularité de présenter des propriétés de transport d'excitons singulets très différentes alors que leur structure chimique ne l'est que modestement. Le transport d'excitons est modélisé en effectuant des simulations cinétiques de Monte Carlo qui permettent l'accès aux propriétés macroscopiques d'intérêt telles que les coefficients de diffusion et les longueurs de diffusion des excitons des deux matériaux. Ensuite, nous discutons de l'existence de multiples états électroniques à transfert de charge dans des mélanges amorphes donneur:accepteur présentant une large différence d'énergie des orbitales frontières ainsi que leurs contributions au photocourant. Nous nous concentrons également sur les aspects énergétiques et dynamiques de ces états électroniques CT interfaciaux de basse énergie en analysant avec un protocole de calcul combinant MD/(TD)DFT/ME le rôle exercé par les désordres statique et dynamique sur la densité d'états des états à transfert de charge. Enfin, nous abordons le rôle des interactions liées à l'environnement local sur la génération des porteurs de charge libres dans les mélanges dopés binaires et ternaires. Dans ces systèmes, les étapes d'ionisation et de dissociation de charge sont contrôlées par les quadrupôles moléculaires des molécules hôtes et dopantes, comme le montre notre approche théorique basée sur des calculs DFT/ME.

Peer-Reviewed Articles

In the following lists of publications, the first author(s) is (are) underlined and the corresponding author(s) is (are) indicated with an asterisk.

P. S. Marqués, G. Londi, B. Yurash, T. Q. Nguyen, S. Barlow, S. R. Marder and D. Beljonne*. Understanding how Lewis acids dope organic semiconductors: a "complex" story. *Submitted* (**2020**)

A. J. Gillett*, A. Privitera, R. Dilmurat, A. Karki, D. Qian, A. Pershin, G. Londi, W. K. Myers, J. Lee, J. Yuan, S. J. Ko, M. K. Riede, F. Gao, G. C. Bazan, A. Rao, T. Q. Nguyen*, D. Beljonne*and R. H. Friend*. The role of charge recombination to spin-triplet excitons in non-fullerene acceptor organic solar cells. *Submitted* (**2020**)

A. Privitera*, R. Warren, G. Londi, P. Kaienburg, J. Liu, A. Sperlich, A. E. Lauritzen, O. Thimm, A. Ardavan, D. Beljonne and M. K. Riede*. Electron spin as a fingerprint for charge generation and transport in doped organic semiconductors. *Submitted* (**2020**)

G. Londi, S. U. Z. Khan, L. Muccioli, G. D'Avino, B. P. Rand and D. Beljonne*. Fate of low-lying charge-transfer excited states in a donor:acceptor blend with large energy offset. *J. Phys. Chem. Lett.* **2020**, *11*, 23, 10219–10226.

Y. Dong, V. C. Nikolis, F. Talnack, Y. C. Chin, J. Benduhn, G. Londi, J. Kublitski, X. Zheng, S. C. B. Mannsfeld, D. Spoltore, L. Muccioli, J. Li, X. Blase, D. Beljonne, J. S. Kim*, A. A. Bakulin, G. D'Avino*, J. R. Durrant* and K. Vandewal*. Orientation dependent molecular electrostatics drives efficient charge generation in homojunction organic solar cells. *Nat. Commun.* **2020**, *11* (1), 4617

A. Privitera, G. Londi, M. K. Riede, G. D'Avino, D. Beljonne*. Molecular quadrupole moments promote ground-state charge generation in doped organic semiconductors *Adv. Funct. Mater.* **2020**, 30, 2004600.

P. S. Marqués, J. M. Andrés Castán, B. A. L. Raul, G. Londi, I. Ramirez, M. S. Pshenichnikov*, D. Beljonne*, K. Walzer, M. Blais, M. Allain, C. Cabanetos and P. Blanchard*. Triphenylamine/tetracyanobutadiene-based π-conjugated push-pull molecules end-capped with arene platforms: synthesis, photophysics, and photovoltaic response. *Chem. Eur. J.* **2020**, *26*, 16422.

M. S. Kotova, G. Londi, J. Junker, S. Dietz, A. Privitera, K. Tvingstedt, D. Beljonne, A. Sperlich* and V. Dyakonov. On the absence of triplet exciton loss pathways in non-fullerene acceptor based organic solar cells. *Mater. Horizons* **2020**, *7* (6), 1641–1649

S. U. Z. Khan, G. Londi, X. Liu, M. A. Fusella, G. D'Avino, L. Muccioli, A. N. Brigeman, B. Niesen, T. C. J. Yang, Y. Olivier, J. T. Dull, N. C. Giebink, D. Beljonne and B. P. Rand*. Multiple charge

transfer states in donor-acceptor heterojunctions with large frontier orbital energy offsets. *Chem. Mater.* **2019**, *31* (17), 6808–6817

G. Londi, R. Dilmurat, G. D'Avino, V. Lemaur, Y. Olivier and D. Beljonne*. Comprehensive modelling study of singlet exciton diffusion in donor-acceptor dyads: when small changes in chemical structure matter. *Phys. Chem. Chem. Phys.* **2019**, *21* (45), 25023–25034

A. Labrunie, G. Londi, S. V. Dayneko, M. Blais, S. Dabos-Seignon, G. C. Welch, D. Beljonne, P. Blanchard* and C Cabanetos*. A triazatruxene-based molecular dyad for single-component organic solar cells. *Chem. Squared* **2018**

J. Benduhn*, F. Piersimoni, G. Londi, A. Kirch, J. Widmer, C. Körner, D. Beljonne, D. Neher, D. Spoltore and K. Vandewal*. Impact of triplet excited states on the open-circuit voltage of organic solar cells. *Adv. Energy Mater.* **2018**, *8* (21), 1800451

List of Abbreviations

APS	ambient photoemission spectroscopy
BHJ	bulk heterojunction
BSE	Bethe-Salpeter equations
CBS	complete basis set
CI	configuration interaction
CS	charge-separation
CR	charge response
CT	charge-transfer
D	donor
DCV	dicyanovinylene
DFT	density functional theory
DOS	density of states
e-h	electron-hole
erf	error function
EA	electron affinity
EL	electroluminescence
ENDOR	electron nuclear double resonance
EPR	electron paramagnetic resonance
EQE	external quantum efficiency
EXX	exact exchange
FE	Frenkel excitations
FED	fragment excitation difference
FF	force field
FRM	first reaction method
GGA	generalized-gradient approximation

GIWAXS	grazing-incidence wide-angle X-ray scattering
GMH	generalized Mulliken-Hush
GWA	*GW* approximation
HF	Hartree-Fock
HOMO	highest occupied molecular orbital
HOSCs	homojunction organic solar cells
INDO	intermediate neglect of differential overlap
IP	ionization potential
LDA	local density approximation
LE	localized exciton
KMC	kinetic Monte Carlo
KS	Kohn-Sham
LEIPS	low-energy inverse photoemission spectroscopy
LRC	long-range corrected
LUMO	lowest unoccupied molecular orbital
MBPTs	many-body perturbation theories
MD	molecular dynamics
ME	microelectrostatic
MLJ	Marcus-Levich-Jortner
NFAs	non-fullerene acceptors
NTOs	natural transition orbitals
OFETs	organic field-effect transistors
OLEDs	organic light-emitting diodes
OSCs	organic solar cells
OT	optimally tuned
PCM	polarizable continuum model
PDA	point dipole – point dipole approximation
PDS	photothermal deflection spectroscopy

PL	photoluminescence
RPA	random phase approximation
RSH	range-separated hybrid
SCF	self-consistent field
SIE	self-interaction error
SR	short-range
SRSH	screened range-separated hybrid
TA	transient absorption
TD	time-dependent
TDA	Tamm-Dancoff approximation
TPA	triphenylamine
PCEs	power conversion efficiencies
UEG	uniform electron gas
UPS	ultraviolet photoelectron spectroscopy
V_{oc}	open-circuit voltage
WFTs	wave function theories
xc	exchange-correlation

Table of Contents

1. Introduction

1.1 Organic Solar Cells

Ever since the very beginning of the first industrial revolution in the second half of the 18th century to nowadays, fossil fuels have been widely used by mankind to produce energy. Despite the wealth brought by technological progresses, it is evident that such an economy based on oil, coal and gasses cannot be sustainable in a long-term period, due to limited energy resources, environment pollution, massive carbon dioxide (CO_2) emissions and all the collateral damages they involve, including global warming. In this respect, 196 state parties gathered in a climate conference and signed the "Paris Agreement", adopted on 12 December 2015, where each country had to determine, plan, and regularly report on the contribution that it undertook to mitigate global warming, with the aim of reducing of CO_2 emissions in the atmosphere by 20% and with the commitment to rely more on renewable energies, among which biomasses, wind and hydro power, solar radiation energy and fuel cells, in a global, forward-looking, green new deal.

Renewable energies only utilize energy sources that are not exhausting Earth resources. Certainly, solar energy is the most viable alternative to fossil-based sources.[1] The interest in the production of electricity directly from sunlight arose in the early 1980's, as the consequence of two oil price shocks (in 1973 and 1979), which boosted the urgencies in gaining independence from fossil fuels. Indeed, most of the solar energy was (and still is) extensively exploited by first-generation crystalline and poly-crystalline silicon-based solar cells, but a new paradigm, resorting to thin film technologies, such as copper indium gallium selenide (CIGS), cadmium telluride (CdTe), amorphous silicon (a-Si), perovskite and organic cells, began to attract the attention of both academic and industrial researchers. The late 1980s truly witnessed an increase of research efforts in the use of organic π-conjugated molecules in the active layer of semiconductor devices like organic light-emitting diodes (OLEDs),[2–4] field-effect transistors (OFETs),[5–7] and solar cells (OSCs).[8–12] In particular, OSCs are photovoltaic devices suitable for new application fields and whose active layer is made of thin films of organic semiconductors. Their success in the market is expected due to the manifold advantages over the silicon-based cells:[1] OSCs are flexible, semi-transparent, lightweight, produced on a large-scale by low-cost printing techniques, disposable and *green* in terms of environmental impact. Among the short-comings: low-efficiency and low-stability, although great strides have been made to improve power conversion efficiencies (PCEs) and the device stability. Over the years, synthetic molecular design along with efforts aimed at optimizing the donor:acceptor (D:A) morphology and operating conditions have led to record PCEs of 11.0%, 11.7%, and 18.2% for all-polymer, polymer:fullerene, and polymer:non-fullerene acceptor (NFA) single-junction bulk heterojunction (BHJ) OSCs, respectively.[13–17] The current challenge is the reduction of energy and voltage losses, driven mostly by recombination of charges via non-radiative decay pathways, in order to reach PCEs > 20%.

In a nutshell, in order to convert solar radiation into electricity (see Figure 1.1), the active layer of an OSC needs to absorb the incoming light efficiently, generate free charge carriers, and transport these carriers to the electrodes for charge extraction and photocurrent production.[18] The paramount work by Tang highlighted that, in order to achieve the highest efficiency for the above mentioned processes, the active layer should be composed by two types of semiconducting materials:[8] an electron-donating, usually hole transport material with a small ionization potential (IP) and an electron-accepting, electron transport material with a large electron affinity (EA). The donor (D) can be either a polymer chain or a small molecule, while fullerene derivatives have played for long time the role of acceptors (A), although small NFA molecules have recently begun to appear within OSC devices, replacing the typically used fullerenes as electron-accepting materials.[16,17,19–21]

When the primary chromophore (usually the D, although the A can harvest light too) absorbs a photon with energy equal or higher to the lowest excited state S_1, one electron is promoted from an occupied to an unoccupied electronic level, *i.e.*, an electronic transition occurs from the ground state S_0 to whatever excited state S_n. Upon a local excitation of a single molecule, a photogenerated, electrically neutral and spatially localized electron-hole (e-h) pair (*i.e.*, an intramolecular Frenkel-type exciton) is created. Unlike inorganic semiconductors, where the binding energies are on the order of few meV and free charge carriers can be photogenerated even at room temperature, excitons in organic semiconductors are strongly bound by Coulombic interactions,[22] as a consequence of the weak screening provided by the low dielectric permittivity of organic materials (between 3 and 5) and strong electron-electron and electron-vibration interactions. At this stage, singlet excitons diffuse in the D phase through a series of energy-transfer (mostly Förster resonant dipole-dipole) processes and must reach the heterointerface with the A phase prior their decay to the ground state. At the D:A interface, excitons either dissociate in a long-range charge-separation (CS) state or a full (or a partial) electronic charge-transfer (CT) from D to A takes place: an intermolecular CT electronic state is formed, where the hole is localized in the D highest occupied molecular orbital (HOMO) and the electron in the A lowest unoccupied molecular orbital (LUMO). In order to create free charge carriers, the strongly interacting e-h pairs need to escape from their Coulomb well and overcome their binding energy, which for intermolecular CT states is smaller than that of the Frenkel exciton, since the hole and the electron are more spatially separated: typical binding energies in π-conjugated systems can be on the order of 0.5 eV. Once apart in the manifold of CS states, the positive and negative charges (polarons) diffuse through the D and A phases to the anode and cathode, respectively, where the charges are collected, and photocurrent is produced.[23–26] Note that the photogeneration of charge carriers can occur by the absorption from either the D or the A, but also by direct excitation of the CT state from the ground state.

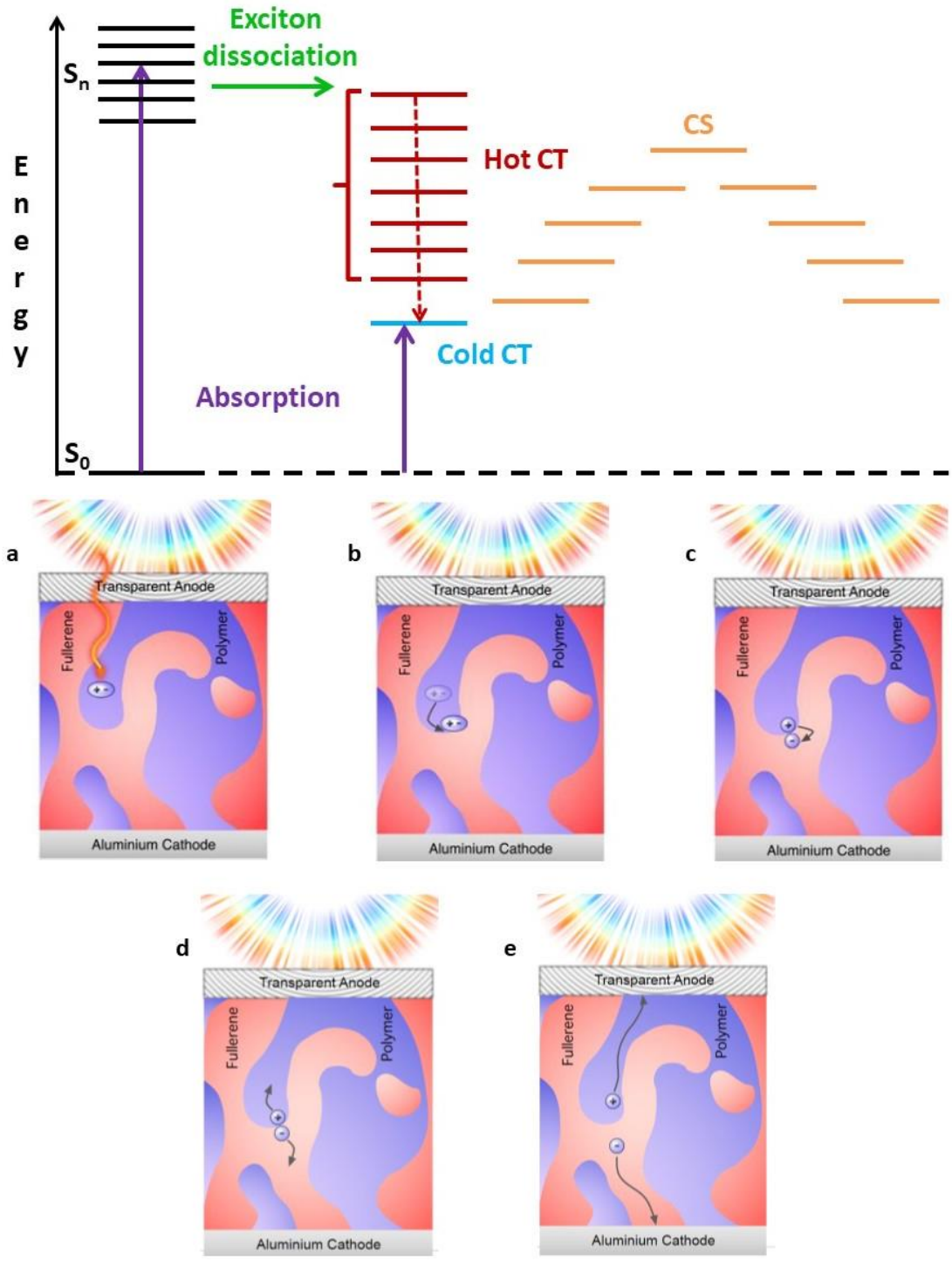

Figure 1.1: Top: electronic state diagram describing the key processes occurring in a polymer:fullerene OSC: a) an above gap excitation from S_0, the ground state of the donor, to S_n, a higher-energy excited state, forms a strongly bound electron-hole (e-h) pair, called exciton; b) the exciton diffuses in the D phase and reaches the D:A interface, where c) exciton dissociation leads to the formation of charge-transfer (CT) states, where the hole resides on the D and the electron on the A; d) at the interface, the strongly interacting e-h pair needs to escape from its Coulomb potential and overcome the binding energy and charge-separation (CS) might then occur from vibrationally excited

("hot") CT states or via thermally relaxed ("cold") CT states (see discussion below); e) in the manifold of CS states, free charge carriers diffuse towards the electrodes for charge collection.

The primary excitations in organic thin films are usually generated in the fs timescale and are delocalized over several molecules, depending on the magnitude of the intermolecular interactions (*i.e.,* electronic couplings) and on that of the energetic disorder among electronic transition energies. Then, the spatial delocalization of the excitation is progressively reduced by a relaxation step exerted by intra- or intermolecular vibrations (in the ps timescale).[25,26] In amorphous thin films, usually the excitation is localized on a single molecule or a limited number of molecular fragments, in contrast to high-ordered crystalline materials, where the excitation can extend over several molecules. When a Frenkel exciton is fully relaxed, it can only migrate by hopping from one molecular site to another in the thin film. The lifetime of excitons is normally on the order of ns and their diffusion lengths, that is the distance covered by excitons during their lifetime, span the range 5-20 nm for typical small molecules and polymers in organic semiconductors (depending on the degree of energetic disorder).[27–29] The concept of BHJ in OSCs,[8] where the active layer is built with a homogeneous blend of a D and an A material, with the two components mixing down to the ~10 nm scale, was introduced almost three decades ago and since then the PCEs rapidly rose outdoing those obtained with bilayer architectures. In such BHJ devices the effective D:A interfacial area is increased, so that all the excitons may reach the interface during their lifetime, be prompt to dissociation and increase the photogeneration efficiency.

In an OSC the most critical (and interesting) photophysical processes occur at the heterointerface with two semiconducting materials, in the realm of CT states. By now it is all over recognized that intermolecular CT states play a paramount role,[22,30–32] since they directly affect the performances of a working device and are intermediates of exciton dissociation, charge separation and recombination process. Indeed, it has been argued that CT states might be a relevant source of loss mechanism,[24] since they can decay radiatively or non-radiatively to the ground state before dissociation into free charge carriers occurs. Although charge separation of CT states is very efficient,[33,34] approaching nearly 100%, the mechanism governing this fast breakup is still an open issue in the community. The question is how CT states can overcome their mutual Coulomb binding energy and separate into free charge carriers contributing to the photocurrent. Several mechanisms have been proposed over the years, supported by experimental results obtained with different techniques and by different research groups, trying to rationalize the still existing dilemma in literature.[35,36,45–49,37–44] A first hypothesis has been proposed in which the singlet exciton might have access to a vibrationally excited CT state and, being the energy of the lowest CT state (E_{CT}) lower than the optical gap of the D absorber (E_{D^*}), an excess of thermal energy in the initial "hot" CT states would provide the required driving force for the charge separation, competing against the Coulomb attraction. A second scenario implies a two-step process, involving CT states which are fully thermalized to their vibrational ground state before splitting up into free charge carriers with the aid of local electric fields across the interface, which make the dissociation of "cold" CT states nearly barrierless. Whether the splitting of charges at the

D:A interface is assisted by the combined role of delocalization effects and vibrationally hot CT states or mediated by weakly bound, thermally relaxed cold CT states is still a debated topic, since several experimental and theoretical efforts pointed to contradicting evidences on the charge carrier generation process, probably due to the different choice of the investigated systems.

For a large photocurrent to be produced, a broad portion of the solar spectrum from visible to infrared needs to be absorbed and organic π-conjugated materials offer the chance to fulfil this requirement, thanks to their large extinction coefficients and intense and broad absorption bands.[23] Another key feature for organic semiconductors is the possibility of finely tailoring their opto-electronic properties by adjusting the relative electron rich/poor strength of their constituting building blocks, extending their π-conjugated framework or through functionalization of their moieties. From an energetic standpoint, a proper energy level alignment of the frontier molecular orbitals of both the D and the A needs to be achieved in order to design an efficient OSC and improve the charge generation yield. In particular, the open-circuit voltage V_{oc}, that is the voltage at zero current, is a key a parameter that must be maximized to boost PCEs. The V_{oc} is directly proportional to E_{CT},[31,50] as among them there is linear correlation with an offset of around 0.6 eV ascribable to radiative (~0.25 eV) and non-radiative (~0.35 eV) losses of the CT pairs.[26] The measured V_{oc} values in OSCs are in general lower than those obtained for inorganic semiconductors or perovskite cells, due to a significant amount of parasitic non-radiative voltage losses, detrimental for OSCs.[51] Since intrinsic radiative decays cannot be avoided, as a direct consequence of the absorption process, sources of photocurrent and voltage losses, such as temperature-dependent non-radiative recombination, must be reduced as much as possible.

According to the so-called "energy gap law",[31,52] non-radiative voltage losses increase with decreasing E_{CT}. One viable way to increase the latter, and consequently the V_{oc}, is to choose a D:A active layer in which the energy offset between E_{D^*} and E_{CT} (*i.e.* the driving force) is minimized, typically below 0.1 eV,[21,32,53–58] a sufficient amount to sustain high charge generation yields (see Figure 1.2). For a long time it has been believed that in fullerene-based systems a minimum offset of ~0.3 eV was necessary as driving force for the electron transfer,[9,36,59] despite evidences indicating that the electron transfer takes place irrespective of the energy difference between E_{D^*} and E_{CT}.[60] On the other hand, recent reports on efficient NFA-based BHJs indicate that the "0.3 eV" requirement may not hold for NFAs, where charge generation can be efficient even for negligible driving forces for the electron transfer.[61–63] To achieve this condition two materials with almost the same EA have to be chosen, when the D in the blend shows the lowest optical gap. In this scenario, feasible with a proper choice of both the D and a NFA,[32,55] the CT state can easily hybridize with the localized excited state on the D and efficient back-electron transfer might occur, which opens a new radiative pathway from the CT state to the ground state, mediated by the localized excited state, thereby increasing the photoluminescence of the D.[32] As non-radiative voltage losses are proportional to the natural logarithm of the external quantum efficiency of emission (EQE_{EL}),[64] the development of D:A blends with efficient photocurrent generation and high values of EQE_{EL} can lead to an increase of PCEs, by reducing substantially non-radiative voltage losses, in some cases down to 0.21 eV.[55] Moreover, when

the driving force gets reduced, exciton dissociation into CT states and charge separation become much slower in the ps timescale, but this should not be an issue as long as they occur faster than competing recombination processes[a].

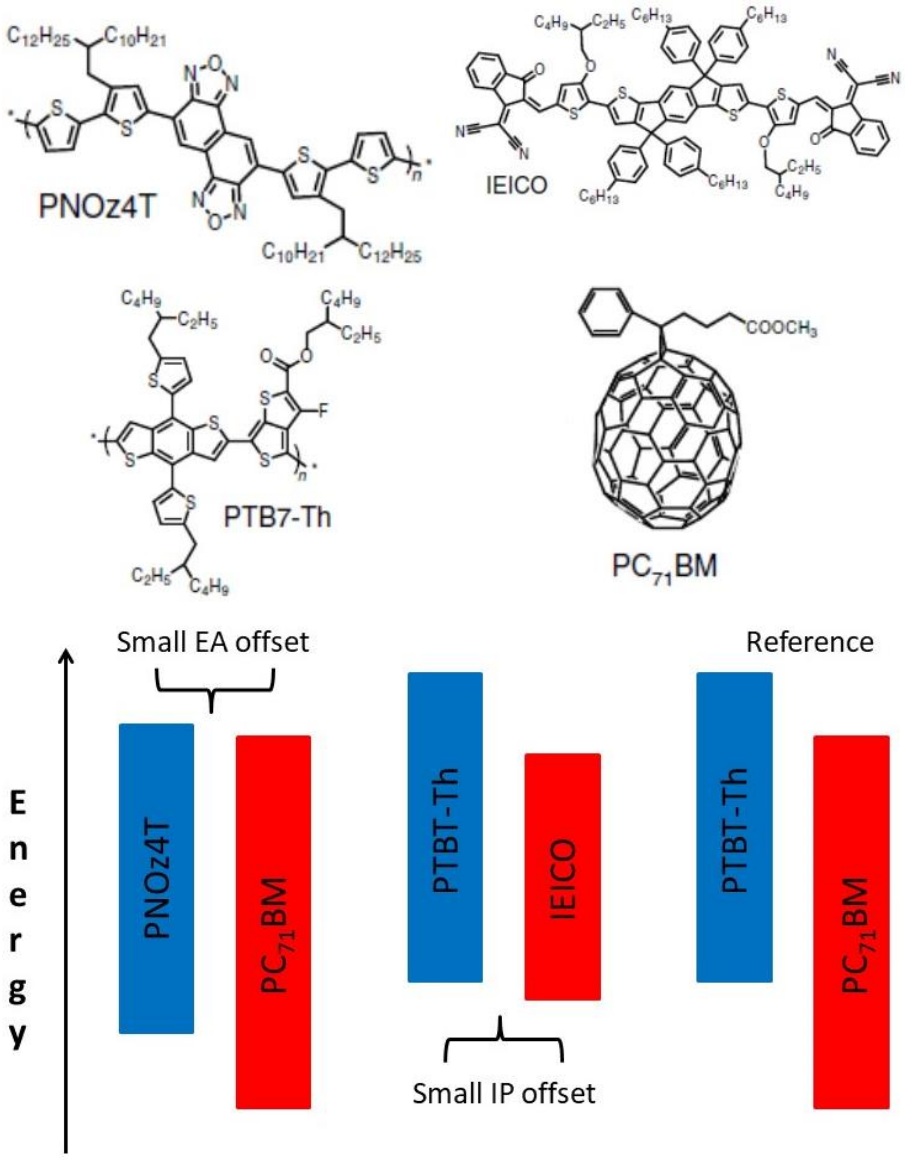

Figure 1.2: Top: molecular structures of the commonly used D polymers (left) and A molecules (right). Bottom: schematic representation of charge transport energy levels in D/A pairs that form blends with a small energy offset between IP and/or EA. Picture adapted from Ref.[55].

[a] In the herein discussion we neglect on purpose the treatment of triplet excited states, although we acknowledge their crucial role in the performances of OSCs and OLEDs.[100–103]

So far, we have discussed the role and the energetics of CT states in OSCs, where the CT process is photoinduced and hence in the excited state. Nonetheless, CT might also occur in the ground state with the formation of a CT complex.[65–69] For instance, an organic host thin film can be doped in a given concentration by "impurities" or dopant molecules, in order to increase the conductivity of the host semiconductors and the charge generation efficiency of the device. In molecular doping, under certain conditions, either a hybridization of the host-dopant frontier molecular orbitals or a ground state (complete or partial) CT process between the host and the dopant can occur.[70,71] For p-type doping, *i.e.*, the dopant is an oxidant of the host material, the formation of a ground state CT complex is favoured when the energy difference between the IP of the host and the EA of the dopant is smaller in magnitude than the Coulomb binding energy between an electron and its geminate hole sitting on nearest neighbour molecules.[72] As a result, a bound CT state with an electron on the dopant and a hole left on the host molecule is generated. At that point, for charge dissociation, the hole must migrate away from the ionized dopant, likely by hopping, and this requires overcoming the binding energy of the CT pair (see Figure 1.3). The last years have witnessed a considerable advancement of the research on doped organic semiconductors. These efforts have led to a better understanding of the relationships between structure and properties in doped materials,[73] as well as to the emergence of novel strategies to dope organic semiconductors, including light-activated dopants,[74] anion exchange processing[75] and the use of Lewis acids complexes as molecular dopants.[76] A thorough comprehension of the elementary steps occurring after the introduction of dopant molecules inside organic layers has allowed for a better control of the doping process. Indeed, such rationalization of molecular doping is essential to develop novel dopants with appropriately tailored energetic levels with the aim of pushing forward the performance of organic devices in which doped layers play a crucial role.

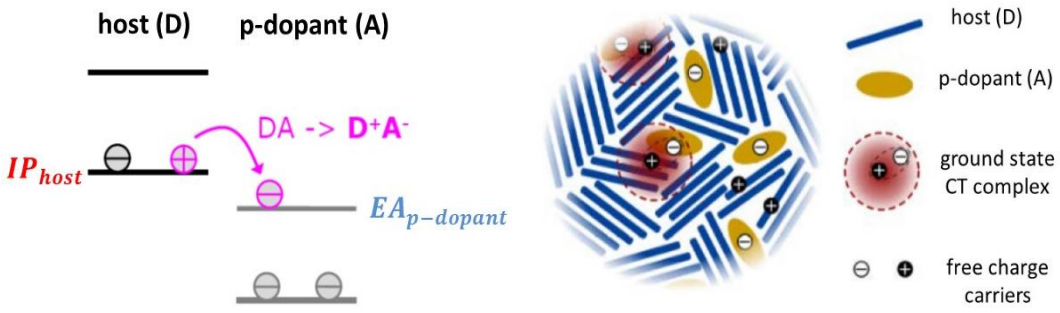

Figure 1.3: Left: scheme of molecular p-type doping, where the dopant is an acceptor. Right: illustration of charged species in a p-doped organic semiconductor film, where a ground state CT complex is thermally dissociated into free charge carriers. Picture taken from Ref.[69].

1.2 Challenges for Modelling

The relative energies of the Frenkel exciton localized on the D (E_{D^*}), the intermolecular CT state (E_{CT}) and the CS state (E_{CS}) affect the rate of the competing processes such as charge separation and charge recombination.[25] For instance, the energy gap between the IP of the D and the EA of the A (the photovoltaic gap Γ of the complex) provides a rough estimation of the E_{CS}, where the hole and the electron are not anymore Coulombically bound (see Figure 1.4):

$$\Gamma = IP_D - EA_A \tag{1.1}$$

where by convention the IP and EA are set positive. On the other hand, Γ differs from E_{CT} (the *optical* gap of the complex) by the exciton binding energy E_B^{eh} between an e-h pair:

$$E_{CT} = \Gamma + E_B^{eh} \tag{1.2}$$

being E_B^{eh} negative and E_{CT} defines in turn the upper limit for the V_{oc}. Therefore, knowledge of such an energetic landscape is thus crucial to design an efficient OSC, by reducing the always present losses mechanism and maximizing the charge generation and PCEs.

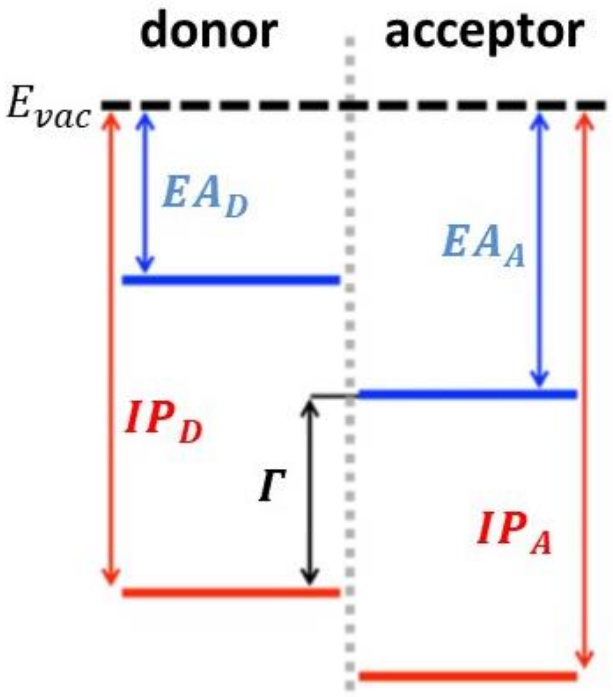

Figure 1.4: Energy level of a generic D:A interface, with definition of the photovoltaic gap Γ. Note that the IP and EA are referred to a common vacuum level E_{vac}. Picture taken from Ref.[77].

In the computational characterization of organic π-conjugated systems many different molecular properties can be determined by *ab-initio* quantum-chemical calculations, casted into two different classes: i) high-level wave function theories (WFTs) and ii) functional theories, like many-body perturbation theory (MBPT) and density functional theory (DFT). Among all these electronic structure methods, DFT offers the best accuracy-to-cost ratio, wide availability, and ease of implementation in the assessment on equal footing of structural, electronic and optical properties of π-conjugated molecules.[78,79] Briefly, in DFT a time-independent one-electron Schrödinger eigenproblem is solved in a self-consistent field (SCF) by treating the electron exchange and correlation effects as approximations, by including them into the exchange-correlation (xc) functional, being a functional of the electronic density itself. Over the years, since the introduction of DFT in 1964,[80,81] hundreds of xc functionals have been developed with the aim of improving the accuracy of the results, as the choice of the xc functional affects both the numerical costs and the accuracy of a DFT calculation. DFT is a ground state theory (see section 2.1) and it can be used to compute plenty of important ground state properties, including molecular structures, vibrational frequencies, electronic band-structures, dipole moments, wave functions and energies of the HOMO and LUMO. Strictly speaking, it is often encountered in literature the trend to physically interpret the HOMO and LUMO energy and their associated gap as meaningful values for many OSC properties, like the IP and EA of the materials and, ultimately, the V_{oc} of the device. It should be noted that in the case of organic semiconductors the HOMO and LUMO energies are poor estimates of the IP and EA for most *semi-local* and standard global hybrid DFT calculations.[82] First, the computation of the IP and EA of a single molecule involves a single-particle charged excitation and DFT is a ground state theory. Secondly, despite HF theory where Koopman's theorem holds, in DFT only by knowing the *exact* xc functional (and it is not yet known) the highest-occupied orbital eigenvalue (*i.e.,* the HOMO energy) would equal the negative of the true vertical IP. However, there exists no similar theorem for any of the other eigenvalues and, in particular, the LUMO eigenvalue does not equal at all the negative of the true vertical EA. Then, if one is only interested in the IP (EA) of a single molecule, the ΔSCF approach offers a fair enough solution: the ground state energies of the neutral molecule and its respective cation (anion) are computed and the IP (EA) is obtained as a total energy difference.[83–85]

Conversely, the calculation of neutral optical excitations requires a time-dependent DFT (TDDFT) treatment (see section 2.2), which is an extension of DFT for excited state properties.[86] Upon an optical excitation, the molecular dipole moment starts to oscillate at a frequency that corresponds to the excitation energy, or in other words, the electronic density becomes TD. Often one relies on the linear response theory, in which the system responses under the application of a small external TD perturbation. In linear response TDDFT, the calculation of excitation energies and optical spectra of atoms, molecules and solids are usually carried out within the Casida equation framework.[87] As in DFT, the choice of the xc functional affects the accuracy and the goodness of the results, but one has to be aware that there exists major challenges in the TDDFT description of Rydberg, long-range CT, double and multiple excitations, just to name a few. In addition, if one is interested in the assessment of the nature of any electronic excitation, it is common praxis to rely on natural transition orbitals (NTOs), that are graphical representations of the linear combination of the occupied (hole-NTO) and

unoccupied (electron-NTO) orbitals contributing to a specific transition associated with an excited state. In organic π-conjugated molecules the lowest optical excitation is usually a HOMO-LUMO transition, but sometimes the excited state of interest may be described by multiple orbital transitions. Therefore, simply taking the HOMO and LUMO wave functions as representatives of the electronic excitation is misleading, since other single-particle transitions can in principle contribute.[79,88]

A word of caution is mandatory when dealing with organic π-conjugated systems in the context of OSCs.[32,78] It is well-known that standard functionals, either semi-local (like PBE used for periodic solids) and global hybrid with some amount of the Hartree-Fock (HF) exchange (like B3LYP for molecules) miss dispersion interactions, do not provide the correct asymptotic behavior of the Coulomb potential (which goes like $-\frac{1}{r}$) and suffer from the electron self-interaction error (SIE). As pointed out further, all these shortcomings are imputable to an improper description of *non-local*, long-range effects. As a result, these functionals are totally inadequate to describe extended π-conjugated molecules or polymers, especially in the case of intra- and intermolecular CT states. In order to mitigate the flaws of standard DFT and TDDFT, a class of hybrid functionals have been recently developed (see section 2.3), under the name of range-separated hybrid (RSH) functionals.[89] Specifically, long-range corrected (LRC) hybrid functionals have proven themselves to be very efficient and accurate in the description of CT excitations of organic π-conjugated molecules and D:A complexes. In LRC functionals, the main idea is the partitioning of the inter-electron Coulomb potential into a short-range (SR) and a long-range (LR) contribution. In the LR domain, the exchange is treated using the full exact HF exchange, while in the SR domain the exchange is treated in a DFT fashion (usually, with a semi-local exchange). By introducing the exact exchange, LR interactions governing CT and charged excitation energies are correctly restored, the SIE is completely cancelled out in the LR limit and the correct asymptotic behavior of the Coulomb potential is recovered. By incorporating the full HF exchange for LR interactions and providing HOMO/LUMO energies that approximate IPs/EAs, this class of functionals is useful in the computational modelling of CT excitations in D:A complexes and optical excitation energies with a significant CT character.[79]

Organic semiconductors are characterized by weak non-covalent van der Waals interactions, which result in ubiquitous structural disorder and localized charge carriers, underlying the molecular character of their opto-electronic properties. Thus, the molecular system of interest is usually either surrounded by some solvent molecules in a solution or embedded in an effective dielectric medium provided by all neighboring molecules. It is nowadays clear that solid-state intermolecular interactions (*i.e.*, polarization energies) are responsible for shifts of the charge transport energy levels in organic semiconductors on the order of eV and they have a crucial role in affecting charge separation and transport at D:A interface in OSCs.[77] In order to mimic the impact of the solid-state environment on isolated molecules, one viable way is to combine optimally tuned LRC-hybrid functionals with a continuum solvation model, like a polarizable continuum model (PCM), or use a slightly adapted LRC-hybrid functional which takes into account the screening of the Coulomb operator. Alternatively, discrete atomistic models, such as microelectrostatic (ME) schemes (see section 2.4), allow for taking into account permanent (static) and induced (dynamic) electrostatic

interactions between localized charges and neutral excitations with their polarizable molecular environment, starting from the molecular electronic structure computed at the DFT level.[90]

In order to fully understand and correctly model the electronic processes occurring at the D:A interface, a realistic description of the local morphology both of molecules in the bulk and at the heterojunction is mandatory. The performances of an OSC based on organic semiconductors thin film depend crucially on the morphology at the D:A interface, which in turn has a critical impact on the strength of electronic couplings between the D and A states (being sensitive to the relative position and orientation of the interacting partners) and even more so on the exciton dissociation and charge transport. Nonetheless, a recent work have highlighted the importance of achieving morphology control, which correlates morphology-related properties (like short-circuit current and fill factor) with PCE in D:fullerenes BHJ OSCs.[91] Such a high degree of control can only be obtained by understanding the subtle relationship between the supramolecular structure-interfacial morphology and the electronic properties of the organic materials used in the active layers. Although DFT is often used in the modelling of D:A complexes, the local morphology at the interface is usually obtained by atomistic molecular dynamics (MD) simulations (see an example in Figure 1.5), which are able to treat disordered large molecular systems at a finite temperature and grasp energetic disorder effects, either of static (positional) or dynamic nature in time.[92]

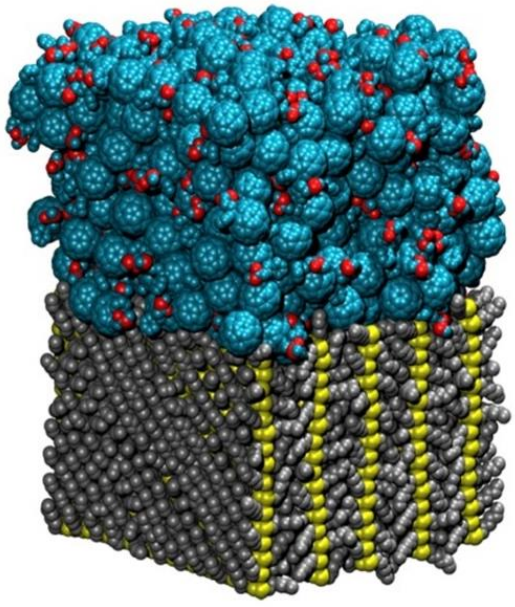

Figure 1.5: A poly(3-hexylthiophene) (P3HT) / phenyl-C61-butyric acid methyl ester ($PC_{61}BM$) heterointerface obtained by means of atomistic molecular dynamics (MD) simulation, adopting a united-atom force field. The sample consists of 5 stacks of 16 P3HT 20-mers (bottom) and 400 $PC_{61}BM$ molecules (topmost). Picture taken from Ref.[48].

The affordable catch is that MD does not treat electrons explicitly, under the assumption that the quantum properties of atoms and molecules and their interaction potentials do not change significantly during the time span of the simulations, whose duration must be long enough to cover the relevant processes of equilibration and evolution of the system. The energy of the molecular system then is expressed by a sum of effective many-body interaction terms through analytical functions and parameters, which define a classical force field. Moreover, MD simulations can deal with large system sizes, up to millions of atoms. Provided that the force field is re-parameterized against high-level of theory calculations (like DFT or post-HF methods) and validated, atomistic MD simulations can provide an accurate description of D:A interfaces.

The electron transfer from a D to an A molecule resulting in the formation of a CT state is a very efficient process and it can be considered as a redox reaction. In 1956 Marcus developed a theory to explain the rate of an electron transfer reaction and, nowadays, Marcus theory[93] is widely used by research to model the kinetics of the utmost photophysical processes in an OSC. For instance, in the semiclassical limit, the rate of the back-electron transfer (*i.e.,* recombination) from the CT state to the ground state follows the equation:

$$\kappa_{nrad} = \frac{2\pi}{\hbar} J_{CT-GS}^2 \sqrt{\frac{1}{4\pi\lambda_{CT} k_B T}} \times \exp\left[-\frac{(-\mathrm{E}_{CT}^{0,0}+\lambda_{CT})^2}{4\lambda_{CT} k_B T}\right] \quad (1.3)$$

where $\hbar$ is the reduced Planck's constant, J_{CT-GS} is the electronic coupling between those states, k_B is the Boltzmann constant, T is the temperature in Kelvin, λ_{CT} is the reorganization energy involved in the process and $E_{CT}^{0,0}$ is the energy of the relaxed CT state. In this framework vibrational modes are treated classically, but a significant part of the reorganization energy (0.2-0.3 eV)[94] comes from high-frequency vibrational modes, which require a quantum treatment: an extension of the Marcus theory, referred as Marcus-Levich-Jortner (MLJ) expression, is often used to account for quantum effects. It is worth stressing that Marcus theory can be used also for modeling the kinetics of exciton dissociation, CT formation, charge recombination and charge diffusion,[95,96] provided that the parameters entering the equation, like electronic couplings (or transfer integrals), reorganization energies and the free Gibbs energies, describe the reaction one wants to investigate. As an example, having access to the electronic coupling between HOMOs (LUMOs) on neighboring molecules is mandatory for modelling hole (electron) transport via hopping, whilst the electronic coupling between a LUMO on the D and a LUMO on the A is relevant for exciton dissociation. Electronic couplings can be assessed with DFT calculations or even with a lower-level of theory, like the intermediate neglect of differential overlap (INDO) method, which belongs to the class of semiempirical methods, successfully employed in the rates calculations for exciton dissociation and charge recombination in prototypical D:A systems.[97,98]

1.3 Objective of the Thesis

The above-mentioned computational tools can be exploited separately or combined, according to the properties of interest of organic π-conjugated molecules in the condensed phase or for shedding some light on parameters that cannot be easily accessed experimentally. Nevertheless, for a complete rationalization of all the processes which take place in an organic semiconductor device at different length- and timescale, multilevel computational approaches combining several techniques are so far the best option.[26] In such a methodology, classical force field MD simulations are typically run for studying the molecular packing behavior in large systems like bulk crystalline or amorphous phases or D:A bilayers or blends. An MD output is a trajectory of all the atomic nuclear coordinates and the dynamic and structural properties of the system can be analysed. Fragments can be extracted from the MD snapshots and then one carries out electronic structure calculations to evaluate the opto-electronic properties as well as electronic parameters and couplings. These parameters can be used as inputs in kinetic Monte Carlo (KMC) simulations for charge or exciton diffusion over large dimensions and long timescale or in ME models to assess the energetic landscape over large areas.

The scope of this thesis is to provide examples where we have resorted to a combination of two or more of these computational methodologies in order to model different topics in the organic semiconductors' community. The common denominator in our research is the application of electronic structure calculations in conjunction with a ME model:[77,90] this dualism has proven itself to be necessary whenever the solid-state energetic landscape of large-scale, complex systems is investigated, although hybridization of molecular orbitals and delocalization of charges and excitations cannot be grasped. In our ME model, the charges are fully localized on molecular units that interact through classical electrostatic forces, under the assumption of zero intermolecular overlap.[99] Molecules are described classically in terms of permanent charges and anisotropic polarizable points (induced dipoles) located at each atomic position. Provided that a careful parametrization of atomic charges and polarizabilities is carried out with DFT calculations, this ME approach can yield qualitative agreements with experimental data in terms of charge transport energy levels and exciton binding energies. The inclusion of long-range electrostatic effects is of relevance, since the IP and EA of molecules in a solid-state environment and the corresponding CT excitation energies depend (often strongly) on mutual intermolecular electrostatic interactions.

The outline of the thesis is structured in the following manner. In Chapter 2, we review most of the theoretical methods used in this manuscript, *i.e.*, DFT and TDDFT. Then, particular attention is paid to RSH hybrid functionals and their applications and how to deal with solid-state environmental effects. In Chapter 3, we compare two small π-conjugated D-bridge-A organic molecules, slightly different in their chemical structures, but largely different in the transport of singlet excitons in amorphous thin films. To achieve an in-depth microscopic picture for the relationships between the chemical structure and the nature of the lowest electronic excitations, we provide a fully atomistic modelling study of the broad energetic landscape and dynamics of singlet electronic excitations in solid films of the two materials, by combining MD/TDDFT/ME methods. Then, transport of singlet

excitons across the pristine thin film is described by performing KMC simulations, which yield the macroscopic properties of interest, such as the diffusion coefficients and the exciton diffusion lengths of the two materials. In Chapter 4, we discuss the existence of multiple electronic CT states in amorphous D:A BHJ blends with large frontier orbital energy offset and their contributions to the photocurrent. We also focus on the energetic and dynamics of interfacial low-lying electronic CT states, by unravelling the different role exerted by static and dynamic disorder to the density of states of the CT states manifold with a combined MD/(TD)DFT/ME computational protocol. We conclude this Chapter by assessing the fast recombination (~ps) from the lowest CT states to the ground state, that should overcome charge separation, hence rendering these tail states silent in EQE measurements. Finally, in Chapter 5 we deal with the role of local environmental interactions on the generation of free charge carriers in doped binary and ternary blends. DFT/ME calculations show a dual effect of molecular quadrupoles of host and dopant molecules on molecular doping, affecting both the ionization (by reshuffling the energy levels of the dopant and the host) and the charge dissociation step (by creating a favourable energy pathway for the hole). In Chapter 6 we draw the summary of the present work and lay down some perspectives in the still bright field of OSCs.

References

(1) Ameri, T.; Dennler, G.; Lungenschmied, C.; Brabec, C. J. Organic Tandem Solar Cells: A Review. *Energy Environ. Sci.* **2009**, *2* (4), 347–363.

(2) Burroughes, J. H.; Bradley, D. D. C.; Brown, A. R.; Marks, R. N.; Mackay, K.; Friend, R. H.; Burns, P. L.; Holmes, A. B. Light-Emitting Diodes Based on Conjugated Polymers. *Nature* **1990**, *347* (6293), 539–541.

(3) Baldo, M. A.; O'Brien, D. F.; You, Y.; Shoustikov, A.; Sibley, S.; Thompson, M. E.; Forrest, S. R. Highly Efficient Phosphorescent Emission from Organic Electroluminescent Devices. *Nature* **1998**, *395* (6698), 151–154.

(4) Friend, R. H.; Gymer, R. W.; Holmes, A. B.; Burroughes, J. H.; Marks, R. N.; Taliani, C.; Bradley, D. D. C.; Dos Santos, D. A.; Brédas, J. L.; Lögdlund, M.; Salaneck, W. R. Electroluminescence in Conjugated Polymers. *Nature*. 1999, pp 121–128.

(5) Allard, S.; Forster, M.; Souharce, B.; Thiem, H.; Scherf, U. Organic Semiconductors for Solution-Processable Field-Effect Transistors (OFETs). *Angew. Chemie Int. Ed.* **2008**, *47* (22), 4070–4098.

(6) Torsi, L.; Magliulo, M.; Manoli, K.; Palazzo, G. Organic Field-Effect Transistor Sensors: A Tutorial Review. *Chem. Soc. Rev.* **2013**, *42* (22), 8612–8628.

(7) Sirringhaus, H. 25th Anniversary Article: Organic Field-Effect Transistors: The Path Beyond Amorphous Silicon. *Adv. Mater.* **2014**, *26* (9), 1319–1335.

(8) Tang, C. W. Two-layer Organic Photovoltaic Cell. *Appl. Phys. Lett.* **1986**, *48* (2), 183–185.

(9) Scharber, M. C.; Mühlbacher, D.; Koppe, M.; Denk, P.; Waldauf, C.; Heeger, A. J.; Brabec, C. J. Design Rules for Donors in Bulk-Heterojunction Solar Cells—Towards 10 % Energy-Conversion Efficiency. *Adv. Mater.* **2006**, *18* (6), 789–794.

(10) Dennler, G.; Scharber, M. C.; Brabec, C. J. Polymer-Fullerene Bulk-Heterojunction Solar Cells. *Adv. Mater.* **2009**, *21* (13), 1323–1338.

(11) Nelson, J. Polymer:Fullerene Bulk Heterojunction Solar Cells. *Mater. Today* **2011**, *14* (10), 462–470.

(12) Wang, T.; Kupgan, G.; Brédas, J.-L. Organic Photovoltaics: Relating Chemical Structure, Local Morphology, and Electronic Properties. *Trends Chem.* **2020**, *2* (6), 535–554.

(13) Zhao, J.; Li, Y.; Yang, G.; Jiang, K.; Lin, H.; Ade, H.; Ma, W.; Yan, H. Efficient Organic Solar Cells Processed from Hydrocarbon Solvents. *Nat. Energy* **2016**, *1* (2), 15027.

(14) Li, Z.; Ying, L.; Zhu, P.; Zhong, W.; Li, N.; Liu, F.; Huang, F.; Cao, Y. A Generic Green Solvent Concept Boosting the Power Conversion Efficiency of All-Polymer Solar Cells to

11%. *Energy Environ. Sci.* **2019**, *12* (1), 157–163.

(15) Liu, Q.; Jiang, Y.; Jin, K.; Qin, J.; Xu, J.; Li, W.; Xiong, J.; Liu, J.; Xiao, Z.; Sun, K.; Yang, S.; Zhang, X.; Ding, L. 18% Efficiency Organic Solar Cells. *Sci. Bull.* **2020**, *65* (4), 272–275.

(16) Cui, Y.; Yao, H.; Zhang, J.; Zhang, T.; Wang, Y.; Hong, L.; Xian, K.; Xu, B.; Zhang, S.; Peng, J.; Wei, Z.; Gao, F.; Hou, J. Over 16% Efficiency Organic Photovoltaic Cells Enabled by a Chlorinated Acceptor with Increased Open-Circuit Voltages. *Nat. Commun.* **2019**, *10* (1), 2515.

(17) Cui, Y.; Yao, H.; Hong, L.; Zhang, T.; Tang, Y.; Lin, B.; Xian, K.; Gao, B.; An, C.; Bi, P.; Ma, W.; Hou, J. Organic Photovoltaic Cell with 17% Efficiency and Superior Processability. *Natl. Sci. Rev.* **2020**, *7* (7), 1239–1246.

(18) Risko, C.; Brédas, J.-L. Small Optical Gap Molecules and Polymers: Using Theory to Design More Efficient Materials for Organic Photovoltaics. In *Top Curr Chem*; Springer, Berlin, Heidelberg, 2013; Vol. 352, pp 1–38.

(19) Zhang, G.; Zhao, J.; Chow, P. C. Y.; Jiang, K.; Zhang, J.; Zhu, Z.; Zhang, J.; Huang, F.; Yan, H. Nonfullerene Acceptor Molecules for Bulk Heterojunction Organic Solar Cells. *Chem. Rev.* **2018**, *118* (7), 3447–3507.

(20) Zhang, H.; Yao, H.; Hou, J.; Zhu, J.; Zhang, J.; Li, W.; Yu, R.; Gao, B.; Zhang, S.; Hou, J. Over 14% Efficiency in Organic Solar Cells Enabled by Chlorinated Nonfullerene Small-Molecule Acceptors. *Adv. Mater.* **2018**, *30* (28), 1800613.

(21) Yuan, J.; Zhang, Y.; Zhou, L.; Zhang, G.; Yip, H. L.; Lau, T. K.; Lu, X.; Zhu, C.; Peng, H.; Johnson, P. A.; Leclerc, M.; Cao, Y.; Ulanski, J.; Li, Y.; Zou, Y. Single-Junction Organic Solar Cell with over 15% Efficiency Using Fused-Ring Acceptor with Electron-Deficient Core. *Joule* **2019**, *3* (4), 1140–1151.

(22) Deibel, C.; Strobel, T.; Dyakonov, V. Role of the Charge Transfer State in Organic Donor–Acceptor Solar Cells. *Adv. Mater.* **2010**, *22* (37), 4097–4111.

(23) Brédas, J.-L.; Norton, J. E.; Cornil, J.; Coropceanu, V. Molecular Understanding of Organic Solar Cells: The Challenges. *Acc. Chem. Res.* **2009**, *42* (11), 1691–1699.

(24) Clarke, T. M.; Durrant, J. R. Charge Photogeneration in Organic Solar Cells. *Chem. Rev.* **2010**, *110* (11), 6736–6767.

(25) Beljonne, D.; Cornil, J.; Muccioli, L.; Zannoni, C.; Brédas, J.-L.; Castet, F. Electronic Processes at Organic−Organic Interfaces: Insight from Modeling and Implications for Opto-Electronic Devices. *Chem. Mater.* **2011**, *23* (3), 591–609.

(26) Cornil, J.; Castet, F.; Beljonne, D. Modeling Organic Solar Cells: What Are the Challenges Ahead? In *Unconventional Thin Film Photovoltaics*; The Royal Society of Chemistry, 2016; pp 367–390.

(27) Athanasopoulos, S.; Hennebicq, E.; Beljonne, D.; Walker, A. B. Trap Limited Exciton Transport in Conjugated Polymers. *J. Phys. Chem. C* **2008**, *112* (30), 11532–11538.

(28) Athanasopoulos, S.; Emelianova, E. V; Walker, A. B.; Beljonne, D. Exciton Diffusion in Energetically Disordered Organic Materials. *Phys. Rev. B* **2009**, *80* (19), 195209.

(29) Menke, S. M.; Holmes, R. J. Exciton Diffusion in Organic Photovoltaic Cells. *Energy Environ. Sci.* **2014**, *7* (2), 499–512.

(30) Vandewal, K. Interfacial Charge Transfer States in Condensed Phase Systems. *Annu. Rev. Phys. Chem.* **2016**, *67* (1), 113–133.

(31) Benduhn, J.; Tvingstedt, K.; Piersimoni, F.; Ullbrich, S.; Fan, Y.; Tropiano, M.; McGarry, K. A.; Zeika, O.; Riede, M. K.; Douglas, C. J.; Barlow, S.; Marder, S. R.; Neher, D.; Spoltore, D.; Vandewal, K. Intrinsic Non-Radiative Voltage Losses in Fullerene-Based Organic Solar Cells. *Nat. Energy* **2017**, *2* (6), 1–6.

(32) Coropceanu, V.; Chen, X.-K.; Wang, T.; Zheng, Z.; Brédas, J.-L. Charge-Transfer Electronic States in Organic Solar Cells. *Nat. Rev. Mater.* **2019**, *4* (11), 689–707.

(33) Lee, J.; Vandewal, K.; Yost, S. R.; Bahlke, M. E.; Goris, L.; Baldo, M. A.; Manca, J. V; Van Voorhis, T. Charge Transfer State Versus Hot Exciton Dissociation in Polymer−Fullerene Blended Solar Cells. *J. Am. Chem. Soc.* **2010**, *132* (34), 11878–11880.

(34) Vandewal, K.; Albrecht, S.; Hoke, E. T.; Graham, K. R.; Widmer, J.; Douglas, J. D.; Schubert, M.; Mateker, W. R.; Bloking, J. T.; Burkhard, G. F.; Sellinger, A.; Fréchet, J. M. J.; Amassian, A.; Riede, M. K.; McGehee, M. D.; Neher, D.; Salleo, A. Efficient Charge Generation by Relaxed Charge-Transfer States at Organic Interfaces. *Nat. Mater.* **2014**, *13* (1), 63–68.

(35) Grancini, G.; Maiuri, M.; Fazzi, D.; Petrozza, A.; Egelhaaf, H.-J.; Brida, D.; Cerullo, G.; Lanzani, G. Hot Exciton Dissociation in Polymer Solar Cells. *Nat. Mater.* **2013**, *12* (1), 29–33.

(36) Ohkita, H.; Cook, S.; Astuti, Y.; Duffy, W.; Tierney, S.; Zhang, W.; Heeney, M.; McCulloch, I.; Nelson, J.; Bradley, D. D. C.; Durrant, J. R. Charge Carrier Formation in Polythiophene/Fullerene Blend Films Studied by Transient Absorption Spectroscopy. *J. Am. Chem. Soc.* **2008**, *130* (10), 3030–3042.

(37) Shoaee, S.; Clarke, T. M.; Huang, C.; Barlow, S.; Marder, S. R.; Heeney, M.; McCulloch, I.; Durrant, J. R. Acceptor Energy Level Control of Charge Photogeneration in Organic Donor/Acceptor Blends. *J. Am. Chem. Soc.* **2010**, *132* (37), 12919–12926.

(38) Bakulin, A. A.; Rao, A.; Pavelyev, V. G.; van Loosdrecht, P. H. M.; Pshenichnikov, M. S.; Niedzialek, D.; Cornil, J.; Beljonne, D.; Friend, R. H. The Role of Driving Energy and Delocalized States for Charge Separation in Organic Semiconductors. *Science* **2012**, *335* (6074), 1340 LP – 1344.

(39) Provencher, F.; Bérubé, N.; Parker, A. W.; Greetham, G. M.; Towrie, M.; Hellmann, C.; Côté, M.; Stingelin, N.; Silva, C.; Hayes, S. C. Direct Observation of Ultrafast Long-Range Charge Separation at Polymer–Fullerene Heterojunctions. *Nat. Commun.* **2014**, *5* (1), 4288.

(40) Bässler, H.; Köhler, A. "Hot or Cold": How Do Charge Transfer States at the Donor–Acceptor Interface of an Organic Solar Cell Dissociate? *Phys. Chem. Chem. Phys.* **2015**, *17* (43), 28451–28462.

(41) Tamura, H.; Burghardt, I. Ultrafast Charge Separation in Organic Photovoltaics Enhanced by Charge Delocalization and Vibronically Hot Exciton Dissociation. *J. Am. Chem. Soc.* **2013**, *135* (44), 16364–16367.

(42) Savoie, B. M.; Rao, A.; Bakulin, A. A.; Gelinas, S.; Movaghar, B.; Friend, R. H.; Marks, T. J.; Ratner, M. A. Unequal Partnership: Asymmetric Roles of Polymeric Donor and Fullerene Acceptor in Generating Free Charge. *J. Am. Chem. Soc.* **2014**, *136* (7), 2876–2884.

(43) Gélinas, S.; Rao, A.; Kumar, A.; Smith, S. L.; Chin, A. W.; Clark, J.; van der Poll, T. S.; Bazan, G. C.; Friend, R. H. Ultrafast Long-Range Charge Separation in Organic Semiconductor Photovoltaic Diodes. *Science* **2014**, *343* (6170), 512 LP – 516.

(44) Caruso, D.; Troisi, A. Long-Range Exciton Dissociation in Organic Solar Cells. *Proc. Natl. Acad. Sci.* **2012**, *109* (34), 13498 LP – 13502.

(45) Vandewal, K.; Ma, Z.; Bergqvist, J.; Tang, Z.; Wang, E.; Henriksson, P.; Tvingstedt, K.; Andersson, M. R.; Zhang, F.; Inganäs, O. Quantification of Quantum Efficiency and Energy Losses in Low Bandgap Polymer:Fullerene Solar Cells with High Open-Circuit Voltage. *Adv. Funct. Mater.* **2012**, *22* (16), 3480–3490.

(46) Dimitrov, S. D.; Bakulin, A. A.; Nielsen, C. B.; Schroeder, B. C.; Du, J.; Bronstein, H.; McCulloch, I.; Friend, R. H.; Durrant, J. R. On the Energetic Dependence of Charge Separation in Low-Band-Gap Polymer/Fullerene Blends. *J. Am. Chem. Soc.* **2012**, *134* (44), 18189–18192.

(47) Hahn, T.; Geiger, J.; Blase, X.; Duchemin, I.; Niedzialek, D.; Tscheuschner, S.; Beljonne, D.; Bässler, H.; Köhler, A. Does Excess Energy Assist Photogeneration in an Organic Low-Bandgap Solar Cell? *Adv. Funct. Mater.* **2015**, *25* (8), 1287–1295.

(48) D'Avino, G.; Mothy, S.; Muccioli, L.; Zannoni, C.; Wang, L.; Cornil, J.; Beljonne, D.; Castet, F. Energetics of Electron–Hole Separation at P3HT/PCBM Heterojunctions. *J. Phys. Chem. C* **2013**, *117* (25), 12981–12990.

(49) D'Avino, G.; Muccioli, L.; Olivier, Y.; Beljonne, D. Charge Separation and Recombination at Polymer-Fullerene Heterojunctions: Delocalization and Hybridization Effects. *J. Phys. Chem. Lett.* **2016**, *7* (3), 536–540.

(50) Vandewal, K.; Tvingstedt, K.; Gadisa, A.; Inganäs, O.; Manca, J. V. Relating the Open-Circuit

Voltage to Interface Molecular Properties of Donor:Acceptor Bulk Heterojunction Solar Cells. *Phys. Rev. B* **2010**, *81* (12), 125204.

(51) Benduhn, J. Ph.D. Thesis, TU Dresden, 2019.

(52) Collado-Fregoso, E.; Pugliese, S. N.; Wojcik, M.; Benduhn, J.; Bar-Or, E.; Perdigón Toro, L.; Hörmann, U.; Spoltore, D.; Vandewal, K.; Hodgkiss, J. M.; Neher, D. Energy-Gap Law for Photocurrent Generation in Fullerene-Based Organic Solar Cells: The Case of Low-Donor-Content Blends. *J. Am. Chem. Soc.* **2019**, *141* (6), 2329–2341.

(53) Liu, J.; Chen, S.; Qian, D.; Gautam, B.; Yang, G.; Zhao, J.; Bergqvist, J.; Zhang, F.; Ma, W.; Ade, H.; Inganäs, O.; Gundogdu, K.; Gao, F.; Yan, H. Fast Charge Separation in a Non-Fullerene Organic Solar Cell with a Small Driving Force. *Nat. Energy* **2016**, *1*, 16089.

(54) Hou, J.; Inganäs, O.; Friend, R. H.; Gao, F. Organic Solar Cells Based on Non-Fullerene Acceptors. *Nat. Mater.* **2018**, *17*, 119.

(55) Qian, D.; Zheng, Z.; Yao, H.; Tress, W.; Hopper, T. R.; Chen, S.; Li, S.; Liu, J.; Chen, S.; Zhang, J.; Liu, X.-K.; Gao, B.; Ouyang, L.; Jin, Y.; Pozina, G.; Buyanova, I. A.; Chen, W. M.; Inganäs, O.; Coropceanu, V.; Brédas, J.-L.; Yan, H.; Hou, J.; Zhang, F.; Bakulin, A. A.; Gao, F. Design Rules for Minimizing Voltage Losses in High-Efficiency Organic Solar Cells. *Nat. Mater.* **2018**, *17* (8), 703–709.

(56) Menke, S. M.; Ran, N. A.; Bazan, G. C.; Friend, R. H. Understanding Energy Loss in Organic Solar Cells: Toward a New Efficiency Regime. *Joule* **2018**, *2* (1), 25–35.

(57) Li, W.; Hendriks, K. H.; Furlan, A.; Wienk, M. M.; Janssen, R. A. J. High Quantum Efficiencies in Polymer Solar Cells at Energy Losses below 0.6 EV. *J. Am. Chem. Soc.* **2015**, *137* (6), 2231–2234.

(58) Kawashima, K.; Tamai, Y.; Ohkita, H.; Osaka, I.; Takimiya, K. High-Efficiency Polymer Solar Cells with Small Photon Energy Loss. *Nat. Commun.* **2015**, *6* (1), 10085.

(59) Coffey, D. C.; Larson, B. W.; Hains, A. W.; Whitaker, J. B.; Kopidakis, N.; Boltalina, O. V; Strauss, S. H.; Rumbles, G. An Optimal Driving Force for Converting Excitons into Free Carriers in Excitonic Solar Cells. *J. Phys. Chem. C* **2012**, *116* (16), 8916–8923.

(60) Falke, S. M.; Rozzi, C. A.; Brida, D.; Maiuri, M.; Amato, M.; Sommer, E.; De Sio, A.; Rubio, A.; Cerullo, G.; Molinari, E.; Lienau, C. Coherent Ultrafast Charge Transfer in an Organic Photovoltaic Blend. *Science* **2014**, *344* (6187), 1001 LP – 1005.

(61) Yan, C.; Barlow, S.; Wang, Z.; Yan, H.; Jen, A. K.-Y.; Marder, S. R.; Zhan, X. Non-Fullerene Acceptors for Organic Solar Cells. *Nat. Rev. Mater.* **2018**, *3*, 18003.

(62) Chen, S.; Wang, Y.; Zhang, L.; Zhao, J.; Chen, Y.; Zhu, D.; Yao, H.; Zhang, G.; Ma, W.; Friend, R. H.; Chow, P. C. Y.; Gao, F.; Yan, H. Efficient Nonfullerene Organic Solar Cells with Small Driving Forces for Both Hole and Electron Transfer. *Adv. Mater.* **2018**, *30* (45),

1804215.

(63) Baran, D.; Kirchartz, T.; Wheeler, S.; Dimitrov, S.; Abdelsamie, M.; Gorman, J.; Ashraf, R. S.; Holliday, S.; Wadsworth, A.; Gasparini, N.; Kaienburg, P.; Yan, H.; Amassian, A.; Brabec, C. J.; Durrant, J. R.; McCulloch, I. Reduced Voltage Losses Yield 10% Efficient Fullerene Free Organic Solar Cells with >1 V Open Circuit Voltages. *Energy Environ. Sci.* **2016**, *9* (12), 3783–3793.

(64) Rau, U. Reciprocity Relation between Photovoltaic Quantum Efficiency and Electroluminescent Emission of Solar Cells. *Phys. Rev. B* **2007**, *76* (8), 85303.

(65) Walzer, K.; Maennig, B.; Pfeiffer, M.; Leo, K. Highly Efficient Organic Devices Based on Electrically Doped Transport Layers. *Chem. Rev.* **2007**, *107* (4), 1233–1271.

(66) Lüssem, B.; Riede, M.; Leo, K. Front Cover: Doping of Organic Semiconductors (Phys. Status Solidi A 1/2013). *Phys. status solidi* **2013**, *210* (1).

(67) Tietze, M. L.; Pahner, P.; Schmidt, K.; Leo, K.; Lüssem, B. Doped Organic Semiconductors: Trap-Filling, Impurity Saturation, and Reserve Regimes. *Adv. Funct. Mater.* **2015**, *25* (18), 2701–2707.

(68) Schwarze, M.; Tress, W.; Beyer, B.; Gao, F.; Scholz, R.; Poelking, C.; Ortstein, K.; Günther, A. A.; Kasemann, D.; Andrienko, D.; Leo, K. Band Structure Engineering in Organic Semiconductors. *Science* **2016**, *352* (6292), 1446–1449.

(69) Tietze, M. L.; Benduhn, J.; Pahner, P.; Nell, B.; Schwarze, M.; Kleemann, H.; Krammer, M.; Zojer, K.; Vandewal, K.; Leo, K. Elementary Steps in Electrical Doping of Organic Semiconductors. *Nat. Commun.* **2018**, *9* (1), 1182.

(70) Li, J.; Duchemin, I.; Roscioni, O. M.; Friederich, P.; Anderson, M.; Da Como, E.; Kociok-Köhn, G.; Wenzel, W.; Zannoni, C.; Beljonne, D.; Blase, X.; D'Avino, G. Host Dependence of the Electron Affinity of Molecular Dopants. *Mater. Horizons* **2019**, *6* (1), 107–114.

(71) Salzmann, I.; Heimel, G.; Oehzelt, M.; Winkler, S.; Koch, N. Molecular Electrical Doping of Organic Semiconductors: Fundamental Mechanisms and Emerging Dopant Design Rules. *Acc. Chem. Res.* **2016**, *49* (3), 370–378.

(72) Privitera, A.; Londi, G.; Riede, M.; D'Avino, G.; Beljonne, D. Molecular Quadrupole Moments Promote Ground-State Charge Generation in Doped Organic Semiconductors. *Adv. Funct. Mater.* **2020**, *30*, 2004600.

(73) Wang, S.-J.; Venkateshvaran, D.; Mahani, M. R.; Chopra, U.; McNellis, E. R.; Di Pietro, R.; Schott, S.; Wittmann, A.; Schweicher, G.; Cubukcu, M.; Kang, K.; Carey, R.; Wagner, T. J.; Siebrecht, J. N. M.; Wong, D. P. G. H.; Jacobs, I. E.; Aboljadayel, R. O.; Ionescu, A.; Egorov, S. A.; Mueller, S.; Zadvorna, O.; Skalski, P.; Jellett, C.; Little, M.; Marks, A.; McCulloch, I.; Wunderlich, J.; Sinova, J.; Sirringhaus, H. Long Spin Diffusion Lengths in Doped Conjugated

Polymers Due to Enhanced Exchange Coupling. *Nat. Electron.* **2019**, *2* (3), 98–107.

(74) Fratini, S.; Nikolka, M.; Salleo, A.; Schweicher, G.; Sirringhaus, H. Charge Transport in High-Mobility Conjugated Polymers and Molecular Semiconductors. *Nat. Mater.* **2020**, *19* (5), 491–502.

(75) Arvind, M.; Tait, C. E.; Guerrini, M.; Krumland, J.; Valencia, A. M.; Cocchi, C.; Mansour, A. E.; Koch, N.; Barlow, S.; Marder, S. R.; Behrends, J.; Neher, D. Quantitative Analysis of Doping-Induced Polarons and Charge-Transfer Complexes of Poly(3-Hexylthiophene) in Solution. *J. Phys. Chem. B* **2020**, *124* (35), 7694–7708.

(76) Yurash, B.; Cao, D. X.; Brus, V. V.; Leifert, D.; Wang, M.; Dixon, A.; Seifrid, M.; Mansour, A. E.; Lungwitz, D.; Liu, T.; Santiago, P. J.; Graham, K. R.; Koch, N.; Bazan, G. C.; Nguyen, T. Q. Towards Understanding the Doping Mechanism of Organic Semiconductors by Lewis Acids. *Nat. Mater.* **2019**, *18* (12), 1327–1334.

(77) D'Avino, G.; Muccioli, L.; Castet, F.; Poelking, C.; Andrienko, D.; Soos, Z. G.; Cornil, J.; Beljonne, D. Electrostatic Phenomena in Organic Semiconductors: Fundamentals and Implications for Photovoltaics. *J. Phys. Condens. Matter* **2016**, *28* (43).

(78) Körzdörfer, T.; Brédas, J. L. Organic Electronic Materials: Recent Advances in the Dft Description of the Ground and Excited States Using Tuned Range-Separated Hybrid Functionals. *Acc. Chem. Res.* **2014**, *47* (11), 3284–3291.

(79) Brédas, J.-L.; Chen, X.; Körzdörfer, T.; Li, H.; Risko, C.; Ryno, S.; Wang, T. *Recent Advances in the Computational Characterization of π-Conjugated Organic Semiconductors*; Boca Raton, 2019.

(80) Hohenberg, P.; Kohn, W. Inhomogeneous Electron Gas. *Phys. Rev.* **1964**, *136* (3B), B864–B871.

(81) Kohn, W.; Sham, L. J. Self-Consistent Equations Including Exchange and Correlation Effects. *Phys. Rev.* **1965**, *140* (4A), A1133–A1138.

(82) Yost, S. R.; Hontz, E.; McMahon, D. P.; Van Voorhis, T. Electronic and Optical Properties at Organic/Organic Interfaces in Organic Solar Cells. In *Top Curr Chem*; Springer, Berlin, Heidelberg, 2014; Vol. 352, pp 103–150.

(83) Richard, R. M.; Marshall, M. S.; Dolgounitcheva, O.; Ortiz, J. V; Brédas, J.-L.; Marom, N.; Sherrill, C. D. Accurate Ionization Potentials and Electron Affinities of Acceptor Molecules I. Reference Data at the CCSD(T) Complete Basis Set Limit. *J. Chem. Theory Comput.* **2016**, *12* (2), 595–604.

(84) Gallandi, L.; Marom, N.; Rinke, P.; Körzdörfer, T. Accurate Ionization Potentials and Electron Affinities of Acceptor Molecules II: Non-Empirically Tuned Long-Range Corrected Hybrid Functionals. *J. Chem. Theory Comput.* **2016**, *12* (2), 605–614.

(85) Knight, J. W.; Wang, X.; Gallandi, L.; Dolgounitcheva, O.; Ren, X.; Ortiz, J. V.; Rinke, P.; Körzdörfer, T.; Marom, N. Accurate Ionization Potentials and Electron Affinities of Acceptor Molecules III: A Benchmark of GW Methods. *J. Chem. Theory Comput.* **2016**, *12* (2), 615–626.

(86) Runge, E.; Gross, E. K. U. Density-Functional Theory for Time-Dependent Systems. *Phys. Rev. Lett.* **1984**, *52* (12), 997–1000.

(87) Casida, M. E. Time-Dependent Density Functional Response Theory for Molecules. In *Recent Advances in Density Functional Methods*; Recent Advances in Computational Chemistry; World Scientific, 1995; Vol. 1, pp 155–192.

(88) Brédas, J. L. Organic Electronics: Does a Plot of the HOMO–LUMO Wave Functions Provide Useful Information? *Chem. Mater.* **2017**, *29* (2), 477–478.

(89) Baer, R.; Neuhauser, D. Density Functional Theory with Correct Long-Range Asymptotic Behavior. *Phys. Rev. Lett.* **2005**, *94* (4), 43002.

(90) D'Avino, G.; Muccioli, L.; Zannoni, C.; Beljonne, D.; Soos, Z. G.; D'Avino, G.; Muccioli, L.; Zannoni, C.; Beljonne, D.; Soos, Z. G.; D'Avino, G.; Muccioli, L.; Zannoni, C.; Beljonne, D.; Soos, Z. G. Electronic Polarization in Organic Crystals: A Comparative Study of Induced Dipoles and Intramolecular Charge Redistribution Schemes. *J. Chem. Theory Comput.* **2014**, *10* (11), 4959–4971.

(91) Jackson, N. E.; Savoie, B. M.; Marks, T. J.; Chen, L. X.; Ratner, M. A. The Next Breakthrough for Organic Photovoltaics? *J. Phys. Chem. Lett.* **2015**, *6* (1), 77–84.

(92) Roscioni, O. M.; Zannoni, C. Molecular Dynamics Simulations and Their Application to Thin-Film Devices. In *Unconventional Thin Film Photovoltaics*; The Royal Society of Chemistry, 2016; pp 391–419.

(93) Marcus, R. A. On the Theory of Oxidation-Reduction Reactions Involving Electron Transfer. I. *J. Chem. Phys.* **1956**, *24* (5), 966–978.

(94) Coropceanu, V.; Cornil, J.; da Silva Filho, D. A.; Olivier, Y.; Silbey, R.; Brédas, J.-L. Charge Transport in Organic Semiconductors. *Chem. Rev.* **2007**, *107* (4), 926–952.

(95) Pelzer, K. M.; Darling, S. B. Charge Generation in Organic Photovoltaics: A Review of Theory and Computation. *Mol. Syst. Des. Eng.* **2016**, *1* (1), 10–24.

(96) Few, S.; Frost, J. M.; Nelson, J. Models of Charge Pair Generation in Organic Solar Cells. *Phys. Chem. Chem. Phys.* **2015**, *17* (4), 2311–2325.

(97) Yi, Y.; Coropceanu, V.; Brédas, J.-L. Exciton-Dissociation and Charge-Recombination Processes in Pentacene/C60 Solar Cells: Theoretical Insight into the Impact of Interface Geometry. *J. Am. Chem. Soc.* **2009**, *131* (43), 15777–15783.

(98) Yi, Y.; Coropceanu, V.; Brédas, J.-L. A Comparative Theoretical Study of Exciton-Dissociation and Charge-Recombination Processes in Oligothiophene/Fullerene and Oligothiophene/Perylenediimide Complexes for Organic Solar Cells. *J. Mater. Chem.* **2011**, *21* (5), 1479–1486.

(99) D'Avino, G.; Vanzo, D.; Soos, Z. G. Dielectric Properties of Crystalline Organic Molecular Films in the Limit of Zero Overlap. *J. Chem. Phys.* **2016**, *144* (3), 34702.

(100) Köhler, A.; Beljonne, D. The Singlet–Triplet Exchange Energy in Conjugated Polymers. *Adv. Funct. Mater.* **2004**, *14* (1), 11–18.

(101) Adachi, C.; Baldo, M. A.; Thompson, M. E.; Forrest, S. R. Nearly 100% Internal Phosphorescence Efficiency in an Organic Light Emitting Device. *J. Appl. Phys.* **2001**, *90* (10), 5048–5051.

(102) Olivier, Y.; Yurash, B.; Muccioli, L.; D'Avino, G.; Mikhnenko, O.; Sancho-García, J. C.; Adachi, C.; Nguyen, T.-Q.; Beljonne, D. Nature of the Singlet and Triplet Excitations Mediating Thermally Activated Delayed Fluorescence. *Phys. Rev. Mater.* **2017**, *1* (7), 75602.

(103) Benduhn, J.; Piersimoni, F.; Londi, G.; Kirch, A.; Widmer, J.; Koerner, C.; Beljonne, D.; Neher, D.; Spoltore, D.; Vandewal, K. Impact of Triplet Excited States on the Open-Circuit Voltage of Organic Solar Cells. *Adv. Energy Mater.* **2018**, *8* (21), 1800451.

2. Methods

In this Chapter, we review the basics of density functional theory (DFT) and time-dependent DFT (TDDFT). The passionate reader will find a comprehensive treatment of these electronic structure methods in several textbooks[1–4] and perspectives.[5–12] Then, we dwell upon range-separated hybrid (RSH) functionals[13,14] and their role in healing the well-known problems of (TD)DFT in the characterization of fundamental and optical gaps, as well as intermolecular charge-transfer (CT) excitations. Finally, we deal with how to properly take into account in a calculation solid-state screening[15] and electrostatic effects,[16] which play a fundamental role in the condensed phase. Atomic units (*a.u.*) are used throughout this Chapter.

2.1 Density Functional Theory

In the Born-Oppenheimer non-relativistic approximation, the time-independent Schrödinger electronic equation for an N-electron molecular system reads:

$$\widehat{\mathcal{H}}_{el}\Psi_{el}(\boldsymbol{r}_i) = E_{el}\Psi_{el}(\boldsymbol{r}_i) \tag{2.1}$$

where $\Psi_{el}(\boldsymbol{r}_i)$ and E_{el} are the electronic wave functions and energies and $\widehat{\mathcal{H}}_{el}$ is the purely electronic Hamiltonian operator:

$$\widehat{\mathcal{H}}_{el} = -\frac{1}{2}\sum_i \nabla_i^2 + \sum_j \sum_{i>j} \frac{1}{r_{ij}} + \sum_i v(\boldsymbol{r}_i) \tag{2.2}$$

The first term is the operator for the kinetic energy of the electrons, the second term represents the repulsion between electrons, r_{ij} being the distance between electrons *i* and *j*. The last term $v(\boldsymbol{r}_i) = -\sum_\alpha \frac{Z_\alpha}{r_{i\alpha}}$ is a one-body operator representing the attraction between the electrons and the nuclei, $r_{i\alpha}$ being the distance between the electrons *i* and the nuclei α. In a more compact expression, the electronic Hamiltonian operator is:

$$\widehat{\mathcal{H}}_{el} = T + V_{ee} + V_{ne} \tag{2.3}$$

Historically, the first approach used in order to solve the many-electron Schrödinger equation was the Hartree-Fock (HF) method, in which the wave function Ψ is approximated by a single Slater determinant[17], satisfying the antisymmetric requirement for fermions;[18] the energy is then minimized according to the variation (minimum) principle:[19]

$$E_0 = \min_{\Psi} \langle \Psi | \widehat{\mathcal{H}} | \Psi \rangle \tag{2.4}$$

where the zero subscript stands for ground state. The exact solution of this eigenvalue problem is very complicated, and it turns out that the N-electron wave function, which depends on 3N spatial

coordinates plus N spin coordinates, contains more information than is needed to describe the quantum state of the system.

By resuming the seminal work of Thomas and Fermi,[20,21] in 1964 Hohenberg and Kohn laid the foundation for DFT.[22] They proved that for molecules with a non-degenerate[a] ground state, the calculation of the ground state molecular energy, likewise other electronic properties that can be expressed as a functional of the density, can be uniquely obtained by the one-particle probability density:

$$\rho(\boldsymbol{r}) = N \sum_{all\ m_s} \int \dots \int |\Psi(\boldsymbol{r}, \boldsymbol{r}_2, \dots, \boldsymbol{r}_N, m_{s1}, .., m_{sN})|^2\, d^3\boldsymbol{r}_2, \dots, d^3\boldsymbol{r}_N \qquad (2.5)$$

which depends on only three variables (x, y, z) and is defined as the probability of finding any electron in a given volume of space around $\boldsymbol{r}$, whose integral over all space gives the total number of electrons $\int \rho(\boldsymbol{r}) dr = N$. With this caveat, the ground state electronic molecular energy E_0 becomes a functional of the ground state electronic density $\rho_0(\boldsymbol{r})$: $E_0 = E_0[\rho_0]$.

In the electronic Hamiltonian (2.2), $v(\boldsymbol{r})$ is the external potential acting on electron *i*, since it is produced by charges external to the system of electrons (the electrostatic field of the nuclei) and is the only term written as a functional of the density (and specific to the system at hands). The first DFT theorem states that the external potential $v(\boldsymbol{r})$ and the number of electrons *N* determine the solutions of the many-electron Schrödinger equation and, for non-degenerate ground states, there exists a "one-to-one" mapping between $v(\boldsymbol{r})$ and $\rho_0(\boldsymbol{r})$. The external potential is a unique functional (up to an arbitrary additive constant) of the ground state electron density and, in turn, $\rho_0(\boldsymbol{r})$ determines univocally and exactly (in principle) the ground state wave function Ψ_0 and energy E_0, as well as other properties. By explicitly emphasizing the direct dependence of the ground state energy E_0 on $v(\boldsymbol{r})$, we write $E_0 = E_v[\rho_0]$ and:

$$E_v[\rho_0] = \langle \Psi | T + V_{ee} + V_{ne} | \Psi \rangle = F[\rho_0] + \int d^3\boldsymbol{r}\, v(\boldsymbol{r}) \rho_0(\boldsymbol{r}) \qquad (2.6)$$

where $V_{ne}[\rho_0] = \int d^3\boldsymbol{r}\, v(\boldsymbol{r}) \rho_0(\boldsymbol{r})$ is known and is system dependent, while the expression of $F[\rho_0] = T[\rho_0] + V_{ee}[\rho_0]$, independent of the external potential, is still nowadays unknown, but the existence of this functional is out of discussion. (From now on, we drop the zero subscript to improve readability).

For the theory to be self-contained, a variational principle is needed. The second DFT theorem states that the true ground state electron density $\rho(\boldsymbol{r})$ minimizes the energy functional $E_v[\rho_{tr}]$, where $\rho_{tr}(\boldsymbol{r})$ is a trial density that satisfies $\int \rho_{tr}(\boldsymbol{r}) d^3\boldsymbol{r} = N$ and $\rho_{tr}(\boldsymbol{r}) \geq 0$, with the inequality such that $E \leq E_v[\rho_{tr}]$. *Stricto sensu,* the variational principle holds only for the exact functional $F[\rho]$, hence for approximate functionals DFT is not anymore supported by the variational principle. Alternatively, one can define separately:

[a] In 1979 Levy extended the DFT theorem to also include degenerate ground states[136].

$$F[\rho] = \min_{\Psi \to \rho} \langle \Psi | T + V_{ee} | \Psi \rangle \tag{2.7}$$

where the minimization runs over all the normalized, antisymmetric N-particle wave functions (*i.e.,* Slater determinants) yielding a given density $\rho(\boldsymbol{r})$ (a N-*representable* density in the jargon[b]), and then:

$$E = \min_{\rho} \{F[\rho] + \int d^3\boldsymbol{r}\, v(\boldsymbol{r})\rho(\boldsymbol{r})\} \tag{2.8}$$

where the minimization runs over all the reasonable (positive) densities satisfying equation (2.5) (the so-called "constrained search" formalism).[23] Therefore, the exact ground state density $\rho(\boldsymbol{r})$ of an interacting N-electron system can be found without solving the electronic Schrödinger equation, provided that:

$$\frac{\delta F[\rho]}{\delta \rho(\boldsymbol{r})} + v(\boldsymbol{r}) = \mu \tag{2.9}$$

where $\frac{\delta F[\rho]}{\delta \rho(\boldsymbol{r})}$ is the functional derivative of F with respect to the density and μ is a Lagrange multiplier ensuring the correct number of electrons. So, concisely, the sum of the kinetic and electron repulsion energies of an N-electron system is a *universal* functional of its density (universal in the sense that it is independent from the external potential) and, if one knew this functional, one could solve for the density and the energy variationally. Yet, no indications were given on how to calculate E from $\rho(\boldsymbol{r})$, nor on how to find $\rho(\boldsymbol{r})$ without finding first the wave function.

A major practical improvement was done in 1965 when Kohn and Sham (KS) (re)-introduced orbitals[c], in order to treat properly the electronic kinetic energy as an explicit functional of the density.[24] They considered a fictitious set of non-interacting electrons, experiencing an external potential $v_s(\boldsymbol{r}_i)$ (the subscript s stand for the reference system) such that the ground state electron density $\rho_s(\boldsymbol{r})$ of the non-interacting system equals the ground state electron density $\rho(\boldsymbol{r})$ of the real interacting one. In the non-interacting system, the one-particle KS Hamiltonian reads:

$$\left(-\frac{1}{2}\nabla^2 + v_s(\boldsymbol{r})\right)\varphi_i^{KS}(\boldsymbol{r}) = \varepsilon_i^{KS}\varphi_i^{KS}(\boldsymbol{r}) \tag{2.10}$$

where, by construction, the ground state wave function Ψ_s is a single Slater determinant of orthonormal KS orbitals φ_i^{KS} of the non-interacting system, the ground state density is obtained from the N lowest KS orbitals $\rho_s(\boldsymbol{r}) = \sum_i \left|\varphi_i^{KS}(\boldsymbol{r})\right|^2$ and ε_i^{KS} are the KS energies. The kinetic energy of non-interacting electrons $T_s[\rho]$ can be evaluated as a sum of orbital contributions:

[b] HK introduced the concept of v-*representability, i.e.,* ground state densities belonging to some external potential. It turns out that not all the densities satisfy this condition and N-*representability* is a looser restriction: every antisymmetric wave function yields a N-*representable* ground state density.

[c] They are spin-orbitals, but here we will deal only with closed-shell approximate functionals, which are a special case in the "unrestricted" KS-DFT for open-shell systems.

$$T_s[\rho] =< \Psi_s|T|\Psi_s >= \sum_i \left\langle \varphi_i \left| -\frac{1}{2}\nabla_i^2 \right| \varphi_i \right\rangle \quad (2.11)$$

and it is reasonable to assume $T_s[\rho]$ as a good approximation for $T[\rho]$ in the $F[\rho]$ functional. The advantage of the KS scheme is the calculation of $T_s[\rho]$, probably the dominant part of $T[\rho]$, indirectly, but exactly via the auxiliary KS orbitals, hoping that $T_s[\rho] \approx T[\rho]$. It is also reasonable to approximate $V_{ee}[\rho]$ with the classical Coulomb self-energy of the electronic distribution (also known as the Hartree potential):

$$V_{ee}[\rho] \approx J[\rho] = \frac{1}{2}\iint \frac{\rho(\boldsymbol{r}_i)\rho(\boldsymbol{r}_j)}{r_{ij}} d^3\boldsymbol{r_i} d^3\boldsymbol{r_j} \quad (2.12)$$

This term does not contain the exchange energy (a quantum effect due to the antisymmetry of the N-electron wave function) and is not free from the self-interaction error (SIE).[25] This spurious interaction of an electron with itself arises from the fact that the electron motion is correlated and in DFT there is no way to distinguish two-particle Coulomb interactions from self-interaction (unlike in wave function theories (WFTs)). The interaction of each electron with the entire electron density (including its own) is included in the Hartree potential. The SIE is then completely removed in the *exact* exchange-correlation (xc) functional, but most of the approximate xc functionals are not free from SIE.

We can now rewrite equation (2.6) by addition and subtraction, so that:

$$F[\rho] = T[\rho] + V_{ee}[\rho] =$$

$$= T_s[\rho] + J[\rho] + T[\rho] - T_s[\rho] + V_{ee}[\rho] - J[\rho] \quad (2.13)$$

and, by consequence, the KS energy functional is:

$$E_v[\rho] = T_s[\rho] + \int d^3\boldsymbol{r}\, v(\boldsymbol{r})\rho(\boldsymbol{r}) + J[\rho] + E_{xc}[\rho] \quad (2.14)$$

where $E_{xc}[\rho] = T[\rho] - T_s[\rho] + V_{ee}[\rho] - J[\rho]$ is the unknown xc functional, composed by kinetic and potential contributions. Variational minimization of equation (2.14) with respect to the KS orbitals leads to the canonical KS equation:

$$\left[-\frac{1}{2}\nabla^2 + v_s[\rho](\boldsymbol{r})\right]\varphi_i(\boldsymbol{r}) = \varepsilon_i\varphi_i(\boldsymbol{r}) \quad (2.15)$$

where $v_s[\rho](\boldsymbol{r}) = v(\boldsymbol{r}) + v_J[\rho](\boldsymbol{r}) + v_{xc}[\rho](\boldsymbol{r})$ and $v_{xc}[\rho](\boldsymbol{r}) = \frac{\delta E_{xc}[\rho]}{\delta\rho(\boldsymbol{r})}$ is the xc potential, which accounts for all non-classical electron interactions. Hence, electrons in atoms, molecules and solids can be regarded as independent particles, moving in a local effective potential. The ground state density of the N-electron interacting system can be found by the one-particle KS equation for the N orbitals and summing the squared of the lowest N occupied orbitals:

$$\rho(\boldsymbol{r}) = \sum_i |\varphi_i(\boldsymbol{r})|^2 \quad (2.16)$$

These equations must be solved self-consistently, since the Coulomb and the xc potential are functionals of the density, as the KS orbitals. Therefore, the solution of the KS equations requires self-consistency with an iterative process, starting from an initial guess for the ground state density that will be used to determine $v_s[\rho](\boldsymbol{r})$. Then, by solving equation (2.15), a new set of KS orbitals will be obtained, the first N of them will serve as the input for the new ground state density in (2.16) and so on. This procedure is repeated until self-consistent field (SCF) is reached, as in the HF method, and it delivers (in principle) the exact density and exact total energy of any interacting, correlated electronic system.

Few considerations are now mandatory. First, the KS orbitals refer to the fictitious reference system of non-interacting electrons, so they have any physical meaning other than providing the exact $\rho(\boldsymbol{r})$. In practice, one finds that the occupied KS orbitals resemble molecular orbitals calculated by the HF theory and they can be used for qualitative discussion of molecular properties. Then, the non-interacting system and the interacting one have the same one-particle density, but the KS ground state wave function Ψ_s and the fully interacting ground state wave function Ψ are in general very different functions: other quantities derived from those wave functions might not be close and, therefore, it is not always safe to approximate $T_s[\rho] \approx T[\rho]$. Finally, if the Koopman's theorem[26] for closed-shell molecules in the HF theory guarantees that each occupied-orbital energy corresponds to the electron removal energy from that orbital, in DFT only by knowing the exact xc functional the highest-occupied KS orbital energy ε_{HOMO}^{KS} would equal the negative of the true ionization potential (IP). Yet, in approximate DFT this is seldom the case. For a finite N-electron system, it turns out that $\varepsilon_{HOMO}^{KS}(N) \approx -IP(N)$ is a reasonable approximation. Unfortunately, $\varepsilon_{LUMO}^{KS}(N)$ is not even close to the negative of the true electron affinity (EA): in fact, $\varepsilon_{LUMO}^{KS}(N) \approx -EA(N) - \Delta_{xc}$, where Δ_{xc} is the so-called "derivative discontinuity", a many-body correction to the KS gap, representing the difference between the highest occupied molecular orbital (HOMO) energy of the (N+1)-electron system and the lowest unoccupied molecular orbital (LUMO) energy of the N-electron system.[27,28]

The best approximation for $E_{xc}[\rho]$ would yield the best results for the electronic ground state properties, but despite all the efforts, its expression is unknown. The quest for the best $E_{xc}[\rho]$ is still a challenge nowadays. Among the large range of proposed xc functionals, the choice for the more convenient one depends on the investigated system and the desired properties. The quality of the results afforded by the selected functional can only be deemed afterwards, comparing the obtained results with the available experimental data. As a first approximation, KS proposed a simple model for $E_{xc}[\rho]$, known as local density approximation (LDA):

$$E_{xc}^{LDA}[\rho] = \int d^3\boldsymbol{r}\, \rho(\boldsymbol{r}) \varepsilon_{xc}^{UEG}(\rho) \tag{2.17}$$

where $\varepsilon_{xc}^{UEG}(\rho)$ is the xc energy density, per unit volume, of a uniform electron gas (UEG) having the local electron density $\rho(\boldsymbol{r})$.[29] In few words: at each point $\boldsymbol{r}$ in space, the xc energy density is approximated by that of an UEG with a density $\rho(\boldsymbol{r})$ everywhere. The LDA xc potential then is:

$$v_{xc}^{LDA}[\rho](\boldsymbol{r}) = \frac{\delta E_{xc}^{LDA}[\rho]}{\delta \rho(\boldsymbol{r})} = \varepsilon_{xc}^{UEG}(\rho(\boldsymbol{r})) + \rho(\boldsymbol{r}) \frac{\delta \varepsilon_{xc}^{UEG}(\rho)}{\delta \rho(\boldsymbol{r})} \tag{2.18}$$

By separating the exchange and the correlation parts in LDA, one can use the Dirac local functional[30] for the exchange energy:

$$E_x^{LDA}[\rho] = -C_x \int d^3\boldsymbol{r}\rho(\boldsymbol{r})^{4/3} \tag{2.19}$$

where C_x is a constant and one can use different analytical parametrizations for the correlation energy. LDA becomes exact in the uniform limit and for non-uniform systems LDA works properly if $\rho(\boldsymbol{r})$ varies extremely slowly with position (*i.e.,* far from nuclei). One of the reasons is that LDA contains a fair amount of error compensation between the exchange and correlation parts. In addition, LDA is not free from SIE and, therefore, the xc potential has the wrong asymptotic behavior of the functional derivative (it goes to zero exponentially fast $v_{xc}^{LDA} \to -e^{-\alpha r}$ in the limit of $r \to \infty$, while it should go like $-\frac{1}{r}$). It turns out that LDA gives accurate results in calculating molecular equilibrium distances (< 5% deviation from experiment), lattice constants of solids (< 2%) and atomic and molecular ground state energies (< 0.5%). On the other hand, molecular atomization energies and bond lengths are highly overestimated. Thus, a further step, beyond LDA, was required.

LDA is a local functional because it involves only the value of $\rho(\boldsymbol{r})$ evaluated at $\boldsymbol{r}$, but an improvement to LDA was given by including a dependence of $E_{xc}[\rho]$ on the local electron density *and* its local gradient $\nabla\rho$. This correction to LDA is called generalized-gradient approximation (GGA):[31,32]

$$E_{xc}^{GGA}[\rho] = \int d^3\boldsymbol{r}\,\rho(\boldsymbol{r})\varepsilon_{xc}^{GGA}(\rho, \nabla\rho) \tag{2.20}$$

One can also write E_{xc}^{GGA} as the sum of the exchange and correlation parts:

$$E_{xc}^{GGA}[\rho] = E_x^{GGA}[\rho] + E_c^{GGA}[\rho] \tag{2.21}$$

Both E_x and E_c are negative and $|E_c|$ is significantly smaller than $|E_x|$, that is the DFT exchange energy, close to the HF exchange. It was clear that any effort to correct LDA should have focused on the improvement of the DFT exchange expression. The exchange part of all GGAs has the expression:[33]

$$E_x^{GGA}[\rho] = \int d^3\boldsymbol{r}\,\rho(\boldsymbol{r})\varepsilon_{xc}^{LDA}(\rho)F_x(s) \tag{2.22}$$

where $F_x(s)$ is the enhancement factor and is written as a function of the dimensionless reduced density gradient. Hundreds of GGA functional exist, developed in the last 40 years: some of them were derived with the aid of empirical parameters, others were not. Reviewing all "The Functional Zoo" is not the purpose of this thesis, but just naming a few (probably the most known): in 1988 the empirical exchange functional proposed by Becke,[31] B88, and the correlation one by Lee, Yang and Parr,[34] LYP, were combined to create BLYP[35] in 1992; then, Perdew, Burke and Ernzerhof[36] in 1996 developed separately a non-empirical functional both for the exchange and the correlation, the PBE. GGAs are defined as *semi-local* in the sense that the xc functional depends both on the density and its first derivatives. Although more accurate atomization energies are usually obtained with GGA

functionals, they miss the exact asymptotic behavior of the functional derivative[37] and they reduce (but do not completely cancel out) the SIE. As an example, in B88 the xc potential decays like $-\frac{1}{r^2}$.

The LDA and GGAs played their crucial part in the success of DFT for the calculation of the electronic structure of atoms, molecules and solids. However, for many purposes they were not accurate enough (by "accuracy" we refer to the "chemical accuracy" of 1 kcal/mol or 0.043 eV). Borrowing an evocative picture by Perdew,[38] the "Jacob's ladder of DFT" (see Figure 2.1) raises up into the heaven of chemical accuracy, starting from the ground level Hartree theory and moving through the LDA and GGAs (first and second rung, respectively).

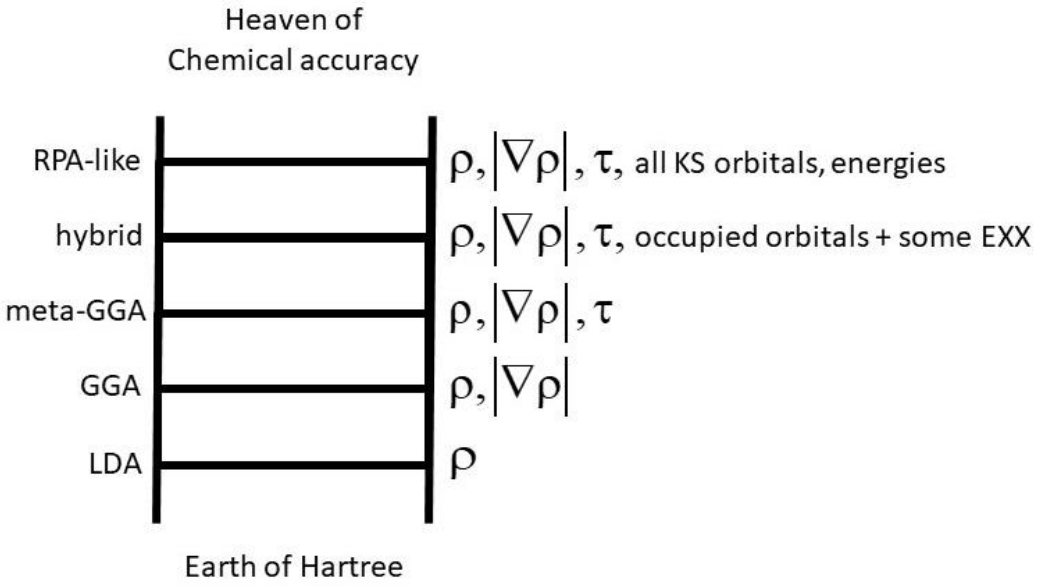

Figure 2.1: Jacob's ladder of DFT. Note that EXX stands for "exact exchange".

In the third rung, meta-GGAs also include a dependence of $E_{xc}[\rho]$ on the second derivatives of the density ∇_ρ^2 and/or on the KS orbital kinetic-energy density:

$$\tau(\boldsymbol{r}) = \frac{1}{2}\sum_i \left|\varphi_i^{KS}(\boldsymbol{r})\right|^2 \tag{2.23}$$

where the sum runs over the occupied KS orbitals. These functionals are partially free from SIE, but the kinetic-energy density is not an explicit functional of the density and the functional derivative cannot be properly evaluated. The dependence of a meta-GGA functional on $\tau(\boldsymbol{r})$ can occur in the exchange part, in the correlation part or in both.

A rung above, global hybrid functionals, widely used within the *generalized* KS scheme,[39] replace a small amount of LDA or GGA local exchange with the exact non-local exchange, a practice based on the adiabatic connection.[40] In DFT, the exchange energy from the Slater determinant is calculated with the same expression as used in the HF theory, but the HF exchange in DFT is *numerically*

different from HF exchange in HF theory, because the KS orbitals are not the same as the HF ones. The HF exchange has the great advantage to cancel out or reducing (depending on the amount) the SIE in a Slater determinant, so that the electron is partly "repelled from itself". The ubiquitous B3LYP[41] and PBE0[42] are classified as global hybrid GGA functionals. Although hybrids often outperform most of the other GGAs and meta-GGAs, they suffer severe and qualitative failures for several properties of interest in organic electronics: for example, they do not solve the fundamental gap problem and they do not describe very well CT excitations. For our purposes, section 2.3 deals with range-separated hybrid (RSH) and long-range corrected (LRC) functionals.[13,14]

Even though DFT is exact, the reasons of its failures hinge on the goodness of the used xc functional and the list of problems grew with increasing of DFT applications. Some of the practical deficiencies include the energy gap dilemma (the KS gap $\varepsilon_{LUMO} - \varepsilon_{HOMO}$ is not equal to the fundamental gap of semiconducting solids, due to lack of Δ_{xc} in the approximate xc functional), the SIE problem, weak van der Waals (dispersive) interactions are missing, strongly correlated systems and CT excitations are poorly treated. Most of these are *non-local* effects and they cannot be treated by local xc functionals. In details:

- the Δ_{xc} is a uniform "jump" in the KS potential, which helps to describe the discontinuity in the chemical potential at integer electron numbers (the electron removal energy is different from the electron insertion energy).[27,28] Part of such discontinuity is given by $T_s[\rho]$ and the remaining discontinuity must be provided by the xc potential $v_{xc}[\rho](\boldsymbol{r})$, since $v(\boldsymbol{r})$ and $v_J[\rho](\boldsymbol{r})$ are continuous in $\rho(\boldsymbol{r})$. Unfortunately, standard LDA and GGA functionals cannot exhibit any Δ_{xc} in $v_{xc}[\rho](\boldsymbol{r})$, because the latter depends explicitly on $\rho(\boldsymbol{r})$ and not on orbitals (like the HF exchange);
- the origin of the SIE lays in the fact that semi-local functionals were derived for exchange and correlation interactions from the exact solution for an UEG. These functionals typically work well in situations with many electrons and a slowly varying electronic density, but they fail in the description of one-electron systems. In HF theory, the exchange contribution totally cancels out the classical Coulomb interaction of one-electron densities, but in semi-local functionals this condition is not met, and a spurious, repulsive SIE remains. As a result, if on the one hand HF tends to localize electron densities, on the other hand semi-local and global hybrid functionals (not free from SIE) tend to overly delocalized electron densities[43] (also known as localization/delocalization error,[44,45] see Figure 2.2);

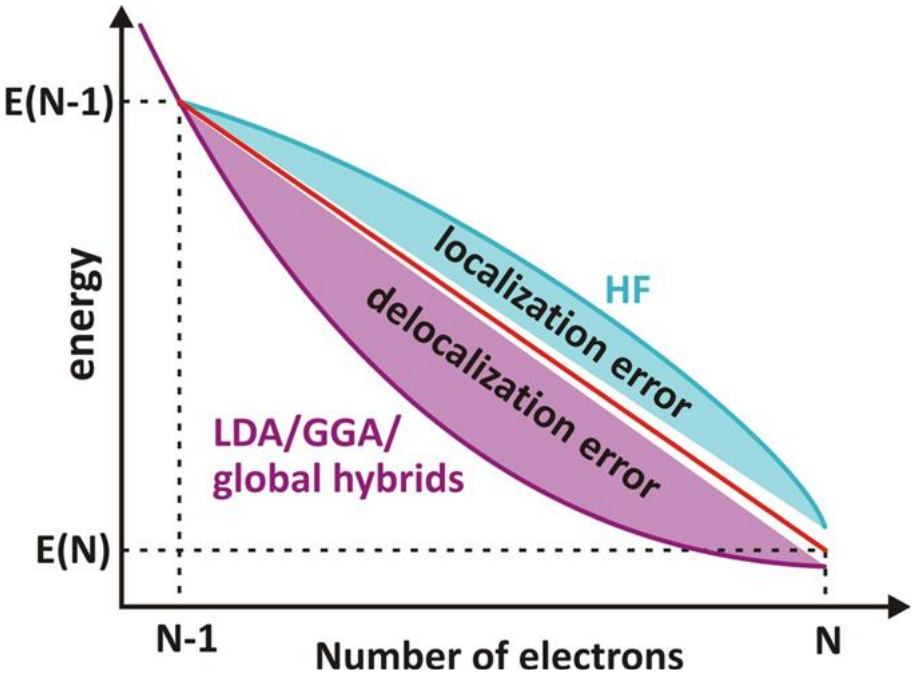

Figure 2.2: Schematic representation of the localization error of HF and the delocalization error in standard DFT functionals. Total energy as a function of a fractional number of electrons when going from a neutral molecule (N) to its cation (N-1), as calculated by standard DFT functionals (purple curve) and HF (cyano curve) in comparison to the exact result (red line). Picture taken from Ref.[14].

- dispersive interactions arise from the correlation of quantum-mechanical fluctuations on the interactive species. Standard semi-local functionals cannot describe long-range, non-local correlation effects. Grimme proposed empirical models to correct the asymptotic behavior, adding an empirical dispersion correction on top of a DFT calculation.[46] The latest DFT-D3[47] version includes atom-pairwise specific dispersion coefficients and first principles cutoff radii and the different local chemical environments of individual atoms are considered when determining the empirical van der Waals coefficient. An alternative approach was the development of van der Waals functionals with a density-dependent non-local correlation, involving non-local interaction between densities at two point in space: vdW-DF2[48] and VV10[49] are an example.

Nevertheless, if the failures of local approximations reside in the exchange part, non-locality errors would be totally expunged by including 100% of exact HF exchange. Thus, exact non-local exchange should be coupled with non-local correlation functionals, in order to describe static correlation effects. This leads us, inevitably, to the fifth rung of the Jacob's ladder. The exact exchange (EXX) energy is a functional of the occupied orbitals, but any simple, similar expression is known for the exact correlation energy, therefore many-body perturbation theories (MBPTs) for the higher-order terms beyond exchange must be involved. The fifth rung then includes unoccupied orbitals in the construction of correlation functionals. For instance, double hybrid functionals[50,51] mix in not only

some EXX, but also some orbital-dependent non-local correlation calculated by second-order Møller-Plesset perturbation (MP2) theory.[52] Another approach, called random phase approximation (RPA), exploits virtual orbitals and includes dispersion interactions. Unfortunately, the introduction of unoccupied orbitals in DFT severely risks misrepresenting the brilliant idea in the KS theory, which is all about occupied orbitals and has the goal of replacing everything that comes from WFTs with simpler density-functional approximations.

2.2 Time-Dependent DFT

DFT was originally developed as a ground state theory, while TDDFT is an extension of DFT for excited state properties. In a non-equilibrium non-relativistic N-electron system, the electronic Hamiltonian reads:

$$\widehat{\mathcal{H}}(t) = -\frac{1}{2}\sum_i \nabla_i^2 + \sum_j \sum_{i>j} \frac{1}{r_{ij}} + \sum_i v(\boldsymbol{r}_i, t) \tag{2.24}$$

where now the last term represents a TD external (scalar) potential operator and the time evolution of the system is ruled by a TD Schrödinger equation:

$$\widehat{\mathcal{H}}(t)\Psi(\boldsymbol{r}_i, t) = i\frac{\partial}{\partial t}\Psi(\boldsymbol{r}_i, t) \tag{2.25}$$

In 1984 Runge and Gross[53] proved that there is a unique, "one-to-one" mapping between the TD density $\rho(\boldsymbol{r}, t)$ and potential $v(\boldsymbol{r}_i, t)$ (up to an additive TD phase factor). In their theorem, they required the potential to be time-analytical and expandable in a Taylor series about the initial time t_0 and they applied this Taylor expansion in the equations of motion for time-derivatives of the current density. For TD systems evolving from an initial wave function Ψ_0, all TD properties can be obtained by knowing the time-evolving density, which identifies the external potential and therefore the wave function $\Psi(\boldsymbol{r}_i, t)$. In other words: for a given initial state, the TD density is a unique functional of the potential (and vice-versa) and all physical observables must be expressed, formally, as functionals of the TD density.

The van Leeuwen theorem[54] allows also to perform the trick that worked so well in static KS DFT: a non-interacting system evolving under an effective potential $v_s[\rho](\boldsymbol{r}, t)$ can reproduce the TD density $\rho(\boldsymbol{r}, t)$ of an interacting system, evolving from Ψ_0 under an effective potential $v(\boldsymbol{r}_i, t)$. The TD density reads:

$$\rho(\boldsymbol{r}, t) = \sum_i |\varphi_i(\boldsymbol{r}, t)|^2 \tag{2.26}$$

where the one-particle KS orbitals $\varphi_i(\boldsymbol{r}, t)$ follow from the TDKS equation:

$$\left[-\frac{1}{2}\nabla^2 + v_s[\rho](\boldsymbol{r}, t)\right]\varphi_i(\boldsymbol{r}, t) = i\frac{\partial}{\partial t}\varphi_i(\boldsymbol{r}, t) \tag{2.27}$$

in which only the N one-particle orbitals, that were initially occupied, are time-propagated and:

$$v_s[\rho](\boldsymbol{r},t) = v(\boldsymbol{r},t) + v_J[\rho](\boldsymbol{r},t) + v_{xc}[\rho](\boldsymbol{r},t) \tag{2.28}$$

where the TD Hartree potential $v_J[\rho](\boldsymbol{r},t)$ depends only on the density at the same time *t* and the last term is defined as the TD xc potential $v_{xc}[\rho](\boldsymbol{r},t)$. Basically, one solves the static KS equations self-consistently making an approximation on $v_{xc}[\rho](\boldsymbol{r})$; then, one let the N initially occupied orbitals time-propagate from an initial t_0(the ground state) to a final time t_1, making an approximation on $v_{xc}[\rho](\boldsymbol{r},t)$. The most common approximation is known as adiabatic approximation, for which the same xc functional from static DFT is used and then it is evaluated with a TD density (*i.e.*, no *memory* effects): briefly, at any given time, the xc potential does not depend on the history of the charge density, but only on its present distribution. However, the idea of self-consistency in static DFT is different from that in TDDFT, where the self-consistency must be built into the time propagation scheme: first, the static KS equations with the ground state density $\rho_0(\boldsymbol{r}) = \rho(\boldsymbol{r},t_0)$ must be solved and then one makes a guess of the TD density $\rho(\boldsymbol{r},t)$ for all times $t_0 \leq t \leq t_1$; a new set of orbitals will be determined by propagating the TDKS equations with $v_s[\rho](\boldsymbol{r},t)$ and they will yield a new density and so on. Therefore, the self-consistent propagation of the TDKS equation is carried out step by step for all times between t_0 and t_1.

One of the most employed applications of TDDFT is spectroscopy. In such field, there is no need to rely directly on the TD density, but one can use the linear response theory and work with frequency-domain equations, in order to calculate electronic excitation energies and excited state properties. Such a theory is widely used whenever one is considering the linear response to a small external TD perturbation $v^{(1)}(\boldsymbol{r},t)$, switched on at t_0. The Fourier transform of the first-order (linear) density response:

$$\rho^{(1)}(\boldsymbol{r},t) = \int dt' \int d^3\boldsymbol{r}' \chi(\boldsymbol{r},t,\boldsymbol{r}',t') v^{(1)}(\boldsymbol{r}',t') \tag{2.29}$$

yields the frequency-dependent density response:

$$\rho^{(1)}(\boldsymbol{r},\omega) = \int d^3\boldsymbol{r}' \chi(\boldsymbol{r},\boldsymbol{r}',\omega) v^{(1)}(\boldsymbol{r}',\omega) \tag{2.30}$$

where $\chi(\boldsymbol{r},\boldsymbol{r}',\omega)$ is the density-density response function and has the Lehman representation in the frequency-domain:

$$\chi(\boldsymbol{r},\boldsymbol{r}',\omega) = \sum_n \frac{\langle\Psi_0|\hat{\rho}(\boldsymbol{r})|\Psi_n\rangle\langle\Psi_n|\hat{\rho}(\boldsymbol{r}')|\Psi_0\rangle}{\omega-\Omega_n+i\eta} + c.c.(-\omega) \tag{2.31}$$

where $\hat{\rho}(\boldsymbol{r})$ is the density operator, $\Omega_n = E_n - E_0$ is the excitation energy of the *n*-th excited state, η is a small positive parameter, the sum runs over all the interacting states Ψ_n and *c.c.* is the complex conjugate of the first term evaluated at $-\omega$. The Lehman representation shows how a frequency-dependent perturbation couples to the excitation spectrum of a system and each excitation can be represented by a pair of poles located at $\omega = \pm\Omega_n - i\eta$, meaning that $\chi(\boldsymbol{r},\boldsymbol{r}',\omega)$ diverges at exact excitation energies.

The TD external potential can be written also as:

$$v(\boldsymbol{r},t) = v^{(0)}(\boldsymbol{r}) + v^{(1)}(\boldsymbol{r},t)\theta(t-t_0) \tag{2.32}$$

and, according to Runge and Gross, we can formally write the TD density as a functional of the TD external potential: $\rho(\boldsymbol{r},t) = \rho[v](\boldsymbol{r},t)$. After few algebra steps, the density-density response function of an N-electron system can be also expressed as:

$$\chi(\boldsymbol{r},t,\boldsymbol{r}',t') = \frac{\delta\rho[v](\boldsymbol{r},t)}{\delta v(\boldsymbol{r}',t')} \tag{2.33}$$

evaluated at the initial potential $v^{(0)}(\boldsymbol{r})$, which is a functional of the initial density: therefore, the linear response function is a functional only of the ground state density. One of the key quantities in TDDFT is the TD xc kernel:

$$f_{xc}(\boldsymbol{r},t,\boldsymbol{r}',t') = \frac{\delta v_{xc}[\rho](\boldsymbol{r},t)}{\delta\rho(\boldsymbol{r}',t')} \tag{2.34}$$

evaluated at the ground state density $\rho(\boldsymbol{r})$. The xc kernel embodies the so-called "dynamical many-body effects" and plays a crucial role in dressing the KS response function, shifting the KS poles to the true excitation energies, and mixing the KS oscillator strengths to form the true oscillator strengths. In the adiabatic approximation, the Fourier transform of the TD xc kernel becomes frequency-independent and purely real, such as:

$$f_{xc}^{A}(\boldsymbol{r},\boldsymbol{r}',\omega) = f_{xc}(\boldsymbol{r},\boldsymbol{r}') = \frac{\delta^2 E_{xc}[\rho]}{\delta\rho(\boldsymbol{r})\delta\rho(\boldsymbol{r}')} \tag{2.35}$$

It is possible then to derive the adiabatic xc kernel associated with any approximate xc functional (LDA, GGAs, global hybrids): by doing this, one replaces the xc kernel at each frequency with its static counterpart.

In linear response TDDFT, the calculation of excitation energies and optical spectra of atoms, molecules and solids are usually carried out within the Casida equation framework.[55] The full derivation of the equation goes beyond the purposes of this work, but the final matrix form allows to obtain the exact excitation energies Ω_n of an N-electron system (in principle, provided that the exact $v_{xc}[\rho](\boldsymbol{r})$ and the exact frequency-dependent xc kernel are known). In most of the quantum-chemical codes, the full Casida equation is simplified by the Tamm-Dancoff approximation (TDA).[56] The eigenvalues of the Casida equation yield Ω_n^2, meaning that the excitation energies come in pairs $(\Omega_n, -\Omega_n)$, excitation and de-excitation (stimulated emission), respectively. In the TDA, all de-excitation processes are neglected, reducing the computational cost, and improving (in some cases) the accuracy of the results, especially for unphysical effects caused by approximate xc kernels. As an example, in open-shell systems it might happen that the triplet excitation energy lies below the ground state energy (the so-called "triplet instability"). TDA can be considered to be the TD-DFT equivalent of the post-HF configuration interaction (CI) approach, with the main difference that the ground and excited state Slater-determinants are now set up from KS orbitals and not from the HF ones.

Similar to DFT, standard TDDFT is not exempt from failures, *i.e.*, in the description of Rydberg, long-range CT, double and multiple excitations, conical intersections and the optical response of solids. Indeed, these are notorious problems where a proper choice of the approximate ground state xc functional is needed or the results given by the chosen xc functional are simply unacceptable. Most of these issues have been solved over the years and in the next paragraph we focus on CT excitations and how to deal with them.

2.3 Range-Separated Hybrid Functionals

In spectroscopy, different excitation gaps are relevant. The *fundamental* (or transport) gap is defined by single-particle charged excitations as the difference between the first IP and the first EA, involving ground state energies of systems with different particle numbers. The *optical* gap, instead, is defined by a two-particle neutral excitation, as the difference between the energies of the lowest dipole-allowed excited state and the ground state, in systems having the same particle numbers. Both gaps are accessible experimentally: the former via photoemission and inverse photoemission spectroscopy (for IP and EA, respectively), the latter via absorption spectroscopy. These two gaps differ by the exciton binding energy between an electron-hole (e-h) pair (see Figure 2.3). Computing the two gaps from first principles is challenging and such demanding calculations rely on state-of-the-art MBPTs. Fundamental gaps can be obtained by calculating the eigenvalues and eigenfunctions of Dyson equations, solved within the *GW* approximation (GWA, where G is the Green function and W is the screened Coulomb potential).[57] Optical gaps can be determined from the Bethe-Salpeter equations (BSE).[58] Ideally, one would like to obtain these gaps from DFT and TDDFT, respectively, but results obtained with semi-local and global hybrid functionals severely underestimate experimental values and/or *GW*-BSE ones.[59,60]

Of utmost interest are CT excitations. According to the definition given by IUPAC, a CT transition is "*an electronic transition in which a large fraction of an electronic charge is transferred from one region of a molecular entity, the electron donor (D), to another, the electron acceptor (A) (intramolecular CT) or from one molecular entity to another (intermolecular CT)"*. These electronic excitations, in general, are characterized by a small spatial overlap between the initial and the final orbital of the excited electron. In molecular complexes, when there is no spatial overlap between the HOMO of the D and the LUMO of the A and the separation r_{DA} between the molecular entities is large but finite, the optical gap is defined by the lowest optical excitation energy (in the Mulliken limit):

$$\mathrm{E}_{CT} = IP_D - EA_A - \frac{1}{r_{DA}} \tag{2.36}$$

with IP_D the ionization potential of the donor and EA_A the electron affinity of the acceptor. The difference $IP_D - EA_A$ directly gives the fundamental gap of the complex. Once the electronic charge is removed from D and transferred to A, the two molecules feel the electrostatic energy $-\frac{1}{r_{DA}}$ of the

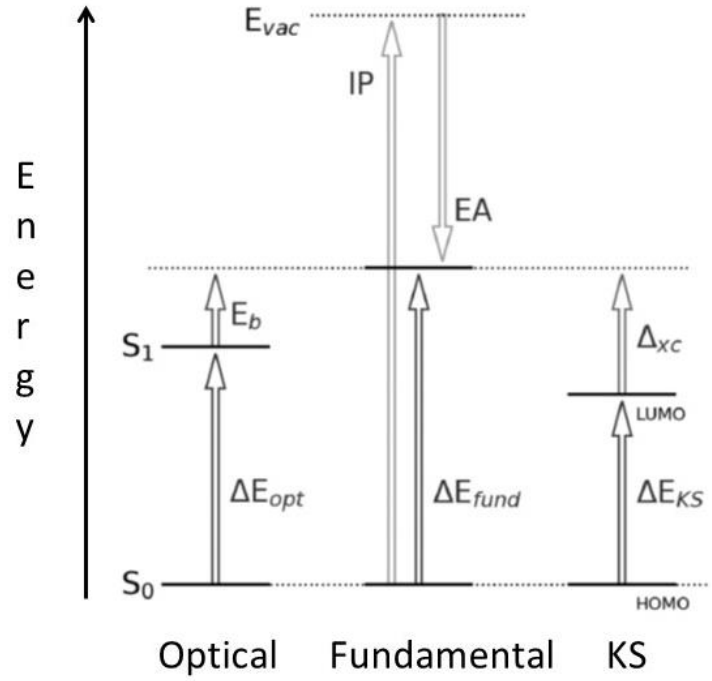

Figure 2.3: Definition of optical ΔE_{opt}, fundamental ΔE_{fund} and DFT KS gap ΔE_{KS}. IP and EA are referred to a common vacuum level E_{vac}. The fundamental gap differs from the optical gap by the exciton binding energy E_b, while the DFT KS gap differs from the fundamental one by the derivative discontinuity Δ_{xc}. Picture slightly adapted from Ref.[43].

induced e-h pair, the so-called "exciton binding energy" E_b. TDDFT in the linear response regime is known to fail in describing such a CT process. Within the adiabatic approximation, all semi-local functionals collapse to the energy difference between the pure KS eigenvalues: $\Delta E_{KS} = \varepsilon_{LUMO}(A) - \varepsilon_{HOMO}(D)$, which underestimates the lowest CT excitation energy due to the missing $-\frac{1}{r}$ tail. Standard global hybrid functionals, with a fraction α of the EXX, mitigate the problem and yield some improvements (although their potential decays asymptotically as $-\frac{\alpha}{r}$), especially when D and A molecules are not too much distant, so that the long-range behavior is not prevailing. However, for large systems, standard global hybrids fail dramatically, poorly underestimating CT excitation energies.[61–64]

In order to solve this issue, the most popular improvement, proposed by Savin and co-workers[65,66] within the *generalized* KS approach[d], is based on RSH functionals. A detailed review of more-than-10-years publications existing in literature on the topic is beyond the scope of this manuscript. Here, we will linger only on the relevant aspects of the method, where the main idea is the partitioning of

[d] In the generalized KS approach, the xc effects are integrated into an additional operator, which combines a local xc contribution with a non-local, HF-like exchange contribution.

the inter-electron Coulomb potential into a short-range (SR) and a long-range (LR) contributions, achieved by the standard error function (erf):

$$\frac{1}{r_{ij}} = \frac{erf(\omega r_{ij})}{r_{ij}} + \frac{1-erf(\omega r_{ij})}{r_{ij}} \tag{2.37}$$

where erf varies smoothly from $\mathrm{erf}(0) = 0$ to $\mathrm{erf}(\infty) = 1$ and ω is the range-separation parameter. The LR and SR components are taken together as usual for the generation of the Hartree potential, but they are treated differently for the exchange term. The LR exchange (the first term in the right-hand side of equation (2.37)) is treated using the full exact HF exchange, while the SR exchange (the second term) is treated in a DFT fashion (usually, with a semi-local GGA exchange). The benefits of this partitioning are two-fold. By introducing the EXX, LR interactions between non-spatially overlapping orbitals are correctly restored, the SIE is completely cancelled out in the LR limit and the correct asymptotic behavior of the Coulomb potential is recovered. At the same time, the use of a DFT SR exchange maintains the compatibility with the DFT correlation: the latter provides a quantitative approximation of the dynamic correlation, while the former mimics the SR static correlation effects. Shortly, RSH functionals counteract at the same time both the spurious effects of HF (the missing static correlation) and the spurious effects of semi-local DFT (the SIE).[14,67,68]

A further improvement can be obtained by including a fraction of HF exchange *also* in the SR part, such as:[69]

$$\frac{1}{r_{ij}} = \frac{\alpha+\beta erf(\omega r_{ij})}{r_{ij}} + \frac{1-[\alpha+\beta erf(\omega r_{ij})]}{r_{ij}} \tag{2.38}$$

where α and β are adjustable parameters. As an example, when using the PBE expression for the GGA xc functional, one obtains:

$$\begin{aligned} E_{xc}^{RSH} = (\alpha+\beta)E_{x,HF}^{LR} + (1-\alpha-\beta)E_{x,PBE}^{LR} + \\ + \alpha E_{x,HF}^{SR} + (1-\alpha)E_{x,PBE}^{SR} + E_{c,PBE} \end{aligned} \tag{2.39}$$

where α quantifies the fraction of HF exchange included in the SR part ($r \to 0$), $\alpha + \beta$ quantifies the fraction of HF exchange included in the LR part ($r \to \infty$) and the PBE correlation is used for the whole range. For a variety of organic molecules α is set to 0.2, although it could be determined from first-principles arguments. For any choice of α, the condition $\alpha + \beta = 1$ guarantees 100% of HF exchange in the LR part and the correct asymptotic behavior in gas-phase.[70–73] RSH functionals where the full HF exchange is switched on in the LR part are also known in the jargon as LRC hybrid functionals, differing from SR (screened) hybrid functionals,[74] where a fraction of HF exchange is only used in the SR part, but none in the LR one. Several groups investigated the performances of RSH functionals in broad classes of molecular systems and every group used their "work horses" functional, so that the encountered formalism is every time slightly different. Other groups dedicated themselves in the development of RSH functionals, as BNL,[75,76] CAM-B3LYP,[69] the family of the LC-ωPBE functionals[77–79] or that of the ωB97 ones.[70,80,81]

Physically, $\frac{1}{\omega}$ quantifies a length scale, that is the distance below which the exchange interaction is dominated by its SR part and above which the exchange interaction is dominated by its LR part. The range-separation parameter ω is a functional of the electron density, whose exact dependence is not known. Furthermore, it can be determined either empirically (*i.e.* by a fit based on reference data) or non-empirically using first principles arguments.[82–84] In the latter scenario, for each specific N-electron system, an optimal value of ω can be found by enforcing the xc functional to obey the DFT version of Koopman's theorem and aligning the negative energy of the HOMO with the gas-phase vertical IP. In practice, one computes the total energy difference between the N-electron and the (N-1)-electron system and tries to minimize the overall error by minimizing the following target function:

$$J^2(\omega) = (\varepsilon_{HOMO}(N,\omega) + IP(N,\omega))^2 \tag{2.40}$$

where we explicitly underline the dependence of the right-hand side of the equation on the ω value. Such a procedure is known as IP-tuning.[71,85,86] In addition, for a better description of the fundamental gap, one can think of the gas-phase vertical EA of the N-electron system as the vertical IP of the (N+1)-electron system, barring relaxation effects. In order to perform a gap-tuning,[71,85] the modified target function to minimize is the following:

$$J^2(\omega) = \sum_{i=0}^{1}(\varepsilon_{HOMO}(N+i,\omega) + IP(N+i,\omega))^2 \tag{2.41}$$

with the hope that, if the derivative discontinuity Δ_{xc} is small and negligible, then the optimally tuned (OT) ω value (implied by both conditions) would be similar. This approach was successfully employed in the calculations of fundamental gaps of small molecules.[14,87–91] The catch in this approach is that the optimal ω value needs to be tuned for each system separately and this does not allow for size consistency of the functional. It was observed that the OT ω value decreases monotonically for systems of increasing size and degree of conjugation.[91,92] Such a phenomenon can be attributed to delocalization effects: the longer the π-conjugation, the more the orbitals delocalize, and, thus, semi-local approximations become more accurate and $\frac{1}{\omega}$ becomes larger. Moreover, it was underlined the importance of a system-dependent ω tuning procedure in RSH functionals. Employing a RSH functional with its "off the shelf" default ω value leads, most of the times, to reasonable approximated results, but unsatisfying if compared to those obtained with an OT ω value: therefore, a non-empirical tuning of the range-separation parameter is the price to pay for an accurate description of ground state and excited state properties, as well as fundamental and optical gaps and intra- and intermolecular CT excitations (pentacene/C60 model complexes) of organic π-conjugated materials in gas-phase.[44,71–73,85,87,91–100] Especially for CT excitations, it was shown that the OT-RSH method is the only DFT-based one capable to correctly predict the reduction of the optical gap with respect to the fundamental gap, namely the exciton binding energy.[88]

2.4. Solid-state Screening Effects and Electrostatics

In many cases, the molecular system of interest is not floating in vacuum but either surrounded by some solvent molecules in a solution or embedded in an effective dielectric medium provided by all neighboring molecules, as in molecular organic solids. In the latter, molecules are bound together by weak van der Waals interactions so that, usually, the molecular identity is retained to a large extent. In molecular solids, the fundamental band gap is much smaller than its gas-phase counterpart (*gap renormalization*),[101,102] due to dielectric screening effects. If a hole is created in a condensed phase material, the polarization of the dielectric medium by the hole generates an effective induced dipole, reducing its IP by a quantity Δ^h. Likewise, when an electron is created, an effective induced dipole is formed, incrementing its EA by a quantity Δ^e. Therefore, the fundamental gap $\Delta E_{fund}$is reduced by the sum of the environmental energies $\Delta^h + \Delta^e$ (see Figure 2.3).[103–105] The gap renormalization is not properly captured by DFT with semi-local and global hybrid functionals: first, the KS gap is different from the fundamental gap by Δ_{xc} and, then, gap renormalization is a non-local, long-range correlation effect associated with the polarization of the condensed medium. We already pointed out that the gas-phase properties of isolated systems can be reproduced accurately with OT-RSH, but the introduction of dielectric screening effects requires different approaches.

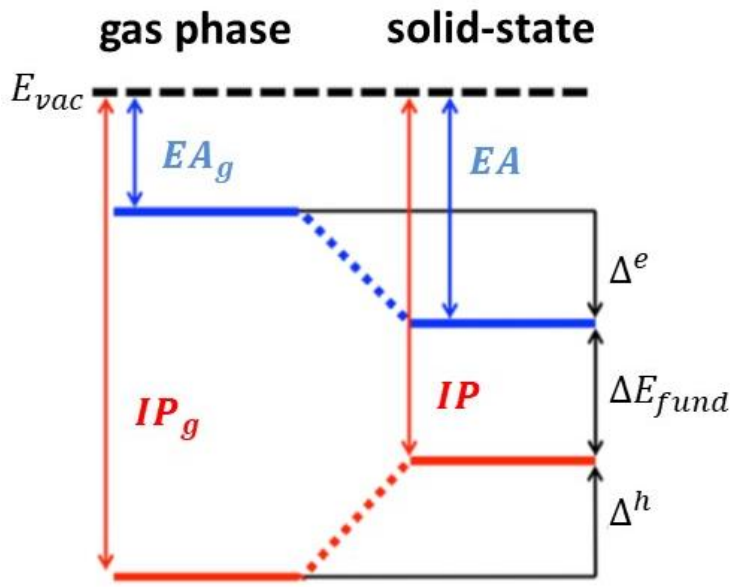

Figure 2.3: Energy level diagram showing the IP and EA in gas-phase and at the solid-state. IP and EA are referred to a common vacuum level E_{vac}. Environmental energies Δ^h and Δ^e contribute to the gap renormalization.

In order to mimic the impact of the solid-state environment on isolated molecules, one way is to combine OT-RSH functionals with a continuum solvation model, like a polarizable continuum model

(PCM).[106] Briefly, the main tenet of PCM is the modelling of solvent molecules as a dielectric medium in which the molecule of interest is embedded, neglecting the atomistic character of the solvent and chemical interactions with the target molecule. The latter is placed within a cavity in a dielectric homogeneous medium, whose dielectric function is $\varepsilon(\boldsymbol{r}) = 1$, and it interacts coulombically with the medium outside the cavity, whose dielectric function is $\varepsilon_s \neq \varepsilon(\boldsymbol{r})$. The total electrostatic potential $\Phi(\boldsymbol{r})$ can be written as a sum of the electrostatic potential generated by the charge density of the isolated target molecule and, owing to the presence of the continuum, a reaction potential. This can be represented by a surface charge residing on the surface of the cavity which contains the target molecule. In this approach, what matters the most is the choice of the cavity and ε_s, as the surface charge is determined by these two parameters and by the isolated molecular charge density. Yet, PCM is an adiabatic approach and neglects the different timescales for the dynamics of the medium polarization, since the solvent responses in two distinct ways to the change of state of the target molecule (*i.e.,* ionization): the electron density within the solvent will react quickly, while the orientational motion of the solvent molecules is much slower.

After this needed digression, gap renormalization is a dielectric response effect that does not require any chemical interaction and PCM is able to capture such response. Therefore, in its first attempt, the proposed approach was to add PCM as a correction on top of OT-RSH calculations, retaining the OT ω value obtained in gas-phase. This allows for an improvement of the fundamental gap of organic solids, since it was observed that ionization energies (IPs and EAs) are strongly influenced by PCM, while the interaction with the dielectric medium has a minor effect on the KS gap (HOMO and LUMO eigenvalues). On the other hand, the PCM correction leads to only minor varations (below 0.1 eV) to CT excitation energies in molecular complexes such as pentacene/C_{60}.[107–110] Later on, it was suggested to directly include PCM in the ω_{PCM} tuning procedure (the notation is introduced to differentiate among ω in gas-phase) and then perform (TD)DFT calculations in the presence of PCM. Although the fundamental gap of organic solids and CT excitation energies of pentacene/C_{60} complex are in remarkable agreement with experimental values, it was already noticed that tuning in the presence of PCM leads to very small ω_{PCM} values, one order of magnitude smaller if compared to gas-phase:[107–109] the smaller ω, the longer the distance at which the exact HF exchange is switched on and the functional becomes closer to a semi-local one. It was also pointed out that, while the small ω_{PCM} parameter can mimic the electrostatic screening, it does not do so in a complete way.[111] Furthermore, there is an exponential decay relationship between the OT ω_{PCM} value and the dielectric constant ε used during the tuning procedure.[110] This is counterintuitive because the range-separated parameter is a functional of the electron density of a given molecule and its gas-phase density should not be different from that at the solid-state.[75,88] Another highlighted drawback is that OT-based results obtained in PCM are not so realistic, since a proper description of an ionization process would require to consider the different timescales on which electronic and nuclear degrees of freedom of the surrounding medium response upon charging the target molecule. The above considerations underlie the problematic aspect of such a procedure.

Alternatively, the renormalization of the fundamental gap due to solid-state polarization effects can be easily introduced (without resorting to PCM in the original formulation)[112] by insisting that the asymptotic Coulomb potential tends to $\frac{1}{\varepsilon r}$ rather than to $\frac{1}{r}$, so that the potential would be properly screened by the dielectric constant ε. According to the relation $\alpha + \beta = \frac{1}{\varepsilon}$, it is enough to set β in equation (2.39), while retaining α and the OT ω gas-phase values. This approach based on more complex functionals is called OT *screened* RSH (OT-SRSH).[107,111,113–115] Bhandari *et al.*[114] showed that one can use SRSH functionals either without PCM or invoking it explicitly. In the former case, the dielectric screening renormalizes the KS HOMO and LUMO eigenvalues, but it does not significantly affect the IPs and EAs. In the latter, the condition $\alpha + \beta = \frac{1}{\varepsilon}$ is further enforced by invoking PCM and setting the condensed phase scalar dielectric constant ε, so that the dielectric screening of the LR electrostatic interactions is treated consistently in both parts of the SRSH-PCM combination. In such a way, the screened Coulomb term corresponding to the LR limit of the RSH functional is consistent with that used in the self-consistent field iterations of the PCM. The parameter β can be accordingly modified to $\beta = \frac{1}{\varepsilon} - \alpha$ or, alternatively, it can be even OT in presence of PCM (β_{PCM}), leaving unchanged α and the OT ω gas phase-values. Then, the new target function to be minimized becomes:[114]

$$J^2(\beta) = \sum_{i=0}^{1}(\varepsilon_H(N+i,\beta) + IP(N+i,\beta))^2 \tag{2.42}$$

In a more sophisticated approach, β_{PCM} is OT in presence of PCM and α changes together with β_{PCM}, while retaining their correct sum $\alpha + \beta_{PCM} = \frac{1}{\varepsilon}$. We note that if α (fraction of HF exchange at SR) is changed, then $(1-\alpha)$ (fraction of DFT exchange at SR) must be changed as well. All the mentioned SRSH methods, that combine explicitly PCM, provide a physically correct and quantitatively accurate renormalization of both the KS and the fundamental gap[114] and an excellent agreement for solvated CT excitations in D:A complexes.[116] Yet, SRSH methods are relatively new-born state-of-the-art procedures and there are still many issues to be solved. A complete assessment of advantages and limitations of SRSH+PCM is still missing and further efforts in this direction need to be produced, especially in fields like organic photocatalysis and photovoltaics.[15]

Another approach which takes into account electrostatic interactions between localized charges and neutral excitations with their polarizable molecular environment is provided by discrete atomistic models, such as microelectrostatic (ME or induced dipole) or charge response (CR) schemes.[16,103,117–121] Here, we will focus on the former, which relies on a classical polarizable points description of the electronic polarization. In a classical ME model, molecules are described in terms of permanent charges and anisotropic polarizable points (or induced dipoles) located at atomic positions. The induced dipole $\boldsymbol{\mu_i}$ at each site *i* is computed in the self-consistent electric field of permanent charges and dipoles themselves, $\boldsymbol{F_i}$ as: $\boldsymbol{\mu_i} = \tilde{\alpha}_i \boldsymbol{F_i}$, where $\tilde{\alpha}_i$ is the linear polarizability tensor associated with atom *i*. In the ME model, the energy is calculated as a sum over the whole system:

$$E = \frac{1}{2}\sum_i (q_i V_i^0 - \boldsymbol{\mu_i} \boldsymbol{F_i^0}) \tag{2.43}$$

where V_i^0 is the electric potential, $\boldsymbol{F_i^0}$ is the electric field at the *i*-th site due to permanent charges $\{q\}$ and the sum runs over atomic sites bearing charge and/or polarizability. Electric potential and field at the *i*-th site are computed from the unscreened contribution for charges and dipoles of all the other molecules in the system and they are updated at every step, until self-consistency of the mutual intermolecular interactions is reached, as shown in Figure 2.4.

This particular ME approach neglects the redistribution of atomic charges (usually done in CR schemes) and the molecular polarization is described only in terms of induces dipoles. The whole molecular polarizability is partitioned over a finite number of polarizable points (*i.e.*, atomic sites) and interactions among dipoles on the same molecules are neglected, so that the sum of the atomic polarizabilities equals the target molecular polarizability. The induced-dipole contribution to the molecular polarizability is spread over atoms proportionally to the static atomic polarizability of the corresponding element. Moreover, the linear response to electric fields is described in term of induced dipoles, whose self-consistent solution is performed in the electrostatic environment provided by a set of permanent point charges, *i.e.*, ESP,[122] CHELPG,[123] and RESP charges,[124] which reproduce the molecular potential via an electric potential fitting scheme. For each specific system, the anisotropic polarizability needs to be computed. The set of atomic charges and polarizabilities of neutral and charged systems, which enter the ME scheme, are computed at the quantum-chemical level (usually DFT). For neutral and charged species the same polarizability is often assumed.

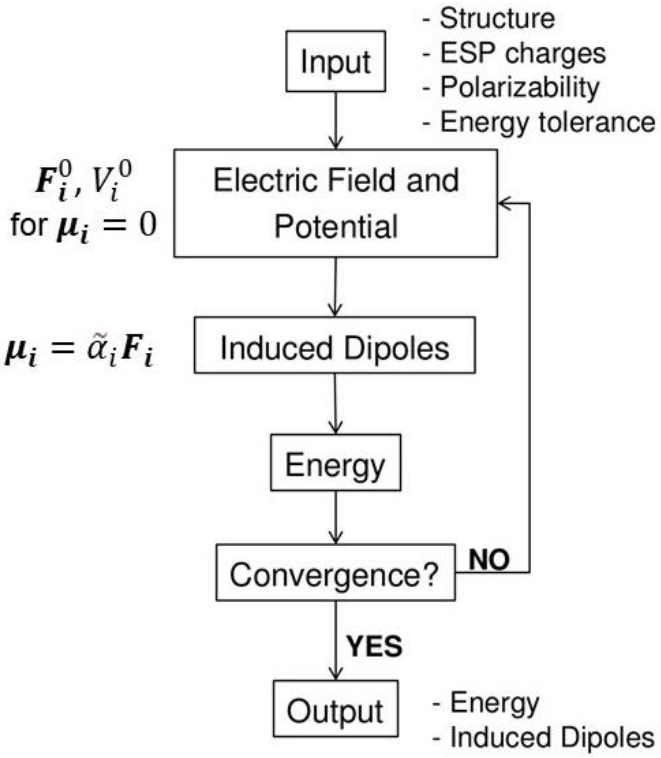

Figure 2.4: Flowchart of a self-consistent ME calculation.

Under the assumption of zero intermolecular overlap,[125] charge carriers are fully localized on molecular units that interact through classical electrostatic forces. In this scenario, the IP and the EA define the transport energy levels for charge carriers in a molecular solid (refer to Figure 2.3). The energy to create a hole or an electron at the *m*-th molecular site from a neutral system is given by:

$$IP_m = IP_m^{gas} + \Delta^h \tag{2.44}$$

$$EA_m = EA_m^{gas} - \Delta^e \tag{2.45}$$

where IP_m^{gas} is the gas-phase IP of molecule *m* and EA_m^{gas} its gas-phase EA and Δ^h and Δ^e are the (already introduced) environmental energies for holes and electrons, respectively. In the above equations, one can reckon an intramolecular contribution, given by the dependence of gas-phase IP/EA on the molecular structure, and an intermolecular one, provided by the environmental energies, *i.e.*, the interaction between the charge carrier residing on molecule *m* and the surrounding medium. Environmental energies, usually, are partitioned in two different terms: $\Delta^x = \Delta_E^x + \Delta_I^x$. The former Δ_E^x is the electrostatic contribution (which is missing in PCM) generated by the interaction between the gas-phase charge distributions of molecules within the system, while the latter Δ_I^x, the so-called "induction" (conversely, present in PCM) accounts for the reorganization of the electron polarization in the field of charged and neutral molecules and this term needs the self-consistence computation of induced dipoles. For a single charge, the induction term can be estimated by the Born equation[126] for the environmental energy in a spherical cavity of radius R inside a dielectric medium with dielectric constant $\varepsilon_r = \frac{\varepsilon}{\varepsilon_0}$:

$$\Delta_I^x = -\frac{e^2}{2R}\left(1 - \frac{1}{\varepsilon_r}\right) \tag{2.46}$$

and it is the main responsible for the large closing of the fundamental gap (around 2 eV), going from gas to condensed phase in organic semiconductors. The induction term should be extrapolated in the infinite-crystal limit and extrapolation is typically done in spherical clusters of increasing radius. The electrostatic term has opposite sign and approximately the same magnitude for positive and negative charges and that is what differentiates hole and electron environmental energies. Δ_E^x depends strictly on the gas-phase charge distribution and on the supramolecular packing, in a larger extent with respect to Δ_I^x. The ME model, thus, relies on a perturbative treatment of intermolecular interactions and assumes linear response to electric fields: Δ_E^x and Δ_I^x can be considered as the first and higher order perturbative corrections to the gas-phase energy levels in the zero-overlap approximation. Indeed, long-range electrostatic and induction interactions are responsible for shifts of the energy levels of charge carries in molecular solids, either crystalline or amorphous (see Figure 2.5), and they have a crucial role in affecting charge transport and charge separation at heterojunctions for photovoltaic applications.[127–134]

A more sophisticated approach entails a different partitioning of the environmental energies as follows. The environmental energy of a generic excitation (either a single-particle charged or a two-particles neutral one) is:

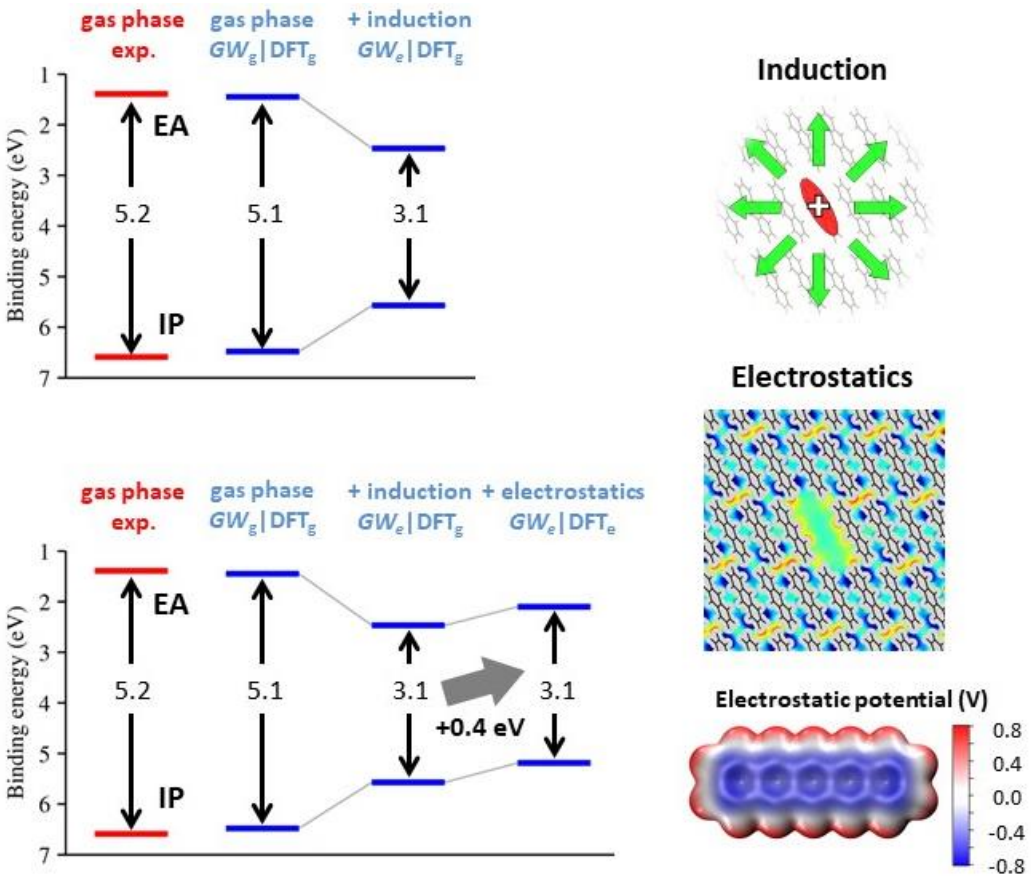

Figure 2.5: Evolution of IP/EA from the gas-phase to the solid-state in pentacene, whose electrostatic potential colour map is also reported. Calculation results (in blue) are presented by progressively introducing the different contributions from intermolecular interactions: induction and electrostatics. The notation GW_x | DFT_y stands for the effects accounted for at the different levels of theory, e.g., GW_e | DFT_g corresponds to a *GW* calculation on an embedded molecule initiated with a gas-phase DFT calculation. Picture slightly adapted from Ref.[135].

$$\Delta^x = \Delta_E^x + \Delta_I^x \qquad \text{or} \qquad \Delta^x = \Delta_E^x + \Delta_{In}^x + \Delta_{Ie}^x \tag{2.47}$$

where the sum $\Delta_n^x = \Delta_E^x + \Delta_{In}^x$ describes the interactions between the excitation and the screened field of the surrounding neutral molecules. It reads:

$$\Delta_n^x = \Delta_E^x + \Delta_{In}^x = \sum_j \delta q_j^x \phi_j^{pc} + \sum_j \delta q_j^x \phi_j^{id} = \sum_j \delta q_j^x \phi_j^{sc} \tag{2.48}$$

where the sum j runs over the atoms of the excited molecule, δq_j^x is the difference between the atomic permanent charges in the excited and the neutral state, $\phi_j^{sc} = \phi_j^{pc} + \phi_j^{id}$ is the self-consistent potential at atomic sites in the neutral system, due to permanent charges of neutral molecules ϕ_j^{pc} and dipoles induced by these charges ϕ_j^{id}. Furthermore, Δ_{Ie}^x accounts for the contribution of dipoles induced by the excitation itself and it is always a stabilizing contribution (< 0). The environmental

energy of an e-h pair includes the Coulomb attraction between opposite charges and the surrounding polarization effects, and its expression is (indexes are dropped for convenience):

$$\Delta^{eh} = \Delta_n^e + \Delta_n^h + V^{eh} + \Delta_I^{eh} \tag{2.49}$$

where $V^{eh} = \sum_{i,j} \frac{\delta q_i^e \delta q_j^h}{r_{ij}}$ is the *bare* (unscreened) electrostatic interaction between the electron and the hole and Δ_I^{eh} is the interaction between the e-h pair and the dipoles induced in the polarizable medium. We define, at last, the exciton binding energy E_B^{eh}(< 0) as:

$$E_B^{eh} = \Delta^{eh} - (\Delta^e + \Delta^h) \tag{2.50}$$

that is the *screened* V^{eh} by the dielectric constant ε of the medium. Then, the CT energy required to create an e-h pair is:

$$E_{CT} = IP^{gas} - EA^{gas} + P^{eh} = IP - EA + E_B^{eh} \tag{2.51}$$

All these electrostatic effects can be computed with an in-house written code for MicroElectroStatic Calculations in molecular solids (MESCal),[117] provided that an accurate parametrization is carried out at the quantum-chemical level, as described above.

References

(1) Parr, R. G.; Yang, W. *Density-Functional Theory of Atoms and Molecules*; Oxford University Press: Oxford, 1989.

(2) Engel, E.; Dreizler, R. M. *Density Functional Theory: An Advanced Course*; Springer: Berlin, 2011.

(3) Marques, M. A. L.; Maitra, N. T.; Nogueira, F. M. S.; Gross, E. K. U.; Rubio, A. *Fundamentals of Time-Dependent Density Functional Theory*; Springer: Heidelberg, 2012.

(4) Ullrich, C. A. *Time-Dependent Density-Functional Theory: Concepts and Applications*; Oxford University Press: Oxford, 2012.

(5) Parr, R. G. Density Functional Theory. *Annu. Rev. Phys. Chem.* **1983**, *34* (1), 631–656.

(6) Parr, R. G.; Yang, W. Density-Functional Theory of the Electronic Structure of Molecules. *Annu. Rev. Phys. Chem.* **1995**, *46* (1), 701–728.

(7) Burke, K. Perspective on Density Functional Theory. *J. Chem. Phys.* **2012**, *136* (15).

(8) Klimeš, J.; Michaelides, A. Perspective: Advances and Challenges in Treating van Der Waals Dispersion Forces in Density Functional Theory. *J. Chem. Phys.* **2012**, *137* (12), 120901.

(9) Burke, K.; Wagner, L. O. DFT in a Nutshell. *Int. J. Quantum Chem.* **2013**, *113* (2), 96–101.

(10) Becke, A. D. Perspective: Fifty Years of Density-Functional Theory in Chemical Physics. *J. Chem. Phys.* **2014**, *140* (18), 0–18.

(11) Yu, H. S.; Li, S. L.; Truhlar, D. G. Perspective: Kohn-Sham Density Functional Theory Descending a Staircase. *J. Chem. Phys.* **2016**, *145* (13).

(12) Maitra, N. T. Perspective: Fundamental Aspects of Time-Dependent Density Functional Theory. *J. Chem. Phys.* **2016**, *144* (22).

(13) Baer, R.; Livshits, E.; Salzner, U. Tuned Range-Separated Hybrids in Density Functional Theory. *Annu. Rev. Phys. Chem.* **2010**, *61* (1), 85–109.

(14) Körzdörfer, T.; Brédas, J. L. Organic Electronic Materials: Recent Advances in the Dft Description of the Ground and Excited States Using Tuned Range-Separated Hybrid Functionals. *Acc. Chem. Res.* **2014**, *47* (11), 3284–3291.

(15) Kronik, L.; Kümmel, S. Dielectric Screening Meets Optimally Tuned Density Functionals. *Adv. Mater.* **2018**, *30* (41), 1–14.

(16) D'Avino, G.; Muccioli, L.; Castet, F.; Poelking, C.; Andrienko, D.; Soos, Z. G.; Cornil, J.; Beljonne, D. Electrostatic Phenomena in Organic Semiconductors: Fundamentals and Implications for Photovoltaics. *J. Phys. Condens. Matter* **2016**, *28* (43).

(17) Slater, J. C. The Theory of Complex Spectra. *Phys. Rev.* **1929**, *34* (10), 1293–1322.

(18) Fock, V. „Selfconsistent Field“ Mit Austausch Für Natrium. *Zeitschrift für Phys.* **1930**, *62* (11), 795–805.

(19) Hartree, D. R.; Hartree, W. Self-Consistent Field, with Exchange, for Beryllium. *Proc. R. Soc. London. Ser. A - Math. Phys. Sci.* **1935**, *150* (869), 9–33.

(20) Thomas, L. H. The Calculation of Atomic Fields. *Math. Proc. Cambridge Philos. Soc.* **1927**, *23* (5), 542–548.

(21) E. Fermi. Un Metodo Statistico per La Determinazione Di Alcune Prioprietà Dell'Atomo. *Endiconti Accad. Naz. dei Lincei* **1927**, *6*, 602–607.

(22) Hohenberg, P.; Kohn, W. Inhomogeneous Electron Gas. *Phys. Rev.* **1964**, *136* (3B), B864–B871.

(23) Levy, M.; Perdew, J. P. The Constrained Search Formulation of Density Functional Theory. In *Density Functional Methods In Physics*; Dreizler, R. M., da Providência, J., Eds.; Springer US, 1985; pp 11–30.

(24) Kohn, W.; Sham, L. J. Self-Consistent Equations Including Exchange and Correlation Effects. *Phys. Rev.* **1965**, *140* (4A), A1133–A1138.

(25) Perdew, J. P.; Zunger, A. Self-Interaction Correction to Density-Functional Approximations for Many-Electron Systems. *Phys. Rev. B* **1981**, *23* (10), 5048–5079.

(26) Koopmans, T. Über Die Zuordnung von Wellenfunktionen Und Eigenwerten Zu Den Einzelnen Elektronen Eines Atoms. *Physica* **1934**, *1* (1), 104–113.

(27) Perdew, J. P.; Levy, M. Physical Content of the Exact Kohn-Sham Orbital Energies: Band Gaps and Derivative Discontinuities. *Phys. Rev. Lett.* **1983**, *51* (20), 1884–1887.

(28) Sham, L. J.; Schlüter, M. Density-Functional Theory of the Energy Gap. *Phys. Rev. Lett.* **1983**, *51* (20), 1888–1891.

(29) Perdew, J. P.; Wang, Y. Accurate and Simple Analytic Representation of the Electron-Gas Correlation Energy. *Phys. Rev. B* **1992**, *45* (23), 13244–13249.

(30) Dirac, P. A. M. Note on Exchange Phenomena in the Thomas Atom. *Math. Proc. Cambridge Philos. Soc.* **1930**, *26* (3), 376–385.

(31) Becke, A. D. Density-Functional Exchange-Energy Approximation with Correct Asymptotic Behavior. *Phys. Rev. A* **1988**, *38* (6), 3098–3100.

(32) Perdew, J. P.; Chevary, J. A.; Vosko, S. H.; Jackson, K. A.; Pederson, M. R.; Singh, D. J.; Fiolhais, C. Atoms, Molecules, Solids, and Surfaces: Applications of the Generalized Gradient Approximation for Exchange and Correlation. *Phys. Rev. B* **1992**, *46* (11), 6671–6687.

(33) Perdew, J. P.; Yue, W. Accurate and Simple Density Functional for the Electronic Exchange Energy: Generalized Gradient Approximation. *Phys. Rev. B* **1986**, *33* (12), 8800–8802.

(34) Lee, C.; Yang, W.; Parr, R. G. Development of the Colle-Salvetti Correlation-Energy Formula into a Functional of the Electron Density. *Phys. Rev. B* **1988**, *37* (2), 785–789.

(35) Gill, P. M. W.; Johnson, B. G.; Pople, J. A.; Frisch, M. J. The Performance of the Becke—Lee—Yang—Parr (B—LYP) Density Functional Theory with Various Basis Sets. *Chem. Phys. Lett.* **1992**, *197* (4), 499–505.

(36) Perdew, J. P.; Burke, K.; Ernzerhof, M. Generalized Gradient Approximation Made Simple. *Phys. Rev. Lett.* **1996**, *77* (18), 3865–3868.

(37) Engel, E.; Chevary, J. A.; Macdonald, L. D.; Vosko, S. H. Asymptotic Properties of the Exchange Energy Density and the Exchange Potential of Finite Systems: Relevance for Generalized Gradient Approximations. *Zeitschrift für Phys. D Atoms, Mol. Clust.* **1992**, *23* (1), 7–14.

(38) Perdew, J. P.; Schmidt, K. Jacob's Ladder of Density Functional Approximations for the Exchange-Correlation Energy. *AIP Conf. Proc.* **2001**, *577* (1), 1–20.

(39) Seidl, A.; Görling, A.; Vogl, P.; Majewski, J. A.; Levy, M. Generalized Kohn-Sham Schemes and the Band-Gap Problem. *Phys. Rev. B* **1996**, *53* (7), 3764–3774.

(40) Becke, A. D. Density-functional Thermochemistry. III. The Role of Exact Exchange. *J. Chem. Phys.* **1993**, *98* (7), 5648–5652.

(41) Stephens, P. J.; Devlin, F. J.; Chabalowski, C. F.; Frisch, M. J. Ab Initio Calculation of Vibrational Absorption and Circular Dichroism Spectra Using Density Functional Force Fields. *J. Phys. Chem.* **1994**, *98* (45), 11623–11627.

(42) Adamo, C.; Barone, V. Toward Reliable Density Functional Methods without Adjustable Parameters: The PBE0 Model. *J. Chem. Phys.* **1999**, *110* (13), 6158–6170.

(43) Brédas, J.-L.; Chen, X.; Körzdörfer, T.; Li, H.; Risko, C.; Ryno, S.; Wang, T. *Recent Advances in the Computational Characterization of π-Conjugated Organic Semiconductors*; Boca Raton, 2019.

(44) Sutton, C.; Körzdörfer, T.; Coropceanu, V.; Brédas, J. L. Toward a Robust Quantum-Chemical Description of Organic Mixed-Valence Systems. *J. Phys. Chem. C* **2014**, *118* (8), 3925–3934.

(45) Bao, J. L.; Gagliardi, L.; Truhlar, D. G. Self-Interaction Error in Density Functional Theory: An Appraisal. *J. Phys. Chem. Lett.* **2018**, *9* (9), 2353–2358.

(46) Grimme, S. Semiempirical GGA-Type Density Functional Constructed with a Long-Range Dispersion Correction. *J. Comput. Chem.* **2006**, *27* (15), 1787–1799.

(47) Grimme, S.; Antony, J.; Ehrlich, S.; Krieg, H. A Consistent and Accurate Ab Initio Parametrization of Density Functional Dispersion Correction (DFT-D) for the 94 Elements H-Pu. *J. Chem. Phys.* **2010**, *132* (15), 154104.

(48) Lee, K.; Murray, É. D.; Kong, L.; Lundqvist, B. I.; Langreth, D. C. Higher-Accuracy van Der Waals Density Functional. *Phys. Rev. B* **2010**, *82* (8), 81101.

(49) Vydrov, O. A.; Van Voorhis, T. Nonlocal van Der Waals Density Functional: The Simpler the Better. *J. Chem. Phys.* **2010**, *133* (24), 244103.

(50) Grimme, S.; Neese, F. Double-Hybrid Density Functional Theory for Excited Electronic States of Molecules. *J. Chem. Phys.* **2007**, *127* (15), 154116.

(51) Goerigk, L.; Grimme, S. Double-Hybrid Density Functionals Provide a Balanced Description of Excited 1La and 1Lb States in Polycyclic Aromatic Hydrocarbons. *J. Chem. Theory Comput.* **2011**, *7* (10), 3272–3277.

(52) Møller, C.; Plesset, M. S. Note on an Approximation Treatment for Many-Electron Systems. *Phys. Rev.* **1934**, *46* (7), 618–622.

(53) Runge, E.; Gross, E. K. U. Density-Functional Theory for Time-Dependent Systems. *Phys. Rev. Lett.* **1984**, *52* (12), 997–1000.

(54) van Leeuwen, R. Mapping from Densities to Potentials in Time-Dependent Density-Functional Theory. *Phys. Rev. Lett.* **1999**, *82* (19), 3863–3866.

(55) Casida, M. E.; Jamorski, C.; Casida, K. C.; Salahub, D. R. Molecular Excitation Energies to High-Lying Bound States from Time-Dependent Density-Functional Response Theory: Characterization and Correction of the Time-Dependent Local Density Approximation Ionization Threshold. *J. Chem. Phys.* **1998**, *108* (11), 4439–4449.

(56) Hirata, S.; Head-Gordon, M. Time-Dependent Density Functional Theory within the Tamm–Dancoff Approximation. *Chem. Phys. Lett.* **1999**, *314* (3), 291–299.

(57) Hedin, L. New Method for Calculating the One-Particle Green's Function with Application to the Electron-Gas Problem. *Phys. Rev.* **1965**, *139* (3A), A796–A823.

(58) Salpeter, E. E.; Bethe, H. A. A Relativistic Equation for Bound-State Problems. *Phys. Rev.* **1951**, *84* (6), 1232–1242.

(59) Blase, X.; Attaccalite, C.; Olevano, V. First-Principles GW Calculations for Fullerenes, Porphyrins, Phtalocyanine, and Other Molecules of Interest for Organic Photovoltaic Applications. *Phys. Rev. B* **2011**, *83* (11), 115103.

(60) Jacquemin, D.; Duchemin, I.; Blase, X. 0–0 Energies Using Hybrid Schemes: Benchmarks of TD-DFT, CIS(D), ADC(2), CC2, and BSE/GW Formalisms for 80 Real-Life Compounds. *J. Chem. Theory Comput.* **2015**, *11* (11), 5340–5359.

(61) Dreuw, A.; Weisman, J. L.; Head-Gordon, M. Long-Range Charge-Transfer Excited States in Time-Dependent Density Functional Theory Require Non-Local Exchange. *J. Chem. Phys.* **2003**, *119* (6), 2943–2946.

(62) Autschbach, J. Charge-Transfer Excitations and Time-Dependent Density Functional Theory: Problems and Some Proposed Solutions. *ChemPhysChem* **2009**, *10* (11), 1757–1760.

(63) Maitra, N. T. Charge Transfer in Time-Dependent Density Functional Theory. *J. Phys. Condens. Matter* **2017**, *29* (42), 423001.

(64) Kümmel, S. Charge-Transfer Excitations: A Challenge for Time-Dependent Density Functional Theory That Has Been Met. *Adv. Energy Mater.* **2017**, *7* (16), 1700440.

(65) Savin, A.; Flad, H.-J. Density Functionals for the Yukawa Electron-Electron Interaction. *Int. J. Quantum Chem.* **1995**, *56* (4), 327–332.

(66) Leininger, T.; Stoll, H.; Werner, H.-J.; Savin, A. Combining Long-Range Configuration Interaction with Short-Range Density Functionals. *Chem. Phys. Lett.* **1997**, *275* (3), 151–160.

(67) Kümmel, S.; Kronik, L. Orbital-Dependent Density Functionals: Theory and Applications. *Rev. Mod. Phys.* **2008**, *80* (1), 3–60.

(68) Cohen, A. J.; Mori-Sánchez, P.; Yang, W. Challenges for Density Functional Theory. *Chem. Rev.* **2012**, *112* (1), 289–320. https://doi.org/10.1021/cr200107z.

(69) Yanai, T.; Tew, D. P.; Handy, N. C. A New Hybrid Exchange-Correlation Functional Using the Coulomb-Attenuating Method (CAM-B3LYP). *Chem. Phys. Lett.* **2004**, *393* (1–3), 51–57.

(70) Chai, J.-D.; Head-Gordon, M. Long-Range Corrected Hybrid Density Functionals with Damped Atom–Atom Dispersion Corrections. *Phys. Chem. Chem. Phys.* **2008**, *10* (44), 6615–6620.

(71) Stein, T.; Kronik, L.; Baer, R. Reliable Prediction of Charge Transfer Excitations in Molecular Complexesusing Time-Dependent Density Functional Theory. *J. Am. Chem. Soc.* **2009**, *131* (8), 2818–2820.

(72) Stein, T.; Eisenberg, H.; Kronik, L.; Baer, R. Fundamental Gaps in Finite Systems from Eigenvalues of a Generalized Kohn-Sham Method. *Phys. Rev. Lett.* **2010**, *105* (26).

(73) Refaely-Abramson, S.; Sharifzadeh, S.; Govind, N.; Autschbach, J.; Neaton, J. B.; Baer, R.; Kronik, L. Quasiparticle Spectra from a Nonempirical Optimally Tuned Range-Separated Hybrid Density Functional. *Phys. Rev. Lett.* **2012**, *109* (22), 1–6.

(74) Henderson, T. M.; Izmaylov, A. F.; Scalmani, G.; Scuseria, G. E. Can Short-Range Hybrids Describe Long-Range-Dependent Properties? *J. Chem. Phys.* **2009**, *131* (4).

(75) Baer, R.; Neuhauser, D. Density Functional Theory with Correct Long-Range Asymptotic

Behavior. *Phys. Rev. Lett.* **2005**, *94* (4), 43002.

(76) Livshits, E.; Baer, R. A Well-Tempered Density Functional Theory of Electrons in Molecules. *Phys. Chem. Chem. Phys.* **2007**, *9* (23), 2932–2941.

(77) Vydrov, O. A.; Heyd, J.; Krukau, A. V.; Scuseria, G. E. Importance of Short-Range versus Long-Range Hartree-Fock Exchange for the Performance of Hybrid Density Functionals. *J. Chem. Phys.* **2006**, *125* (7).

(78) Vydrov, O. A.; Scuseria, G. E. Assessment of a Long-Range Corrected Hybrid Functional. *J. Chem. Phys.* **2006**, *125* (23).

(79) Vydrov, O. A.; Scuseria, G. E.; Perdew, J. P. Tests of Functionals for Systems with Fractional Electron Number. *J. Chem. Phys.* **2007**, *126* (15).

(80) Chai, J. Da; Head-Gordon, M. Systematic Optimization of Long-Range Corrected Hybrid Density Functionals. *J. Chem. Phys.* **2008**, *128* (8).

(81) Lin, Y. S.; Li, G. De; Mao, S. P.; Chai, J. Da. Long-Range Corrected Hybrid Density Functionals with Improved Dispersion Corrections. *J. Chem. Theory Comput.* **2013**, *9* (1), 263–272.

(82) Perdew, J. P.; Parr, R. G.; Levy, M.; Balduz, J. L. Density-Functional Theory for Fractional Particle Number: Derivative Discontinuities of the Energy. *Phys. Rev. Lett.* **1982**, *49* (23), 1691–1694.

(83) Levy, M.; Perdew, J. P.; Sahni, V. Exact Differential Equation for the Density and Ionization Energy of a Many-Particle System. *Phys. Rev. A* **1984**, *30* (5), 2745–2748.

(84) Perdew, J. P.; Levy, M. Comment on ``Significance of the Highest Occupied Kohn-Sham Eigenvalue''. *Phys. Rev. B* **1997**, *56* (24), 16021–16028.

(85) Stein, T.; Kronik, L.; Baer, R. Prediction of Charge-Transfer Excitations in Coumarin-Based Dyes Using a Range-Separated Functional Tuned from First Principles. *J. Chem. Phys.* **2009**, *131* (24).

(86) Salzner, U.; Baer, R. Koopmans' Springs to Life. *J. Chem. Phys.* **2009**, *131* (23), 231101.

(87) Refaely-Abramson, S.; Baer, R.; Kronik, L. Fundamental and Excitation Gaps in Molecules of Relevance for Organic Photovoltaics from an Optimally Tuned Range-Separated Hybrid Functional. *Phys. Rev. B - Condens. Matter Mater. Phys.* **2011**, *84* (7), 22–25.

(88) Kronik, L.; Stein, T.; Refaely-Abramson, S.; Baer, R. Excitation Gaps of Finite-Sized Systems from Optimally Tuned Range-Separated Hybrid Functionals. *J. Chem. Theory Comput.* **2012**, *8* (5), 1515–1531.

(89) Faber, C.; Boulanger, P.; Attaccalite, C.; Duchemin, I.; Blase, X. Excited States Properties of Organic Molecules: From Density Functional Theory to the GW and Bethe–Salpeter Green's

Function Formalisms. *Philos. Trans. R. Soc. A Math. Phys. Eng. Sci.* **2014**, *372* (2011), 20130271.

(90) Autschbach, J.; Srebro, M. Delocalization Error and "Functional Tuning" in Kohn-Sham Calculations of Molecular Properties. *Acc. Chem. Res.* **2014**, *47* (8), 2592–2602.

(91) Sun, H.; Autschbach, J. Electronic Energy Gaps for π-Conjugated Oligomers and Polymers Calculated with Density Functional Theory. *J. Chem. Theory Comput.* **2014**, *10* (3), 1035–1047.

(92) Körzdörfer, T.; Sears, J. S.; Sutton, C.; Brédas, J. L. Long-Range Corrected Hybrid Functionals for π-Conjugated Systems: Dependence of the Range-Separation Parameter on Conjugation Length. *J. Chem. Phys.* **2011**, *135* (20).

(93) Körzdörfer, T.; Parrish, R. M.; Marom, N.; Sears, J. S.; Sherrill, C. D.; Brédas, J. L. Assessment of the Performance of Tuned Range-Separated Hybrid Density Functionals in Predicting Accurate Quasiparticle Spectra. *Phys. Rev. B - Condens. Matter Mater. Phys.* **2012**, *86* (20), 1–9.

(94) Körzdörfer, T.; Parrish, R. M.; Sears, J. S.; Sherrill, C. D.; Brédas, J. L. On the Relationship between Bond-Length Alternation and Many-Electron Self-Interaction Error. *J. Chem. Phys.* **2012**, *137* (12).

(95) Sutton, C.; Körzdörfer, T.; Gray, M. T.; Brunsfeld, M.; Parrish, R. M.; Sherrill, C. D.; Sears, J. S.; Brédas, J. L. Accurate Description of Torsion Potentials in Conjugated Polymers Using Density Functionals with Reduced Self-Interaction Error. *J. Chem. Phys.* **2014**, *140* (5).

(96) Zhang, C. R.; Sears, J. S.; Yang, B.; Aziz, S. G.; Coropceanu, V.; Brédas, J. L. Theoretical Study of the Local and Charge-Transfer Excitations in Model Complexes of Pentacene-C60 Using Tuned Range-Separated Hybrid Functionals. *J. Chem. Theory Comput.* **2014**, *10* (6), 2379–2388.

(97) Minami, T.; Nakano, M.; Castet, F. Nonempirically Tuned Long-Range Corrected Density Functional Theory Study on Local and Charge-Transfer Excitation Energies in a Pentacene/C60 Model Complex. *J. Phys. Chem. Lett.* **2011**, *2* (14), 1725–1730.

(98) Minami, T.; Ito, S.; Nakano, M. Functional Dependence of Excitation Energy for Pentacene/C60 Model Complex in the Nonempirically Tuned Long-Range Corrected Density Functional Theory. *Int. J. Quantum Chem.* **2013**, *113* (3), 252–256.

(99) Kuritz, N.; Stein, T.; Baer, R.; Kronik, L. Charge-Transfer-like Π→π* Excitations in Time-Dependent Density Functional Theory: A Conundrum and Its Solution. *J. Chem. Theory Comput.* **2011**, *7* (8), 2408–2415.

(100) Karolewski, A.; Stein, T.; Baer, R.; Kümmel, S. Communication: Tailoring the Optical Gap in Light-Harvesting Molecules. *J. Chem. Phys.* **2011**, *134* (15), 1–5.

(101) Sato, N.; Seki, K.; Inokuchi, H. Polarization Energies of Organic Solids Determined by Ultraviolet Photoelectron Spectroscopy. *J. Chem. Soc. Faraday Trans. 2 Mol. Chem. Phys.* **1981**, *77* (9), 1621–1633.

(102) Neaton, J. B.; Hybertsen, M. S.; Louie, S. G. Renormalization of Molecular Electronic Levels at Metal-Molecule Interfaces. *Phys. Rev. Lett.* **2006**, *97* (21), 216405.

(103) Bounds, P. J.; Munn, R. W. Polarization Energy of a Localized Charge in a Molecular Crystal. *Chem. Phys.* **1979**, *44* (1), 103–112.

(104) Bounds, P. J.; Munn, R. W. Polarization Energy of a Localized Charge in a Molecular Crystal. II. Charge-Quadrupole Energy. *Chem. Phys.* **1981**, *59* (1), 41–45.

(105) Bounds, P. J.; Munn, R. W. Polarization Energy of a Localized Charge in a Molecular Crystal.III Submolecule Treatment. *Chem. Phys.* **1981**, *59* (1), 47–53.

(106) Tomasi, J.; Mennucci, B.; Cammi, R. Quantum Mechanical Continuum Solvation Models. *Chem. Rev.* **2005**, *105* (8), 2999–3094.

(107) Zheng, Z.; Brédas, J. L.; Coropceanu, V. Description of the Charge Transfer States at the Pentacene/C60 Interface: Combining Range-Separated Hybrid Functionals with the Polarizable Continuum Model. *J. Phys. Chem. Lett.* **2016**, *7* (13), 2616–2621.

(108) De Queiroz, T. B.; Kümmel, S. Charge-Transfer Excitations in Low-Gap Systems under the Influence of Solvation and Conformational Disorder: Exploring Range-Separation Tuning. *J. Chem. Phys.* **2014**, *141* (8).

(109) De Queiroz, T. B.; Kümmel, S. Tuned Range Separated Hybrid Functionals for Solvated Low Bandgap Oligomers. *J. Chem. Phys.* **2015**, *143* (3).

(110) Sun, H.; Ryno, S.; Zhong, C.; Ravva, M. K.; Sun, Z.; Körzdörfer, T.; Brédas, J. L. Ionization Energies, Electron Affinities, and Polarization Energies of Organic Molecular Crystals: Quantitative Estimations from a Polarizable Continuum Model (PCM)-Tuned Range-Separated Density Functional Approach. *J. Chem. Theory Comput.* **2016**, *12* (6), 2906–2916.

(111) Zheng, Z.; Egger, D. A.; Brédas, J. L.; Kronik, L.; Coropceanu, V. Effect of Solid-State Polarization on Charge-Transfer Excitations and Transport Levels at Organic Interfaces from a Screened Range-Separated Hybrid Functional. *J. Phys. Chem. Lett.* **2017**, *8* (14), 3277–3283.

(112) Refaely-Abramson, S.; Sharifzadeh, S.; Jain, M.; Baer, R.; Neaton, J. B.; Kronik, L. Gap Renormalization of Molecular Crystals from Density-Functional Theory. *Phys. Rev. B - Condens. Matter Mater. Phys.* **2013**, *88* (8), 1–5.

(113) Manna, A. K.; Refaely-Abramson, S.; Reilly, A. M.; Tkatchenko, A.; Neaton, J. B.; Kronik, L. Quantitative Prediction of Optical Absorption in Molecular Solids from an Optimally Tuned Screened Range-Separated Hybrid Functional. *J. Chem. Theory Comput.* **2018**, *14* (6),

2919–2929.

(114) Bhandari, S.; Cheung, M. S.; Geva, E.; Kronik, L.; Dunietz, B. D. Fundamental Gaps of Condensed-Phase Organic Semiconductors from Single-Molecule Calculations Using Polarization-Consistent Optimally Tuned Screened Range-Separated Hybrid Functionals. *J. Chem. Theory Comput.* **2018**, *14* (12), 6287–6294.

(115) Cho, E.; Coropceanu, V.; Brédas, J.-L. Electronic Structure of Multicomponent Organic Molecular Materials: Evaluation of Range-Separated Hybrid Functionals. *J. Chem. Theory Comput.* **2020**, *16* (6), 3712–3719.

(116) Bhandari, S.; Dunietz, B. D. Quantitative Accuracy in Calculating Charge Transfer State Energies in Solvated Molecular Complexes Using a Screened Range Separated Hybrid Functional within a Polarized Continuum Model. *J. Chem. Theory Comput.* **2019**, *15* (8), 4305–4311.

(117) D'Avino, G.; Muccioli, L.; Zannoni, C.; Beljonne, D.; Soos, Z. G.; D'Avino, G.; Muccioli, L.; Zannoni, C.; Beljonne, D.; Soos, Z. G.; D'Avino, G.; Muccioli, L.; Zannoni, C.; Beljonne, D.; Soos, Z. G. Electronic Polarization in Organic Crystals: A Comparative Study of Induced Dipoles and Intramolecular Charge Redistribution Schemes. *J. Chem. Theory Comput.* **2014**, *10* (11), 4959–4971.

(118) Tsiper, E. V; Soos, Z. G. Charge Redistribution and Polarization Energy of Organic Molecular Crystals. *Phys. Rev. B* **2001**, *64* (19), 195124.

(119) Soos, Z. G.; Tsiper, E. V; Pascal, R. A. Charge Redistribution and Electronic Polarization in Organic Molecular Crystals. *Chem. Phys. Lett.* **2001**, *342* (5), 652–658.

(120) Poelking, C.; Tietze, M.; Elschner, C.; Olthof, S.; Hertel, D.; Baumeier, B.; Würthner, F.; Meerholz, K.; Leo, K.; Andrienko, D. Impact of Mesoscale Order on Open-Circuit Voltage in Organic Solar Cells. *Nat. Mater.* **2015**, *14* (4), 434–439.

(121) Thole, B. T. Molecular Polarizabilities Calculated with a Modified Dipole Interaction. *Chem. Phys.* **1981**, *59* (3), 341–350.

(122) Besler, B. H.; Merz Jr., K. M.; Kollman, P. A. Atomic Charges Derived from Semiempirical Methods. *J. Comput. Chem.* **1990**, *11* (4), 431–439.

(123) Breneman, C. M.; Wiberg, K. B. Determining Atom-Centered Monopoles from Molecular Electrostatic Potentials. The Need for High Sampling Density in Formamide Conformational Analysis. *J. Comput. Chem.* **1990**, *11* (3), 361–373.

(124) Woods, R. J.; Chappelle, R. Restrained Electrostatic Potential Atomic Partial Charges for Condensed-Phase Simulations of Carbohydrates. *J. Mol. Struct. THEOCHEM* **2000**, *527* (1), 149–156.

(125) D'Avino, G.; Vanzo, D.; Soos, Z. G. Dielectric Properties of Crystalline Organic Molecular

Films in the Limit of Zero Overlap. *J. Chem. Phys.* **2016**, *144* (3), 34702.

(126) Born, M. Volumen Und Hydratationswärme Der Ionen. *Zeitschrift für Phys.* **1920**, *1* (1), 45–48.

(127) D'Avino, G.; Mothy, S.; Muccioli, L.; Zannoni, C.; Wang, L.; Cornil, J.; Beljonne, D.; Castet, F. Energetics of Electron-Hole Separation at P3HT/PCBM Heterojunctions. *J. Phys. Chem. C* **2013**, *117* (25), 12981–12990.

(128) Idé, J.; Méreau, R.; Ducasse, L.; Castet, F.; Bock, H.; Olivier, Y.; Cornil, J.; Beljonne, D.; D'Avino, G.; Roscioni, O. M.; Muccioli, L.; Zannoni, C. Charge Dissociation at Interfaces between Discotic Liquid Crystals: The Surprising Role of Column Mismatch. *J. Am. Chem. Soc.* **2014**, *136* (7), 2911–2920.

(129) D'Avino, G.; Olivier, Y.; Muccioli, L.; Beljonne, D. Do Charges Delocalize over Multiple Molecules in Fullerene Derivatives? *J. Mater. Chem. C* **2016**, *4* (17), 3747–3756.

(130) D'Avino, G.; Muccioli, L.; Olivier, Y.; Beljonne, D. Charge Separation and Recombination at Polymer-Fullerene Heterojunctions: Delocalization and Hybridization Effects. *J. Phys. Chem. Lett.* **2016**, *7* (3), 536–540.

(131) Li, J.; Duchemin, I.; Roscioni, O. M.; Friederich, P.; Anderson, M.; Da Como, E.; Kociok-Köhn, G.; Wenzel, W.; Zannoni, C.; Beljonne, D.; Blase, X.; D'Avino, G. Host Dependence of the Electron Affinity of Molecular Dopants. *Mater. Horizons* **2019**, *6* (1), 107–114.

(132) Londi, G.; Dilmurat, R.; D'Avino, G.; Lemaur, V.; Olivier, Y.; Beljonne, D. Comprehensive Modelling Study of Singlet Exciton Diffusion in Donor-Acceptor Dyads: When Small Changes in Chemical Structure Matter. *Phys. Chem. Chem. Phys.* **2019**, *21* (45), 25023–25034.

(133) Privitera, A.; Londi, G.; Riede, M.; D'Avino, G.; Beljonne, D. Molecular Quadrupole Moments Promote Ground-State Charge Generation in Doped Organic Semiconductors. *Adv. Funct. Mater.* **2020**, *30*, 2004600.

(134) D'Avino, G.; Duhm, S.; Della Valle, R. G.; Heimel, G.; Oehzelt, M.; Kera, S.; Ueno, N.; Beljonne, D.; Salzmann, I. Electrostatic Interactions Shape Molecular Organization and Electronic Structure of Organic Semiconductor Blends. *Chem. Mater.* **2020**, *32* (3), 1261–1271.

(135) Li, J.; D'Avino, G.; Duchemin, I.; Beljonne, D.; Blase, X. Accurate Description of Charged Excitations in Molecular Solids from Embedded Many-Body Perturbation Theory. *Phys. Rev. B* **2018**, *97* (3), 1–13.

(136) Levy, M. Universal Variational Functionals of Electron Densities, First-Order Density Matrices, and Natural Spin-Orbitals and Solution of the v-Representability Problem. *Proc. Natl. Acad. Sci.* **1979**, *76* (12), 6062 LP – 6065.

A Comprehensive Modelling Study of Singlet Exciton Diffusion on Push-Pull Molecules

In this Chapter, within the context of their use as donor materials in bulk heterojunction (BHJ) organic solar cells (OSCs), we compare two small π-conjugated donor-Bridge-acceptor organic molecules differing mainly by the number of thiophene rings in their bridging motifs (1 ring in **1** and 2 rings in **2**, see chemical structures in Figure 3.1), with the aim of rationalizing the origin for the enhancement in singlet exciton diffusion coefficient and length in **1** with respect to **2**. It was experimentally suggested that the higher power conversion efficiencies (PCEs) of **1** could partly arise from an improved exciton diffusion. To achieve an in-depth microscopic picture for the relationships between the primary chemical structure and the nature of the lowest electronic excitations, we provide a fully atomistic modelling study of the energetics and dynamics of singlet electronic excitations in solid films of the two materials. In order to gain access to the morphology of these materials, classical molecular dynamics (MD) simulations on the pristine molecules are performed. On the resulting morphologies, time-dependent density functional theory (TDDFT) and microelectrostatic (ME) calculations are carried out to assess the nature of the relevant electronic excitations and their broadly disordered energy landscape. Then, the internal and external reorganization energies are evaluated as well as the exciton couplings between neighboring molecules that are injected into an energy transfer rate expression taken from the Marcus-Levich-Jortner (MLJ) formalism. Based on these rates, kinetic Monte Carlo (KMC) simulations are performed to model the transport of singlet excitons and achieve the diffusion coefficient and the exciton diffusion length. In addition to a longer excited state lifetime associated with a more pronounced intramolecular charge-transfer character, our calculations reveal that singlet excitons in **1** are capable to funnel through long-distance hopping percolation pathways, presumably as a result of the less anisotropic shape of the molecule that favours long-range 3D transport.

The work presented in this Chapter is published in G. Londi, R. Dilmurat, G. D'Avino, V. Lemaur, Y. Olivier and D. Beljonne. Comprehensive modelling study of singlet exciton diffusion in donor-acceptor dyads: when small changes in chemical structure matter. *Phys. Chem. Chem. Phys.* **2019**, *21* (45), 25023–25034.

3.1 Introduction

Small modifications in the primary chemical structure of the electro-active molecules in BHJ OSCs can turn into large changes in their photo-physical behavior and the resulting opto-electronic response at the device dimensions. We report such an example here, where the focus is on the nature and dynamics of singlet excitations in two small π-conjugated organic molecules: a {4-[5-(2-Phenyl-1,1-dicyanoeth-1-en-2-yl)-2-thienyl]phenyl}diphenylamine (TPA-T-DCV-Ph) compound and a 1-{5'-[4-(diphenylamino)phenyl]-2,2'-bithien-5-yl}ethylidene)malononitrile (TPA-2T-DCV-Me) one, referred to as **1** and **2**, respectively, in Figure 3.1.

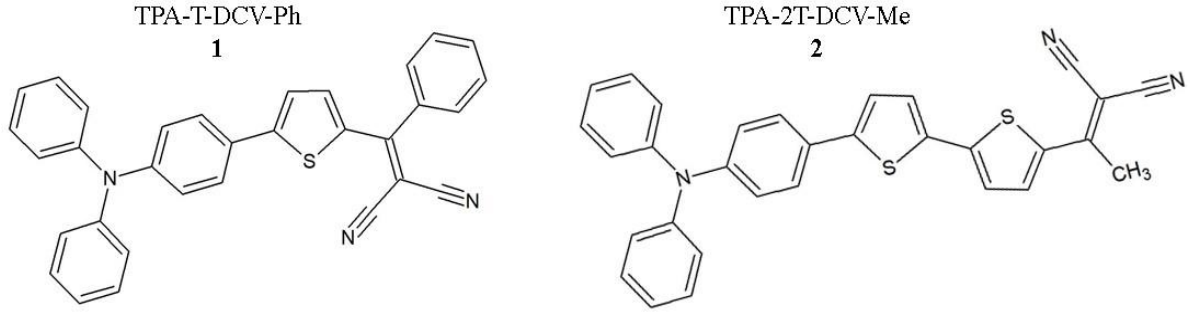

Figure 3.1: Chemical structures of **1** (left) and **2** (right).

These π-conjugated molecules belong to the class of *push-pull* systems, and were designed with the purpose of introducing a partial intramolecular charge-transfer (CT) character into the lowest exciton states. As these excitons likely feature reduced Coulomb binding energy associated with larger electron-hole (e-h) separation, they should also be more prompt to dissociation into separated charges at the interface with fullerene electron acceptors. The two donor-π-acceptor molecules both comprise a triphenylamine (TPA) fragment, acting as a donor (D), and a dicyanovinylene moiety (DCV), acting as an acceptor (A), linked through either a thiophene (in **1**) or a bithiophene (in **2**) π-linker. Electronic excited states in these molecules can be pictured as resulting from the mixing between Frenkel excitations (FE) on the π-conjugated spacer and through-bridge intramolecular D-A CT ones. While admixture of CT configurations would red-shift the excitation energies, overlapping e-h configurations predominantly feed the oscillator strength, hence enabling large absorption cross-sections in the visible and efficient solar light harvesting. The synthesis of the two dyes, their electrochemical and time-resolved photoluminescence (PL) characterization along with OSC device fabrication and testing have been reported elsewhere.[1–3]

Because it features a more extended conjugated backbone, one would anticipate that **2** has a significantly red-shifted optical absorption yielding better overlap with the solar emission spectrum and should thus outperform **1** when used as a D in a BHJ OSC. It turns out, however, that this is not the case, with significantly larger PCEs reported for **1** (>5%) compared to **2** (~2%) in vacuum-

evaporated single solar cells using fullerenes as A molecules. Changes in morphology can be ruled out, as the same trend is observed irrespective of whether the active layer is solution-processed or vacuum-processed. Instead, it was suggested[3] that this improvement at least partly arises from a more efficient singlet exciton diffusion in amorphous films of **1**. As a matter of fact, the reported exciton diffusion length was measured using PL quenching experiments to be significantly larger in **1** (~26 nm) compared to **2** (~10 nm). This result was attributed to the concerted effects of the longer exciton lifetime, ~1.6 ns in **1** versus less than 1 ns in **2**, together with the reduced energetic disorder in the smaller molecule.

3.2 Theoretical Methodology

3.2.1 Molecular Dynamics Simulations

In order to model the morphology of these materials, classical force field (FF) MD simulations were carried out. The employed FF was derived from Dreiding,[4] while re-parameterizing the soft inter-ring torsional potentials against reference MP2/cc-pVDZ calculations, as required for an accurate description of the conformational degrees of freedom (see Figure 3.11 and 3.12 in Additional data). Amorphous phases of the two compounds (from now on **1a** and **2a**) were built using the amorphous builder tool of Materials Studio 6.0 package, which implements periodic boundary conditions. The protocol consisted of the following steps: 1) creation of an initial configuration of 1000 molecules in a large 3D periodic cubic box (initial density $\sim 0.2\ \mathrm{g\ cm^{-3}}$); 2) a MD run in the canonical (NVT) ensemble at 1000 K for 200 ps to randomize molecular orientations; 3) a MD run in the isothermal-isobaric (NPT) ensemble at 1000 K for 1 ns, compressing the sample by progressively increasing the pressure from 1 atm to 1 GPa; 4) a NPT-MD run at 1 GPa for 600 ps, gradually cooling down the system from 1000 to 298 K; 5) a NPT-MD run at 298 K for 800 ps, releasing the pressure from 1 GPa to 1 atm; and finally 6) a NPT-MD run for 2.5 ns at 298 K and 1 atm. In addition, for **1**, a crystalline 8x6x5 triclinic supercell (from now on **1x**) was generated based on the experimentally resolved crystallographic unit cell,[5] in order to reach a comparable size in term of numbers of molecules within the simulation box (960 molecules for 1**x** and 1000 molecules for 1**a**). The crystalline supercell was submitted to the following steps: 1) a NVT-MD run for 200 ps run at 298 K; 2) a NPT-MD run for 2.5 ns at 298 K and 1 atm. For both the amorphous and crystalline NPT-MD final runs of 2.5 ns, 500 ps were needed for equilibration and 2 ns for production, saving snapshots every 5 ps along the trajectory. The Nosé-Hoover thermostat and the Berendsen barostat (for NPT runs) were adopted. The electrostatic interactions were considered by calculating the ESP atomic charges on the isolated molecule at the MP2/cc-pVDZ level. MP2 calculations were performed with the GAUSSIAN09 suite,[6] while Materials Studio 6.0 was adopted for the FF MD simulations.

The reparametrized FF was first benchmarked against experimental data by running simulations on **1x**. Our NPT-MD simulations on the cry crystalline supercell at standard conditions yield a density $d_{MD} = 1.23\ \mathrm{g}\ cm^{-3}$, in perfect agreement with the experimental value of $d_{EXP} = 1.24\ \mathrm{g}\ cm^{-3}$. The

densities of amorphous samples were $d_{MD} = 1.02\ \mathrm{g}\,cm^{-3}$ for **1a** (lower than that of the crystal, as expected) and $d_{MD} = 0.97\ \mathrm{g}\,cm^{-3}$ for **2a** (see Table 3.3 in Additional data) Moreover, the orientational order in the amorphous samples was assessed by computing the second-rank order parameter $P_2 = \langle\frac{3cos^2\theta-1}{2}\rangle$, where θ is the angle between the long molecular axis and a given reference axis and angular brackets denote the average over the production MD trajectory. We obtained $P_2 \approx 0.00$ for **1a** and $P_2 \approx 0.01$ for **2a**, testifying the isotropic nature of the amorphous samples.

3.2.2 Excited State Energetics

Electronic structure calculations were performed to track the excited state energetics for molecular snapshots extracted along the MD trajectories. An optimally tuned (OT) range-separated hybrid (RSH) functional ωB97X-D was employed.[7,8] Optimized ω values in RSH functionals are usually strongly system-dependent, in particular for π-conjugated molecules, yet turn out to have very similar values here for **1** ($\omega = 0.139\ Bohr^{-1}$) and **2** ($\omega = 0.141\ Bohr^{-1}$). These values were kept fixed throughout the DFT and TDDFT simulations, carried out using GAUSSIAN09 with the 6-31G(d,p) basis set, except where otherwise specified.

The effect of the polarizable molecular environment on intramolecular excitations energies was accounted for by means of classical ME calculations.[9,10] In a nutshell, the ME scheme allows the calculation of a perturbative correction (Δ^x, the exciton polarization energy) to gas-phase TDDFT lowest energy excitation (S_1). The ME model was parametrized with gas-phase ESP atomic charges[11] calculated at the DFT and TDDFT ωB97X-D/6-311++G(d,p) level for the ground (S_0) and the excited (S_1) state, respectively. The polarizability tensor of the ground state molecule, computed at the same above-mentioned level of theory, was adopted to describe both S_0 and S_1.

TDDFT calculations were repeated for all individual molecules extracted from the last MD frame and for 20 molecules (extracted from 400 snapshots) followed along the 2 ns trajectory, thus allowing to build some statistics in space and time. The fluctuations of S_1 excitation energy can be quantified by the standard deviation σ_{tot} of its distribution. These fluctuations can be split into two distinct contributions, according to the relevant timescales of the fluctuations: a static contribution (*i.e.*, presenting negligible variations over the time scales characterizing exciton lifetimes, ~1 ns), which results from the different environment experienced by each molecule, and a dynamic contribution, associated with faster molecular motions:

$$\sigma_{tot} = \sqrt{\sigma_{stat}^2 + \sigma_{dyn}^2} \tag{3.1}$$

σ_{tot} is obtained as the full S_1 standard deviation for all molecules extracted from the last MD frame. In order to assess the dynamic contribution, 20 molecules were randomly selected, and their excitation

energies tracked along the 2 ns MD trajectory. The fluctuations around their individual mean lead to the dynamical variance:

$$\sigma_{dyn}^2 = \frac{1}{n}\sum_{i,k}(E_{ik} - \overline{E_k})^2 \tag{3.2}$$

where E_{ik} is the S_1 energy of molecule *k* at time *i*, $\overline{E_k}$ is the mean energy of molecule *k*, and *n* is the number of samples. σ_{stat} is then obtained by subtraction from equation (3.1).

3.2.3 Singlet Exciton Hopping Rates and Diffusion

Singlet exciton diffusion in the amorphous phase of two materials was reproduced using a hopping transport model, which is fully justified owing to the much smaller excitonic couplings (<100 meV) compared to the total relaxation energies (~500 meV). The hopping rate was computed using the non-adiabatic semiclassical MLJ expression that accounts for quantum tunneling effects:[12]

$$\kappa_{if} = \frac{2\pi}{\hbar} V_{if}^2 \sqrt{\frac{1}{4\pi\lambda_s k_B T}} \times$$

$$\times \sum_n \left\{ exp\left(-S_{eff}\right) \frac{S_{eff}^n}{n!} \times exp\left[-\frac{\left(\Delta G_{if}^0 + \lambda_s + n\hbar\omega_{eff}\right)^2}{4\lambda_s k_B T} \right] \right\} \tag{3.3}$$

where κ_{if} is the exciton hopping rate between molecular sites *i* and *f*; V_{if} is the corresponding exciton coupling; λ_s is the external reorganization energy; $\hbar$ is the reduced Planck's constant, k_B is the Boltzmann constant; T is the temperature; ΔG_{if}^0 is the free Gibbs energy difference involved in the hopping mechanism; $\hbar\omega_{eff}$ is the energy of an effective high-frequency intramolecular vibrational mode (the carbon-carbon stretching) that assists the exciton hopping; $S = \lambda_i/(\hbar\omega_{eff})$ is the Huang-Rhys factor, which measures the internal reorganization energy λ_i.

Our atomistic calculations were used to provide reliable parameters for equation (3.3). Site energies were drawn from a Gaussian distribution with standard deviation σ_{stat} and then used to compute inter-site free energy differences ΔG_{if}^0. The dynamic disorder σ_{dyn} is instead related to the total reorganization energy, and specifically for linear exciton-phonon coupling to a bath of classical harmonic modes:

$$\lambda_{tot} = \frac{\sigma_{dyn}^2}{k_B T} \tag{3.4}$$

In turn, λ_{tot} comprises two different contributions:

$$\lambda_{tot} = \lambda_i + \lambda_s \tag{3.5}$$

where the internal part, λ_i, arises from the difference in the equilibrium geometries between the molecule ground state (S_0) and the first excited state (S_1), while the external part, λ_s, is due to the structural relaxation of the surrounding medium upon energy transfer. Since high-frequency modes are quantum in nature, λ_i can be more safely estimated with the 4-point approach based on DFT/TDDFT calculations in gas-phase, namely:

$$\lambda_i = E(S_1|r_0) - E(S_1|r_1) + E(S_0|r_1) - E(S_0|r_0) \tag{3.6}$$

where $E(S_m|r_n)$ indicated the energy of the state S_m at the geometry optimized for the state S_n. We note that the geometry optimization in the excited state was performed starting from the ground state geometry and freezing the soft torsional angles, in order to account only for the contribution from the high-frequency modes (and thus avoid double-counting, since the low-frequency modes enter λ_i through the classical MD simulations). The external contribution was then calculated by subtraction from the total reorganization energy, according to equations (3.4) and (3.5).

The exciton couplings, V_{if}, between molecules in the amorphous samples were computed at the TDDFT level, resorting to the fragment excitation difference (FED) scheme.[13] The molecular pairs (dimers) were selected according to geometrical criteria: electronic couplings were computed for dimers with less than 20 Å distance between their center of mass and whose atom-atom distance was found to be smaller than 6 Å. The FED scheme is a diabatization procedure that relies on the calculation of the attachment density (the density of the electron promoted in the transition) and the detachment density (the hole density created in the transition).[14] The electronic couplings are obtained through a unitary transformation that yields the localized diabatic states by maximizing the excitation density difference between the two molecules involved in the energy transfer process. While exchange and overlap might contribute at short intermolecular distances, the Coulomb term is expected to dominate at long range, where it should decay following the usual Förster-like R^{-3} dipole-dipole interaction.

Finally, KMC simulations employing the first reaction method (FRM) algorithm[15] were performed to assess exciton diffusion coefficient and length. Such a stochastic approach involves the following steps: (1) initialization of the system at time $t = 0$; (2) calculation of the hopping rates from MLJ equation; (3) quantifying the time for hopping events between an initial (*i*) and a final site (*f*) using the following equation:

$$\Delta t_{if} = -\frac{\ln(r)}{\kappa_{if}} \tag{3.7}$$

where r is a random number generated between 0 and 1 and κ_{if} is MLJ hopping rate; (4) selecting the event with the smallest Δt_{if} for the exciton to hop and update its position; (5) updating the time $t = t + \Delta t_{if}$ if t is less than the simulation time (10 ns), else stop the simulation. In order to obtain statistically relevant results, and because of the sizeable energetic disorder, a large number of simulations were required (*i.e.*, one million). From the TD mean-square displacements, averaged singlet exciton diffusion coefficient and diffusion length, L_d, are related through:

$$L_d = \sqrt{D\,\tau_1} \tag{3.8}$$

with τ_1 the exciton lifetime.

3.3 Results and Discussion

3.3.1 Excited State Electronic Structure

The ground state equilibrium geometry of the two molecules was optimized at the ωB97X-D/6-31G(d,p) level. To get insight into the nature of the lowest electronic excitations in the two molecules, we first performed gas-phase TDDFT calculations at the ground state geometries. Multiple metrics allow assessing the character of electronic excitations.[16,17] Here, we opted for the overlap, Φ_s, between the hole and electron densities shown in Figure 3.2 for the two molecules. Pure CT excitations correspond to non-overlapping e-h density ($\Phi_s = 0$), while fully FE excitations lead to $\Phi_s = 1$. The CT or FE character of the excitation depends strictly on the molecular geometry and its fluctuations around equilibrium, as well as on the choice of the exchange-correlation functional.

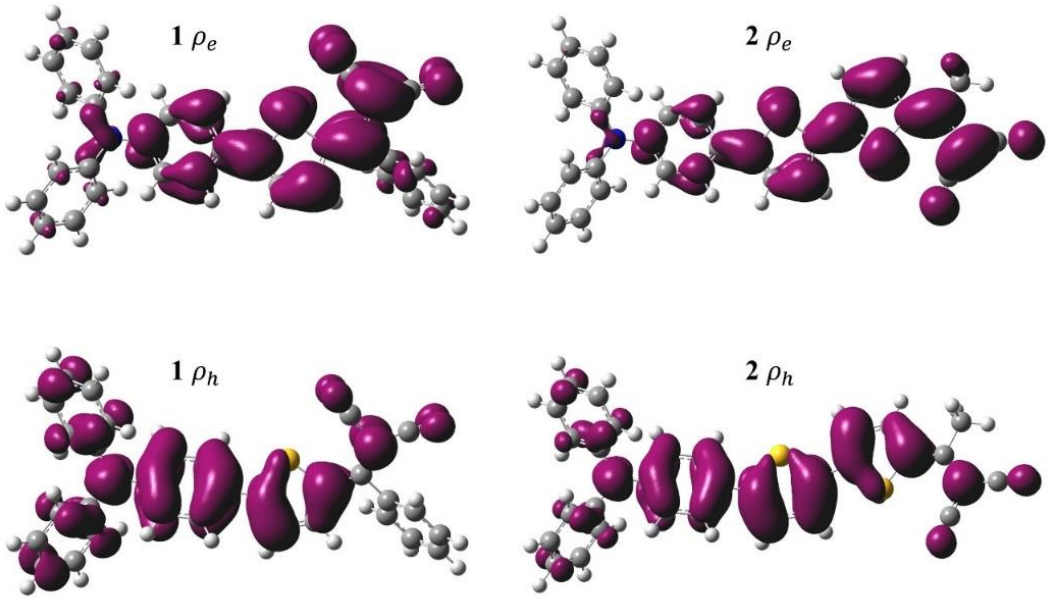

Figure 3.2: Electron (ρ_e) and hole (ρ_h) densities calculated in the attachment/detachment formalism for S_1 in **1** (left) and **2** (right), as obtained at the OT-RSH TDDFT level (ωB97X-D/6-31G(d,p)) based on gas-phase equilibrium ground state geometries.

TDDFT calculations in gas-phase were also performed to assess the vertical excitation energies. The S_0-S_1 transition energy is 3.15 eV in **1** (with an oscillator strength of 1.167), and 3.04 eV in **2** (with

an oscillator strength of 1.657). The excitation energies obtained for single molecules are close to the mean values obtained by sampling the gas-phase conformations using MD simulations in Figure 3.5 (see below).The e-h density plots in Figure 3.2 show that S_1 has a mixed π-π^*/CT character,[18] with both hole and electron density spreading over most of the π-system in both compounds. This translates into Φ_s values of ~0.66 in **1** and ~0.72 in **2**. Thus, extending the bridge from one to two thiophene rings slightly reduces the CT character of the electronic excitations. We next repeated the TDDFT calculations on all molecules individually extracted from the last MD frame of the three investigated samples (the amorphous **1a** and **2a** and the crystalline **1x**).

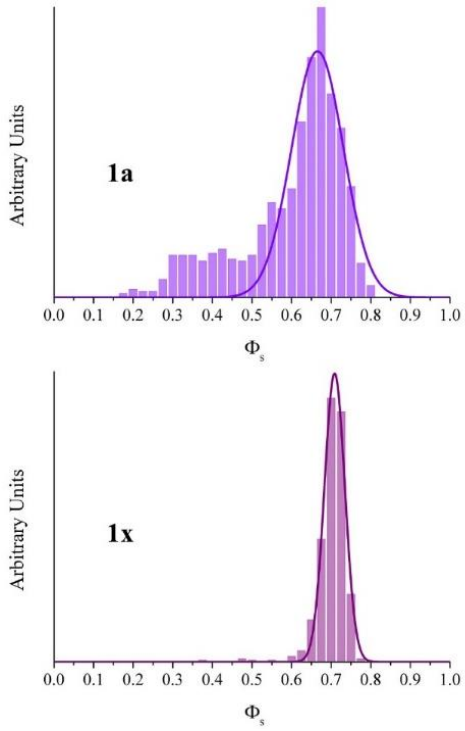

	$\langle\Phi_s\rangle \pm \sigma$
1a	0.67 ± 0.07
1x	0.71 ± 0.03
2a	0.73 ± 0.05

Figure 3.3: Room-temperature MD distributions of e-h density overlaps Φ_s in S_1 for **1a**, **1x** and **2a**. The averaged Φ_s values and their standard deviations are also reported in the table. Solid lines are Gaussian fits.

The results, reported in Figure 3.3, show a broad distribution of the e-h overlap factors around the values predicted at the equilibrium geometries, clearly associated with thermal fluctuations in the conformation of the molecules. In particular, rotations around the single bonds connecting the donor to the bridge and the bridge to the acceptor modulate the coupling between the donor and the acceptor groups of the molecule and, therefore, the amount of CT-FE admixture. It is interesting to point out that Φ_s distributions in wave function overlap are asymmetric, showing a long tail at low Φ_s values that correspond to low-energy conformations, hence possibly slowing down exciton diffusion. As expected, the molecules in the long-range ordered **1x** explore a much smaller region of the conformational space, hence the narrower Φ_s distribution. Very interestingly, Figure 3.4

demonstrates that the S_1 excitation energy and its CT character are correlated, at least in the low-energy region, with larger CT admixture (lower Φ_s) translating into red-shifted excitations. This is particularly pronounced for molecule **1**, where conformations yielding the lowest excitation energies are predominantly CT-like, with Φ_s approaching 0.3.

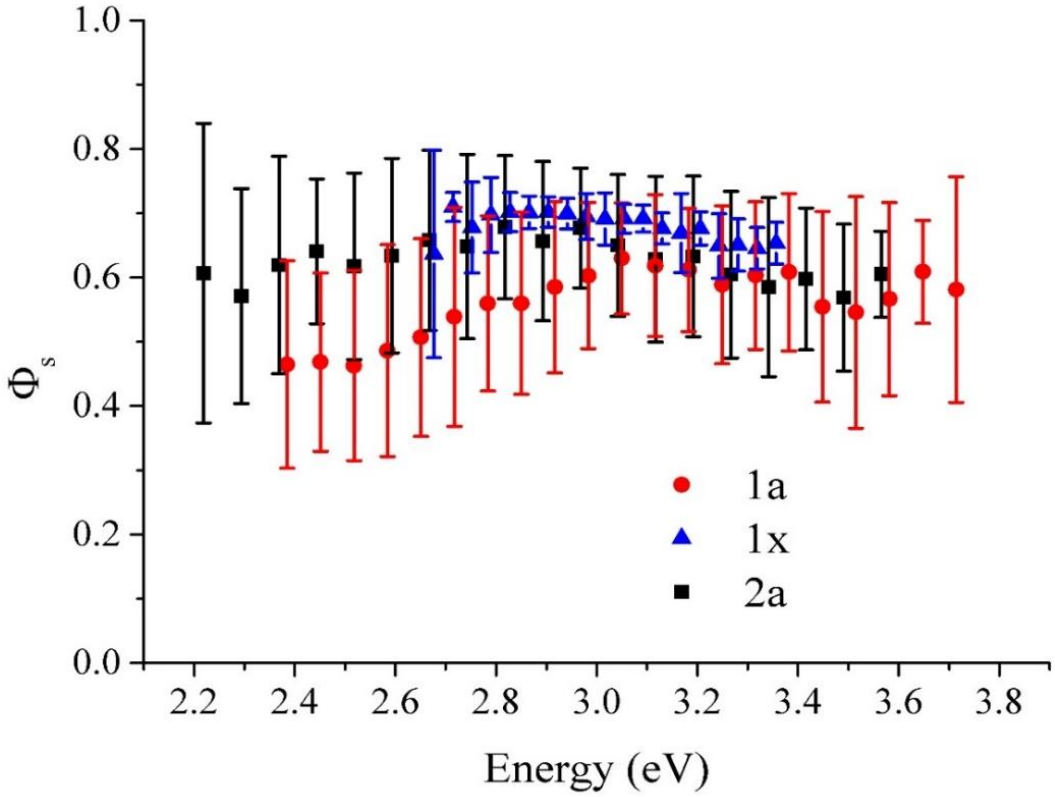

Figure 3.4: Plotted e-h density overlap Φ_s versus transition energy to S_1, as obtained at the OT-RSH TDDFT level on MD geometries for **1a** (red dots), **1x** (blue triangles) and **2a** (black squares). Data set standard deviation at room-temperature is represented by vertical bars. In the low-energy part (below ~3 eV) the correlation coefficient for **1a** is $R^2 = 0.95$, while for **2a** is $R^2 = 0.76$.

From sampling of the configurational space at room-temperature, exciton density of states (DOS) distributions were calculated for single molecules either in gas-phase or embedded in a fully atomistic electrostatic embedding. The results, portrayed in Figure 3.5, show broad, Gaussian-like, DOS primarily governed by changes in molecular conformation, with different standard deviations obtained in absence versus in presence of the polarizable environment ($\Delta\sigma_{total} < 30$ meV). The environmental effects primarily contribute with a shift of the distributions, by 0.17 eV for **1a**, 0.13 eV for **1x** and 0.10 eV for **2a**. These small energy corrections reflect the reduced ionic character of the lowest electronic excitations – for the sake of comparison, excess positive or negative charges are typically stabilized by about 1 eV energy corrections in polarizable molecular crystals.[9,19,20] The most striking feature from Figure 3.5 is the rather similar mean values predicted in the amorphous phase

of the two molecules, despite the more extended π-bridge in **2** compared to **1**. This is ascribed to the increased CT character in the shorter molecule, as documented above, that compensates for its reduced conjugation length.

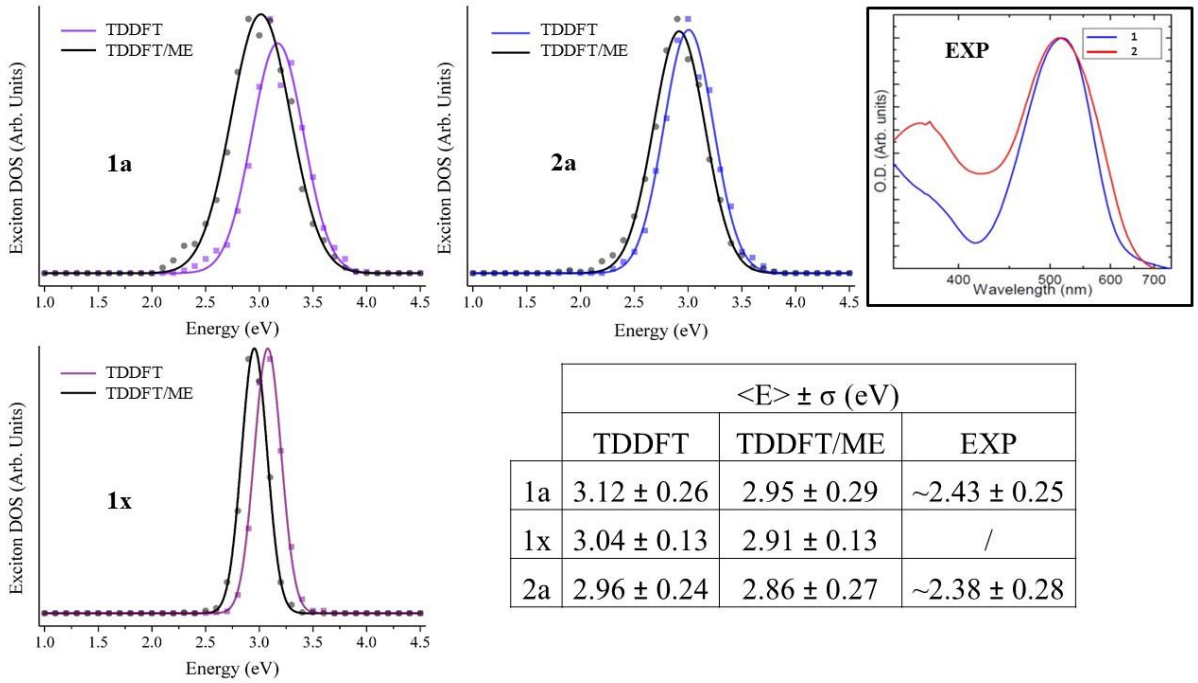

	<E> ± σ (eV)		
	TDDFT	TDDFT/ME	EXP
1a	3.12 ± 0.26	2.95 ± 0.29	~2.43 ± 0.25
1x	3.04 ± 0.13	2.91 ± 0.13	/
2a	2.96 ± 0.24	2.86 ± 0.27	~2.38 ± 0.28

Figure 3.5: Exciton density of states (DOS) for the lowest electronic excitation based on gas-phase TDDFT calculations (coloured) and accounting for electrostatic embedding TDDFT/ME (in black). Averaged excitation energies and their standard deviations are also reported in the table. Solid lines are Gaussian fits. In the inset, the measured absorption spectra of neat films of **1** and **2** taken from Refs.[2,3] are showed; their extracted excitation energies and full width half maximum values are also reported.

We stress that these predictions both qualitatively and quantitatively match with thin-film optical absorption measurements reported in Refs.[2,3] and in the inset of Figure 3.5. There, the transition energies measured at λ_{max} for the two molecules almost coincide and the spectral lineshapes can be reasonably fitted with Gaussian functions of standard deviations close to those predicted by theory, although a quantitative comparison with experiment is hampered by the lack of quantum nuclear effects (*i.e.*, Franck-Condon structure) and by the assumption of excitons strictly localized on molecular units in the calculations. Moreover, it should be stressed that these large σ values refer to the total width, which encompasses static and dynamic disorder (see Table 3.1). As a side note, we remark that, besides its obvious narrower character, the centre of the energy distribution predicted in **1x** is almost iso-energetic with that in **1a**. While this might sound surprising at first glance, this is once again the result between the interplay of molecular conformation (on averaged more planar in the crystalline phase) and CT-FE mixing (reduced CT character in the crystal). We believe this is a

potentially important result, as local crystalline domains embedded in an otherwise amorphous matrix usually act as trapping sites. This would not be the case for exciton transport in **1**, which thus should be more resilient to positional disorder and morphological inhomogeneities.

Another molecular characteristic that, in addition to being relevant for the excited state lifetime and therefore the singlet exciton diffusion length, directly probes the nature of the electronic excited states is the radiative decay rate Γ_{rad}. This quantity may be related to the nature of the excited states in the two compounds, since a larger CT character would result in a smaller transition dipole moment and, hence, a smaller Γ_{rad}. From a perturbative treatment of light-matter interactions, the spontaneous emission rate Γ_{rad} writes:[21]

$$\Gamma_{rad} = n\frac{\omega_{eg}^3|\vec{\mu}_{eg}^2|}{3\pi\varepsilon_0\hbar c^3} \tag{3.9}$$

where ω_{eg} is the transition frequency from the excited to the ground state, $\vec{\mu}_{eg}$ the transition dipole moment, ε_0 the dielectric vacuum permittivity, $\hbar$ the reduced Planck constant, c the speed of light, and $n = \sqrt{\varepsilon_r}$ the refractive index of the medium, here set equal to 1.49 for a poly(methyl) acrylate (PMMA) matrix (for comparison to experiments reported in Ref.[3]). For the three investigated samples, the calculated radiative exciton lifetime, τ_{rad}, averaged over all accessible conformations as explored by room-temperature MD simulations, amounts to 2.6 ns in **1a**, 1.5 ns in **1x** and 1.9 ns in **2a**. The radiative lifetimes are in line with expectations based on the character of the electronic exited states, with a larger value for **1** reflecting an increased CT contribution in the amorphous phase. They are also on par with the total lifetimes measured in amorphous films of the two dyes, respectively 2.6 ns and less than 1 ns in **1** and **2**, respectively.[2,3] PL quantum yield measurements[5] using an integrating sphere yield a value of 46% in a powder of **1** that, combined with the PL total lifetime, provides an experimental estimate for τ_{rad} of about 3.5 ns, in fair agreement with the theoretical value of 2.6 ns. This comforts us in the robustness of our theoretical methodology to properly reproduce the nature and energetics of singlet optical excitations in the molecular materials at hands. While we are here averaging over the full, broad, exciton DOS, it is likely that low-energy molecular sites contribute predominantly to the PL signal, after (partial) thermalization of the energy carriers.

3.3.2 Singlet Exciton Hopping Rates

Excited state energetics enters the MLJ rates in three different ways: (i) the Gibbs free energy, via the static energetic disorder; (ii) the external, classical (low-frequency) and (iii) the internal, quantum (high-frequency) contributions to the nuclear reorganization energies. All these energies can be obtained from our atomistic simulations, provided some educated guess on timescale separations. Namely, processes that are slow (fast) compared to hopping events were considered static (dynamic). From now on, we will analyze only the exciton diffusion properties for the amorphous pristine materials to provide a better comparison among our investigated samples. The calculated data that feed the MLJ equation for **1a** and **2a** are collected in Table 3.1.

Table 3.1: Calculated σ_{tot}, σ_{stat} and σ_{dyn} values, along with λ_{tot}, λ_i and λ_s ones. σ_{EXP} values extracted from a Gaussian fit of the experimental absorption spectra are also indicated (from Ref.[2,3]).

	$\boldsymbol{\sigma_{tot}}$ **(eV)**	$\boldsymbol{\sigma_{EXP}}$ **(eV)**	$\boldsymbol{\sigma_{stat}}$ **(eV)**	$\boldsymbol{\sigma_{dyn}}$ **(eV)**	$\boldsymbol{\lambda_{tot}}$ **(eV)**	$\boldsymbol{\lambda_i}$ **(eV)**	$\boldsymbol{\lambda_s}$ **(eV)**
1a	0.294	0.25	0.270	0.115	0.514	0.245	0.269
2a	0.268	0.28	0.243	0.113	0.494	0.296	0.198

The energetic disorder is primarily sourced by nuclear motions that are slow relative to exciton hopping, and thus static in nature. These likely involve large-amplitude changes in the conformation of the molecules, which are slowed down by packing effects in the solid. Much faster (internal) reorganization in bond lengths mediated by high-frequency stretching/breathing modes and small (external) rearrangement around the intramolecular equilibrium geometry induced by the environment contribute with similar weights to the total reorganization energy.

We now discuss the exciton couplings, V_{if}, mediating singlet exciton hopping and the MLJ hopping rates, κ_{if}. The FED values are plotted as a function of the intermolecular distance between centers of mass in Figure 3.6a. For comparison, we show in Figure 3.6b the corresponding couplings obtained by retaining only Coulomb interactions in the point dipole – point dipole approximation (PDA). As documented previously,[13] this approximation fails at short distances where it produces erroneously large couplings. At long distances, FED and PDA show the expected inverse cubic distance dependence. A more useful metric for the interactions between molecules is the electronic connectivity or effective coordination number, defined as the number, $n(V_{th})$, of neighbor molecules f coupled to a central molecule i with a coupling V_{if} larger than a given threshold value V_{th}. As expected, $n(V_{th})$ decreases with V_{th} to reach values close to zero for couplings larger than ~40 meV (see Figure 3.6c).

The two molecules show similar evolutions with, on average, 2-6 molecules displaying exciton couplings in the range 10-25 meV. Combining these couplings with the internal and external reorganization energies listed in Table 3.1, we obtained the distributions of nearest neighbor exciton hopping rates, shown in Figure 3.7. These span about six orders of magnitude in timescales with a long tail at small κ_{if} corresponding to unlikely events associated with poorly connected molecules. For both molecules, the rate distributions peak at around 0.1-1 ps^{-1}, which is significantly faster than the exciton lifetimes, thus allowing for multiple jumps during the exciton lifespan.

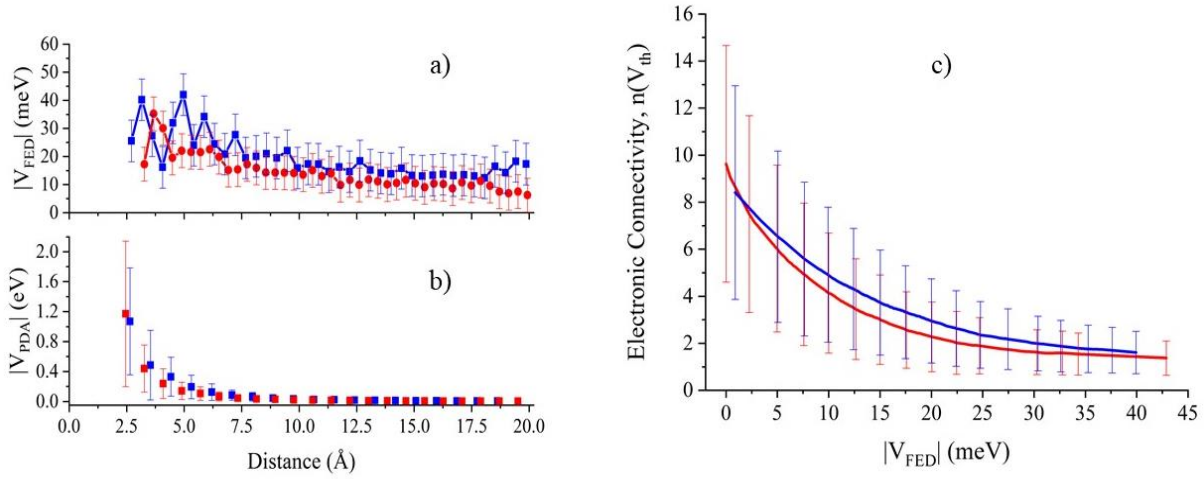

Figure 3.6: Left: exciton coupling calculated with a) the FED scheme and b) in the point dipole - point dipole approximation (PDA) for the **1a** (in red) and **2a** (in blue). Right: electronic connectivity calculated with the FED scheme for **1a** (in red) and **2a** (in blue). Data set standard deviation is represented by vertical bars.

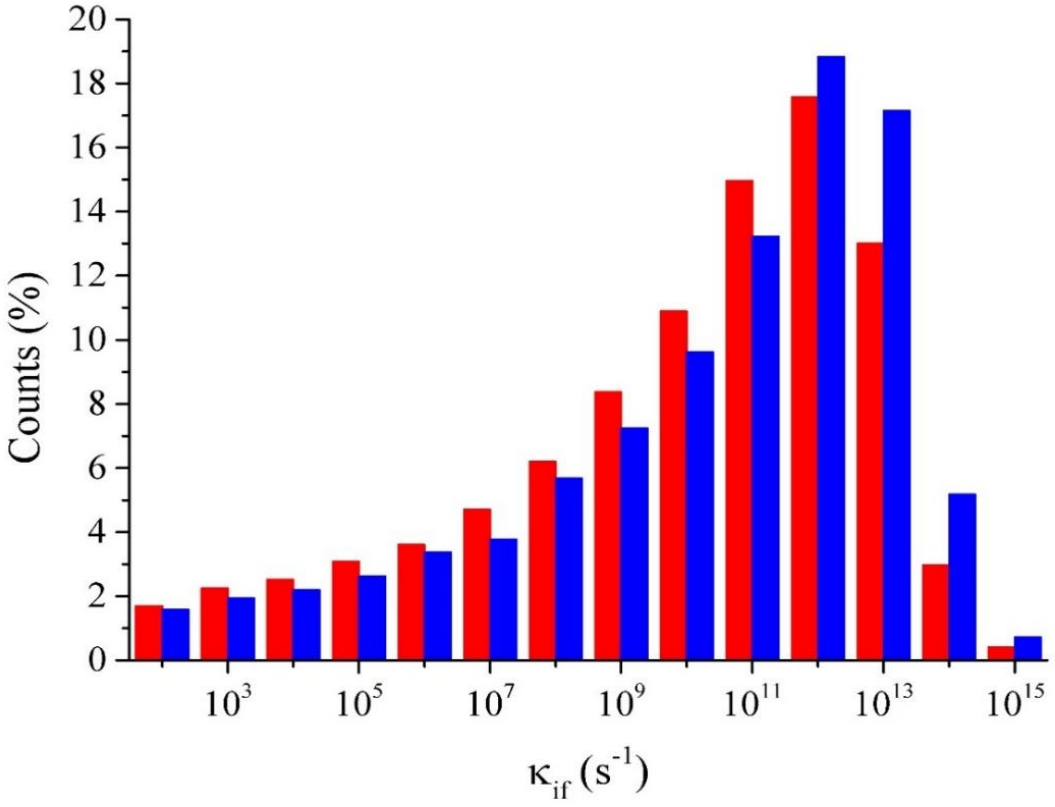

Figure 3.7: MLJ exciton hopping rates κ_{if} distribution calculated for **1a** (in red) and **2a** (in blue).

3.3.3 Singlet Exciton Diffusion

KMC simulations were performed to model exciton dynamics. In a first set of simulations, we assumed as initial conditions a broad band excitation, that is all molecular sites were excited with the same probability irrespective of their energy. We start by analysing the time evolution of the average exciton energy. The results, reported in Figure 3.8, clearly show two different regimes. At early time after light absorption (<10 ps), there is a rapid and large (~0.5 eV) drop in energy attributed to non-equilibrium relaxation processes from initially hot energy carriers. At longer timescales, the system keeps cooling down at a much smaller pace, with no sign of full thermalization during the exciton lifetime.

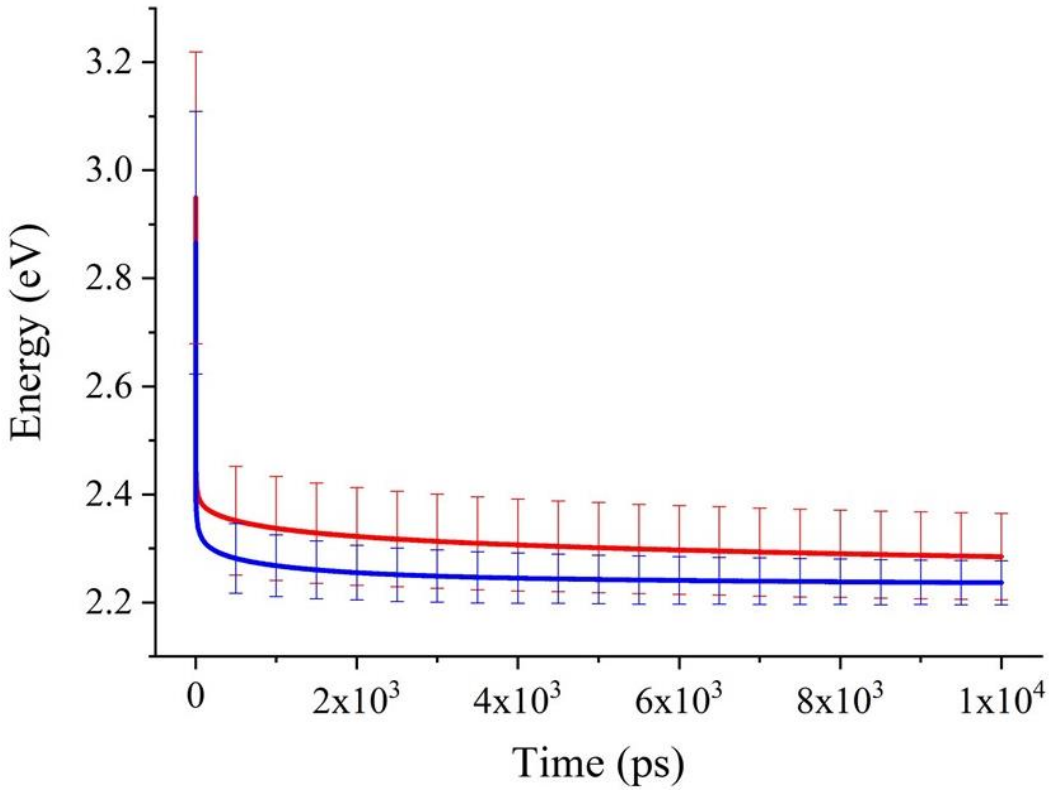

Figure 3.8: Average exciton energy as a function of the simulation time for **1a** (in red) and **2a** (in blue). Data set standard deviation is represented by vertical bars.

At this point, we can already conclude that exciton diffusion in these disordered molecular materials proceeds largely in a non-equilibrium manner. This is corroborated by the calculated mean square displacement over time ratio in Figure 3.9. In the normal diffusion regime, this ratio should converge to a time-independent value at equilibrium conditions, which is not reached during the excited state lifetime in our simulations. Yet, for the sake of simplicity, we will keep referring to the equilibrium concept of diffusion coefficient in the following. With this caveat, it is interesting to notice that, for simulation times commensurate with the singlet lifetime (1-2 ns), D is slightly larger for **1** compared

to **2** (see Figure 3.10a and Table 3.2). We will return to this point later but the consequence of this difference in diffusion coefficient, together with the longer-lived singlet exciton, is that molecule **1** shows a significantly larger exciton diffusion length than **2** (see Figure 3.9b and Table 3.2, where we used the measured total lifetimes). In view of the multifaceted aspect and complexity of the modelling approach, the calculated L_d values are in remarkable agreement with experiment, as shown in Table 3.2.

Table 3.2: Calculated diffusion coefficient D at exciton lifetime and exciton diffusion length L_d for **1a** and **2a**. The experimental values in Ref.[2,3] for the latter are also reported.

	D (cm^2 s^{-1})	EXP L_d (nm)	CALC L_d (nm)
1a	1.53x10^{-3}	~26	18
2a	1.28x10^{-3}	~10	10

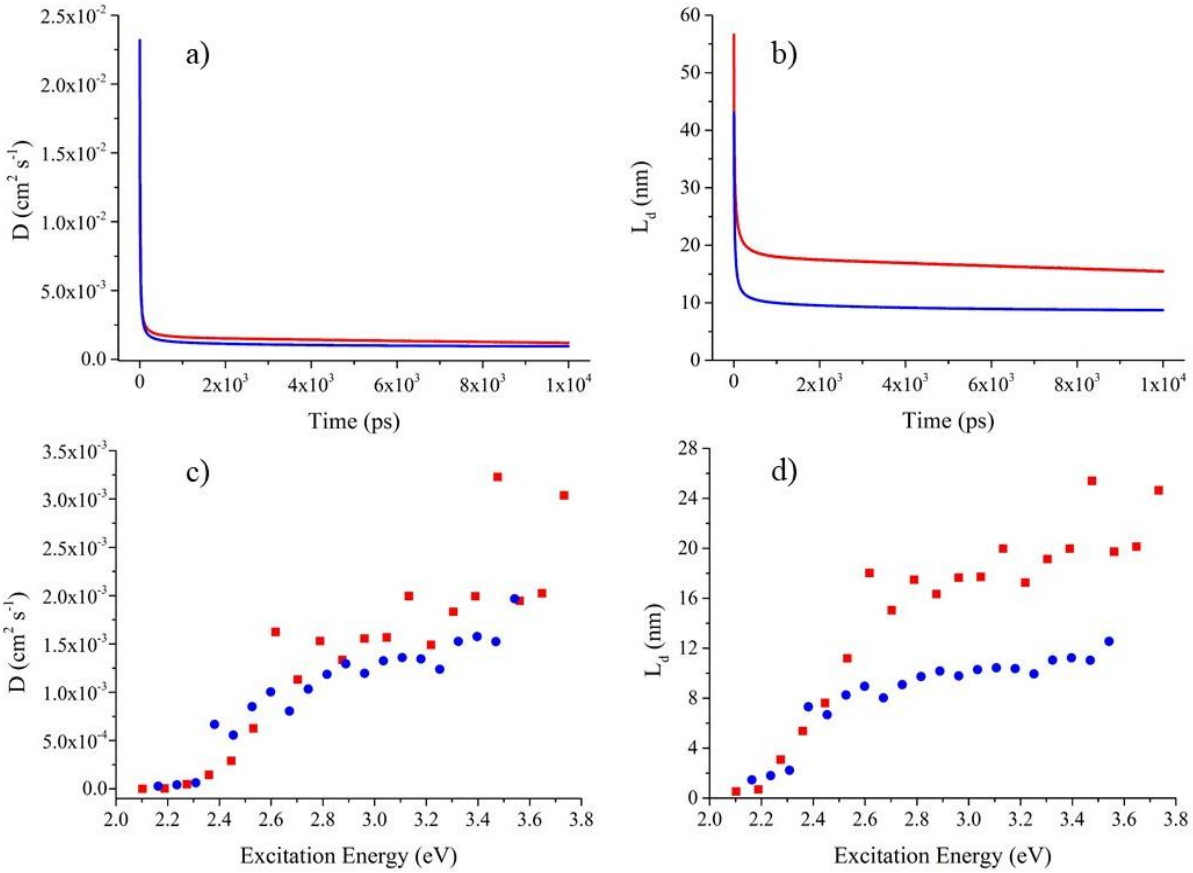

Figure 3.9: In the upper panel, the calculated a) diffusion coefficient, D, and b) exciton diffusion length, L_d, for **1a** (in red) and **2a** (in blue). In the bottom panel, the same quantities, respectively in c) and in d), were calculated using the energy-selective excitations method.

We discussed before the origin for the difference in exciton lifetimes between the two molecules, namely the various amount of CT admixture into the lowest electronic excitations. In view of the very similar exciton coupling and rate distributions shown on Figures 3.6a and 3.7, respectively, it is, however, not obvious why **1** features an improved diffusion coefficient over **2**. We believe this is rooted in the more efficient percolation pathways available for excitons in the shorter molecule, in analogy with the random resistance network for charge transport in organics.[22] To test this idea, we assessed the averaged length covered by excitons that hop between molecular sites within a given range of rates. The corresponding distributions are shown for the two molecules in Figure 3.10, considering hopping frequencies for the most likely events (in the range of 10^9 – 10^{11} s^{-1}). The distributions are clearly shifted towards longer distances for **1** compared to **2**, rationalizing the difference in diffusion coefficient. Thus, it appears that there are more long-distance continuous hopping pathways the excitons can funnel through in the smaller compound **1**, presumably because of its reduced anisotropic shape favouring 3D transport.

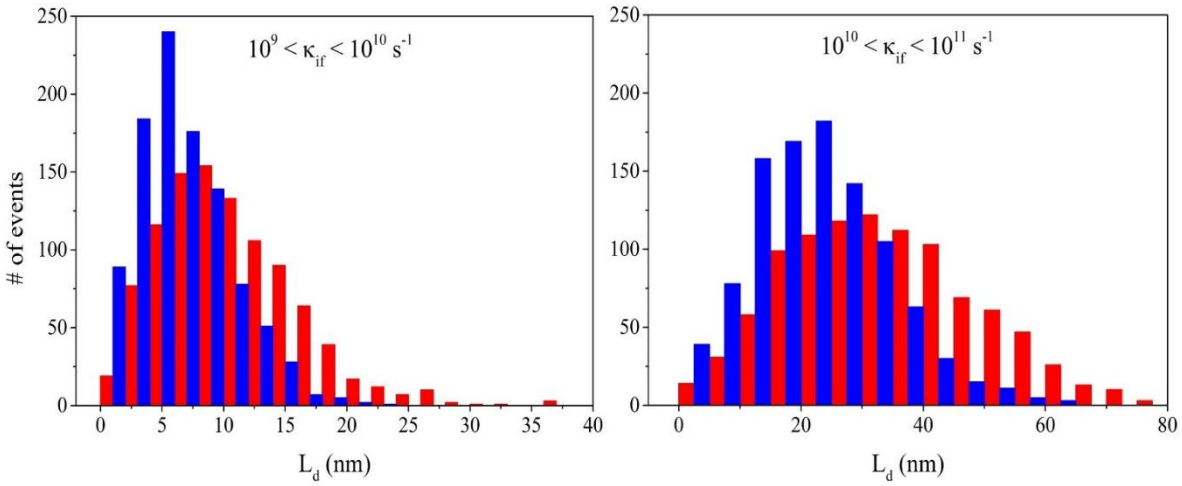

Figure 3.10: Percolation pathways calculated in two different ranges of exciton hopping rates for **1a** (in red) and **2a** (in blue).

To close this part, we would like to come back to the non-equilibrium nature of singlet exciton transport in these molecular materials. As previously proposed by Bässler and co-workers,[23] a useful set of numerical experiments to probe energetic disorder in organics is to run diffusion simulations using energy-selective excitations, namely generating excitons only on molecular sites matching a given energy window. Consistent with the disorder model, Figure 3.9c and 3.9d shows a strong dependence of the effective diffusion coefficient and length with excitation energy. While high-energy excitons can easily find electronically coupled nearest neighbours with lower energy and thus undergo fast downhill migration, excitons at the bottom of the DOS are instead surrounded by a smaller number of thermally accessible sites and move via slow uphill hopping events.

3.4 Conclusions

We have carried out a comprehensive theoretical investigation of the nature and dynamics of electronic excitations in two small π-conjugated organic molecules that differ mostly by one thiophene ring in their bridging unit. Earlier experimental reports point to a somewhat unexpected increase in PCEs for **1** with respect to **2** in vacuum-evaporated OSCs using fullerenes as acceptors, a result that was explained by the improved singlet exciton diffusion in **1**. It was tentatively concluded that the larger diffusion coefficient and diffusion length in the shorter molecule stem from a longer exciton lifetime and a reduced energetic disorder. Our multiscale computation approach, combining MD/TDDFT/ME calculations to KMC simulations, yields similar overall conclusions, yet for slightly different reasons. The MD/TDDFT/ME results show that the lowest singlet electronic excitations in these molecules have a mixed CT-FE nature, which largely fluctuates in time and space as a result of conformational motion. On average **1** displays a slightly more pronounced CT admixture, which explains why it absorbs at about the same wavelength as **2**, despite its shorter conjugated backbone. As a consequence of its increased CT character, **1** features a longer (radiative) lifetime compared to **2**, in line with the experimental findings and in part responsible for the extended exciton diffusion lengths. The full spectral linewidths of the excitation energy distributions are very large (> 0.2 eV) in both molecules because of both conformation and dielectric disorder in the amorphous films. In such a disordered energy landscape, exciton diffusion proceeds largely in a non-equilibrium regime during the finite excited state lifetime. Close to equilibrium, the diffusion coefficient predicted by KMC simulations is larger for **1** compared to **2**, although the total energetic disorder computed for the two molecules is comparable. The difference in exciton migration in fact reflects the existence of long-range, efficient percolation pathways, likely arising from the slightly less anisotropic shape of **1** prompting three-dimensional transport. As a concluding remark, it is important to highlight that the amount of energy disorder probed by ps transient experiments as performed in Ref.[3] is only a fraction of the total disorder, because in addition to the ultrafast energy drop at very early timescales, full energy relaxation has not completed during the exciton lifetime. Rather, fs-resolved PL measurements using energy-selective excitations are required to cover the broad dynamic range in energy distribution present in these inherently disordered soft molecular materials. Despite, or perhaps thanks to, their large energetic disorder, molecules such as **1** appear to be very promising candidates for energy photoconversion.

References

(1) Bakiev, A. N.; Selivanova, D. G.; Lunegov, I. V; Vasyanin, A. N.; Maiorova, O. A.; Gorbunov, A. A.; Shklyaeva, E. V; Abashev, G. G. Novel Thiophene-Containing Push-Pull Chromophores That Include Carbazole and Triphenylamine Moieties: Study of Optical and Electrochemical Properties. *Chem. Heterocycl. Compd.* **2016**, *52* (6), 379–387.

(2) Kozlov, O. V; Liu, X.; Luponosov, Y. N.; Solodukhin, A. N.; Toropynina, V. Y.; Min, J.; Buzin, M. I.; Peregudova, S. M.; Brabec, C. J.; Ponomarenko, S. A.; Pshenichnikov, M. S. Triphenylamine-Based Push–Pull Molecule for Photovoltaic Applications: From Synthesis to Ultrafast Device Photophysics. *J. Phys. Chem. C* **2017**, *121* (12), 6424–6435.

(3) Kozlov, O. V; Luponosov, Y. N.; Solodukhin, A. N.; Flament, B.; Douhéret, O.; Viville, P.; Beljonne, D.; Lazzaroni, R.; Cornil, J.; Ponomarenko, S. A.; Pshenichnikov, M. S. Simple Donor-Acceptor Molecule with Long Exciton Diffusion Length for Organic Photovoltaics. *Org. Electron.* **2018**, *53*, 185–190.

(4) Mayo, S. L.; Olafson, B. D.; Goddard, W. A. DREIDING: A Generic Force Field for Molecular Simulations. *J. Phys. Chem.* **1990**, *94* (26), 8897–8909.

(5) Courtesy of Enikolopov Institute of Synthetic Polymeric Materials of the Russian Academy of Sciences.

(6) M. J. Frisch, G. W. Trucks, H. B. Schlegel, G. E. Scuseria, M. A. Robb, J. R. Cheeseman, G. Scalmani, V. Barone, B. Mennucci, G. A. Petersson, H. Nakatsuji, M. Caricato, X. Li, H. P. Hratchian, A. F. Izmaylov, J. Bloino, G. Zheng, J. L. Sonnenberg, M. Had, 2009. Gaussian 09, Revision D.01.

(7) Chai, J.-D.; Head-Gordon, M. Long-Range Corrected Hybrid Density Functionals with Damped Atom–Atom Dispersion Corrections. *Phys. Chem. Chem. Phys.* **2008**, *10* (44), 6615–6620.

(8) Chai, J. Da; Head-Gordon, M. Systematic Optimization of Long-Range Corrected Hybrid Density Functionals. *J. Chem. Phys.* **2008**, *128* (8).

(9) D'Avino, G.; Muccioli, L.; Zannoni, C.; Beljonne, D.; Soos, Z. G.; D'Avino, G.; Muccioli, L.; Zannoni, C.; Beljonne, D.; Soos, Z. G.; D'Avino, G.; Muccioli, L.; Zannoni, C.; Beljonne, D.; Soos, Z. G. Electronic Polarization in Organic Crystals: A Comparative Study of Induced Dipoles and Intramolecular Charge Redistribution Schemes. *J. Chem. Theory Comput.* **2014**, *10* (11), 4959–4971.

(10) D'Avino, G.; Muccioli, L.; Castet, F.; Poelking, C.; Andrienko, D.; Soos, Z. G.; Cornil, J.; Beljonne, D. Electrostatic Phenomena in Organic Semiconductors: Fundamentals and Implications for Photovoltaics. *J. Phys. Condens. Matter* **2016**, *28* (43).

(11) Besler, B. H.; Merz Jr., K. M.; Kollman, P. A. Atomic Charges Derived from Semiempirical

Methods. *J. Comput. Chem.* **1990**, *11* (4), 431–439.

(12) Jortner, J. Temperature Dependent Activation Energy for Electron Transfer between Biological Molecules. *J. Chem. Phys.* **1976**, *64* (12), 4860–4867.

(13) Hsu, C.-P.; You, Z.-Q.; Chen, H.-C. Characterization of the Short-Range Couplings in Excitation Energy Transfer. *J. Phys. Chem. C* **2008**, *112* (4), 1204–1212.

(14) Head-Gordon, M.; Grana, A. M.; Maurice, D.; White, C. A. Analysis of Electronic Transitions as the Difference of Electron Attachment and Detachment Densities. *J. Phys. Chem.* **1995**, *99* (39), 14261–14270.

(15) Gillespie, D. T. A General Method for Numerically Simulating the Stochastic Time Evolution of Coupled Chemical Reactions. *J. Comput. Phys.* **1976**, *22* (4), 403–434.

(16) Olivier, Y.; Sancho-Garcia, J.-C.; Muccioli, L.; D'Avino, G.; Beljonne, D. Computational Design of Thermally Activated Delayed Fluorescence Materials: The Challenges Ahead. *J. Phys. Chem. Lett.* **2018**, *9* (20), 6149–6163.

(17) Evans, E. W.; Olivier, Y.; Puttisong, Y.; Myers, W. K.; Hele, T. J. H.; Menke, S. M.; Thomas, T. H.; Credgington, D.; Beljonne, D.; Friend, R. H.; Greenham, N. C. Vibrationally Assisted Intersystem Crossing in Benchmark Thermally Activated Delayed Fluorescence Molecules. *J. Phys. Chem. Lett.* **2018**, *9* (14), 4053–4058.

(18) Kozlov, O. V; Luponosov, Y. N.; Ponomarenko, S. A.; Kausch-Busies, N.; Paraschuk, D. Y.; Olivier, Y.; Beljonne, D.; Cornil, J.; Pshenichnikov, M. S. Ultrafast Charge Generation Pathways in Photovoltaic Blends Based on Novel Star-Shaped Conjugated Molecules. *Adv. Energy Mater.* **2015**, *5* (7), 1401657.

(19) Castet, F.; D'Avino, G.; Muccioli, L.; Cornil, J.; Beljonne, D.; D'Avino, G.; Muccioli, L.; Cornil, J.; Beljonne, D. Charge Separation Energetics at Organic Heterojunctions: On the Role of Structural and Electrostatic Disorder. *Phys. Chem. Chem. Phys.* **2014**, *16* (38), 20279–20290.

(20) D'Avino, G.; Olivier, Y.; Muccioli, L.; Beljonne, D. Do Charges Delocalize over Multiple Molecules in Fullerene Derivatives? *J. Mater. Chem. C* **2016**, *4* (17), 3747–3756.

(21) Vallée, R. A. L.; Van Der Auweraer, M.; De Schryver, F. C.; Beljonne, D.; Orrit, M. A Microscopic Model for the Fluctuations of Local Field and Spontaneous Emission of Single Molecules in Disordered Media. *ChemPhysChem* **2005**, *6* (1), 81–91.

(22) Sirringhaus, H. 25th Anniversary Article: Organic Field-Effect Transistors: The Path Beyond Amorphous Silicon. *Adv. Mater.* **2014**, *26* (9), 1319–1335.

(23) Bässler, H.; Schweitzer, B. Site-Selective Fluorescence Spectroscopy of Conjugated Polymers and Oligomers. *Acc. Chem. Res.* **1999**, *32* (2), 173–182.

Additional data

In the Dreiding FF parametrization, the torsion terms were expressed as:

$$E_T = \sum_{n=1}^{6} \frac{1}{2} B_n (1 - d_n \cos(n\phi)) \tag{3.10}$$

A fitting procedure was set up, where B_n and d_n were adjustable parameters, to reproduce as close as possible the minima and the barriers of the energy profiles. MP2/cc-pVDZ calculations highlight that **1** and **2** tend to be almost in the same conformation regarding the torsion angle between the TPA phenyl ring and the thiophene unit and the thiophene itself and the DCV group. Then, for **2** the two thiophene units should adopt the usual *anti* conformation, while for **1** two twisted almost isoenergetic conformers are found with respect to the torsion between the DCV and the terminal phenyl group and no planarization in the solid-state should be expected for this torsion due to the large energetic barrier (about 6 kcal mol^{-1}) at 0° and 180°.

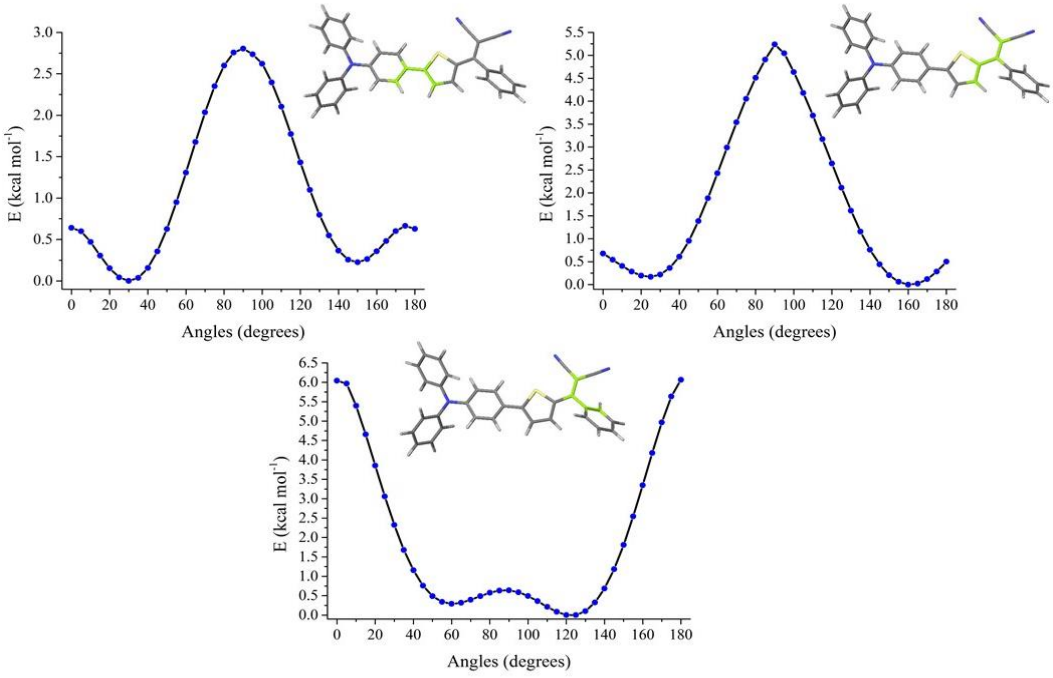

Figure 3.11: MP2/cc-pVDZ calculated characteristic torsion potentials of **1**. In each of the three graphs, the atoms in light green are those involved in the definition of the 0° dihedral angle.

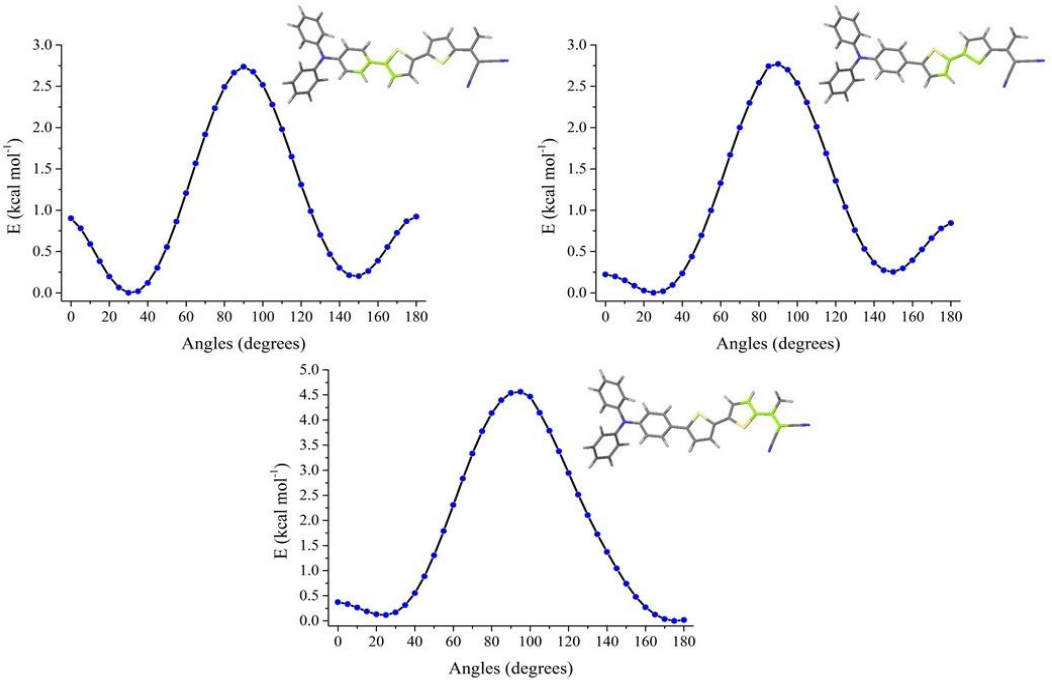

Figure 3.12: MP2/cc-pVDZ calculated characteristic torsion potentials of **2**. In each of the three graphs, the atoms in light green are those involved in the definition of the 0° dihedral angle.

The parametrized FF was validated by performing MD simulations on a **1x** triclinic supercell. In order to reach comparable dimensions of the supercell in terms of size and number of molecules, the crystallographic **1** unit cell was replicated 8 times along *a*, 6 times along *b* and 5 times along *c*, conserving the triclinic simmetry.

Table 3.3: Cell parameters from the equilibrated MD simulations for the three samples and the obtained density

	***a* (Å)**	***b* (Å)**	***c* (Å)**	***α* (°)**	***β* (°)**	***γ* (°)**	***d* (g cm^{-3})**	***# molecules***
1x	86.12	83.07	88.54	89.9	100.3	90.0	1.23	960
1 ***unit cell***	10.75 (x8)	13.95 (x6)	17.40 (x5)	90.0	99.4	90.0	1.24	4
1a	92.06	92.06	92.06	90.0	90.0	90.0	1.02	1000
2a	94.96	94.96	94.96	90.0	90.0	90.0	0.97	1000

Charge-transfer Excited States in Donor:Acceptor Blends with Large Energy Offset

In this Chapter, we provide a comprehensive microscopic model for the analysis of the energetics and dynamics of the *first* electronic CT state in donor:acceptor (D:A) bulk heterojunction (BHJ) blends, showing wide optical bandgaps and large frontier orbital energy offset. Specifically, we focus on N,N′-di(1-naphthyl)-N,N′-diphenyl-(1,1′-biphenyl)-4,4′-diamine (NPB) : 1,4,5,8,9,11-hexaazatriphenylenehexacarbonitrile (HAT-CN) blends (see chemical structures in Figure 4.1). Although not at all appealing for their performances, these BHJ systems are nevertheless a very interesting case study for resolving the existing dilemmas about the nature and fate of interfacial charge-transfer (CT) states, as these can be probed over an unusually large energy window. By varying the blend composition and temperature, we unravel the static and dynamic contributions to the disordered density of states (DOS) of the CT states manifold, and assess their recombination to the ground state. Our accurate computational protocol entails a combination of molecular dynamics (MD) simulations, density functional theory (DFT) and time-dependent (TD) DFT calculations, and a microelectrostatic (ME) model, specifically designed to include environmental effects. We observe that the CT DOS is broadened mostly because of both conformational disorder associated with the NPB flexibility and electrostatic disorder due to the HAT-CN quadrupolar layout, and is essentially static on the timescale of charge separation/recombination. We also predict fast (~ps) non-radiative decay from the lowest CT states that should overcome charge separation hence rendering these tail states EQE silent. Therefore, the tail of CT DOS does not contribute to charge generation but rather to recombination This is fully confirmed by comparison to experimental sensitive absorption versus external quantum efficiency (EQE) measurements showing that the CT DOS explored by EQE is cropped at low energy. In such a case, the standard procedure of fitting the tail of the EQE signal with a Gaussian function to extract static and dynamic disorder becomes unreliable.

The work presented in this Chapter is published in G. Londi, S. U. Z. Khan, L. Muccioli, G. D'Avino, B. P. Rand and D. Beljonne. Fate of low-lying charge-transfer excited states in a donor:acceptor blend with large energy offset. *J. Phys. Chem. Lett.* **2020**, *11*, 23, 10219–10226.

4.1 Introduction

In the quest for optimally performing materials in D:A BHJ architectures, the current target is minimizing sources of photocurrent and (more importantly) voltage losses. The most important losses in organic solar cells (OSCs) deal with the fate of tightly bound, intermolecular electron–hole (e-h) pairs, electronic states that are generated at the D:A interface upon a CT process.[1] The production of separated charges from those states requires that holes and electrons overcome their Coulomb binding energy instead of recombining to the ground state, a binding that depends on the electrostatic landscape at the interface[2,3] and on the amount of the spatial delocalization of the electron and hole wave functions.[4] In order to understand how carrier generation and recombination are affected by CT states, a better comprehension of their origin and DOS is crucial. More specifically, some key issues that are currently under inquiry include the origin of the broadening of the CT state line-shape (static and dynamic disorder)[5–9] and the existence and origin of multiple CT states (electronic, vibronic, or morphology induced).[10–14] One step towards addressing these issues is to identify D:A systems that display unique CT state characteristics, in order to probe their CT state energies in novel ways.

In this respect, a system like NPB:HAT-CN is characterized by wide optical bandgaps and large frontier orbital energy offset (*i.e.*, large energetic driving force for charge separation), Typically, such a combination of materials shows also a small energy offset between the donor highest occupied molecular orbital (HOMO) and the acceptor lowest unoccupied molecular orbital (LUMO), leading to an intrinsically low open circuit voltage (V_{oc}), that conversely should be maximized to boost power conversion efficiencies (PCEs). Nonetheless, through a series of experimental measurements and theoretical simulations, the existence of multiple electronic CT states, broadened by energetic disorder sourcing from the fluctuations of intramolecular conformations and by the disordered intermolecular environment, was confirmed (see Figure 4.2).[15]

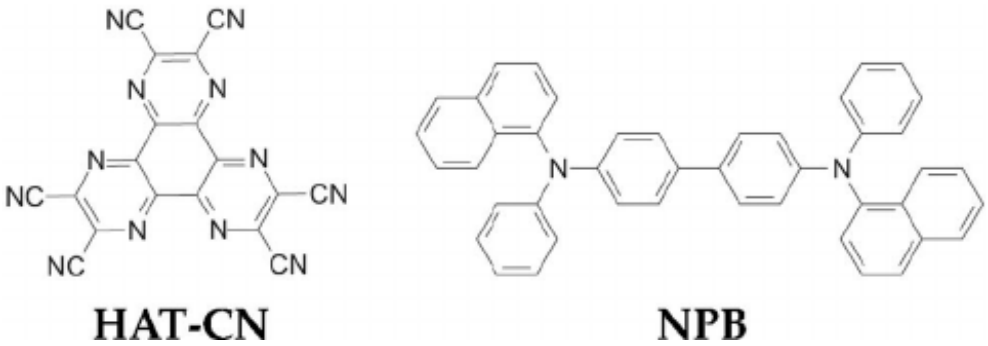

Figure 4.1: Chemical structures of HAT-CN and NPB.

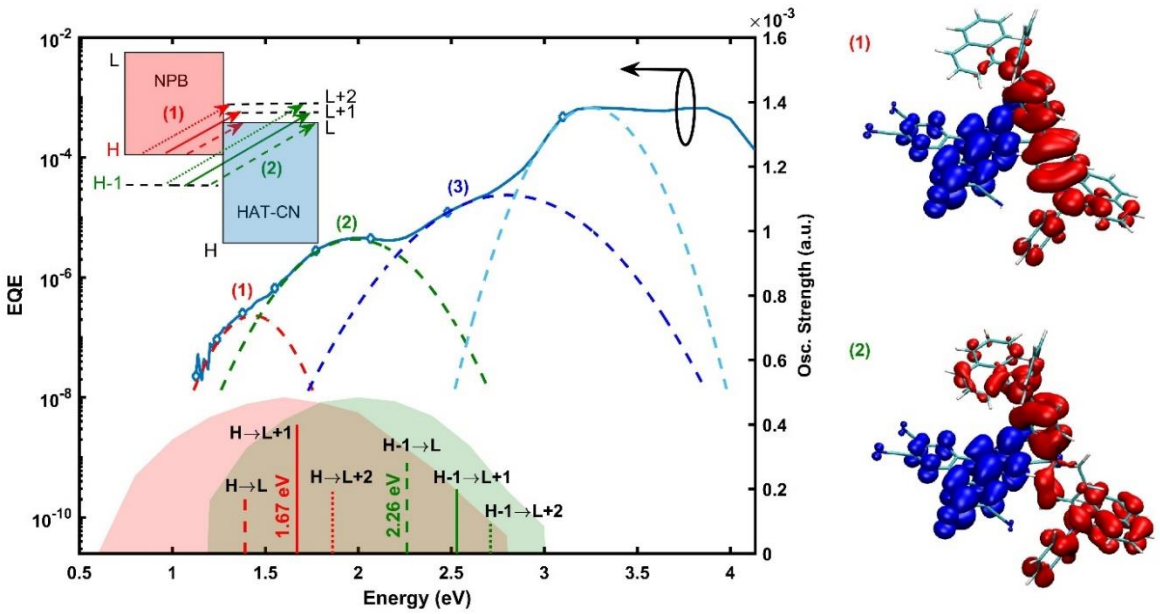

Figure 4.2: External quantum efficiency (EQE) spectrum of a NPB:HAT-CN BHJ device at 66.0% HAT-CN molar fraction (blue solid line). Four Gaussian functions fit to the EQE spectrum, CT_1 (dashed red line), CT_2 (dashed green line), CT_3 (dashed blue line) and the NPB Frenkel exciton (dashed light blue line) are also shown. The red, green shaded Gaussians established from theoretical simulations correspond to the energetic distribution of CT_1, and CT_2. The red and green delta lines represent CT energies calculated from TDDFT of an NPB:HAT-CN dimer, among which are two primary ones with their electron (blue) and hole (red) densities shown at the right. The inset displays transitions from NPB HOMO (H) and HOMO-1 (H-1) to HAT-CN LUMOs (L, L+1 and L+2), which contribute mostly to the e-h density of the lowest CT states. The CT_3 region represents higher energy CT states, associated with transitions from deeper HOMO levels of NPB to higher energy LUMO levels of HAT-CN, along with some contribution from NPB polaron absorption.

Besides the experimental EQE spectrum, Figure 4.2 shows, for an amorphous simulated sample at 10% HAT-CN molar fraction, the calculated DOS for the two lowest-energy CT excitations (red shaded region for CT_1 and green shaded region for CT_2), which closely match the two lowest-energy EQE features. The CT_1 transitions correspond to transitions from the NPB HOMO to the HAT-CN LUMOs, while CT_2 relates to analogous excitations from the NPB HOMO-1 (see sketch in the figure inset). This analysis is further corroborated by TDDFT calculations on an NPB:HAT-CN dimer extracted from the MD sample (vertical bars), which show two series of absorption bands, CT_1 (red) and CT_2 (green), each of which consist of three transitions to the acceptor HAT-CN LUMO levels. It was then argued that these very broad CT features in the EQE spectrum resulted from a combination of three different factors, namely: (i) the presence of three nearly degenerate acceptor levels for the HAT-CN molecule; (ii) the large fluctuation of NPB molecular energy levels due to conformational effects in the disordered structure; (iii) the variations in the local environment of the molecules resulting in a marked energetic disorder due to intermolecular electrostatic interactions.

Indeed, CT states come with their own energy spectrum (or DOS), which is typically quite broad for various reasons: including that D:A blends often comprise a heterogeneous distribution of local microstructures, and the coupling between the electronic excitations and the nuclear degrees of freedom or the involvement of multiple electron and/or hole states. One way to analyze the manifold of excited states is by means of EQE measurements, which provide a measure of the exciton DOS, weighted by the contribution of the different states to the photocurrent.[16] Despite several investigations, the detailed origin for the DOS and the role of "hot" versus "cold", relaxed CT states in charge separation and recombination are still controversial.[17–19]

4.2 Theoretical Methodology

4.2.1 Molecular Dynamics Simulations

Three different films of NPB and HAT-CN at different relative concentrations were prepared by vapor co-deposition on graphene, by means of NVT non-equilibrium MD simulations,[20–22] for a final film thickness exceeding in all cases 10 nm. All simulations were performed with the NAMD code.[23] Systems were modelled with a previously developed united atom force field (FF) for organic light emitting diode (OLED) materials,[24] which allows for an integration timestep of 2 fs. Charges of the united atoms were obtained by fitting the electrostatic potential (ESP charges) calculated at the optimized PBE0/def2-TZVP geometry. In the FF validation procedure, the FF parameters were optimized for reproducing the experimental crystal cells and densities of several polyaromatic compounds. NPB was taken as a test molecule outside the training set, giving an overall error of 1.1%. For HAT-CN, we obtained a lower but reasonable agreement between the calculated cell dimensions a=b=23.464 Å, c=15.75 Å, and the experimental ones a=b=23.637 Å, c=14.83 Å.[25]

A horizontal graphene surface of 76.136 Å × 76.572 Å was chosen as a simple rigid and chemically compatible support and kept fixed during all the simulations. The vertical side of the simulation box was set to 400 Å to leave ample space for deposited molecules and avoid interactions between the two sides of the graphene + blend slab, since 3D periodic boundary conditions were used. Deposition proceeded by randomly selecting the chemical species of the new molecule to be added at each step according to the desired molar fraction. Every new molecule was placed at about 20 Å above the forming organic layer, endowed with a velocity of 1 Å ps^{-1} directed parallelly to the normal to the graphene surface, and the dynamic of the system evolved for 100 ps at 500 K. At the end of this deposition step, if the last deposited molecule had desorbed, the step was repeated without randomizing again the molecular species, otherwise a further molecule was inserted following the same scheme. As a consequence of the randomness of the deposition, the final compositions do not match exactly the mol:mol ratio given in input (NPB:HAT-CN = 1:3, 9:1, 29:1). The actual compositions were of 239 NPB and 761 HAT-CN for the 1:3 sample (with HAT-CN molar fraction of 76.1 %, or 67.5% in weight), 897 and 103 for the 9:1 sample (10.3%, 7% in weight), and 1145 and 55 for the 29:1 sample (4.6%, 3% in weight). The three systems were subsequently cooled and

equilibrated at 300 K, and subsequently at 200 K and 100 K. At each temperature, equilibration was continued until no appreciable drift of the total energy was detected, compared to its thermal fluctuations. Molecular geometries were then extracted from the equilibrated configurations and used for electronic structure calculations.

4.2.2 Electronic Structure Calculations

Ionization potentials IP_{NPB}^{gas} and electron affinities EA_{HAT-CN}^{gas} were computed at the gas-phase DFT level with the range-separated hybrid (RSH) ωB97X-D functional[26] along with the 6-311++G(d,p) basis set using the GAUSSIAN16 suite.[27] These transport levels were evaluated as total energy differences between charged and neutral species, correcting for the inaccuracies of the FF in describing molecular geometries as follows. The gas-phase energy of a generic electronic state is calculated as:

$$E(R_{MD}) = E^{GW}(R_X) + [E^{DFT}(R_{MD}) - E^{DFT}(R_X)] \qquad (4.1)$$

where R_{MD} labels the geometry of a given molecule in the MD sample and R_X is a reference geometry, taken from the bulk crystal structure of both species. In practice, the energy at the crystal geometry was calculated with the *GW* approximation (GWA), which ensure accurate absolute values, and the energy deviations from it, as obtained from classical MD simulation geometries, were evaluated with DFT. Gas-phase *GW* calculations were performed with the FIESTA code, starting from DFT calculations, based on the PBE0 functional, obtained with the ORCA package.[28] A partial self-consistent scheme on the eigenvalues (ev*GW*) was exploited, along with Gaussians basis set of the Dunning's correlation-consistent family (cc-pVXZ, where X = 2, 3). Then, quasi-particle energy levels were extrapolated to the complete basis set limit.[29] The universal Weigend Coulomb fitting set of functions was used as auxiliary basis in the resolution of identity (RI-V) approach.

ME calculations[30,31] were parametrized with ESP atomic charges and polarizability tensor calculated with DFT at the ωB97X-D/6-311++G(d,p) level. ESP charges were computed for all molecules in one equilibrated MD configuration, in neutral, positively (for NPB) and negatively (HAT-CN) charged states. The polarizability tensor was calculated at neutral NPB and HAT-CN reference geometries, and the polarizability of charged species was set equal to that of neutral ones. Polarization energies for holes (Δ^+) and electrons (Δ^-) were calculated for spherical clusters of increasing radius centered at the molecule of interest, and then extrapolated to the bulk, infinite radius limit. The solid-state energy levels for holes on NPB and electrons on HAT-CN can be expressed as: $IP_{NPB} = IP_{NPB}^{gas} + \Delta^+$ and $EA_{HAT-CN} = EA_{HAT-CN}^{gas} + \Delta^-$. The energy of CT states was calculated for molecular NPB:HAT-CN pairs in close contact, which were selected from MD samples by applying PBC in the *XY* plane and including only molecules in the bulk region, *i.e.*, excluding the molecules within 4 nm from the graphene substrate and vacuum interface in order to avoid empty spaces (in the spherical clusters) in the *z* direction. The photovoltaic gap is defined as $E_{GAP} = IP_{NPB} - EA_{HAT-CN}$. The optical gap instead is $E_{CT} = E_{GAP} + E_B$, where $E_B < 0$ is the Coulomb exciton interaction

between closely spaced electron and holes. The latter is calculated with self-consistent ME calculations as the screened interaction between hole and electron charge densities.

The effect of intramolecular structural relaxation upon charging was considered by calculating, separately for NPB and HAT-CN, the intramolecular reorganization energy λ^q, averaged on the charging and discharging processes:

$$\lambda^q = \frac{|E^q(R_0) - E^q(R_q)| + |E^0(R_q) - E^0(R_0)|}{2} \quad 4.2)$$

where q stands for the charge on the molecule and R_0, R_q indicate the equilibrium geometries of neutral and charged states. Geometries were optimized at the DFT level (ωB97X-D/6-31G(d,p)), keeping the molecular soft degrees of freedom (dihedral angles) frozen, as to account only the contribution from high-frequency modes.[32,33] This avoids double counting electron-vibration interactions, since the contribution of low-frequency vibrations was evaluated classically from MD simulations (σ^x_{low} in Tables 4.2 and 4.3). With this caveat, the total internal reorganization energy for CT formation / recombination is $\lambda_{int} = \lambda^+_{NPB} + \lambda^-_{HAT-CN} = 262$ meV, with $\lambda^+_{NPB} = 184$ meV and $\lambda^-_{HAT-CN} = 78$ meV.

The conformational disorder was assessed with gas-phase DFT calculations performed at the MD geometries, quantifying the fluctuations of the NPB HOMO and the HAT-CN LUMO. The high- and low-frequency contributions to the dynamic conformational disorder were separated by means of a Fourier filter procedure applied to the time series of molecular orbital energies computed along the MD trajectories at 300 K (see Figure 4.9 in Additional data). The low- (high-)frequency disorder σ^x_{low} (σ^x_{high}) was evaluated as the standard deviation of the time series fluctuations (around the mean value of each molecule) after applying a low-pass (high-pass) filter to the original data (10 ps long trajectory sampled every 10 fs). The filter employed a rectangular function with energy cutoff equal to k_BT (~200 cm^{-1}). The variances of the frequency-filtered time series were averaged over 5 NPB and 5 HAT-CN molecules to obtain the standard deviations in Table 4.1. Low- and high-frequency fluctuations were found to be uncorrelated. By filtering out the high-frequency contribution, the data in Table 4.1 allowed also the estimation of the static component of the total energetic disorder $\sigma^x_{tot} = \sqrt{\sigma^{2\,x}_{stat} + \sigma^{2\,x}_{low}}$, where σ^x_{tot} was obtained as the full IP_{NPB} / EA_{HAT-CN} / $E_{GAP/CT}$ standard deviation for all NPB:HAT-CN pairs extracted from the MD configurations.

Table 4.1: Standard deviations (in meV) of the intramolecular energy levels dynamic fluctuations along the MD trajectory, partitioned into the low- and high-frequency components disorder $\sigma_{low}^{x}$and σ_{high}^{x}, with $\sigma_{dyn}^{x} = \sqrt{\sigma^{2}{}_{low}^{x} + \sigma^{2}{}_{high}^{x}}$. The samples are labelled according to the HAT-CN molar fraction and the MD simulation temperature.

	NPB			HAT-CN		
% / T (K)	σ_{low}^{IP}	σ_{high}^{IP}	σ_{dyn}^{IP}	σ_{low}^{EA}	σ_{high}^{EA}	σ_{dyn}^{EA}
4.6 / 100	59	40	71	11	39	40
4.6 / 300	87	67	110	19	60	63
76.1 / 100	68	39	78	14	36	38
76.1 / 300	102	60	118	19	54	57

Non-radiative rates between the (first) CT state and the ground state were calculated with a perturbative approach with the semiclassical Marcus-Levich-Jortner (MLJ) expression:

$$\kappa_{NRAD} = \frac{2\pi}{\hbar} J^{2} \sqrt{\frac{1}{4\pi\lambda_{env} k_{B} T}} \times$$
$$\times \sum_{n} \left\{ exp\left(-S_{eff}\right) \frac{S_{eff}^{n}}{n!} \times exp\left[-\frac{\left(-E_{CT}^{0,0} + \lambda_{env} + n\hbar\omega_{eff}\right)^{2}}{4\lambda_{env} k_{B} T} \right] \right\} \quad (4.3)$$

where J is the electronic coupling between those states, computed with the generalized Mulliken-Hush (GMH) scheme in equation (4.4), $\hbar$ is the reduced Planck's constant, k_B is the Boltzmann constant, T is the temperature in Kelvin, λ_{env} is the environmental reorganization energy (see Table 4.3) computed from σ_{low}^{x} as $\lambda_{env} = \frac{\sigma^{2}{}_{low}^{x}}{2k_B T}$, $\omega_{eff} = 0.15$ eV is the energy of an effective high-frequency intramolecular vibration (typically the C-C stretching), $S = \lambda_{int}/(\hbar\omega_{eff})$ is the corresponding Huang-Rhys factor, and $E_{CT}^{0,0} = E_{CT} - \lambda_{int}$ is the *GW*/ME energy, where λ_{int} is removed to avoid double-counting with the term $n\hbar\omega_{eff}$.

The electronic couplings were computed for NPB:HAT-CN dimers in the 4.6% and 76.1% of HAT-CN samples at 300 K at DFT/TD-DFT ωB97X-D/6-311G(d,p) level of theory, and using a polarized continuum model (PCM),[34] setting the scalar dielectric constant $\varepsilon = 3.0$ and $\varepsilon = 2.6$ for the sample at 4.6% and 76.1% of HAT-CN, respectively. The dielectric constant of the medium was obtained as the ratio between the unscreened interaction between an e-h pair (V_{eh}) and the corresponding screened exciton binding energy (E_B), both quantities accessible via ME calculations. The range-separation parameter ω was set to 0.09 Bohr^{-1}, a value which ensures, as it should be, a strong intermolecular

CT character of the first excited state in NPB:HAT-CN dimer calculations. The electronic couplings in equation (4.3) were calculated as:[35]

$$J = \frac{\vec{\mu}_{GS-CT} E_{CT}^{0,0}}{\sqrt{\Delta\mu_{GS-CT}^2 + 4\vec{\mu}_{GS-CT}^2}} \tag{4.4}$$

where $\vec{\mu}_{GS-CT}$ is the transition dipole moment, and $\Delta\mu_{GS-CT}$ the difference between the CT state permanent dipole moment and the ground state one.

The CT absorption band of a single NPB:HAT-CN dimer was calculated as a Franck-Condon progression:

$$Abs(E) = \vec{\mu}_{GS-CT}^2 \sum_{n=0}^{n_{max}} \frac{e^{-S} S^n}{n!} \delta\left(E - E_{CT}^{0,0} - n\hbar\omega_{eff}\right) \tag{4.5}$$

where δ is the Dirac delta function. The absorption spectrum of the blend was computed as the superposition of CT bands of NPB:HAT-CN dimers in the sample, summing up the intensity of the individual vibronic transitions in bins of 100 meV. The CT band width was sourced from the energetic disorder of the sample and the convergence of the spectral shape was obtained with $n_{max} = 8$.

4.3 Results and Discussion

4.3.1 Morphology of Amorphous Blends

Three NPB:HAT-CN blends of increasing HAT-CN molar fraction (4.6%, 10.3%, 76.1%; about one thousand molecules per sample) were simulated with atomistic MD simulations, adopting a non-equilibrium protocol that reproduces vapor co-deposition.[20–22,36,37] Deposition simulations were performed at 500 K and were followed by equilibration runs at 100 K and 300 K. The final structure of the sample with the highest HAT-CN molar fraction at 300 K is displayed in Figure 4.3, showing also the two components separately, in order to highlight the occurrence of micro-segregation in the blend. The electric potential 3D maps in Figure 4.3 show major differences in the charge distributions of the two molecules: HAT-CN is a flat and rigid molecule, characterized by symmetrically distributed and strongly dipolar cyano groups attached to the π core. In contrast, NPB features a weakly polarized charge density and presents a dumbbell shape, together with a certain conformational freedom conferred by rotations about phenyl-phenyl and N-phenyl bonds (see Figure 4.10 in Additional data). From the differences in shape and molecular charge distribution between NPB and HAT-CN, one can surmise that their intermolecular interactions are very different, hence promoting phase separation with respect to the entropically favored full mixing, even in the solid-state, and simulations show that this is actually the case. This segregation determines separate migration pathways for holes (in NPB) and electrons (in HAT-CN) from the interface to the electrodes, while still maintaining close D:A contacts. In particular, some π-stacked hetero-dimers were observed, with the HAT-CN azatriphenylene core adjacent and parallel to the central biphenyl

moiety of NPB (see Figure 4.11 in Additional data). However, the structural analysis of the samples ruled out the presence of any particular orientational or positional order, except within 1 nm from the boundary with the graphene layer used as a support (not shown in Figure 4.3). Molecules in this region and at the very top of the sample, where there is a free surface, were therefore not included in electronic structure calculations.

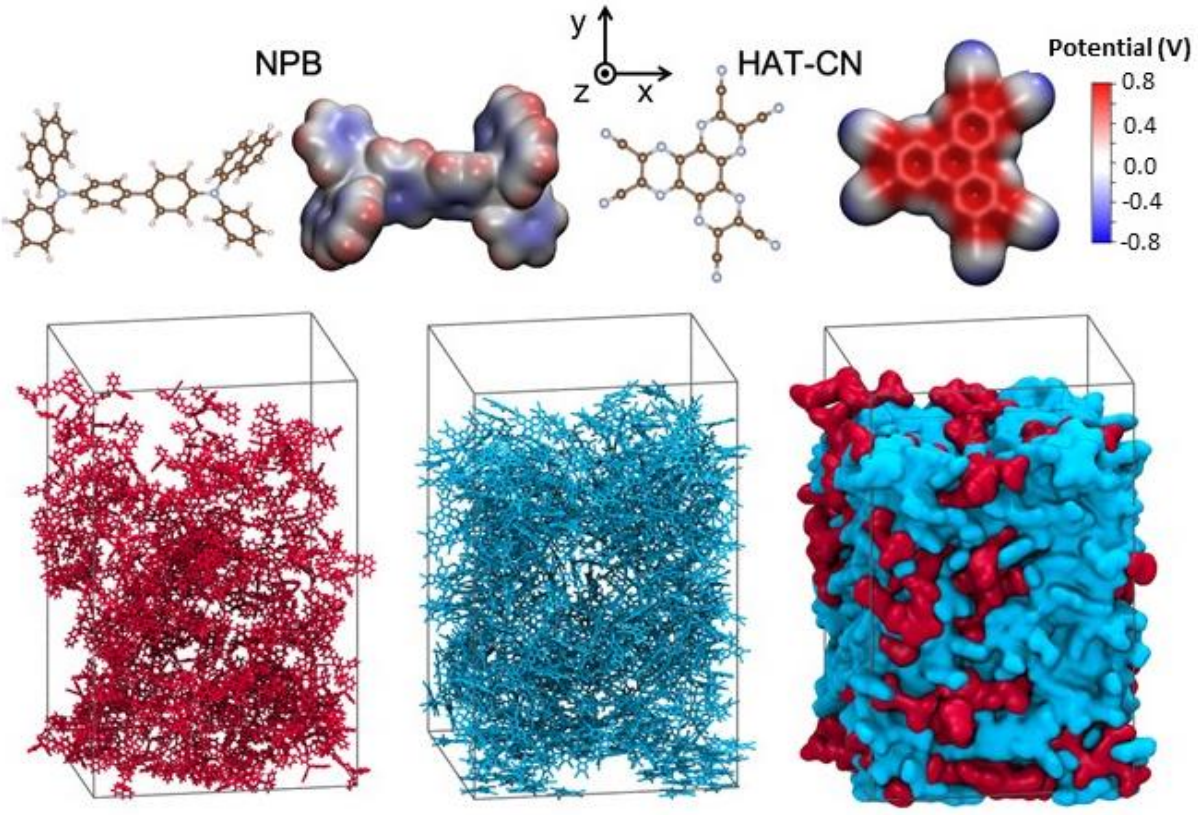

Figure 4.3: Top: Molecular structures and electric potential color maps of N,N′-di(1-naphthyl)-N,N′-diphenyl-(1,1′-biphenyl)-4,4′-diamine (NPB) and 1,4,5,8,9,11-hexaaza triphenylene hexacarbonitrile (HAT-CN). Bottom: snapshots of the simulated sample at concentrations 24.9% NPB:76.1% HAT-CN. From the left to the right, visualizations of NPB molecules only (in red), HAT-CN only (in cyan), and the whole sample with an isosurface representation.

4.3.2 Nature and Origin of Low-Lying Charge-Transfer States

Our account of the electronic properties in NPB:HAT-CN blends starts from the analysis of the charge transport energy levels in the solid-state. Figure 4.4 shows the average values (and standard deviations as error bars) of the EA of HAT-CN and the IP of NPB as a function of composition and temperature. Both IP_{NPB} and $EA_{HAT\text{-}CN}$ increase substantially and approximately linearly with the HAT-CN molar fraction, although the limited number of investigated samples does not allow to establish whether the growth is linear like in other binary molecular blends.[38,39] This linearity reflects averaging of the

electrostatic potentials of the two components. As reported in Table 4.2, moving from 4.6% to 76.1% of HAT-CN at 300 K, the mean IP_{NPB} increases from 6.00 eV to 6.80 eV, with a remarkable shift of 0.8 eV due to the electrostatic interactions with HAT-CN, while the mean EA_{HAT-CN} increases by 0.72 eV, from 4.24 to 4.96 eV. The increase in IP and EA of the two molecules in HAT-CN-rich blends is in line with similar results on the host-dependence of energy levels[29] and on zinc phthalocyanine (ZnPc):F_8ZnPc blends.[38,40] In our case, the electrostatic landscape is governed by the strong quadrupole moment of the HAT-CN molecule, characterized by electron withdrawing groups at the periphery of the π core, which generally leads to a stabilization of occupied and empty levels.

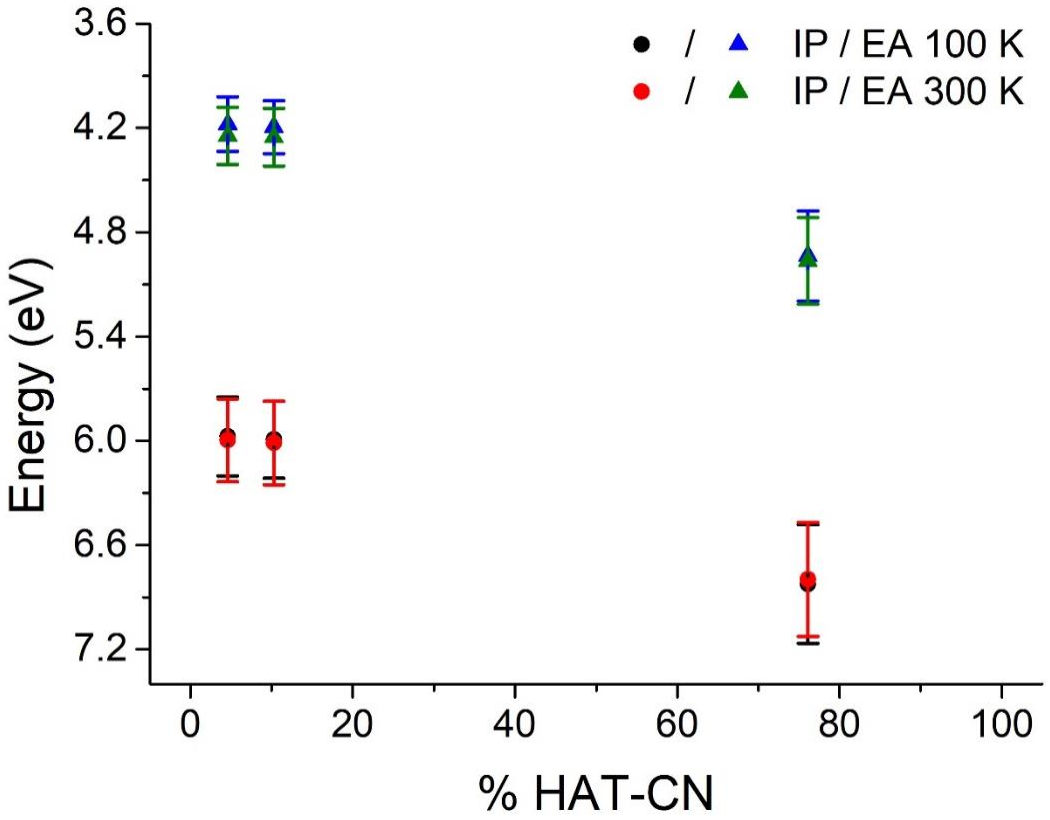

Figure 4.4: Average electron affinity (EA) of HAT-CN (blue and green triangles) and ionization potential (IP) of NPB (black and red circles) as a function of temperature and HAT-CN molar fraction. Vertical bars represent standard deviations.

The calculation of IP_{NPB} and EA_{HAT-CN} also provides a first validation of the methodology, since these values can be compared with experimental data measured on vapor deposited thin films of the two pure compounds: for NPB, IPs of 5.4-5.5 eV were measured by ultraviolet photoelectron spectroscopy (UPS),[41,42] while the EA of HAT-CN was reported to be larger than 4.9 eV as probed with low-energy inverse photoemission spectroscopy (LEIPS),[43] and estimated to be about 4.8 eV by comparison between UPS measurements on NPB:HAT-CN and NPB:F_4TCNQ films.[44] To further validate our results, it is also worth mentioning that UPS studies on mixed NPB:HAT-CN thin films

indicate an increase of IP_{NPB} at increasing HAT-CN molar fraction.[42] The rather strong composition effects in Figure 4.4 contrasts with the effect of temperature, hardly detectable considering the standard deviations of IP_{NPB} and $EA_{HAT\text{-}CN}$, suggesting a minor effect exerted by thermal fluctuations in these blends. Therefore, in the following, we will mainly focus on the results at 300 K (see Table 4.4 in Additional data for those obtained at 100 K). Since the shifts in the energy levels of NPB and HAT-CN are so similar, overall the photovoltaic gap defined as $E_{GAP} = IP_{NPB} - EA_{HAT-CN}$ (see below) is not expected to change significantly with HAT-CN molar fraction.

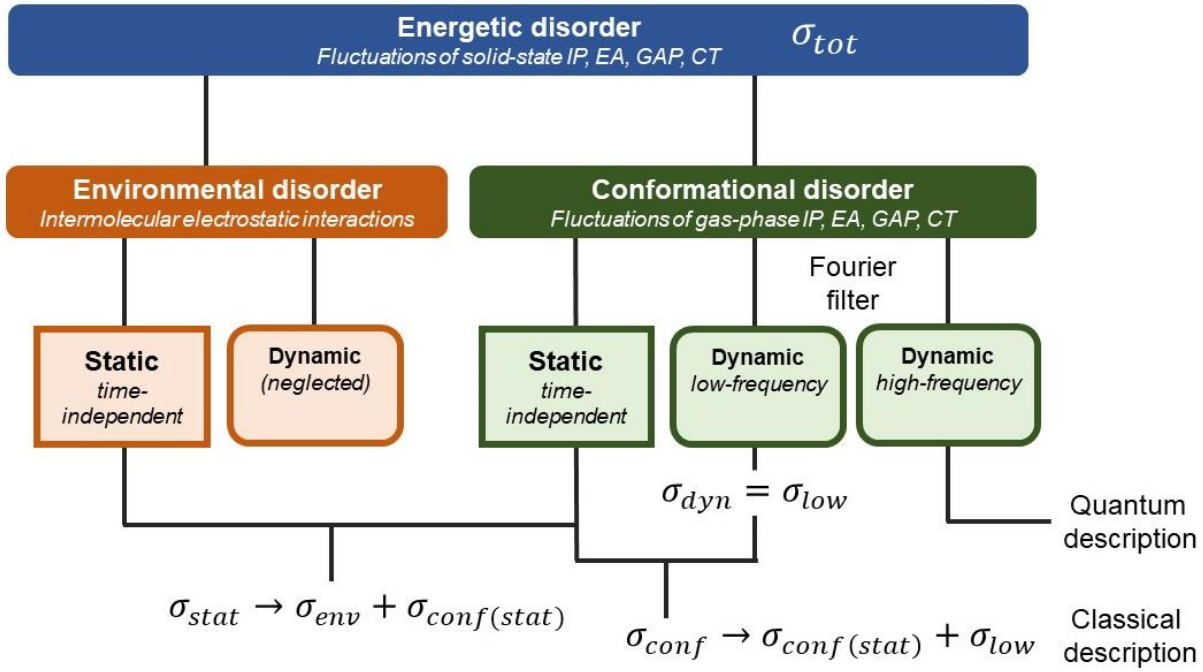

Figure 4.5: Logical scheme explaining the partitioning of the different contributions to the total energetic disorder σ_{tot}^{x}. DFT/ME calculations were carried out in order to compute the IP of all NPB and the EA of all HAT-CN in the last MD frame of each blend. This yielded a distribution of charge carrier energy levels (IP and EA) characterized by a standard deviation σ_{tot}^{x}. This contains a component related to the environmental disorder and the other related to conformational disorder σ_{conf}^{x}, which can be extracted from gas-phase DFT fluctuations of IP and EA. In turn, σ_{conf}^{x} has two contributions: a static and a dynamic part. The latter σ_{dyn}^{x} is composed by intramolecular low- and high-frequency components. By applying a Fourier filter to DFT time series of molecular orbital energies, computed along the MD trajectories at 300 K, we were able to distinguish between σ_{low}^{x} and σ_{high}^{x}. The latter contribution was removed from σ_{conf}^{x}, so that σ_{conf}^{x} is thus made of the static $\sigma_{conf(stat)}^{x}$ and the low-frequency dynamic σ_{low}^{x} part of the conformational disorder. As regards the environmental one, we assumed σ_{env}^{x} to be static in time, neglecting its dynamic character. Therefore, within the static part σ_{stat}^{x}, there are both σ_{env}^{x} and $\sigma_{conf(stat)}^{x}$.The same reasoning can be extended to the case where x stands for GAP or CT, as in Table 4.3.

Having established the dependence on composition and temperature of the average IP and EA, we now focus on energetic disorder, *i.e.*, the spread of energy levels. In order to provide a deeper insight, data in Table 4.2 dissect the total energetic disorder obtained from our atomistic simulations (standard deviation σ_{tot}^{x}, where x stands for IP or EA) into different contributions, as depicted in Figure 4.5. Specifically, energetic disorder can be characterized in terms of its physical origin, and here we distinguish between conformational (σ_{conf}^{x}, an intramolecular contribution related to different molecular geometries sampled in MD simulations) and environmental disorder (σ_{env}^{x}, due to intermolecular electrostatic interactions). Energetic disorder can also be classified according to timescales as being of static (σ_{stat}^{x}) or dynamic (σ_{low}^{x}) nature. While static disorder is mostly sourced by inhomogeneity in the electrostatic environment of the CT pairs, dynamic disorder includes contributions from intramolecular low-frequency modes (below 200 cm^{-1}) that are correctly described by our classical MD simulations in the temperature range explored. We note that, unlike recent studies addressing dynamic disorder in disordered molecular blends with multilevel computational approaches,[45–47] the IP and EA fluctuations due to high-frequency vibrations were filtered out in the calculation of energetic disorder, which hence accounts only for low-frequency classical modes. The contribution from high-frequency vibrations was then included in a proper quantum-mechanical framework in the calculation of the absorption spectrum and non-radiative recombination rates, as in equations (4.3) and (4.5).

Table 4.2: Average energy of single carrier transport levels (in eV) and standard deviations σ_{tot}^{x} (in meV, where x stands for IP or EA) in NPB:HAT-CN blends at 300 K. Energy fluctuations (in meV) were also quantified according to their nature: intramolecular σ_{conf}^{x}, intermolecular σ_{env}^{x}, static σ_{stat}^{x} and low-frequency dynamic disorder σ_{low}^{x}.

% HAT-CN	IP_{NPB}	σ_{tot}^{IP}	σ_{conf}^{IP}	σ_{env}^{IP}	σ_{stat}^{IP}	σ_{low}^{IP}
4.6	6.00	239	179	161	223	87
10.3	6.01	241	188	164	222	94
76.1	6.80	328	183	274	311	102

% HAT-CN	EA_{HAT-CN}	σ_{tot}^{EA}	σ_{conf}^{EA}	σ_{env}^{EA}	σ_{stat}^{EA}	σ_{low}^{EA}
4.6	4.24	165	57	151	164	19
10.3	4.25	166	47	155	165	19
76.1	4.96	249	42	244	249	19

Environmental effects due to long-range intermolecular electrostatic interactions represent the predominant contribution to the total energetic disorder. The environmental disorder σ_{env}^{x} comparably affects IP_{NPB} and $EA_{HAT\text{-}CN}$ and markedly increases with the HAT-CN molar fraction, revealing that the main source of electrostatic disorder is indeed the strongly polarized charge density of the acceptor molecule. The conformational disorder σ_{conf}^{x} is, instead, only weakly sensitive to composition, but different between the two molecules. The calculated σ_{conf}^{x} are indeed much larger for NPB, owing to the flexible molecular structure of the donor molecule, characterized by soft torsional degrees of freedom, as compared to the rather rigid HAT-CN acceptor. This dissimilarity between the two components is even more pronounced when looking at the conformational low-frequency dynamic disorder σ_{low}^{x}, which is the sole contribution with a clear temperature dependence, in a way compatible with that prescribed for coupled classical harmonic oscillators. In summary, electrostatic and conformational fluctuations similarly contribute to the energetic disorder in IP_{NPB}, while the spread in $EA_{HAT\text{-}CN}$ is essentially determined by the former.

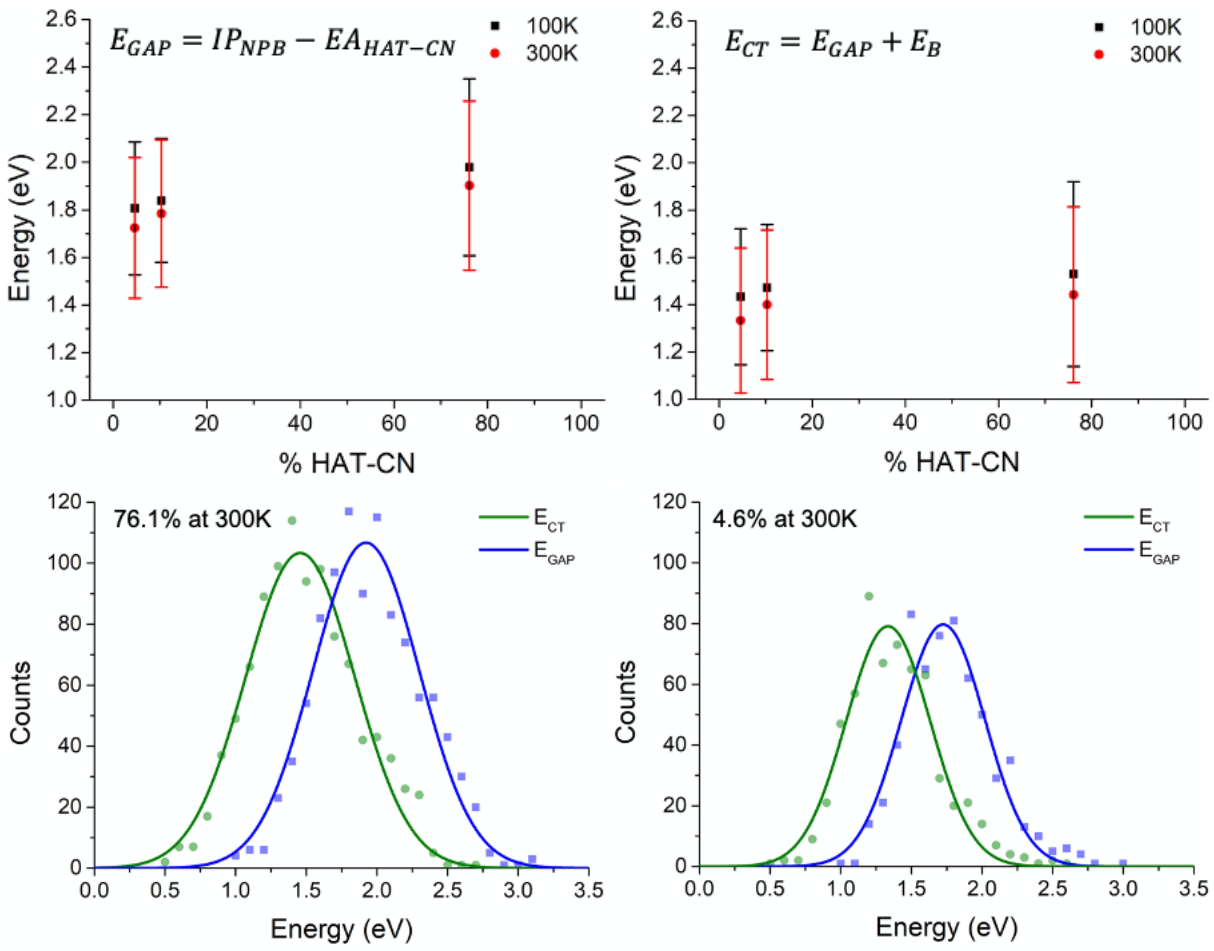

Figure 4.6: Top: Average photovoltaic gap (E_{GAP}) and CT state energies (E_{CT}) for NPB:HAT-CN pairs as a function of HAT-CN molar fraction and temperature. Vertical bars represent standard deviations. Bottom: CT density of states (DOS) and distribution of gap energies at two different HAT-CN molar fractions at 300 K. Continuous lines are Gaussian fits.

The analysis of CT excitations, whose statistics was gathered on NPB:HAT-CN dimers in our MD-simulated samples, is presented in Figure 4.6 and Table 4.3 (see also Table 4.5 and Figure 4.12 in Additional data for data at 100 K). As anticipated in the discussion of the transport levels, notwithstanding their large variations with the blend composition, the mean photovoltaic gap $E_{GAP} = IP_{NPB} - EA_{HAT-CN}$ changes by less than 0.2 eV, going from 1.72 eV at 4.6% to 1.90 eV at 76.1% of HAT-CN. The mean energy of the first CT state, E_{CT}, shows even smaller variations with composition. The exciton binding energy, $E_B = E_{CT} - E_{GAP}$, is predicted to be about -0.4 eV, in line with typical values expected in organic semiconductors.[48] The large standard deviation σ_{tot}^{CT}, reaching 371 meV at high HAT-CN molar fraction, is dominated by the fluctuations in the photovoltaic gap, rather than by those in the binding energy. It is largely due to the rough electrostatic landscape produced by HAT-CN molecules and to the conformational disorder of flexible NPBs, both contributions being essentially static in time. The broad distribution of CT states energies observed experimentally in EQE spectra (see below) could be hence imputable to the energetic disorder in the hole and electron energy levels.

Table 4.3: Average photovoltaic gap (E_{GAP}), CT state (E_{CT}), exciton binding energies (E_B) (in eV) and standard deviations σ_{tot}^{x} (in meV, where x stands for GAP or CT) for NPB:HAT-CN pairs at 300 K as a function of HAT-CN molar fraction. Energy fluctuations (in meV) were also quantified according to their nature: intramolecular σ_{conf}^{x}, intermolecular σ_{env}^{x}, static σ_{stat}^{x} and low-frequency dynamic disorder σ_{low}^{x}. Environmental reorganization energies λ_{env} (in meV) were calculated as $\lambda_{env} = \frac{{\sigma^2}_{low}^{x}}{2k_BT}$. Note that for photovoltaic gaps and CT state energies the intermolecular σ_{env}^{x} and low-frequency dynamic disorder σ_{low}^{x} coincide and thus are given just once.

% HAT-CN	E_{GAP}	σ_{tot}^{GAP}	σ_{conf}^{GAP}	σ_{env}^{GAP}	σ_{stat}^{GAP}	σ_{low}^{GAP}	λ_{env}
4.6	1.72	296	184	238	282	89	155
10.3	1.78	310	191	239	295	96	181
76.1	1.90	355	184	339	340	104	209

% HAT-CN	E_{CT}	σ_{tot}^{CT}	σ_{stat}^{CT}	E_B	σ_B
4.6	1.33	306	293	-0.39	123
10.3	1.40	316	301	-0.38	118
76.1	1.44	371	357	-0.46	133

4.3.3 Non-Radiative Recombination of Charge-Transfer States

The existence of an important contribution from static, temperature-independent, disorder in the real system is confirmed by the fits of low-energy portion of the EQE spectra at different temperatures. Experimental EQE spectra of a NPB:HAT-CN BHJ solar cell with 66.0% of HAT-CN are shown in Figure 4.7a for temperatures ranging from 110 K to 296 K (see Additional data for further details in the EQE measurements). With decreasing temperature, the EQE steadily decreases as the generation and transport of charge carriers become increasingly difficult.[49,50] Despite the decrease in magnitude, the EQE spectral shape is mostly preserved but has a small red-shift of the lowest-energy CT peak with decreasing temperature. Following Burke *et al.*,[5] we performed a fit of EQE spectra to extract the static and dynamic contributions to the total energetic disorder as a function of temperature. As shown in Figure 4.7b, the linear extrapolation of σ_{EQE}^2 to 0 K provides an estimate for the static disorder of 150 meV (see Table 4.6 in Additional data). Therefore, static disorder dominates the CT spectral linewidth even at room temperature, quite contrary to observations on most fullerene-based archetypal OSCs,[51] but qualitatively in agreement with the theoretical data presented in Table 4.3 for NPB:HAT-CN blends.

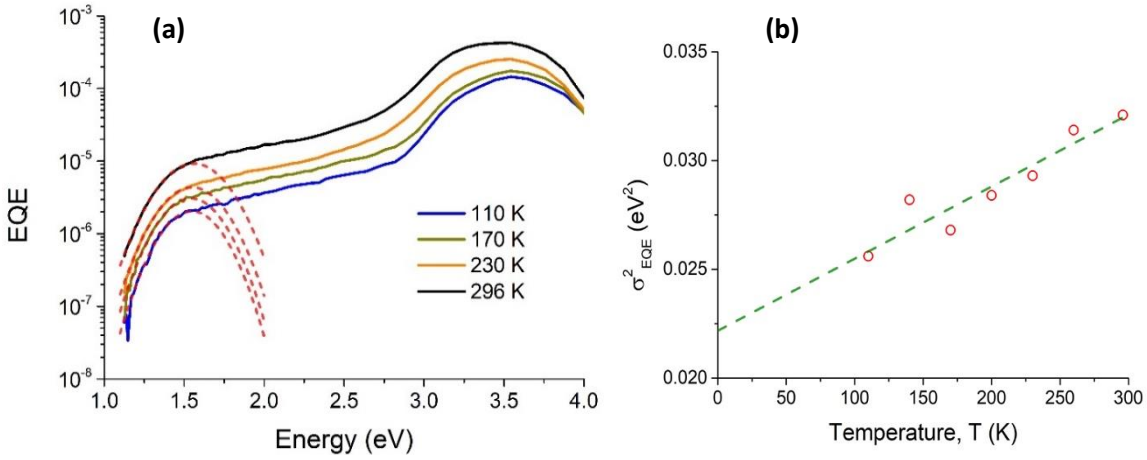

Figure 4.7: a) Temperature-dependent external quantum efficiency (EQE) spectra of a NPB:HAT-CN BHJ solar cell with 66.0% of HAT-CN (solid lines). Lowest-energy CT spectra were fitted, following Burke *et al.*'s approach,[5] considering a Gaussian CT energetic distribution (dashed red lines). b) Temperature dependence of the variance of the energetic disorder extracted from a Gaussian fit of EQE spectra. The extrapolation to 0 K (dashed green line) allows to estimate a static, temperature-independent, disorder of 150 meV.

A quantitative comparison between the calculated and the EQE-derived disorder requires some caution, since the EQE spectral shape may be severely affected by charge recombination. A first hint that the EQE spectrum is not able to fully capture the CT DOS is provided by the striking difference with the absorption (photothermal deflection spectroscopy, PDS) spectrum, shown in Figure 4.8a.

The comparison between the two spectra reveals that the lowest-energy transition, peaking at around 1.2 eV in the PDS, is almost absent in the EQE. In order to rationalize this dissimilarity, we exploit the in-depth knowledge of the CT DOS from our calculations to consider non-radiative recombination, an intrinsic process causing severe voltage losses in organic photovoltaic devices.[17,52] Within the MLJ framework, non-radiative recombination rates (κ_{NRAD}) were computed and their average values binned over small (100 meV) energy intervals are shown in Figure 4.8a (the full data set is given in Figure 4.13 and 4.14 in Additional data). Irrespective of the blend composition, the rates exceed 10^{12} s^{-1} for CT energies below 1.5 eV and decrease by several orders of magnitude at increasing CT energies, a trend that is reminiscent of the energy-gap law.[53,54] Such large rates for the lowest-energy CT states suggest that these excitations strongly recombine to the ground state before charge dissociation can occur, explaining the difference in shape of the measured EQE and absorption spectra. Thus, unlike higher-energy CT or Frenkel excitations, the lowest-energy CT states are photovoltaically inactive in NPB:HAT-CN blends, viz. they do not contribute to photocurrent generation, and may be responsible for large voltage losses.[52,54]

The analysis above allows us to conclude that the EQE spectra are not fully representative of the actual CT DOS, at least in large offset, low gap, D:A blends, as non-radiative processes tend to crop the low-energy tails of the probed distributions. As such, the results of common Gaussian fits of the tail of EQE spectra to extract the band maximum and width should be taken with caution. Note that the EQE fit in Figure 4.8a seems to yield a peak position that is ~0.7 eV apart from the first absorption peak, hence the associated standard deviation cannot be interpreted as a measure of the energetic disorder in the lowest-energy CT state. The next question that arises is whether optical absorption, electroluminescence (EL) or photoluminescence (PL) measurements provide a more representative proxy for the DOS of the system, and hence would be more suited to quantify the total energetic disorder. Figure 4.8b compares the experimental and calculated absorption spectra and the calculated CT DOS. The last two quantities were computed taking into account the coupling to an effective quantum vibrational mode, in order to describe the broadening due to vibronic progression and allow for a fair comparison with the experimental absorption. The calculated absorption matches well with experiment, capturing the peak position, yet overestimating the bandwidth. Moreover, calculations show that the absorption spectrum gives a close reproduction of the low-energy tail of the CT DOS, since transition dipole moments do not feature orders of magnitude variations in the energy range of interest. These results suggest that absorption spectra, although more challenging to collect experimentally for weakly-absorbing intermolecular excitons, can provide a faithful description of the CT DOS in D:A blends, and independent of the spectral region (*i.e.*, infrared versus visible). In contrast, emission spectra suffer from the competition with non-radiative processes as does EQE and should thus be interpreted equally with care.

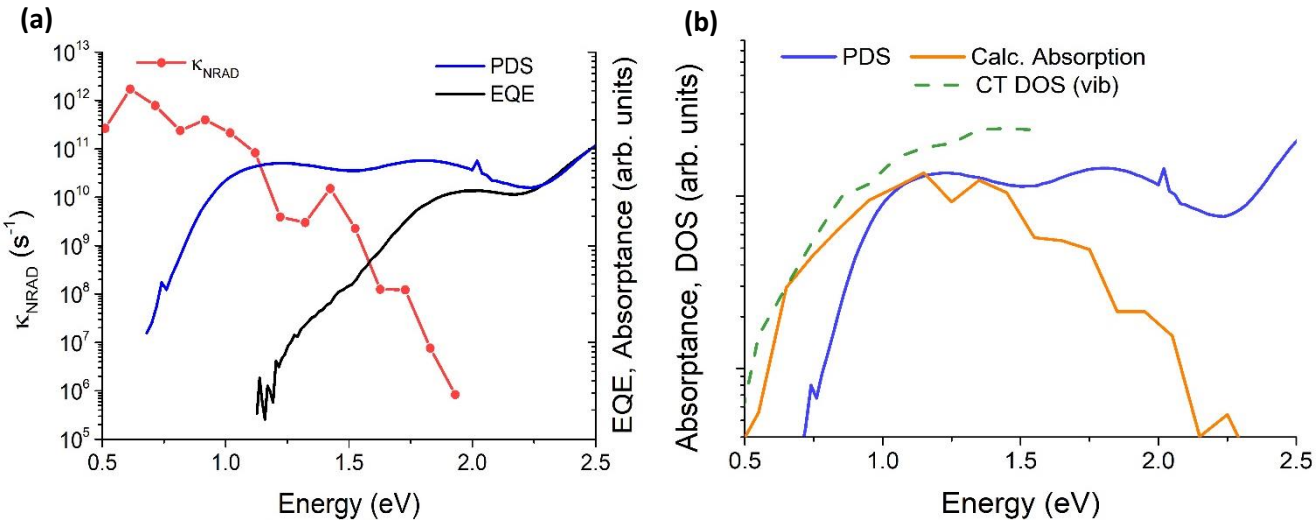

Figure 4.8: a) External quantum efficiency (EQE) spectrum (solid black line) and absorptance spectrum (solid blue line) of a NPB:HAT-CN film measured by photothermal deflection spectroscopy (PDS)[15]. Red points show the average calculated non-radiative decay rates of CT excitations to the ground state as a function of the excitations energy. The six orders of magnitude drop of κ_{NRAD} in the CT states energy window rationalizes the stark difference between EQE and PDS spectra. b) PDS spectrum compared to the calculated one (solid orange line) and to the calculated vibrationally-broadened CT density of states (DOS) (dashed green line). Experimental and calculated data refer to samples with 4.6 % of HAT-CN at 300 K.

The origin for the CT energetic disorder in organic photovoltaic systems was recently debated in the literature.[17–19] Specifically, different conclusions regarding the relative contributions from static versus dynamic (thermally-activated) disorder were reached in research papers on D:A blends based on fullerene derivatives. Comparable static and dynamic disorder was found for polymer:phenyl-C61-butyric acid methyl ester ($PC_{61}BM$) blends,[55] while a picture solely based on dynamic disorder due to low-frequency intramolecular mode seemed to be able to correctly describe small molecule-C_{60} systems.[49] For the latter family of systems, the evidence for a temperature-independent energetic disorder was very recently ascribed to the zero-point motion of quantum vibrational modes.[19] Besides raising some concerns on the experimental determination of the disorder, our microscopic analysis suggests that the answer to the paramount question regarding the nature of the disorder depends markedly on the system investigated and, most importantly, on the way it is probed. If, on the one hand, it is plausible that the static environmental disorder is almost negligible for blends of donor molecules diluted in electrically neutral fullerenes, this contribution can be substantial in the presence of molecules featuring polar groups, such as the NPB:HAT-CN system investigated here, and whose broad CT state spectral signature is mostly due to static disorder (both conformational and electrostatic), with temperature-dependent dynamic disorder having a much lower impact.

4.4 Conclusions

The nature of low-lying CT states in NPB:HAT-CN amorphous D:A blends was investigated with a multiscale computational approach. We found that the rather wide CT DOS broadening is dominated by static disorder and arises from both conformational and electrostatic landscape variations, which in turn originate from NPB flexibility and HAT-CN quadrupoles. The large broadening and the deep LUMO levels of HAT-CN ensure that a large portion of the CT DOS lies below 1.5 eV, where non-radiative decay to the ground state becomes predominant over charge separation. This energetic situation has two important consequences, sometimes not adequately considered in the literature: i) the tail of the CT DOS cannot be probed via EQE, EL, or PL measurements, and more importantly for OSC applications, it does not contribute to charge generation but rather to recombination; ii) in such a case, the standard procedure of fitting the tail of the EQE signal with a Gaussian function to extract static and dynamic disorder becomes unreliable.

References

(1) Fusella, M. A.; Brigeman, A. N.; Welborn, M.; Purdum, G. E.; Yan, Y.; Schaller, R. D.; Lin, Y. L.; Loo, Y.-L.; Voorhis, T. Van; Giebink, N. C.; Rand, B. P. Band-like Charge Photogeneration at a Crystalline Organic Donor/Acceptor Interface. *Adv. Energy Mater.* **2018**, *8* (9), 1701494.

(2) D'Avino, G.; Mothy, S.; Muccioli, L.; Zannoni, C.; Wang, L.; Cornil, J.; Beljonne, D.; Castet, F. Energetics of Electron-Hole Separation at P3HT/PCBM Heterojunctions. *J. Phys. Chem. C* **2013**, *117* (25), 12981–12990.

(3) Castet, F.; D'Avino, G.; Muccioli, L.; Cornil, J.; Beljonne, D. Charge Separation Energetics at Organic Heterojunctions: On the Role of Structural and Electrostatic Disorder. *Phys. Chem. Chem. Phys.* **2014**, *16* (38), 20279–20290.

(4) D'Avino, G.; Muccioli, L.; Olivier, Y.; Beljonne, D. Charge Separation and Recombination at Polymer-Fullerene Heterojunctions: Delocalization and Hybridization Effects. *J. Phys. Chem. Lett.* **2016**, *7* (3), 536–540.

(5) Burke, T. M.; Sweetnam, S.; Vandewal, K.; McGehee, M. D. Beyond Langevin Recombination: How Equilibrium Between Free Carriers and Charge Transfer States Determines the Open-Circuit Voltage of Organic Solar Cells. *Adv. Energy Mater.* **2015**, *5* (11), 1500123.

(6) Sánchez-Carrera, R. S.; Paramonov, P.; Day, G. M.; Coropceanu, V.; Brédas, J.-L. Interaction of Charge Carriers with Lattice Vibrations in Oligoacene Crystals from Naphthalene to Pentacene. *J. Am. Chem. Soc.* **2010**, *132* (41), 14437–14446.

(7) Tummala, N. R.; Zheng, Z.; Aziz, S. G.; Coropceanu, V.; Brédas, J.-L. Static and Dynamic Energetic Disorders in the C 60 , PC 61 BM, C 70 , and PC 71 BM Fullerenes. *J. Phys. Chem. Lett.* **2015**, *6* (18), 3657–3662.

(8) Unger, T.; Wedler, S.; Kahle, F.-J.; Scherf, U.; Bässler, H.; Köhler, A. The Impact of Driving Force and Temperature on the Electron Transfer in Donor–Acceptor Blend Systems. *J. Phys. Chem. C* **2017**, *121* (41), 22739–22752.

(9) Tummala, N. R.; Elroby, S. A.; Aziz, S. G.; Risko, C.; Coropceanu, V.; Brédas, J.-L. Packing and Disorder in Substituted Fullerenes. *J. Phys. Chem. C* **2016**, *120* (31), 17242–17250.

(10) Belova, V.; Beyer, P.; Meister, E.; Linderl, T.; Halbich, M.-U.; Gerhard, M.; Schmidt, S.; Zechel, T.; Meisel, T.; Generalov, A. V.; Anselmo, A. S.; Scholz, R.; Konovalov, O.; Gerlach, A.; Koch, M.; Hinderhofer, A.; Opitz, A.; Brütting, W.; Schreiber, F. Evidence for Anisotropic Electronic Coupling of Charge Transfer States in Weakly Interacting Organic Semiconductor Mixtures. *J. Am. Chem. Soc.* **2017**, *139* (25), 8474–8486.

(11) Chen, X.-K.; Coropceanu, V.; Brédas, J.-L. Assessing the Nature of the Charge-Transfer

Electronic States in Organic Solar Cells. *Nat. Commun.* **2018**, *9* (1), 5295.

(12) Lin, Y. L.; Zhang, F.; Kerner, R. A.; Yang, T. C.-J.; Kahn, A.; Rand, B. P. Variable Charge Transfer State Energies at Nanostructured Pentacene/C 60 Interfaces. *Appl. Phys. Lett.* **2018**, *112* (21), 213302.

(13) Lin, Y. L.; Fusella, M. A.; Rand, B. P. The Impact of Local Morphology on Organic Donor/Acceptor Charge Transfer States. *Adv. Energy Mater.* **2018**, *8* (28), 1702816.

(14) Ding, K.; Liu, X.; Forrest, S. R. Charge Transfer and Collection in Dilute Organic Donor–Acceptor Heterojunction Blends. *Nano Lett.* **2018**, *18* (5), 3180–3184.

(15) Khan, S. U. Z.; Londi, G.; Liu, X.; Fusella, M. A.; D'Avino, G.; Muccioli, L.; Brigeman, A. N.; Niesen, B.; Yang, T. C. J.; Olivier, Y.; Dull, J. T.; Giebink, N. C.; Beljonne, D.; Rand, B. P. Multiple Charge Transfer States in Donor-Acceptor Heterojunctions with Large Frontier Orbital Energy Offsets. *Chem. Mater.* **2019**, *31* (17), 6808–6817.

(16) Lin, Y. L.; Fusella, M. A.; Kozlov, O. V.; Lin, X.; Kahn, A.; Pshenichnikov, M. S.; Rand, B. P. Morphological Tuning of the Energetics in Singlet Fission Organic Solar Cells. *Adv. Funct. Mater.* **2016**, *26* (35), 6489–6494.

(17) Lin, Y. L.; Fusella, M. A.; Rand, B. P. The Impact of Local Morphology on Organic Donor/Acceptor Charge Transfer States. *Adv. Energy Mater.* **2018**, *8* (28), 1702816.

(18) Vandewal, K.; Albrecht, S.; Hoke, E. T.; Graham, K. R.; Widmer, J.; Douglas, J. D.; Schubert, M.; Mateker, W. R.; Bloking, J. T.; Burkhard, G. F.; Sellinger, A.; Fréchet, J. M. J.; Amassian, A.; Riede, M. K.; McGehee, M. D.; Neher, D.; Salleo, A. Efficient Charge Generation by Relaxed Charge-Transfer States at Organic Interfaces. *Nat. Mater.* **2014**, *13* (1), 63–68.

(19) Panhans, M.; Hutsch, S.; Benduhn, J.; Schellhammer, K. S.; Nikolis, V. C.; Vangerven, T.; Vandewal, K.; Ortmann, F. Molecular Vibrations Reduce the Maximum Achievable Photovoltage in Organic Solar Cells. *Nat. Commun.* **2020**, *11* (1), 1–10.

(20) Muccioli, L.; D'Avino, G.; Zannoni, C. Simulation of Vapor-Phase Deposition and Growth of a Pentacene Thin Film on C60 (001). *Adv. Mater.* **2011**, *23* (39), 4532–4536.

(21) D'Avino, G.; Muccioli, L.; Zannoni, C. From Chiral Islands to Smectic Layers: A Computational Journey Across Sexithiophene Morphologies on C 60. *Adv. Funct. Mater.* **2015**, *25* (13), 1985–1995.

(22) Roscioni, O. M.; D'Avino, G.; Muccioli, L.; Zannoni, C. Pentacene Crystal Growth on Silica and Layer-Dependent Step-Edge Barrier from Atomistic Simulations. *J. Phys. Chem. Lett.* **2018**, *9* (23), 6900–6906.

(23) Phillips, J. C.; Braun, R.; Wang, W.; Gumbart, J.; Tajkhorshid, E.; Villa, E.; Chipot, C.; Skeel, R. D.; Kalé, L.; Schulten, K. Scalable Molecular Dynamics with NAMD. *J. Comput. Chem.* **2005**, *26* (16), 1781–1802.

(24) Moral, M.; Son, W.-J.; Sancho-García, J. C.; Olivier, Y.; Muccioli, L. Cost-Effective Force Field Tailored for Solid-Phase Simulations of OLED Materials. *J. Chem. Theory Comput.* **2015**, *11*, 3383–3392.

(25) Szalay, P. S.; Galán-Mascarós, J. R.; Clérac, R.; Dunbar, K. R. HAT(CN)6: A New Building Block for Molecule-Based Magnetic Materials. *Synth. Met.* **2001**, *122* (3), 535–542.

(26) Lin, Y. S.; Li, G. De; Mao, S. P.; Chai, J. Da. Long-Range Corrected Hybrid Density Functionals with Improved Dispersion Corrections. *J. Chem. Theory Comput.* **2013**, *9* (1), 263–272.

(27) Frisch, M. J.; Trucks, G. W.; Schlegel, H. B.; Scuseria, G. E.; Robb, M. A.; Cheeseman, J. R.; Scalmani, G.; Barone, V.; Petersson, G. A.; Nakatsuji, H.; Li, X.; Caricato, M.; Marenich, A. V; Bloino, J.; Janesko, B. G.; Gomperts, R.; Mennucci, B.; Hratchian, H. P.; Ortiz, J. V; Izmaylov, A. F.; Sonnenberg, J. L.; Williams-Young, D.; Ding, F.; Lipparini, F.; Egidi, F.; Goings, J.; Peng, B.; Petrone, A.; Henderson, T.; Ranasinghe, D.; Zakrzewski, V. G.; Gao, J.; Rega, N.; Zheng, G.; Liang, W.; Hada, M.; Ehara, M.; Toyota, K.; Fukuda, R.; Hasegawa, J.; Ishida, M.; Nakajima, T.; Honda, Y.; Kitao, O.; Nakai, H.; Vreven, T.; Throssell, K.; Montgomery Jr., J. A.; Peralta, J. E.; Ogliaro, F.; Bearpark, M. J.; Heyd, J. J.; Brothers, E. N.; Kudin, K. N.; Staroverov, V. N.; Keith, T. A.; Kobayashi, R.; Normand, J.; Raghavachari, K.; Rendell, A. P.; Burant, J. C.; Iyengar, S. S.; Tomasi, J.; Cossi, M.; Millam, J. M.; Klene, M.; Adamo, C.; Cammi, R.; Ochterski, J. W.; Martin, R. L.; Morokuma, K.; Farkas, O.; Foresman, J. B.; Fox, D. J. Gaussian 16 Revision C.01. Gaussian Inc. Wallingford CT 2016.

(28) Neese, F. Software Update: The ORCA Program System, Version 4.0. *WIREs Comput. Mol. Sci.* **2018**, *8* (1).

(29) Li, J.; Duchemin, I.; Roscioni, O. M.; Friederich, P.; Anderson, M.; Da Como, E.; Kociok-Köhn, G.; Wenzel, W.; Zannoni, C.; Beljonne, D.; Blase, X.; D'Avino, G. Host Dependence of the Electron Affinity of Molecular Dopants. *Mater. Horizons* **2019**, *6* (1), 107–114.

(30) D'Avino, G.; Muccioli, L.; Zannoni, C.; Beljonne, D.; Soos, Z. G.; D'Avino, G.; Muccioli, L.; Zannoni, C.; Beljonne, D.; Soos, Z. G.; D'Avino, G.; Muccioli, L.; Zannoni, C.; Beljonne, D.; Soos, Z. G. Electronic Polarization in Organic Crystals: A Comparative Study of Induced Dipoles and Intramolecular Charge Redistribution Schemes. *J. Chem. Theory Comput.* **2014**, *10* (11), 4959–4971.

(31) D'Avino, G.; Muccioli, L.; Castet, F.; Poelking, C.; Andrienko, D.; Soos, Z. G.; Cornil, J.; Beljonne, D. Electrostatic Phenomena in Organic Semiconductors: Fundamentals and Implications for Photovoltaics. *J. Phys. Condens. Matter* **2016**, *28* (43).

(32) Londi, G.; Dilmurat, R.; D'Avino, G.; Lemaur, V.; Olivier, Y.; Beljonne, D. Comprehensive Modelling Study of Singlet Exciton Diffusion in Donor-Acceptor Dyads: When Small Changes in Chemical Structure Matter. *Phys. Chem. Chem. Phys.* **2019**, *21* (45), 25023–25034.

(33) Marqués, P. S.; Andrés Castán, J. M.; Raul, B. A. L.; Londi, G.; Ramirez, I.; Pshenichnikov, M. S.; Beljonne, D.; Walzer, K.; Blais, M.; Allain, M.; Cabanetos, C.; Blanchard, P.; Simón Marqués, P.; Castán, J. M. A.; Raul, B. A. L.; Londi, G.; Ramirez, I.; Pshenichnikov, M. S.; Beljonne, D.; Walzer, K.; Blais, M.; Allain, M.; Cabanetos, C.; Blanchard, P. Triphenylamine/Tetracyanobutadiene-Based π-Conjugated Push–Pull Molecules End-Capped with Arene Platforms: Synthesis, Photophysics, and Photovoltaic Response. *Chem. – A Eur. J.* **2020**, *26* (69), 16422–16433.

(34) Tomasi, J.; Mennucci, B.; Cammi, R. Quantum Mechanical Continuum Solvation Models. *Chem. Rev.* **2005**, *105* (8), 2999–3094.

(35) Cave, R. J.; Newton, M. D. Generalization of the Mulliken-Hush Treatment for the Calculation of Electron Transfer Matrix Elements. *Chem. Phys. Lett.* **1996**, *249* (1–2), 15–19.

(36) Tonnelé, C.; Stroet, M.; Caron, B.; Clulow, A. J.; Nagiri, R. C. R.; Malde, A. K.; Burn, P. L.; Gentle, I. R.; Mark, A. E.; Powell, B. J. Elucidating the Spatial Arrangement of Emitter Molecules in Organic Light-Emitting Diode Films. *Angew. Chemie Int. Ed.* **2017**, *56* (29), 8402–8406.

(37) Lee, T.; Sanzogni, A.; Zhangzhou, N.; Burn, P. L.; Mark, A. E. Morphology of a Bulk Heterojunction Photovoltaic Cell with Low Donor Concentration. *ACS Appl. Mater. Interfaces* **2018**, *10* (38), 32413–32419.

(38) Schwarze, M.; Tress, W.; Beyer, B.; Gao, F.; Scholz, R.; Poelking, C.; Ortstein, K.; Günther, A. A.; Kasemann, D.; Andrienko, D.; Leo, K. Band Structure Engineering in Organic Semiconductors. *Science* **2016**, *352* (6292), 1446–1449.

(39) Graham, K. R.; Ndjawa, G. O. N.; Conron, S. M.; Munir, R.; Vandewal, K.; Chen, J. J.; Sweetnam, S.; Thompson, M. E.; Salleo, A.; McGehee, M. D.; Amassian, A. The Roles of Structural Order and Intermolecular Interactions in Determining Ionization Energies and Charge-Transfer State Energies in Organic Semiconductors. *Adv. Energy Mater.* **2016**, *6* (22), 1601211.

(40) Privitera, A.; Londi, G.; Riede, M.; D'Avino, G.; Beljonne, D. Molecular Quadrupole Moments Promote Ground-State Charge Generation in Doped Organic Semiconductors. *Adv. Funct. Mater.* **2020**, *30*, 2004600.

(41) Hill, I. G.; Kahn, A. Organic Semiconductor Heterointerfaces Containing Bathocuproine. *J. Appl. Phys.* **1999**, *86* (8), 4515–4519.

(42) Amsalem, P.; Wilke, A.; Frisch, J.; Niederhausen, J.; Vollmer, A.; Rieger, R.; Müllen, K.; Rabe, J. P.; Koch, N. Interlayer Molecular Diffusion and Thermodynamic Equilibrium in Organic Heterostructures on a Metal Electrode. *J. Appl. Phys.* **2011**, *110* (11), 113709.

(43) Yoshida, H.; Yoshizaki, K. Electron Affinities of Organic Materials Used for Organic Light-Emitting Diodes: A Low-Energy Inverse Photoemission Study. *Org. Electron.* **2015**, *20*, 24–

30.

(44) Falkenberg, C.; Olthof, S.; Rieger, R.; Baumgarten, M.; Muellen, K.; Leo, K.; Riede, M. The Role of Energy Level Matching in Organic Solar Cells- Hexaazatriphenylene Hexacarbonitrile as Transparent Electron Transport Material. *Sol. Energy Mater. Sol. Cells* **2011**, *95* (3), 927–932.

(45) Tummala, N. R.; Zheng, Z.; Aziz, S. G.; Coropceanu, V.; Brédas, J.-L. Static and Dynamic Energetic Disorders in the C60, PC61BM, C70, and PC71BM Fullerenes. *J. Phys. Chem. Lett.* **2015**, *6* (18), 3657–3662.

(46) D'Avino, G.; Olivier, Y.; Muccioli, L.; Beljonne, D. Do Charges Delocalize over Multiple Molecules in Fullerene Derivatives? *J. Mater. Chem. C* **2016**, *4* (17), 3747–3756.

(47) de Silva, P.; Van Voorhis, T. QM/MM Study of Static and Dynamic Energetic Disorder in the Emission Layer of an Organic Light-Emitting Diode. *J. Phys. Chem. Lett.* **2018**, *9* (6), 1329–1334.

(48) Mikhnenko, O. V.; Blom, P. W. M.; Nguyen, T. Q. Exciton Diffusion in Organic Semiconductors. *Energy and Environmental Science*. 2015, pp 1867–1888.

(49) Tvingstedt, K.; Benduhn, J.; Vandewal, K. Temperature Dependence of the Spectral Line-Width of Charge-Transfer State Emission in Organic Solar Cells; Static vs. Dynamic Disorder. *Mater. Horizons* **2020**, *7* (7), 1888.

(50) Baranovskii, S. D. Theoretical Description of Charge Transport in Disordered Organic Semiconductors. *Phys. status solidi* **2014**, *251* (3), 487–525.

(51) Benduhn, J. Ph.D. Thesis, TU Dresden, 2019.

(52) Azzouzi, M.; Yan, J.; Kirchartz, T.; Liu, K.; Wang, J.; Wu, H.; Nelson, J. Nonradiative Energy Losses in Bulk-Heterojunction Organic Photovoltaics. *Phys. Rev. X* **2018**, *8* (3), 031055.

(53) Bixon, M.; Jortner, J.; Cortes, J.; Heitele, H.; Michel-Beyerle, M. E. Energy Gap Law for Nonradiative and Radiative Charge Transfer in Isolated and in Solvated Supermolecules. *J. Phys. Chem.* **1994**, *98* (30), 7289–7299.

(54) Benduhn, J.; Tvingstedt, K.; Piersimoni, F.; Ullbrich, S.; Fan, Y.; Tropiano, M.; McGarry, K. A.; Zeika, O.; Riede, M. K.; Douglas, C. J.; Barlow, S.; Marder, S. R.; Neher, D.; Spoltore, D.; Vandewal, K. Intrinsic Non-Radiative Voltage Losses in Fullerene-Based Organic Solar Cells. *Nat. Energy* **2017**, *2* (6), 1–6.

(55) Kahle, F. J.; Rudnick, A.; Bässler, H.; Köhler, A. How to Interpret Absorption and Fluorescence Spectra of Charge Transfer States in an Organic Solar Cell. *Mater. Horizons* **2018**, *5* (5), 837–848.

(56) Vandewal, K.; Tvingstedt, K.; Gadisa, A.; Inganäs, O.; Manca, J. V. Relating the Open-Circuit

Voltage to Interface Molecular Properties of Donor:Acceptor Bulk Heterojunction Solar Cells. *Phys. Rev. B* **2010**, *81* (12), 125204.

(57) Linderl, T.; Zechel, T.; Hofmann, A.; Sato, T.; Shimizu, K.; Ishii, H.; Brütting, W. Crystalline versus Amorphous Donor-Acceptor Blends: Influence of Layer Morphology on the Charge-Transfer Density of States. *Phys. Rev. Appl.* **2020**, *13* (2), 24061.

Additional data

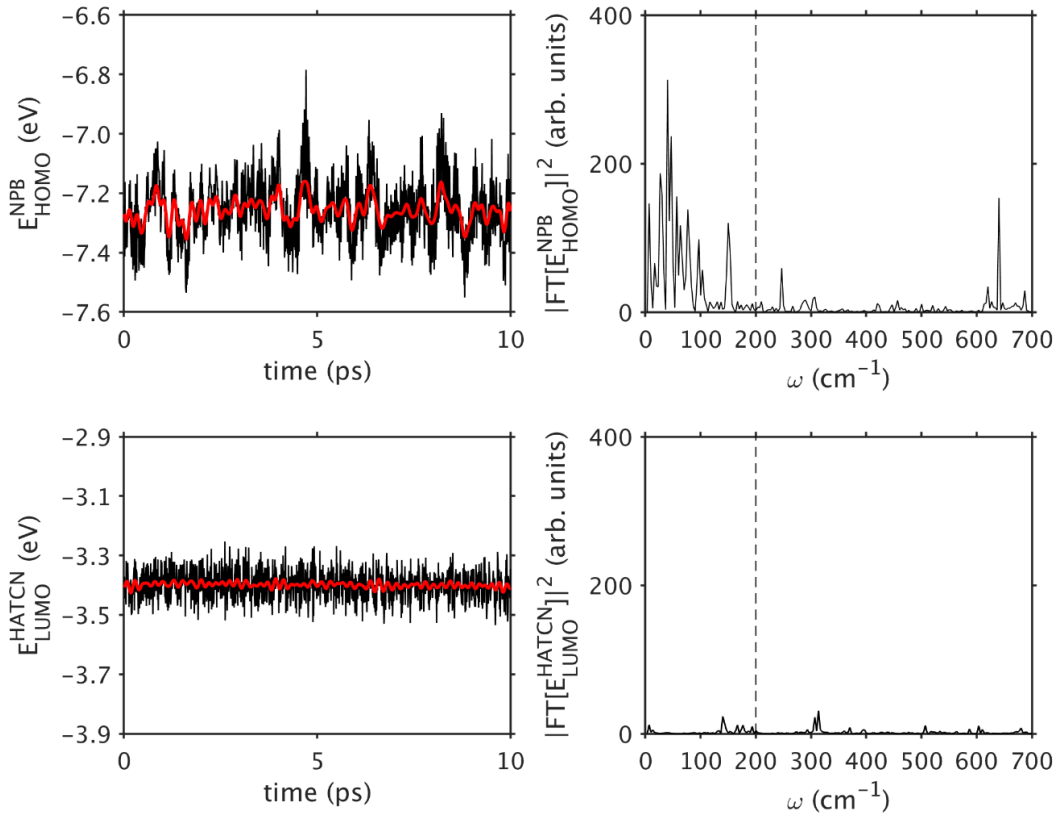

Figure 4.9: Illustration of the frequency filtering procedure applied to the charge transport energy levels of NPB and HAT-CN molecules. Left panels: time series, as computed from MD geometries (black line) and after removing the high-frequency component (red line). Right panels: the power spectra of the unfiltered data, the vertical dashed line marks the 200 cm^{-1} cutoff frequency used to discriminate between low- and high-frequency components. These data refer to the 4.6% of HAT-CN sample at 300 K

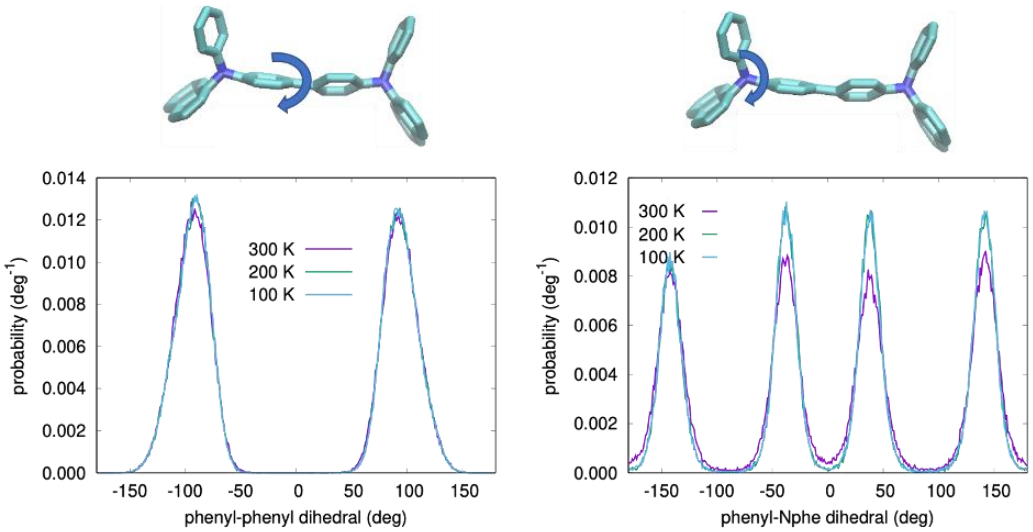

Figure 4.10: Distribution of the two main NPB dihedral angles for the sample at 4.6% HAT-CN molar fraction, as obtained from MD simulations at three different temperatures.

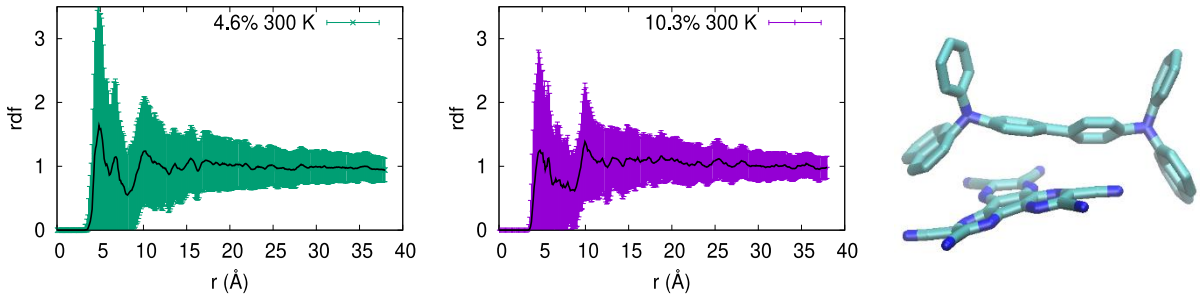

Figure 4.11: Radial distribution function of NPB:HAT-CN pairs at two different concentrations. A typical configuration corresponding to intermolecular distances of about 5 Å is shown on the right.

Table 4.4: Average energy of single carrier transport levels (in eV) and standard deviations σ_{tot}^{x} (in meV, where x stands for IP or EA). Energy fluctuations (in meV) were also quantified according to their nature: intramolecular σ_{conf}^{x}, intermolecular σ_{env}^{x}, static σ_{stat}^{x} and low-frequency dynamic disorder σ_{low}^{x}.

% HAT-CN	IP_{NPB}	σ_{tot}^{IP}	σ_{conf}^{IP}	σ_{env}^{IP}	σ_{stat}^{IP}	σ_{low}^{IP}
4.6	5.98	227	173	154	219	59
10.3	5.99	222	172	156	213	64
76.1	6.82	342	180	285	335	68

% HAT-CN	EA_{HAT-CN}	σ_{tot}^{EA}	σ_{conf}^{EA}	σ_{env}^{EA}	σ_{stat}^{EA}	σ_{low}^{EA}
4.6	4.18	157	36	149	157	11
10.3	4.19	152	16	152	152	12
76.1	4.94	260	14	259	259	14

Table 4.5: Average photovoltaic gap (E_{GAP}), CT state (E_{CT}), exciton binding energies (E_B) (in eV) and standard deviations σ_{tot}^{x} (in meV, where x stands for GAP or CT) on selected NPB:HAT-CN pairs at 100 K as a function of HAT-CN molar fraction. Energy fluctuations (in meV) were also quantified according to their nature: intramolecular σ_{conf}^{x}, intermolecular σ_{env}^{x}, static σ_{stat}^{x} and low-frequency dynamic disorder σ_{low}^{x}. Environmental reorganization energies λ_{env} (in meV) were calculated as $\lambda_{env} = \frac{\sigma^{2}{}_{low}^{x}}{2k_BT}$. Note that for photovoltaic gaps and CT state energies the intermolecular σ_{env}^{x} and low-frequency dynamic disorder σ_{low}^{x} coincide and thus are given just once.

% HAT-CN	E_{GAP}	σ_{tot}^{GAP}	σ_{conf}^{GAP}	σ_{env}^{GAP}	σ_{stat}^{GAP}	σ_{low}^{GAP}	λ_{env}
4.6	1.81	280	185	227	273	60	210
10.3	1.84	260	164	220	252	65	243
76.1	1.98	371	173	346	365	69	278

% HAT-CN	E_{CT}	σ_{tot}^{CT}	σ_{stat}^{CT}	E_B	σ_B
4.6	1.44	288	281	-0.37	117
10.3	1.48	267	259	-0.36	110
76.1	1.53	390	384	-0.45	129

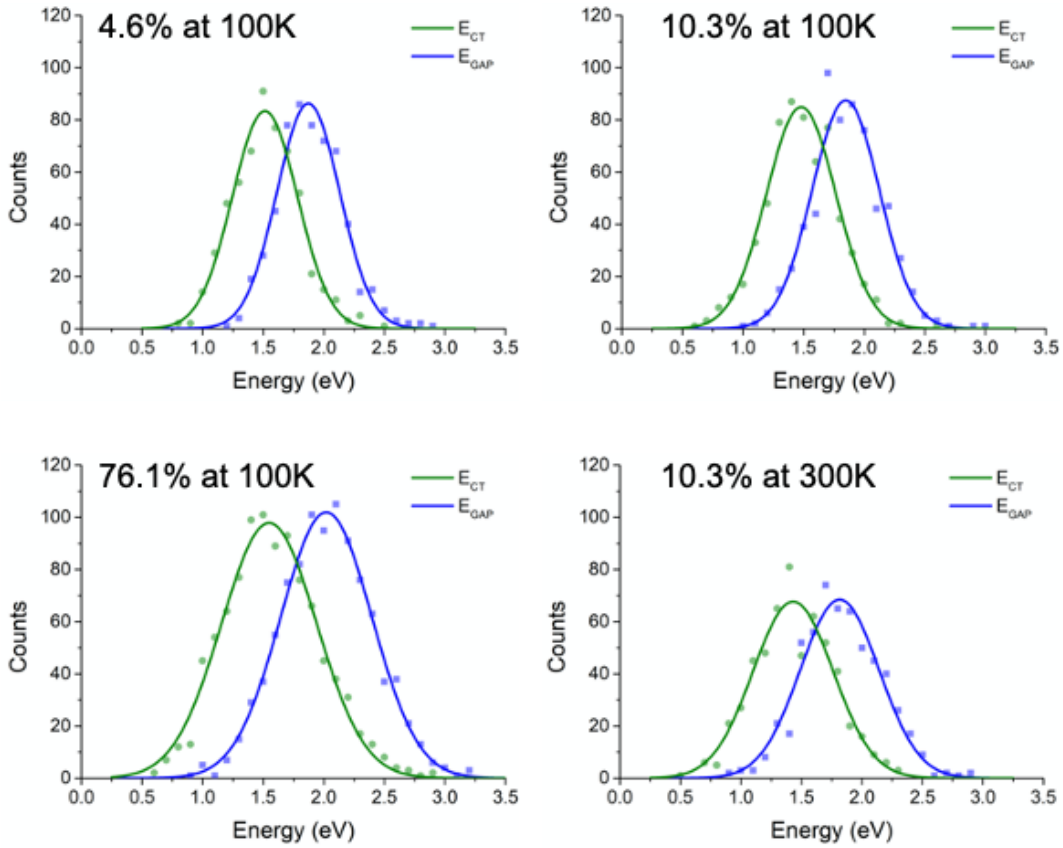

Figure 4.12: CT density of states (DOS) and distribution of gap energies at 4.6% and 76.1% HAT-CN molar fraction at 100 K (left) and at 10.3% HAT-CN molar fraction at 100 K and 300 K (right). Continuous lines are Gaussian fits.

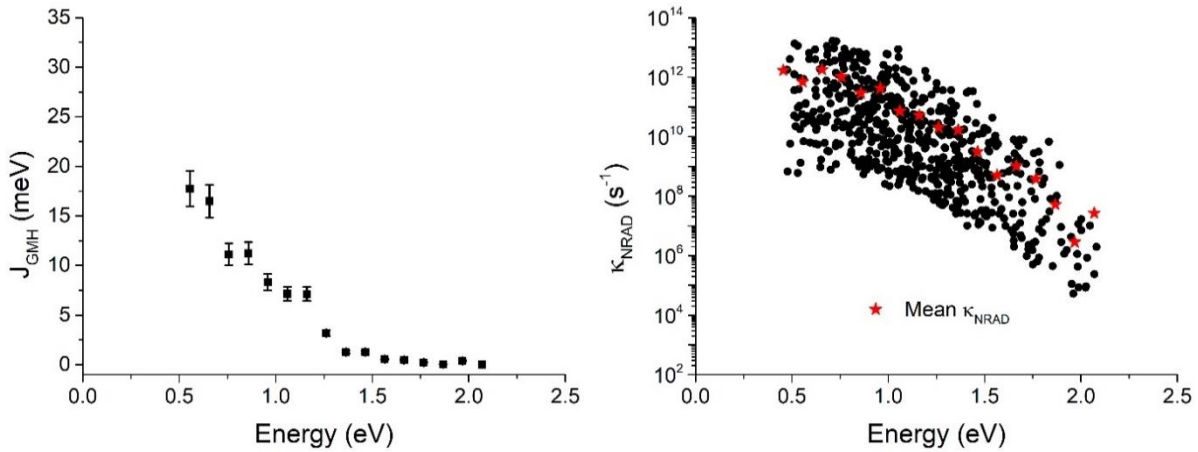

Figure 4.13: (left) Electronic coupling between the CT and the ground state computed with the generalized Mulliken-Hush (GMH) scheme. Squares and error bars show mean values and standard deviations calculated over energy bins. (right) Non-radiative recombination rates for the select NPB-HAT-CN pairs in the sample (black dots) and their average over energy bins (red stars). Data calculated for the sample at 76.1% HAT-CN molar fraction at 300 K.

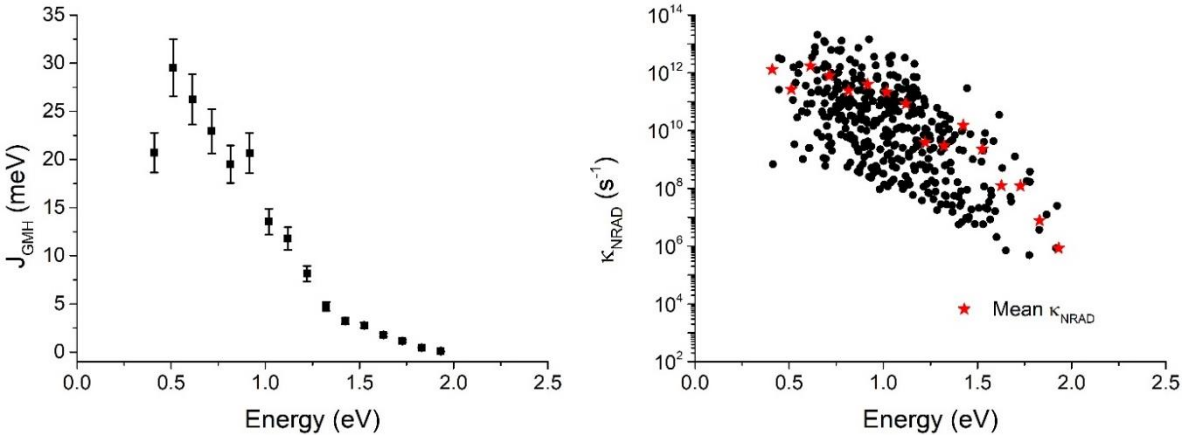

Figure 4.14: (left) Electronic coupling between the CT and the ground state computed with the generalized Mulliken-Hush (GMH) scheme. Squares and error bars show mean values and standard deviations calculated over energy bins. (right) Non-radiative recombination rates for the select NPB-HAT-CN pairs in the sample (black dots) and their average over energy bins (red stars). Data calculated for the sample at 4.6% HAT-CN molar fraction at 300 K.

EQE measurements

Samples for the EQE measurements were made on patterned ITO substrates (Colorado Concept Coatings). Substrates were cleaned by successive sonications in deionized water (15 min), acetone (10 min), and isopropanol (10 min) at 40 °C. Following the sonication step, the substrates were treated by oxygen plasma for 10 min.

Solar cell samples for the EQE measurements were made by thermally co-evaporating 100 nm of NPB (Nichem) and HAT-CN (Nichem) in a thermal evaporator (Angstrom Engineering Inc.), under ~10^{-7} torr base pressure, followed by 10 nm bathocuproine (BCP) (Lumtec) and 100 nm aluminum (Kurt J. Lesker Company) depositions. NPB and BCP were purified through thermal gradient sublimation, HAT-CN was used as purchased.

Temperature-dependent EQE spectra were measured by placing the sample inside a liquid N_2 based cryostat (Janis VNF-100). The temperature was controlled by a LakeShore 335 Cryogenic Temperature Controller. Monochromatic light was generated using Newport TLS-300X, which was chopped at 390 Hz with an optical chopper. The short-circuited device photocurrent was amplified by a current preamplifier (SR570, Stanford Research Systems) and detected by a lock-in amplifier (SR830, Stanford Research Systems). The incoming photon quantities from the monochromatic light source were estimated using calibrated Si and Ge photodiodes (Newport corporation). The cryostat was cooled down to 110 K first and then brought up to the room temperature while taking the measurements. Room temperature EQE spectra before and after cooling did not show any sign of device degradation due to the temperature change.

In the framework of Marcus theory of electron transfer, a Gaussian function fitted to the low-energy edge of the EQE spectrum is commonly used as an approximation to the lowest-energy CT absorption line-shape,[56] a technique that only considers vibronic broadening of the spectrum. However, Burke *et al.*[5] demonstrated that, when a Gaussian CT energetic distribution is assumed with a peak E_{CT} and standard distribution σ_{stat}, the overall CT absorption line-shape remains Gaussian with a shifted effective CT energy ($E_{CT(exp.)}$). The modified absorption line-shape also demonstrates an effective reorganization energy ($\lambda_{(exp.)}$). These effective CT spectral quantities are related to E_{CT} and reorganization energy (λ) of the electron transfer process as:

$$E_{CT(exp.)} = E_{CT} - \frac{\sigma_{stat}^2}{2k_BT} \tag{4.6}$$

$$\lambda_{(exp.)} = \lambda + \frac{\sigma_{stat}^2}{2k_BT} \tag{4.7}$$

which can be extracted by fitting a Marcus type Gaussian line-shape to the low-energy EQE tail. The introduction of the static disorder in the CT absorption line-shape introduces a temperature dependence in the experimentally extracted CT state energy, which is clear from the $E_{CT(exp.)}$ and $\lambda_{(exp.)}$ values (see Figure 4.15a and 4.15b) extracted from Figure 4.7a. A linear fitting to $E_{CT(exp.)}$ gives σ_{stat} of ~150 meV, responsible for the static broadening of the lowest-energy CT EQE spectra. According to Burke *et al.*'s treatment of CT EQE spectra, the total variance of the CT EQE line-shape is:

$$\sigma_{EQE}^2 = \sigma_{stat}^2 + 2\lambda k_BT \tag{4.8}$$

where $\sigma_{dyn}^2 = 2\lambda k_BT$ is the contribution from the dynamic (vibrational) broadening of the CT spectra. The relative contribution of static disorder at a specific temperature could be defined as:[57]

$$D_{stat}(T) = \frac{\sigma_{stat}^2}{\sigma_{stat}^2 + 2\lambda k_BT} \tag{4.9}$$

The CT EQE lineshape, proposed by Burke *et al.*[5] considering a Gaussian energetic distribution of the CT states, is given as a function of incident photon energy (E):

$$EQE_{CT}(E) \propto \frac{1}{E\sqrt{2\pi(\sigma_{stat}^2 + 2\lambda k_B\mathrm{T})}} \exp\left(\frac{-(E_{CT}+\lambda-E)^2}{2\sigma_{stat}^2 + 4\lambda k_BT}\right) \tag{4.10}$$

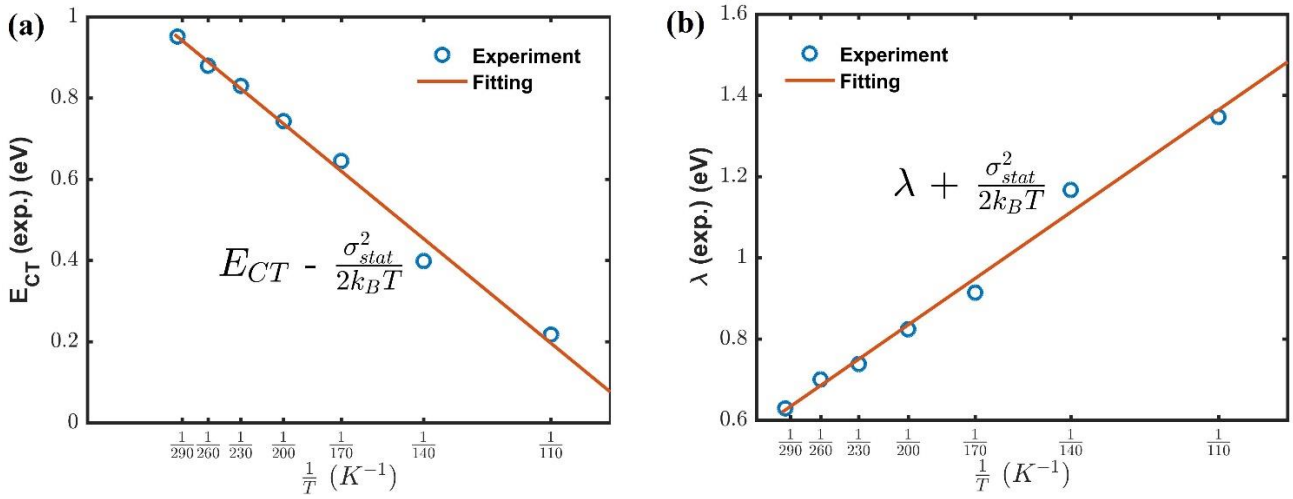

Figure 4.15: Effective a) lowest-energy CT state ($E_{CT(exp.)}$) and b) reorganization ($\lambda_{(exp.)}$) energies extracted from Figure 4.7a. Fitting straight lines (in red) to the experimental data (blue circles) reveal peak of the CT energetic distribution (E_{CT}) at 1.40 eV and reorganization energy (λ) of 0.19 eV. The lowest-energy CT absorption peak ($E_{CT} + \lambda$) is at ~1.59 eV. The standard deviation of the CT energetic distribution (σ_{stat}) is 150 meV, from both a) and b).

Table 4.6: Static (σ_{stat}) and dynamic (σ_{dyn}) disorder contribution to the total CT EQE spectral broadening (σ_{tot}). Static disorder contribution to the total linewidth (D_{stat}) is dominant at all temperatures in a NPB:HAT-CN BHJ solar cell with 66.0% of HAT-CN.

Temperature, T (K)	σ_{stat} (meV)	$\sigma_{dyn} = \sqrt{2k_B\lambda T}$ (meV)	$\sigma_{tot} = \sqrt{{\sigma_{stat}}^2 + {\sigma_{dyn}}^2}$ (meV)	$D_{stat}(T) = \frac{\sigma_{stat}^2}{\sigma_{tot}^2}$ (%)
110	150	60	162	85.73
140	150	67	164	83.66
170	150	74	167	80.68
200	150	80	170	77.85
230	150	86	173	75.18
260	150	92	176	72.64
296	150	98	179	70.22

The Role of Molecular Quadrupole Moments in Doped Organic Semiconductors

In this Chapter, we investigate the role of local environmental interactions on the generation of free charge carriers in doped organic layers. By means of a classical ME model, a dual effect of molecular quadrupole moments of host and dopant molecules on doping is demonstrated in doped binary (ZnPc:F6-TCNNQ and F_8ZnPc:F6-TCNNQ) and ternary (ZnPc:F_8ZnPc:F6-TCNNQ) blend (see molecular structures in Figure 5.1). Based on an in-depth atomistic modelling of electrostatic and dielectric phenomena in molecular solids, we show that charge-quadrupole interactions affect both the ionization step (by reshuffling the energy levels of the dopant and the host) and the charge dissociation step (by creating a favourable energy pathway for the hole). Interestingly, in addition to long-range electrostatics characterizing the energy landscape of ordered molecular films, we observe that the substitution of a host molecule with F6-TCNNQ has a significant short-range effect, namely the ionization potential (IP) of the host molecules next to a dopant impurity strongly differ (up to 0.4 eV) from the IPs of the host molecules further away. This electrostatic contribution is due to the difference in quadrupole moment between F6-TCNNQ and the host molecules, and it significantly affects the host-dopant gap $\Gamma_{hd} = IP_{host} - EA_{dop}$, which, on average, amounts to 0.63 eV for ZnPc and 0.86 eV for F_8ZnPc. When accounting for screened electron-hole (e-h) Coulomb interactions (V_{eh}~ 0.65 eV for all samples), we find an overall energy barrier that is close to zero for the ionization step in a binary ZnPc:F6-TCNNQ blend, while in F_8ZnPc:F6-TCNNQ this barrier is 0.2 eV larger. Most interestingly, the explicit calculation of the energy profile for charge separation reveals that the quadrupole moments of dopant impurities can positively impact this crucial step.

The work presented in this Chapter is published in A. Privitera, G. Londi, M. K. Riede, G. D'Avino, D. Beljonne. Molecular quadrupole moments promote ground-state charge generation in doped organic semiconductors *Adv. Funct. Mater.* **2020**, 30, 2004600.

5.1. Introduction

Charge generation in doped organic semiconductors consists of two elementary steps.[1–3] The first step involves either a hybridization of the host-dopant frontier molecular orbitals or a ground state integer charge-transfer (CT) process between the host and the dopant.[4–6] For p-type doping, the latter is favoured when the energy difference between the IP of the host and the EA of the dopant (*i.e.*, the host-dopant gap Γ_{hd}) is smaller in magnitude than the Coulomb binding energy (V_{eh}) between an electron and its geminate hole sitting on nearest neighbour molecules.[7] In such conditions, a bound CT state with an electron added to the dopant and a hole left on the host molecule is generated.[8,9] This is the ionization step. The second step, namely the charge dissociation, then consists of the spatial migration of the hole (for p-doping) away from the ionized acceptor that requires overcoming the Coulomb binding of the CT pair, which usually amounts to several hundreds of meV.[3,10] The energetic and kinetic aspects of both steps need to be concomitantly optimized in order to maximize the overall charge generation efficiency, which calls for a control of the interactions between the molecules at the microscopic level. Tuning these microscopic interactions can be achieved by molecular and material engineering. For instance, the energy levels in an organic semiconductor and the Fermi energy can be simultaneously tuned by taking advantage of molecular quadrupolar interactions.[11] This result was achieved by co-evaporating a host mixture between zinc-phthalocyanine (ZnPc) and its eight-times fluorinated counterpart (F_8ZnPc) together with the p-type dopant F6-TCNNQ. Such mixtures are very interesting because they provide an effective and practical approach to finely control the p-doping efficiency of F6-TCNNQ upon tuning the host energy levels, as a function of the ZnPc:F_8ZnPc molar ratio.[11–13]

5.2. Theoretical Methodology

Gas-phase ground state geometry optimizations were carried out at the DFT level with the GAUSSIAN16[14] suite, using the PBE0 functional and the cc-pVTZ basis set. The point group symmetry (D_{4h} for ZnPc and F_8ZnPc, and C_{2h} for F6-TCNNQ) was retained during the optimizations. Gas-phase *GW* calculations were performed starting from Kohn-Sham eigenstates calculated for the optimized molecular structures with the ORCA package.[15] A partial self-consistent scheme on the eigenvalues (ev*GW*) was used, along with the cc-pVXZ basis set (where X = D, T). Then, quasiparticle energy levels were extrapolated to the complete basis set (CBS) limit.[16] The universal Weigend Coulomb fitting set of functions was used as auxiliary basis in the resolution of identity (RI-V) approach. ev*GW* calculations were performed with the Fiesta package.[8]

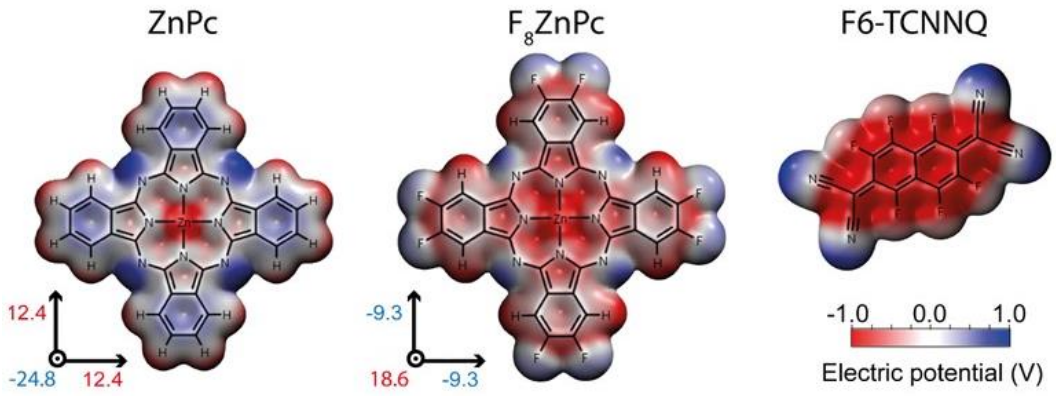

Figure 5.1: Molecular structures and electrostatic properties (electric potential color maps and molecular quadrupole components expressed in Debye-Å) of ZnPc, F_8ZnPc and F6-TCNNQ, as obtained from DFT calculations at the PBE0/cc-pVTZ level of theory (see Table 5.4 in Additional data).

ME calculations were parametrized with ESP atomic charges and polarizability tensor calculated with DFT at the PBE0/cc-pVTZ level of theory. ESP charges were computed for all the neutral species, for the positively charged ZnPc and F_8ZnPc and for the negatively charged F6-TCNNQ. The polarizability of charged species was set equal to that of neutral ones. The ME scheme, implemented in the MESCal code,[17] relies on a point-charge description of the molecular charge distributions and on polarizability tensor distributed at atomic sites. The solid-state charge carrier transport levels were calculated as:

$$IP = IP_g + \Delta^h \tag{5.1}$$

$$EA = EA_g - \Delta^e \tag{5.2}$$

in which environmental effects entail an induction and an electrostatic contribution:

$$\Delta^x = \Delta_I^x + \Delta_E^x \tag{5.3}$$

where *x* labels the charged excitation (electron or hole). The induction Δ_I^x term describes the dynamical response of the surrounding dielectric medium to the presence of a charge carrier. The electrostatic Δ_E^x term corresponds to the energy to charge a molecule in the electric field of all other molecules in the neutral crystal.[18]

CT states with localized charges are modelled as classical e-h pairs. The binding energy V_{eh} of ion pairs is computed as the sum of screened Coulomb interactions between a hole residing on a host molecule (ZnPc or a F_8ZnPc) and an electron on the F6-TCNNQ dopant:

$$V_{eh} = \frac{1}{\varepsilon_r} \sum_{i,j} \frac{\delta q_i^e \delta q_j^h}{r_{ij}} \tag{5.4}$$

where $\varepsilon_r = 3.2$ is the computed dielectric constant of the medium, δq_i^e (δq_j^h) is the difference between the atomic charge of the anion (cation) compared to the neutral molecule and r_{ij} is the interatomic distance.

The structural relaxation energies $\lambda^{\pm}$ upon charging were computed at the DFT level (PBE0/cc-pVTZ) by comparing the vertical and the adiabatic IP of the hosts and EA and of the dopant. In F6-TCNNQ the dihedral angles involving the dicyanovinyl groups were kept frozen during the optimizations, in order to get rid of low-frequency contributions to $\lambda = \lambda^+ + \lambda^-$. Specifically, $\lambda^+ = 20\ meV$ for ZnPc, $\lambda^+ = 37\ meV$ for F_8ZnPc and $\lambda^- = 131 meV$ for F6-TCNNQ.

Molecular stacks were built following the recipe described in Ref.[13], starting from the crystallographic structure of CuPc,[19] replacing the Cu atoms with Zn ones and replicating the unit cell along the 3 directions. All the ME calculations were carried out by employing a 5x17x3 stack with 300 Å in-place cut-off which ensures the convergence of the Δ_E^x term. On the other hand, induction energies Δ_I^x were calculated for spherical clusters of increasing radii extracted from the bulk structure and centered at the molecule of interest and extrapolated for an infinite system.

5.3. Results and Discussion

5.3.1. Binary Blends

Initially, we calculated the gas-phase IP and EA of the host (ZnPc and F_8ZnPc) and p-dopant (F6-TCNNQ) molecules at the ev*GW* level. The obtained values, reported in Figure 5.2, indicate an increase in both the molecular IP and EA by ~0.5 eV upon fluorination, as a result of the strong, inductive, electron-withdrawing effects induced by the fluorine atoms.[20] The huge energy difference in the gas-phase between the EA of F6-TCNNQ (4.44 eV) and the IP of the host (6.41 eV for ZnPc and 6.91 eV for F_8ZnPc) would completely impede ground state CT.

The situation changes dramatically when accounting for environmental solid-state effects on the energy levels of both the host and dopant molecules.[16,21] In molecular solids, the IP and EA values depend strongly on collective, long-range, electrostatic effects associated with the varying charge density distributions in the neutral and ionized molecules. These include induction effects, describing the dielectric screening of the polarizable medium to an excess charge, and electrostatic interactions, brought about by the molecular electrical multipole moments. In our case, electrostatic interactions are led by the quadrupole term, since the molecules of interest are centrosymmetric and have no dipole moment.[13] We considered the case of a F6-TCNNQ dopant as a single substitutional impurity in two pristine lattices, the first made of ZnPc molecules and the second of F_8ZnPc ones. We specifically studied films (2D slab calculations) of the two compounds, composed of molecular stacks whose axes lie in the film plane, leading to an edge-on molecular orientation with respect to the slab normal, as represented in Figure 5.3. This molecular orientation was proposed from previous grazing-incidence wide-angle X-ray scattering (GIWAXS) analysis and is in line with literature studies.[2,11,13]

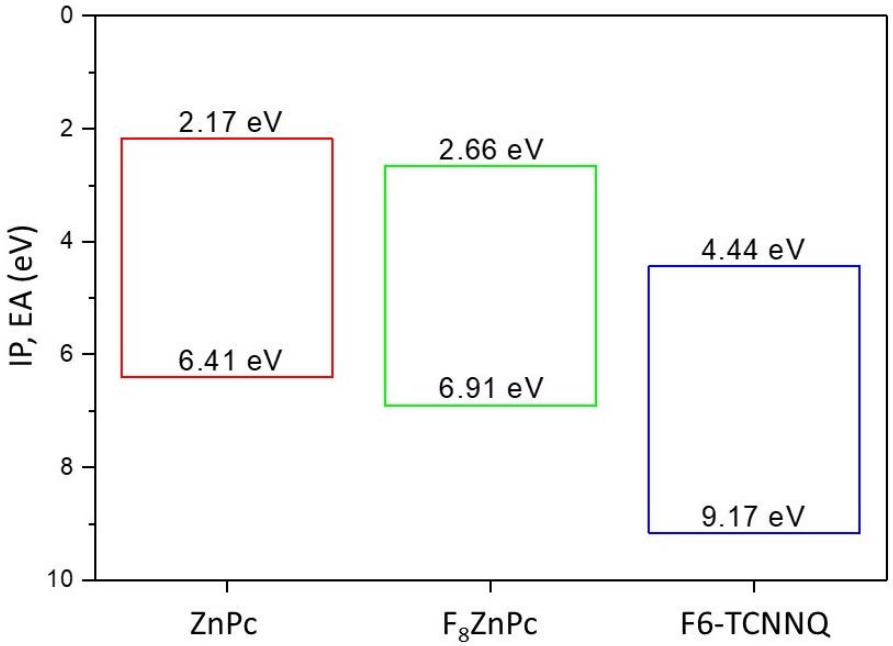

Figure 5.2: IP and EA of the hosts (ZnPc and F_8ZnPc) and the dopant (F6-TCNNQ) molecules. IPs and EAs were obtained from gas-phase ev*GW* calculations extrapolated in the CBS limit.

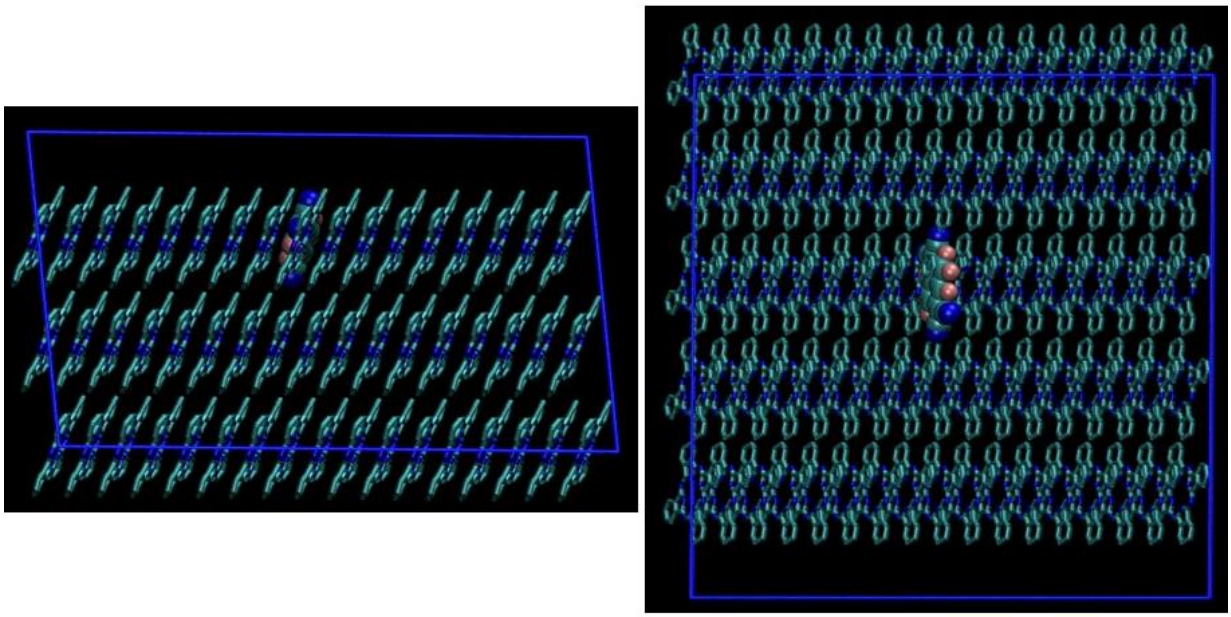

Figure 5.3: Two illustrations (side view on the left, top view on the right) of the molecular stack used for ME calculations carried out using MESCal The stack is composed by 5x17x3 ZnPc molecules in an edge-on orientation, where the central ZnPc molecule of the topmost layer is substituted with a F6-TCNNQ acceptor. Hydrogen atoms are omitted for clarity. A similar stack was used for all the simulations at different ZnPc:F_8ZnPc ratios.

ME calculations reveal large environmental effects on charge energetics, as shown in Figure 5.4a and 5.4b and reported on Table 5.1. In line with earlier findings, we notice that induction interactions reduce the host-dopant gap by ~2 eV irrespective on the host material, as a result of the similar dielectric susceptibilities of organic solids. On top of induction, the electrostatic contribution further affects the energy levels with an amplitude and sign that depend on the host material. Namely, these interactions are determined by the component of the traceless quadrupolar tensor perpendicular to the molecular plane, which is negative in ZnPc and positive in F_8ZnPc because of the inverted polarity of C-F versus C-H bonds. In Figure 5.4a and 5.4b, we distinguish between the IP of a host molecule in the pristine host material (open circle) and a host molecule next to the dopant along the π stacking axis (full circle), which is the most important direction for both charge motion and electrostatic interactions. We notice that the sign of the electrostatic shifts of the energy levels of both the dopant (EA, blue triangle) and of its neighbouring host molecule (IP, full circle) is the same as the pristine host (IP, open circle). Electrostatic shifts are negative in the ZnPc host (Figure 5.4a) and positive in F_8ZnPc (Figure 5.4b). This determines a 1 eV difference in the EA of the F6-TCNNQ depending on the host material, in line with recent findings by some of us.[16] Interestingly, we also observe that the levels of host molecules strongly depend on their position with respect to the dopant, being the IP of the molecule near the dopant significantly different (0.3-0.4 eV) from that of a host molecule in the pristine host or at infinite distance from the dopant. The position dependence of the host levels can be ascribed to the quadrupolar interaction with the dopant, characterized by an electrostatic layout that is markedly different from that of the replaced host molecule. As it originates from the quadrupole of the single dopant molecule, this effect is rather short-ranged and has an appreciable impact only on the nearest-neighbour molecules.

Table 5.1: Tabulated values (in eV) of the IPs of ZnPc and F_8ZnPc, respectively, and the EA of F6-TCNNQ for the pristine ZnPc and F_8ZnPc films, and for the ZnPc:F6-TCNNQ and F_8ZnPc:F6-TCNNQ binary blends.

	$\boldsymbol{IP_g}$(host)	Δ_I^h	Δ_E^h	$\boldsymbol{IP}$(host)	$\boldsymbol{EA_g}$(dop)	Δ_I^e	Δ_E^e	$\boldsymbol{EA}$(dop)
Pristine ZnPc	6.41	-0.99	-0.47	4.95	2.17	-1.01	0.46	2.72
Pristine F_8ZnPc	6.91	-1.00	0.36	6.27	2.66	-1.02	-0.36	4.04
ZnPc: F6-TCNNQ	6.41	-0.95	-0.09	5.37	4.44	-1.20	0.96	4.68
F_8ZnPc: F6-TCNNQ	6.91	-0.95	0.62	6.58	4.44	-1.20	-0.1	5.74

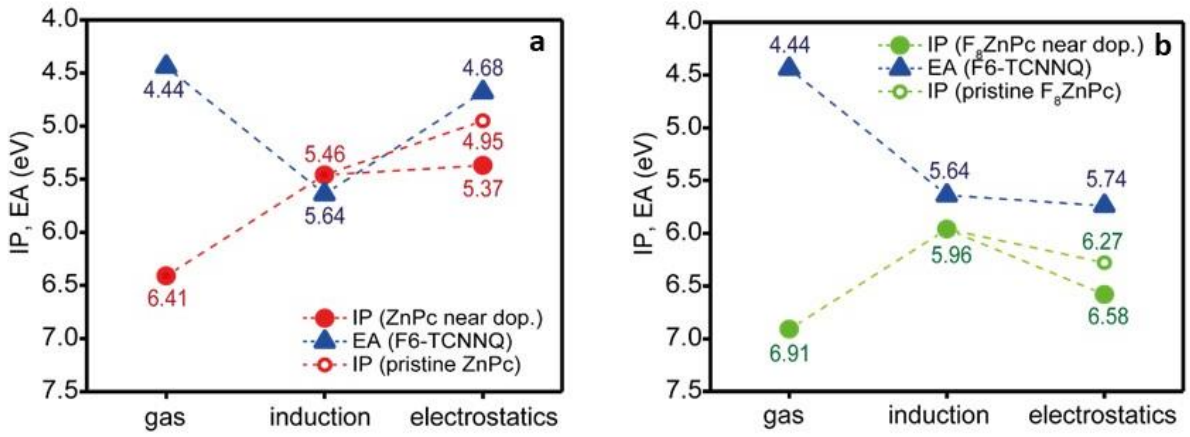

Figure 5.4: Effect of induction and electrostatic interactions on the transport energy levels of the dopant (blue triangles) and the host molecules, either next to the dopant (full circle) or in the pristine film (open circle). Specifically, a) binary blend composed of ZnPc (host, red dots) and F6-TCNNQ (dopant, blue triangles) and b) binary blend composed of F_8ZnPc (host, green dots) and F6-TCNNQ (dopant, blue triangles). Energy levels are referred to a common vacuum level.

5.3.2. Ternary Blends

We now turn the attention to the energy levels of ternary blends composed by a mixed ZnPc:F_8ZnPc host, doped with a F6-TCNNQ molecule. ME calculations were carried out for different host mixing ratios, ranging from pure ZnPc to pure F_8ZnPc. For the 1:1 ratio, we opted for an alternating ZnPc:F_8ZnPc mixed-stack motif, which is expected to be the most stable structure for π-stacked molecules with opposite quadrupoles. A similar alternating packing was recently resolved for a 1:1 co-crystal of pentacene and perfluoropentacene.[18] Crystalline supercells of blends with different ratio were created in a similar way but with a different alternating periodicity (one ZnPc molecule every two F_8ZnPc molecules, and vice versa). Calculations for the energy levels in undoped ZnPc:F_8ZnPc blends of different composition (see Figure 5.7 and Table 5.5 in Additional data) are in substantial agreement with the similar ones reported by Schwarze e*t al.*.[13]

The energy levels of host and dopant molecules in ternary blends are shown in Figure 5.5a. Since different microscopic configurations can be generated upon introducing a dopant in the ZnPc:F_8ZnPc blends (for the 1:1 ratio, the dopant can be placed both at ZnPc and F_8ZnPc site; more configurations are possible for other host compositions), the figure displays the average over the possible microstructures (for specific values see Figure 5.8 in Additional data). Calculations in Figure 5.5a show that the energy levels of host molecules and dopant evolve linearly with the ZnPc molar ratio, as all the molecules probe an effective quadrupolar field resulting from the additive contributions sourced by the two host molecules. Most importantly, this translates into a host-dopant gap Γ_{hd} that does not significantly vary with the host mixing ratio, leading to the conclusion that replacing a

significant fraction of ZnPc molecules by electron-poor F_8ZnPc should not be overly detrimental to ionization, at least from an energetic point of view.

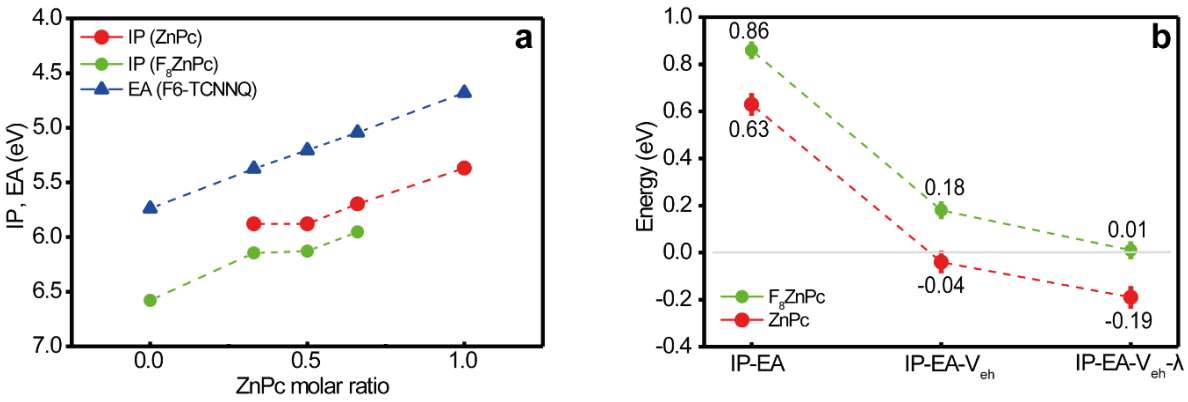

Figure 5.5: a) Effect of the solid-state interactions on the IPs of ZnPc (red circles) and F_8ZnPc (green circles) and the EA of F6-TCNNQ (blue triangles) in ZnPc:F_8ZnPc blends doped with F6-TCNNQ as a function of ZnPc molar ratio. The data correspond to averages over different microscopic hosts-dopant configurations. b) Energies of the CT state where the electron is localized on the F6-TCNNQ and the hole either on the nearest-neighbour ZnPc or F_8ZnPc. The CT energy was calculated by considering different contributions, namely (1) the Γ_{hd} energy difference, (2) the e-h Coulomb interaction (V_{eh}), and (3) the relaxation energy of the CT state (λ).

On average, when accounting for the whole range of host chemical composition, Γ_{hd} ranges from 0.63 eV for ZnPc to 0.86 eV in F_8ZnPc. This energy difference is largely compensated by the screened e-h Coulomb binding energy V_{eh} (~0.65 eV), making the overall ionization process barrier-free for ZnPc, while still significantly activated (energy barrier ~0.2 eV) for F_8ZnPc. This is in good agreement with the high ionization efficiency experimentally measured in the ZnPc:F6-TCNNQ blends.[11] Conversely, the energy to ionize the dopant in the F_8ZnPc host remains positive and larger than the thermal energy, which points to a low ionization efficiency, in line with previous experimental results.[11] In addition to V_{eh}, we considered the role played by structural reorganization upon charging, quantified by $\lambda = \lambda^+ + \lambda^- = 0.15\,eV$, being λ^+ and λ^- the hole and electron reorganization energies of host and dopant, respectively. This contribution, which we computed in gas-phase, represents an upper estimate of the relaxation energy in the solid-state where molecular geometries are constrained. Structural reorganization further stabilizes the CT state, hence making the ionization step energetically more favourable. When accounting for this contribution in full (the geometric relaxation might be partly hindered by steric constraints in condensed phase), the ionization remains considerably more favourable (by ~200 meV) in ZnPc compared to F_8ZnPc. Considering the typical error bar (~100 meV) on the calculated energies and other approximations used in the model (*i.e.*, the neglect of dynamic disorder), a limited electron transfer between the tail states of the dopant

and F_8ZnPc molecules cannot be excluded from simulations, as it could not be ruled out on the basis of previous electron paramagnetic resonance (EPR) data.[11]

5.3.3. Charge Separation

Moving on further, we discuss the results of ME calculations explicitly targeting the e-h separation energy profile along the π stacking direction. Figure 5.6 and Table 5.3 report the energies of the CT states and the Coulomb binding energies V_{eh} as a function of the hole distance from the F6-TCNNQ anion for the ZnPc:F6-TCNNQ and F_8ZnPc:F6-TCNNQ binary blends and for ternary blends with 1:1 ZnPc:F_8ZnPc composition, distinguishing the two cases where the dopant sits at the molecular site of ZnPc or F_8ZnPc.

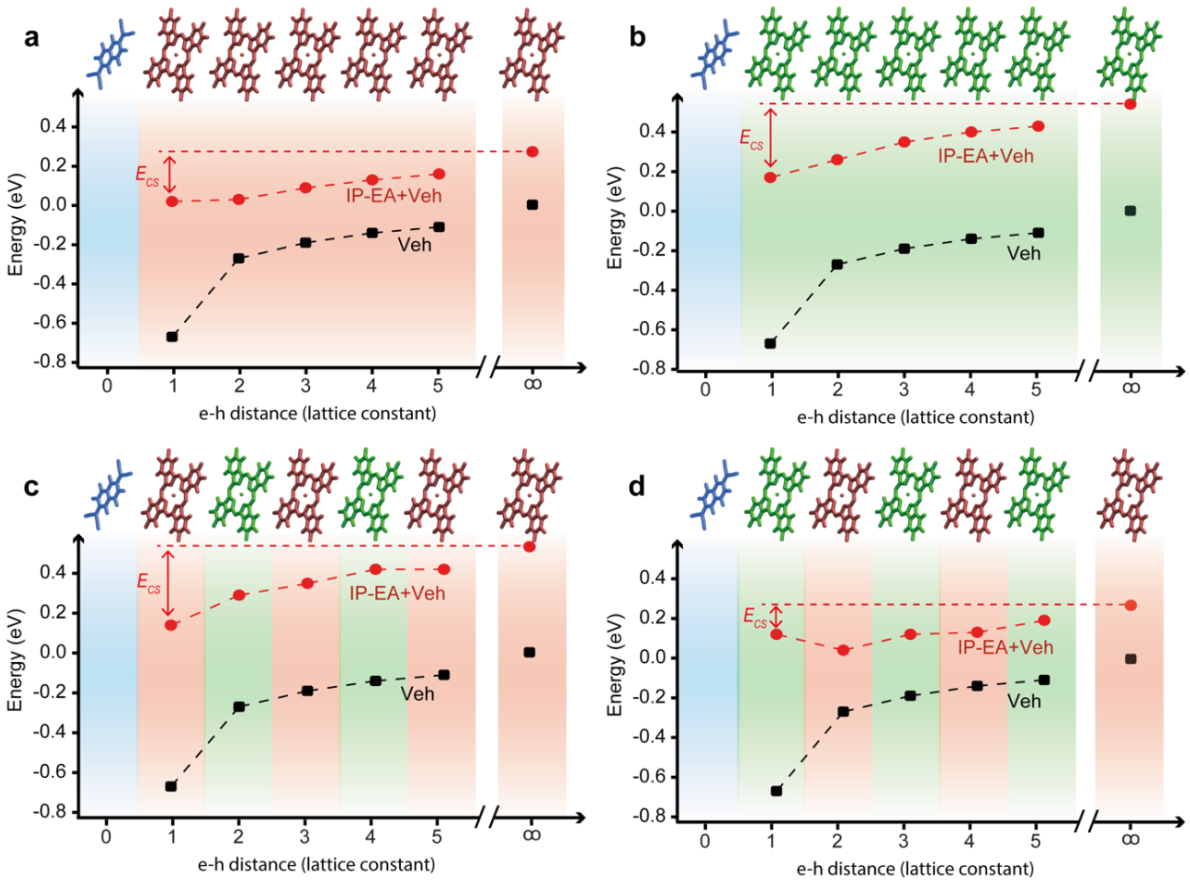

Figure 5.6: Energies of CT states (red dots), with the electron localized on the F6-TCNNQ and the hole on host molecules, as a function of the e-h distance along the π stacking direction. The screened Coulomb binding energies, $V_{eh}(r_{eh})$ (black squares) and the energy barrier for charge separation (E_{cs}) are also shown. The calculations are reported for a) ZnPc:F6-TCNNQ, b) F_8ZnPc:F6-TCNNQ binary blends, c) and d) two 1:1 configurations of ZnPc:F_8ZnPc:F6-TCNNQ ternary blends.

Remarkably, these calculations highlight that the energy barrier for charge separation (E_{cs}) of the CT state is significantly lower than the mere Coulomb binding energy V_{eh} ~ 0.65 eV (compare red and black lines in Figure 5.6). This is essentially due to the effect of the quadrupolar field of the F6-TCNNQ dopant, that destabilizes CT states with charges localized on neighbouring molecules (see also Figure 5.9 and Table 5.6 in Additional data). The magnitude of this effect depends however on the host composition and on the dopant location, with E_{cs} ranging from 0.37 eV in F_8ZnPc (Figure 5.6b), down to 0.15 eV in the ZnPc:F_8ZnPc blend when the impurity substitutes a ZnPc molecule (Figure 5.6d). In the latter case, and similarly in ZnPc:F6-TCNNQ (Figure 5.6a), the energy profile for charge separation is rather flat, rationalizing the possibility for a thermally-activated charge separation observed for these two systems. This energy level bending effect sourced by intermolecular electrostatic interactions, similar to those previously reported in the context of photoinduced charge separation at donor:acceptor interfaces,[22–25] provide a decisive contributions to holes to escape the Coulomb well of their parent dopant.

Table 5.3: Tabulated values (in eV) of Γ_{hd}, V_{eh} and CT state energies as a function of the distance from the F6-TCNNQ molecule along the z-direction. The CT state energy was calculated by considering different contributions, namely (1) the Γ_{hd} energy difference, (2) the e-h Coulomb interaction (V_{eh}). The studied configurations are the same as reported in Figure 5.6.

		1	**2**	**3**	**4**	**5**
ZnPc binary blend	$\mathbf{\Gamma_{hd}}$	0.69	0.30	0.28	0.27	0.27
	$\mathbf{V_{eh}}$	-0.67	-0.27	-0.19	-0.14	-0.11
	$\boldsymbol{E_{CT}}$	0.02	0.03	0.09	0.13	0.16
F_8ZnPc binary blend	$\mathbf{\Gamma_{hd}}$	0.84	0.53	0.54	0.54	0.54
	$\mathbf{V_{eh}}$	-0.67	-0.27	-0.19	-0.14	-0.11
	$\boldsymbol{E_{CT}}$	0.17	0.26	0.35	0.40	0.43
1:1 ternary blend (conf 1)	$\mathbf{\Gamma_{hd}}$	0.81	0.56	0.54	0.56	0.53
	$\mathbf{V_{eh}}$	-0.67	-0.27	-0.19	-0.14	-0.11
	$\boldsymbol{E_{CT}}$	0.14	0.29	0.35	0.42	0.42
1:1 ternary blend (conf 2)	$\mathbf{\Gamma_{hd}}$	0.79	0.31	0.31	0.27	0.30
	$\mathbf{V_{eh}}$	-0.67	-0.27	-0.19	-0.14	-0.11
	$\boldsymbol{E_{CT}}$	0.12	0.04	0.12	0.13	0.19

5.4. Conclusions

This work delved into the effect of the environmental solid-state interactions on the generation of free charge carriers by doping organic semiconductors. We carried out these investigations on a model system comprising ZnPc:F_8ZnPc blends, as a host, p-doped with F6-TCNNQ. This ternary blend allowed to control doping efficiency by simply varying the ZnPc molar ratio.[11] The theoretical work disclosed the fundamental role of charge-quadrupolar interactions emerging at different length scales on both (1) the ionization and (2) the charge dissociation steps of molecular doping. Namely, the presence of a substitutional F6-TCNNQ molecule in the host lattice strongly influence the IP of the nearest-neighbour molecules without significantly affecting those further apart, ultimately controlling both steps of the doping process. As for the ionization step, this short-range electrostatic contribution significantly increases (up to 0.4 eV) the host-dopant gap. After considering the e-h Coulomb interaction, the energy barrier for the formation of a bound CT state between nearest-neighbour molecules becomes close to zero for ZnPc:F6-TCNNQ and is ~0.2 eV larger for F_8ZnPc:F6-TCNNQ, in line with the larger ionization efficiency measured in the former blend. The charge dissociation step is expected to be very inefficient on the sole consideration of the Coulomb binding energy of the generated holes to their ionized acceptors, with V_{eh} as large as ~0.65 eV. Remarkably, however, this is largely alleviated by the short-range perturbation of the quadrupole moment of the dopant impurity that, destabilizing CT states between nearest-neighbour molecules, results in a more favourable energy landscape for charge dissociation, with residual effective energy barriers in the range 0.15-0.37 eV depending on the host composition and local micro-structural configuration.

References

(1) Tietze, M. L.; Pahner, P.; Schmidt, K.; Leo, K.; Lüssem, B. Doped Organic Semiconductors: Trap-Filling, Impurity Saturation, and Reserve Regimes. *Adv. Funct. Mater.* **2015**, *25* (18), 2701–2707.

(2) Tietze, M. L.; Benduhn, J.; Pahner, P.; Nell, B.; Schwarze, M.; Kleemann, H.; Krammer, M.; Zojer, K.; Vandewal, K.; Leo, K. Elementary Steps in Electrical Doping of Organic Semiconductors. *Nat. Commun.* **2018**, *9* (1), 1182.

(3) Schwarze, M.; Gaul, C.; Scholz, R.; Bussolotti, F.; Hofacker, A.; Schellhammer, K. S.; Nell, B.; Naab, B. D.; Bao, Z.; Spoltore, D.; Vandewal, K.; Widmer, J.; Kera, S.; Ueno, N.; Ortmann, F.; Leo, K. Molecular Parameters Responsible for Thermally Activated Transport in Doped Organic Semiconductors. *Nat. Mater.* **2019**, *18* (3), 242–248.

(4) Salzmann, I.; Heimel, G.; Duhm, S.; Oehzelt, M.; Pingel, P.; George, B. M.; Schnegg, A.; Lips, K.; Blum, R.-P.; Vollmer, A.; Koch, N. Intermolecular Hybridization Governs Molecular Electrical Doping. *Phys. Rev. Lett.* **2012**, *108* (3), 35502.

(5) Méndez, H.; Heimel, G.; Winkler, S.; Frisch, J.; Opitz, A.; Sauer, K.; Wegner, B.; Oehzelt, M.; Röthel, C.; Duhm, S.; Többens, D.; Koch, N.; Salzmann, I. Charge-Transfer Crystallites as Molecular Electrical Dopants. *Nat. Commun.* **2015**, *6* (1), 8560.

(6) Salzmann, I.; Heimel, G.; Oehzelt, M.; Winkler, S.; Koch, N. Molecular Electrical Doping of Organic Semiconductors: Fundamental Mechanisms and Emerging Dopant Design Rules. *Acc. Chem. Res.* **2016**, *49* (3), 370–378.

(7) Li, J.; D'Avino, G.; Pershin, A.; Jacquemin, D.; Duchemin, I.; Beljonne, D.; Blase, X. Correlated Electron-Hole Mechanism for Molecular Doping in Organic Semiconductors. *Phys. Rev. Mater.* **2017**, *1* (2), 1–9.

(8) Blase, X.; Attaccalite, C.; Olevano, V. First-Principles GW Calculations for Fullerenes, Porphyrins, Phtalocyanine, and Other Molecules of Interest for Organic Photovoltaic Applications. *Phys. Rev. B* **2011**, *83* (11), 115103.

(9) da Silva Filho, D. A.; Coropceanu, V.; Gruhn, N. E.; de Oliveira Neto, P. H.; Brédas, J.-L. Intramolecular Reorganization Energy in Zinc Phthalocyanine and Its Fluorinated Derivatives: A Joint Experimental and Theoretical Study. *Chem. Commun.* **2013**, *49* (54), 6069–6071.

(10) Kim, J.-M.; Yoo, S.-J.; Moon, C.-K.; Sim, B.; Lee, J.-H.; Lim, H.; Kim, J. W.; Kim, J.-J. N-Type Molecular Doping in Organic Semiconductors: Formation and Dissociation Efficiencies of a Charge Transfer Complex. *J. Phys. Chem. C* **2016**, *120* (17), 9475–9481.

(11) Warren, R.; Privitera, A.; Kaienburg, P.; Lauritzen, A. E.; Thimm, O.; Nelson, J.; Riede, M. K. Controlling Energy Levels and Fermi Level En Route to Fully Tailored Energetics in

Organic Semiconductors. *Nat. Commun.* **2019**, *10* (1), 5538.

(12) Warren, P. R.; Hardigree, J. F. M.; Lauritzen, A. E.; Nelson, J.; Riede, M. Tuning the Ambipolar Behaviour of Organic Field Effect Transistors via Band Engineering. *AIP Adv.* **2019**, *9* (3), 35202.

(13) Schwarze, M.; Tress, W.; Beyer, B.; Gao, F.; Scholz, R.; Poelking, C.; Ortstein, K.; Günther, A. A.; Kasemann, D.; Andrienko, D.; Leo, K. Band Structure Engineering in Organic Semiconductors. *Science* **2016**, *352* (6292), 1446–1449.

(14) Frisch, M. J.; Trucks, G. W.; Schlegel, H. B.; Scuseria, G. E.; Robb, M. A.; Cheeseman, J. R.; Scalmani, G.; Barone, V.; Petersson, G. A.; Nakatsuji, H.; Li, X.; Caricato, M.; Marenich, A. V; Bloino, J.; Janesko, B. G.; Gomperts, R.; Mennucci, B.; Hratchian, H. P.; Ortiz, J. V; Izmaylov, A. F.; Sonnenberg, J. L.; Williams-Young, D.; Ding, F.; Lipparini, F.; Egidi, F.; Goings, J.; Peng, B.; Petrone, A.; Henderson, T.; Ranasinghe, D.; Zakrzewski, V. G.; Gao, J.; Rega, N.; Zheng, G.; Liang, W.; Hada, M.; Ehara, M.; Toyota, K.; Fukuda, R.; Hasegawa, J.; Ishida, M.; Nakajima, T.; Honda, Y.; Kitao, O.; Nakai, H.; Vreven, T.; Throssell, K.; Montgomery Jr., J. A.; Peralta, J. E.; Ogliaro, F.; Bearpark, M. J.; Heyd, J. J.; Brothers, E. N.; Kudin, K. N.; Staroverov, V. N.; Keith, T. A.; Kobayashi, R.; Normand, J.; Raghavachari, K.; Rendell, A. P.; Burant, J. C.; Iyengar, S. S.; Tomasi, J.; Cossi, M.; Millam, J. M.; Klene, M.; Adamo, C.; Cammi, R.; Ochterski, J. W.; Martin, R. L.; Morokuma, K.; Farkas, O.; Foresman, J. B.; Fox, D. J. Gaussian 16 Revision C.01. 2016.

(15) Neese, F. Software Update: The ORCA Program System, Version 4.0. *WIREs Comput. Mol. Sci.* **2018**, *8* (1).

(16) Li, J.; Duchemin, I.; Roscioni, O. M.; Friederich, P.; Anderson, M.; Da Como, E.; Kociok-Köhn, G.; Wenzel, W.; Zannoni, C.; Beljonne, D.; Blase, X.; D'Avino, G. Host Dependence of the Electron Affinity of Molecular Dopants. *Mater. Horizons* **2019**, *6* (1), 107–114.

(17) D'Avino, G.; Muccioli, L.; Zannoni, C.; Beljonne, D.; Soos, Z. G.; D'Avino, G.; Muccioli, L.; Zannoni, C.; Beljonne, D.; Soos, Z. G.; D'Avino, G.; Muccioli, L.; Zannoni, C.; Beljonne, D.; Soos, Z. G. Electronic Polarization in Organic Crystals: A Comparative Study of Induced Dipoles and Intramolecular Charge Redistribution Schemes. *J. Chem. Theory Comput.* **2014**, *10* (11), 4959–4971.

(18) D'Avino, G.; Duhm, S.; Della Valle, R. G.; Heimel, G.; Oehzelt, M.; Kera, S.; Ueno, N.; Beljonne, D.; Salzmann, I. Electrostatic Interactions Shape Molecular Organization and Electronic Structure of Organic Semiconductor Blends. *Chem. Mater.* **2020**, *32* (3), 1261–1271.

(19) Hoshino, A.; Takenaka, Y.; Miyaji, H. Redetermination of the Crystal Structure of α-Copper Phthalocyanine Grown on KCl. *Acta Crystallogr. Sect. B Struct. Sci.* **2003**, *59* (3), 393–403.

(20) Brendel, M.; Krause, S.; Steindamm, A.; Topczak, A. K.; Sundarraj, S.; Erk, P.; Höhla, S.;

Fruehauf, N.; Koch, N.; Pflaum, J. The Effect of Gradual Fluorination on the Properties of FnZnPc Thin Films and FnZnPc/C60 Bilayer Photovoltaic Cells. *Adv. Funct. Mater.* **2015**, *25* (10), 1565–1573.

(21) D'Avino, G.; Muccioli, L.; Castet, F.; Poelking, C.; Andrienko, D.; Soos, Z. G.; Cornil, J.; Beljonne, D. Electrostatic Phenomena in Organic Semiconductors: Fundamentals and Implications for Photovoltaics. *J. Phys. Condens. Matter* **2016**, *28* (43).

(22) Castet, F.; D'Avino, G.; Muccioli, L.; Cornil, J.; Beljonne, D.; D'Avino, G.; Muccioli, L.; Cornil, J.; Beljonne, D. Charge Separation Energetics at Organic Heterojunctions: On the Role of Structural and Electrostatic Disorder. *Phys. Chem. Chem. Phys.* **2014**, *16* (38), 20279–20290.

(23) D'Avino, G.; Mothy, S.; Muccioli, L.; Zannoni, C.; Wang, L.; Cornil, J.; Beljonne, D.; Castet, F. Energetics of Electron-Hole Separation at P3HT/PCBM Heterojunctions. *J. Phys. Chem. C* **2013**, *117* (25), 12981–12990.

(24) Athanasopoulos, S.; Tscheuschner, S.; Bässler, H.; Köhler, A. Efficient Charge Separation of Cold Charge-Transfer States in Organic Solar Cells Through Incoherent Hopping. *J. Phys. Chem. Lett.* **2017**, *8* (9), 2093–2098.

(25) Idé, J.; Méreau, R.; Ducasse, L.; Castet, F.; Bock, H.; Olivier, Y.; Cornil, J.; Beljonne, D.; D'Avino, G.; Roscioni, O. M.; Muccioli, L.; Zannoni, C. Charge Dissociation at Interfaces between Discotic Liquid Crystals: The Surprising Role of Column Mismatch. *J. Am. Chem. Soc.* **2014**, *136* (7), 2911–2920.

Additional data

Molecular quadrupole moments are defined as:

$$Q_{ij} = \int \rho(\boldsymbol{r}) \left(r_i r_j - \frac{1}{3} |\boldsymbol{r}|^2 \delta_{ij} \right) d^3\boldsymbol{r} \tag{5.5}$$

where *i* and *j* label Cartesian components and $\rho(\boldsymbol{r})$ is the molecular charge density, including nuclei.

Table 5.4: Principal components of the traceless quadrupole tensors (in Debye·Å) of ZnPc, F_8ZnPc and F6-TCNNQ molecules, obtained from DFT calculations at the PBE0/cc-pVTZ level of theory. Q_1 and Q_2 are the components in the molecular plane, Q_3 is perpendicular to that. The principal axes of ZnPc, F_8ZnPc are given in Figure 5.1.

	Q_1 (Debye·Å)	**Q_2 (Debye·Å)**	**Q_3 (Debye·Å)**
ZnPc	12.4	12.4	-24.8
F_8ZnPc	-9.3	-9.3	18.6
F6-TCNNQ	-40.9	6.0	34.9

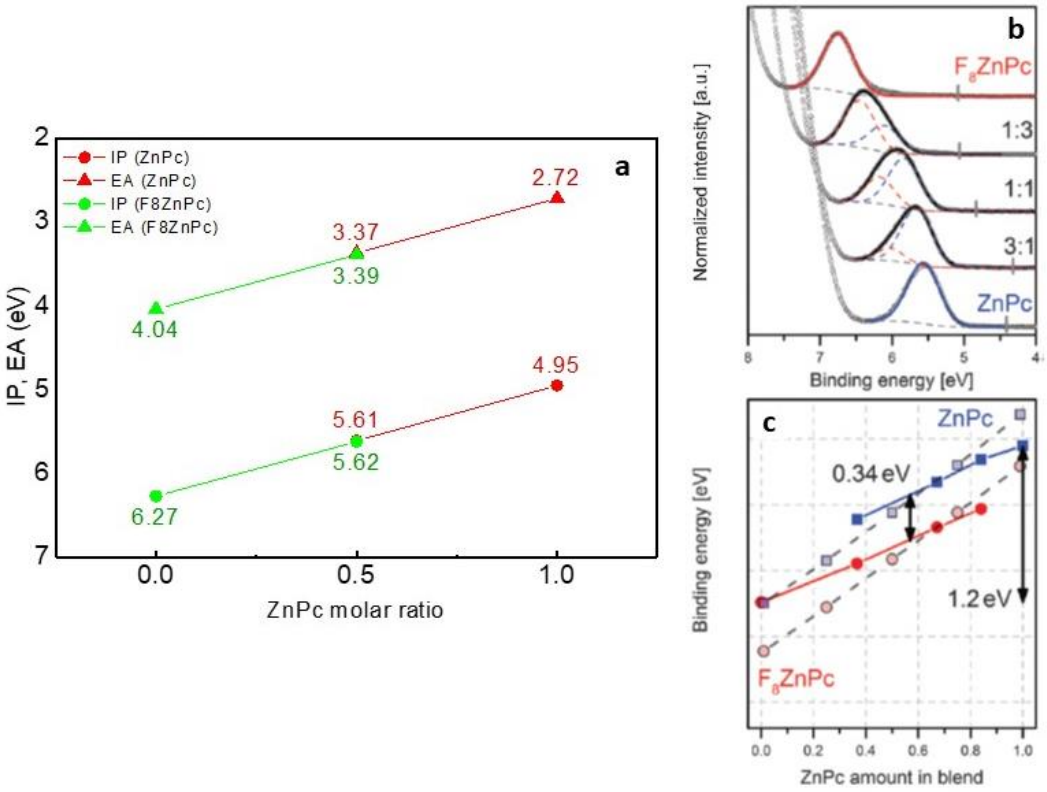

Figure 5.7: a) Solid-state effects on the IPs (circles) and EAs (triangles) of ZnPc (red) and F_8ZnPc (green) molecules in ZnPc:F_8ZnPc host blends as a function of ZnPc molar ratio; b) ultraviolet photoemission spectroscopy (UPS) data (gray circles) and fits (solid lines) for mixed blends of ZnPc:F_8ZnPc; c) maximum positions of HOMO distributions of ZnPc (blue squares) and F_8ZnPc (red circles) over ZnPc content are shown together with simulation results (dashed lines) of the IP of ZnPc (light blue squares) and FnZnPc (light red circles). Pictures taken from Ref.[13].

Table 5.5: Tabulated values (in eV) of the IP and EA of ZnPc and F_8ZnPc, as well induction Δ_I^x and electrostatic Δ_E^x contributions (in eV), as a function of ZnPc molar ratio. The values refer to Figure 5.7.

ZnPc (m.r.)	IP_g	Δ_I^h	Δ_E^h	IP	EA_g	Δ_I^e	Δ_E^e	EA
0.0	6.91	-1.00	0.36	6.27	2.66	-1.02	-0.36	4.04
0.5 (F_8ZnPc)	6.91	-1.00	-0.29	5.62	2.66	-1.02	0.29	3.39
0.5 (ZnPc)	6.41	-0.99	0.19	5.61	2.17	-1.01	-0.19	3.37
1.0	6.41	-0.99	-0.47	4.95	2.17	-1.01	0.46	2.72

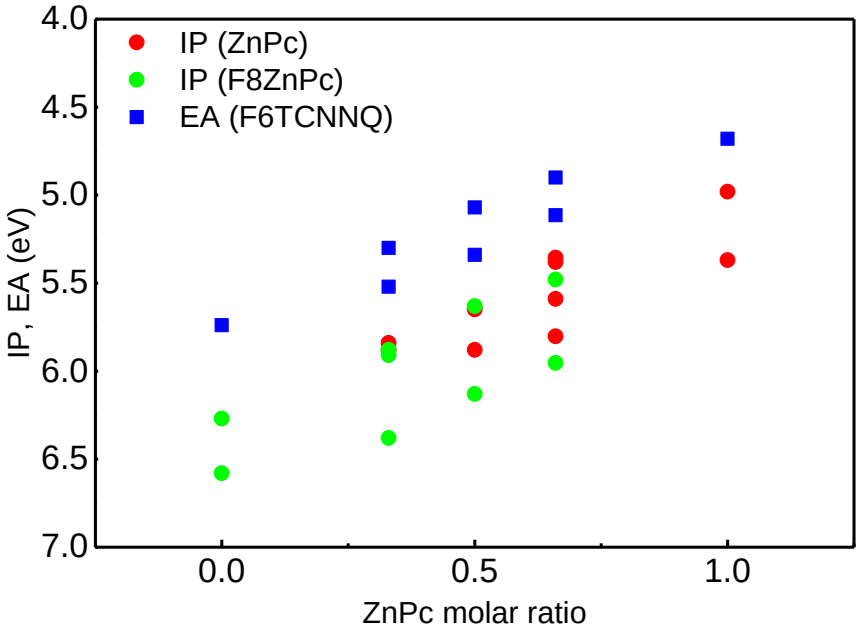

Figure 5.8: Solid-state effects on the IPs of ZnPc (red circles) and F_8ZnPc (green circles) and the EA of F6-TCNNQ (blue triangles) in ZnPc:F_8ZnPc blends doped with F6-TCNNQ as a function of ZnPc molar ratio. For every molar ratio, different arrangements of the ZnPc and F_8ZnPc host molecules around the dopant were considered to explore variations of the energetics on detailed microstructure configurations.

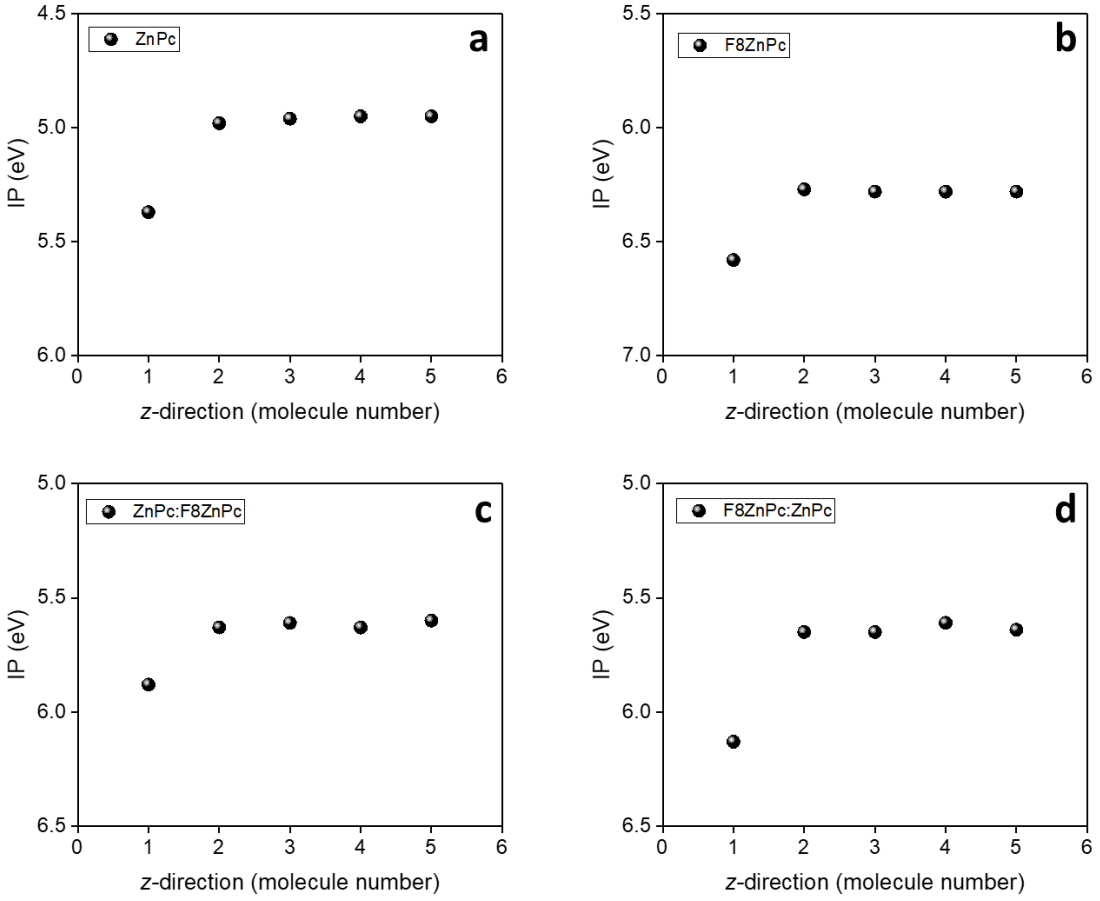

Figure 5.9: Solid-state effects on the IPs of the host molecules as a function of their distance from the F6-TCNNQ molecule for the a) ZnPc:F6-TCNNQ and b) F_8ZnPc:F6-TCNNQ binary blends, for c) and d) ternary blends with 1:1 ZnPc:F_8ZnPc composition, distinguishing the two cases where the dopant sits at the molecular site of ZnPc or F_8ZnPc.

Table 5.6: Tabulated values (in eV) of the IP of either ZnPc or F_8ZnPc reported in Figure 5.9 and induction Δ_I^h and electrostatic Δ_E^xcontributions, as a function of the distance from the F6-TCNNQ molecule along the *z*-direction. The studied configurations are the same as reported in Figure 5.6.

		1	**2**	**3**	**4**	**5**
ZnPc binary blend	Δ_I^h	-0.95	-1.00	-1.00	-1.00	-1.00
	Δ_E^h	-0.09	-0.43	-0.45	-0.46	-0.46
	IP_{host}	5.37	4.98	4.96	4.95	4.95
F_8ZnPc binary blend	Δ_I^h	-0.95	-1.00	-1.00	-1.00	-1.00
	Δ_E^h	0.62	0.36	0.37	0.37	0.37
	IP_{host}	6.58	6.27	6.28	6.28	6.28
1:1 ternary blend (conf 1)	Δ_I^h	-0.95	-1.00	-1.00	-1.00	-1.00
	Δ_E^h	0.42	-0.28	0.20	-0.28	0.19
	IP_{host}	5.88	5.63	5.61	5.63	5.60
1:1 ternary blend (conf 2)	Δ_I^h	-0.95	-1.00	-1.00	-1.00	-1.00
	Δ_E^h	0.17	0.24	-0.26	0.20	-0.27
	IP_{host}	6.13	5.65	5.65	5.61	5.64

6. Summary and Perspectives

Throughout this thesis, we have seen how setting up a proper multilevel computational methodology is mandatory for a complete understanding of the processes that occur in an organic semiconductor device at different length- and timescale. In particular, it is essential to combine electronic structure methods with a framework suitable for taking into account the solid-state environmental effects, as a microelectrostatic (ME) model, in the assessment of the energetic landscape of large-scale, complex systems. These methodologies allow for capturing the effects of solid-state electronic polarization on gap renormalization and screening of the electrostatic electron-hole interactions. Indeed, the inclusion of electrostatic effects is of utmost importance, since the charge transport energy levels of molecules embedded in a solid-state environment and the corresponding charge-transfer (CT) excitation energies depend on mutual intermolecular electrostatic interactions.

We have seen that such a marriage between electronic structure methods and a ME model has been useful in Chapter 3 in the evaluation of strongly hybridized Frenkel-CT electronic excitations and their broad energetic landscape in amorphous thin films of two π-conjugated organic *push-pull* molecules, slightly differing in their molecular structure. By means of these calculations, we have been able to model with stochastic kinetic Monte Carlo (KMC) simulations the transport of singlet excitons, compute macroscopic properties, like the exciton diffusion coefficient and diffusion length, and ultimately rationalize the different energetics and dynamics of the two systems under investigation. We have found that in one of these materials singlet excitons are capable of funnelling through long-distance hopping percolation pathways, presumably as a result of the less anisotropic shape of the molecule that favours long-range 3D transport.[1]

In Chapter 4, we have added another piece to the whole story, by modelling intermolecular CT states excited states at the NPB:HAT-CN heterointerface in amorphous blends that display large frontier orbital energy offset. Also in this case the ME model has played a fundamental role in the characterization of the ultrabroad CT state spectrum, composed by multiple CT excitations, each with its distribution.[2] We have gone further this finding and we have investigated the energetics and dynamics of low-lying electronic CT states, carrying out an analysis as a function of the blend composition and temperature. We have managed in disentangling the contributions to the overall energetic disorder according to their physical origin (conformational and environmental) and nature (static and dynamic). Among the latter, the energetic static disorder, either conformational or electrostatic) plays a major role in the disordered density of states of the CT states manifold. We have finally assessed their fast recombination to the ground state, proving that low-lying CT states are photovoltaically inactive at least in these large offset blends, that is they do not contribute to photocurrent generation and may be responsible for large voltage losses in those systems.[3]

Finally, in Chapter 5, we have modelled ground state CT complexes between a host and a p-type dopant and we have investigated the role of local environmental interactions on the generation of free

charge carriers in doped binary (ZnPc:F6-TCNNQ and F_8ZnPc:F6-TCNNQ) and ternary (ZnPc:F_8ZnPc:F6-TCNNQ). By means of *GW*/ME calculations, we have disclosed the paramount role of charge-quadrupolar interactions on both the ionization (by reshuffling the energy levels of the dopant and the host) and the charge dissociation step (by creating a favourable energy pathway for the hole) in molecular doping. These findings pave the way for attractive strategies for improving the doping efficiency and conductivity in doped organic semiconductors by tailoring molecular quadrupole moments of the host and/or dopant.[4]

In almost 30 years of experimental and theoretical efforts since the very first appearance of a bulk heterojunction (BHJ) organic solar cell (OSC),[5] we have gained a vast body of knowledge related to intermolecular CT states, either via a thermally or photo-induced electron transfer, and the role they play in mediating exciton diffusion, charge separation and recombination. Much has been learned also in understanding how local morphology at the interface, environmental electrostatic interactions, charge or exciton delocalization, hybridization and energetic disorder (static vs dynamic) affect the energetic landscape of CT states, the fate of charges and their transport properties. What is still missing is a full comprehension of how CT states dissociate into free charge carriers, either via vibrationally excited (hot) or fully thermalized (cold) CT states. The hope is that researchers will solve this so long debated topic in the next 30 years. In all of this, our work aims at providing to the community robust and reliable theoretical evidence, supported by experimental data, that might contribute to the complete understanding of the photophysical processes within a working OSC and then might guide researchers teams in the design of new organic materials and blends, with the ultimate goal of approaching as much as possible the Shockley-Queisser limit of 33%, standing so far as unattainable.[6]

Notoriously, OSCs (red full dots in Figure 6.1) suffered from a "sudden stop" in terms of power conversion efficiencies (PCEs). It seemed that, using only fullerene derivatives as electron-acceptor (A) molecules in vacuum- or in solution-processed solar cells, the maximum achievable PCE was doomed to not surpass 12%.[7–9] Undoubtedly, fullerenes have outstanding electron withdrawing abilities and high electron mobilities. The peculiar shape of fullerenes offers them 3D electron transport properties and the capability of forming favorable blend morphologies that balance charge generation and transport.[10] On the other hand, the lowest excited state in fullerenes is only weakly absorbing in the visible region of the solar spectrum and their photoluminescence efficiency is low. The elevated difficulty in tuning their opto-electronic properties increases the complexity in chemical modifications of their backbone and makes fullerenes less likely to gain complementary light harvesting to the donor (D) counterpart. In addition, the bottleneck is also represented by the high amount of energy (voltage) losses (in the range of 0.8-1.0 eV) in OSCs using fullerene derivatives, even in the case of low exciton-dissociation driving forces depending on the choice of the small-molecule or polymer D.[11]

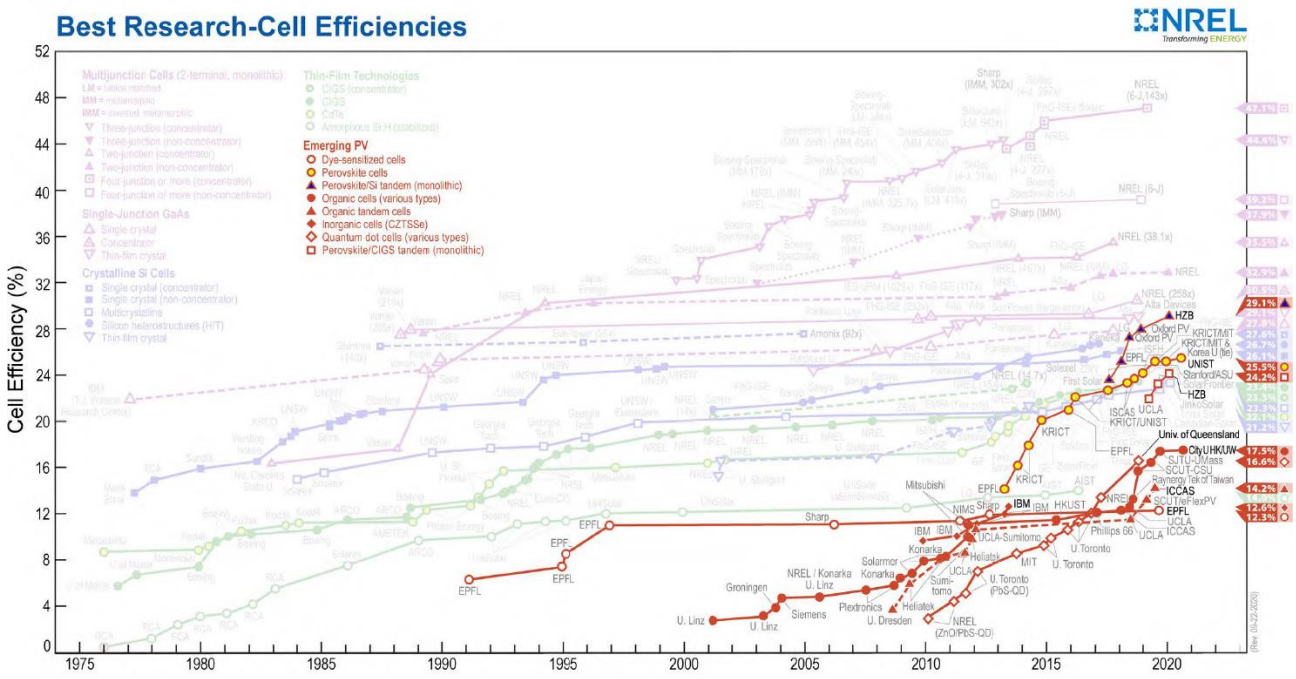

Figure 6.1: NREL certified state-of-the-art efficiencies form emerging photovoltaic technologies from 1976 to the present.

The replacement of fullerenes in OSCs was therefore necessary and the rapid development of a new class of materials known as non-fullerene acceptors[10] (NFAs) was the spark that ignited once again the interest in OSCs and boosted the run in academics and industry for reaching a new world record PCE. As often happens, technologic progress precedes necessarily fundamental research and nowadays, as embraceable, most of the scientific publications regarding OSCs deals with NFAs, because they are simply more appealing, "hotter" topics. The novelty in small molecule NFAs lies in the fact that they exhibit stronger light absorption and offer more flexibility with respect to fullerene derivatives in terms of tailoring their opto-electronic properties and tuning the energy levels of the molecule, which suit best to those of the chosen D. Indeed, many efforts have been paid to the molecular optimization of the D:NFA pair in order to minimize the energy offset between either the IP or the EA of both the D and the NFA component, which increases the energy of the interfacial CT states and contributes in the decrease of voltage losses.[12] As a result, NFAs enable much reduced non-radiative voltage losses, leading to OSCs with PCEs outperforming those obtained based on fullerene derivatives:[10,13,14] for instance, PCEs of over 18% have been achieved for single-junction BHJ OSCs.[15] We note that recently the importance of the energy offset between the EA of the D and the NFA has been questioned. Karuthedath *et al.* have demonstrated that charge generation does not depend on the EA offset, but rather charge generation efficiency of low bandgap NFA-based BHJ OSCs increases with the IP offset, reaching its maximum for offsets of around 0.5 eV.[16]

It is now clear in the community that, in order to reach PCEs > 20%, all superfluous non-radiative loss pathways must be identified and removed. For instance, Gillet *et al.* have shown that the majority of charge recombination events frequently proceeds via the non-emissive NFA triplet exciton (T_1),

especially when there is a low energy T_1 localized either on the D and the NFA. In PM6:Y6 blends (see molecular structure in Figure 6.2), almost 90% of the recombination occurs non-radiatively via the NFA T_1. Nevetherless excellent PCEs can still be realized, thanks to the particular π-π molecular packings of Y6 molecules in thin films, which simultaneously promotes the formation of delocalized and emissive excitons and a delocalization of electron wave functions at the D:A interfaces, significantly reducing the Coulomb attraction of the CT state.[17] Remarkably, in blends like PTB7-Th:IEICO-2F, where experimental data show no recombination via T_1, an hybridization between the NFA T_1 and the triplet CT (^{3}CT) state occurs that reduces the rate of back-electron transfer from ^{3}CT to T_1, thereby favoring the ^{3}CT to dissociate rather than recombine.

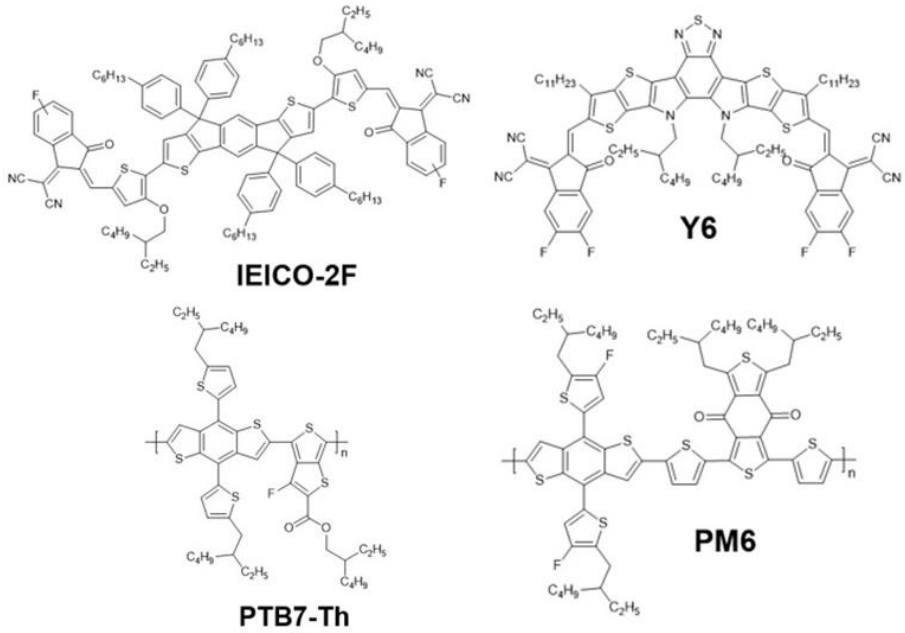

Figure 6.2: Molecular structure of NFAs (top) and donors (bottom).

As shown in Figure 6.3a, in the PTB7-Th:IEICO-2F complex, the energy ordering of the singlet ^{1}CT and ^{3}CT energies are surprisingly inverted from expected, when considering exchange interactions,[18] with the ^{3}CT higher than the ^{1}CT by ~70 meV. By performing a rigid scan of the ^{1}CT and ^{3}CT excitation energies as a function of the D:A separation, it has been shown that below ~5 Å, the ^{1}CT is rapidly stabilised, while the ^{3}CT is destabilised. The inversion of ^{1}CT and ^{3}CT in PTB7-Th:IEICO-2F arises from hybridization between the localized exciton (LE) and CT states, the magnitude of which has an exponential dependence on distance. Crucially, the NFA singlet S_1 is higher in energy than the ^{1}CT and the T_1 is lower than the ^{3}CT: this explains why hybridization stabilizes the ^{1}CT and destabilizes the ^{3}CT (see inset in Figure 6.3). In this case, the main driver for hybridization is the enhanced CT-LE electronic coupling, due to a significant overlap between the NFA and the polymer backbone. Due to the strong destabilization of the ^{3}CT at close D:A distances, it will be energetically favorable for the electron and hole to remain distant from the interface in this configuration. In

contrast, the PM6:Y6 complex displays the expected singlet-triplet CT energy ordering, with the ^{1}CT higher in energy than the ^{3}CT at small D:A distances (see Figure 6.3b). The insight provided by this work demonstrates the importance of T_1 on the non-radiative voltage losses in NFA OSCs. If the formation of T_1 can be suppressed by favoring the ^{3}CT-T_1 hybridization, a clear route to obtaining PCEs > 20% exists.

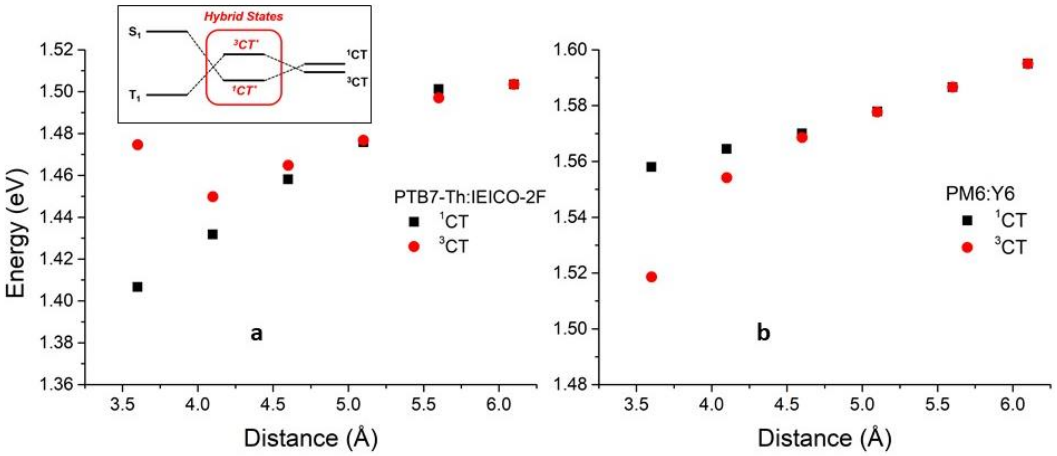

Figure 6.3: The results of a rigid scan of the ^{1}CT and ^{3}CT energies for a representative a) PTB7-Th:IEICO-2F and b) PM6:Y6 configuration as a function of D:A separation. The inset shows a representation of the effect of CT-LE hybridization on the energetic ordering of the ^{1}CT and ^{3}CT. It is important to bear in mind that the diabatic states localized on the NFA are higher in energy than the corresponding CT states in the singlet manifold, while the reverse is true in the triplet manifold. CT-LE hybridization therefore stabilises the ^{1}CT, whilst destabilising the ^{3}CT.

Despite the advantages, NFAs are still lagging behind fullerene derivatives in terms of charge transport properties.[19] The reason for the difference between these two classes of materials can be linked to their molecular shape. NFAs are characterised by highly anisotropic conjugated structures, and their 2D geometry makes the molecular packing, domain orientation and blend morphology crucial for the electron mobility and charge separation.[20] Recently, Mondelli *et al.* have shown that single crystal NFA molecules tend to arrange themselves in different *n*-dimensional packing motifs (*i.e.*, herringbone, brickwork, reticular) and, as a result, their molecular organization and topological connectivity, as well as the strength of π-π interactions, crucially affect the charge carrier transport properties.[21] NFAs molecules, such as IDIC or IDTBR (see Figure 6.4), crystallize with different lattice systems unit cells, that in turn results in different packing motifs, *i.e.*, IDIC in a brickwork fashion with 2D π-π stacking, while IDTBR in a reticular architecture with a 3D π-π stacking.

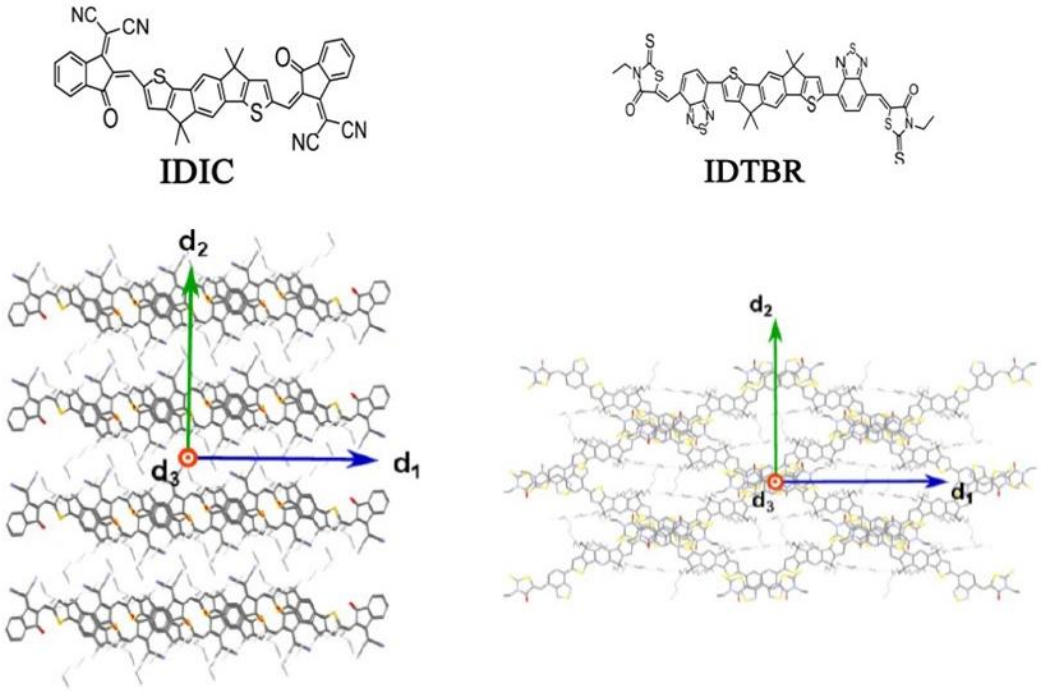

Figure 6.4: Molecular structures and top view of the 2D (left) and 3D (right) packing motif, with d_1, d_2, d_3 directions superimposed. Hydrogen atoms have been omitted for clarity.

In this framework, it would be useful to establish a correlation between the molecular packing motif dimensionality and the electron transport properties, *i.e.*, on which extent charges delocalize in single NFA crystals, as they tend to keep the same molecular arrangement also when deposited in thin films. Such a correlation can only be achieved by theoretical simulations with the resolution of a tight-binding model built from spatially and time-resolved calculations, which will shed some light on the density of electronic states for electrons and their energy-dependent intermolecular delocalization, as previously done for fullerene derivatives.[22]

The PCE improvements with the use of NFAs have resulted from molecular engineering and local morphology control.[12,14] However, the intrinsic energy offset in D:A BHJ induces significant voltage losses,[23] which limit the highest achievable open-circuit voltage V_{oc}. Moreover, optimization of the blend morphology, finding the best balance between exciton diffusion length and efficient charge transport has always been challenging.[24,25] Therefore, is it really necessary to rely on OSCs with D:A architectures? An appealing solution to such drawbacks would be the fabrication of single material devices, as homojunction OSCs (HOSCs), which offer the potential for relatively easy processing and morphology control, leading also to high charge generation quantum yields. Recently Dong *et al.* have reported an efficient photocurrent generation in α-sexithiophene(6T)-based HOSC,[26] in the absence of an electron accepting material, reaching an external quantum efficiency (EQE) of 44% and a V_{oc} of 1.61 V, which is astonishing for a device acting as a HOSC. Transient absorption (TA) spectroscopy measurements have shown that the photoexcitation of pristine α-6T films leads to efficient and ultrafast charge carrier generation from excitons, indicating that charge generation

happens in the bulk of the pristine α-6T. Using specific processing parameters, films with two molecular orientations, mainly standing and mainly lying, have been fabricated and an energy offset of 0.4 eV between the IPs at these two orientations has been measured via ambient photoemission spectroscopy (APS) (see Figure 6.5a). This energy difference δ~0.4 eV determines favourable conditions for the charge separation.

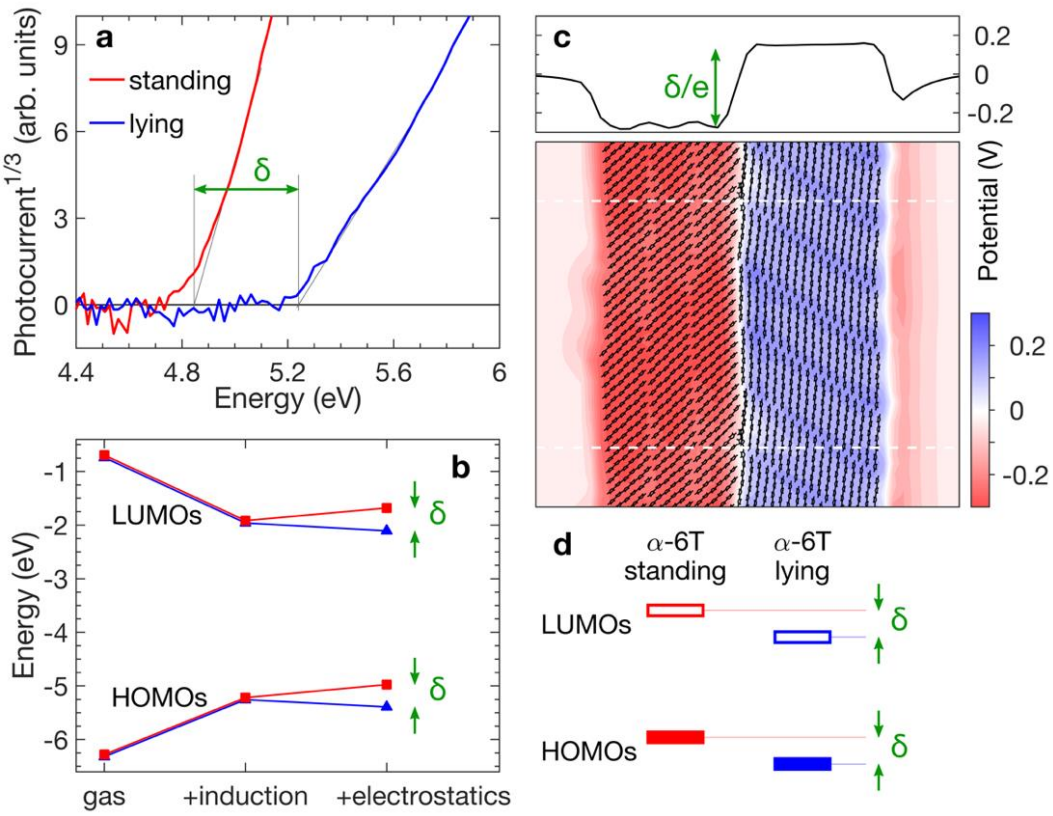

Figure 6.5: a) Ambient photoemission spectroscopy (APS) results for α-6T thin films with standing and lying orientations presenting an energy difference δ~0.4 eV between their HOMO levels. b) Evolution of HOMO and LUMO levels calculated from embedded *GW* calculations for an interface between two domains with standing and lying α-6T molecules. Results are presented by progressively adding induction (dielectric response) and electrostatic intermolecular interactions to gas-phase levels. This shows that the offset δ between standing and lying molecules is entirely sourced by electrostatics. c) Maps of the electrostatic potential illustrating the step-like variation across the standing-lying interface. d) Sketch of the energy levels of standing and lying α-6T molecules, playing the role of electron D and A component, respectively.

Moreover, state-of-the-art calculations based on embedded *GW* methods have revealed that the energy offset δ is dictated by the different orientations of the molecular quadrupoles at the standing/lying grain boundaries, which dictate a step in the electrostatic potential across the interface (see Figure 6.5b and 6.5c) that affects occupied and unoccupied levels. Standing and lying α-6T

molecules behave therefore as the electron donating and the accepting components of a conventional organic heterojunction, in virtue of the intrinsic D–A dual nature of α-6T. The energy difference δ could also lead to the occurrence of CT transitions, where an electron is transferred from the standing to the lying domain. The optical absorption spectrum obtained with embedded Bethe-Salpeter equations (BSE) calculations in Figure 6.6 reveals the complexity of the excited state manifold, which is heavily affected by delocalization and hybridization between molecular (Frenkel, with high oscillator strength) and CT excitons. The brightest hybrid Frenkel-CT exciton is computed at 2.42 eV (in Figure 6.6c) and one of the two nearly degenerate lowest-energy excitations, placed just ~50 meV below the brightest exciton, is an inter-domain CT state with hole and electron localised in the standing and lying domains, respectively (in Figure 6.6b) and can act as a gateway for an efficient charge splitting.

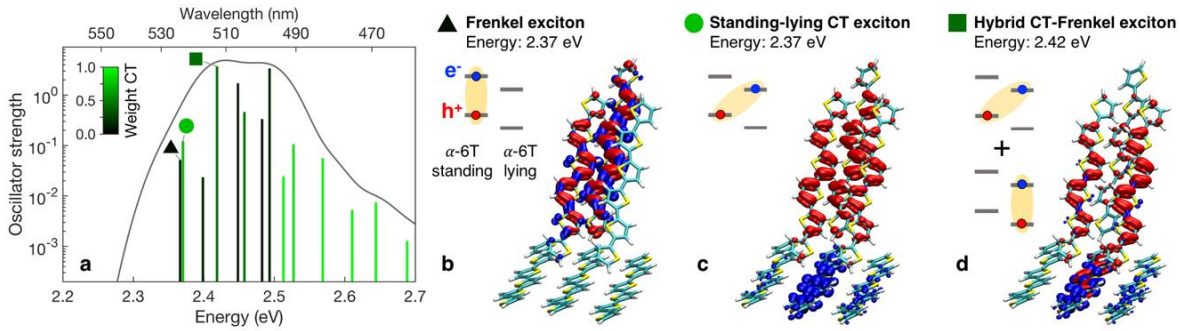

Figure 6.6: a) Embedded BSE absorption spectrum of the standing-lying α-6T interface. Bar colours quantify the weight of inter-layer CT states of each excitation, showing that the lowest-energy region of the spectrum presents states that have a pronounced charge separation. b-d) Electron-hole density plots and the corresponding simplified energy-level sketches of representative low-energy excitations.

The ordered morphology and the contact between different crystal facets are crucial to dissociate excitons, and grain boundaries in single component polycrystalline systems could be exploited as heterojunctions. Thus, this work has the merit of reshaping the common understanding in the role of D and A in OSCs where this character is not only fixed by the primary chemical structure of the molecules but can also be modulated by interfacial packing and molecular electrostatics engineering in order to generate energy offsets in single materials and facilitate charge generation pathways.

At last, in the context of molecular doping, which brings multiple benefits such as enhanced charge carrier density and electrical conductivity, improved charge injection and larger charge carrier mobility thanks by filling traps,[27–31] it has been shown that Lewis acids, like tris(pentafluorophenyl)borane (BCF), are promising candidates for the p-doping of organic semiconductors. However, a clear understanding of the mechanistic aspects of the doping chemistry by BCF is still missing. A first attempt has been provided by Yurash *et al*. by proposing a 3-step

process where complexation of BCF with traces of water leads first to the formation of a strong Brønsted acid, which, in turn, protonates one (or multiple) cyclopentadithiophene (CPDT) unit of the poly-cyclopentadithiophene-benzothiadiazole (PCPDTBT) polymer backbone (see Figure 6.7).[32]

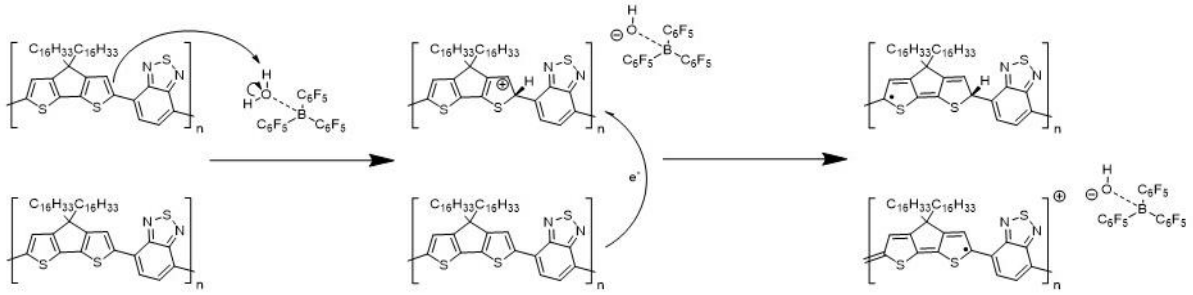

Figure 6.7: The doping mechanism of PCPDTBT by BCF in three steps.

As a result of this mechanism, the presence of two active radical species has been detected by combined DFT calculations and electron nuclear double resonance (ENDOR) spectroscopy measurements, and a conductivity increase in the polymer film doped with BCF has been observed. Nevertheless, a later on study by Arvind *et al.* questioned the occurrence of such mechanism.[33] Although they have used the model polymer poly(3-hexylthiophene) (P3HT) doped by BCF, electron paramagnetic resonance (EPR) measurements have revealed the presence of only the free radical cation on the P3HT backbone, as well as the absence of the other radical species such as the neutral radical on the protonated chain. Therefore, another mechanism has been proposed, consistent with the experimental observations:

$$X + BCF{:}H_2O \longrightarrow X^{\cdot +} + (BCF{:}OH)^- + \tfrac{1}{2}\, H_2$$

where X stands for the polymer, either PCPDTBT or P3HT. It has been also proposed that the reaction might proceeds in a similar fashion to that suggested for PCPDTBT by Yurash *et al.*, but then two neutral protonated radical species subsequently react together to eliminate H_2 and regenerate a neutral closed-shell P3HT. Alternatively, two protonated P3HT cations could react to give two polarons and H_2, or a protonated cation and a protonated radical could react to give a polaron, neutral P3HT, and H_2. In this respect, DFT calculations based on range-separated hybrid (RSH) functionals will help in shedding some light on the dominating mechanism for doping polymer films, namely by computing the energetics for the electron transfer to pristine polymer chains and also quantifying the thermodynamics of the reactions, proposed by two different research groups.

References

(1) Londi, G.; Dilmurat, R.; D'Avino, G.; Lemaur, V.; Olivier, Y.; Beljonne, D. Comprehensive Modelling Study of Singlet Exciton Diffusion in Donor-Acceptor Dyads: When Small Changes in Chemical Structure Matter. *Phys. Chem. Chem. Phys.* **2019**, *21* (45), 25023–25034.

(2) Khan, S. U. Z.; Londi, G.; Liu, X.; Fusella, M. A.; D'Avino, G.; Muccioli, L.; Brigeman, A. N.; Niesen, B.; Yang, T. C. J.; Olivier, Y.; Dull, J. T.; Giebink, N. C.; Beljonne, D.; Rand, B. P. Multiple Charge Transfer States in Donor-Acceptor Heterojunctions with Large Frontier Orbital Energy Offsets. *Chem. Mater.* **2019**, *31* (17), 6808–6817.

(3) Londi, G.; Khan, S.-U.-Z.; Muccioli, L.; D'Avino, G.; Rand, B. P.; Beljonne, D. Fate of Low-Lying Charge-Transfer Excited States in a Donor:Acceptor Blend with a Large Energy Offset. *J. Phys. Chem. Lett.* **2020**, *11* (23), 10219–10226.

(4) Privitera, A.; Londi, G.; Riede, M.; D'Avino, G.; Beljonne, D. Molecular Quadrupole Moments Promote Ground-State Charge Generation in Doped Organic Semiconductors. *Adv. Funct. Mater.* **2020**, *30*, 2004600.

(5) Tang, C. W. Two-layer Organic Photovoltaic Cell. *Appl. Phys. Lett.* **1986**, *48* (2), 183–185.

(6) Shockley, W.; Queisser, H. J. Detailed Balance Limit of Efficiency of P-n Junction Solar Cells. *J. Appl. Phys.* **1961**, *32* (3), 510–519.

(7) Cheng, Y.-J.; Yang, S.-H.; Hsu, C.-S. Synthesis of Conjugated Polymers for Organic Solar Cell Applications. *Chem. Rev.* **2009**, *109* (11), 5868–5923.

(8) Li, Y. Molecular Design of Photovoltaic Materials for Polymer Solar Cells: Toward Suitable Electronic Energy Levels and Broad Absorption. *Acc. Chem. Res.* **2012**, *45* (5), 723–733.

(9) Hu, H.; Chow, P. C. Y.; Zhang, G.; Ma, T.; Liu, J.; Yang, G.; Yan, H. Design of Donor Polymers with Strong Temperature-Dependent Aggregation Property for Efficient Organic Photovoltaics. *Acc. Chem. Res.* **2017**, *50* (10), 2519–2528.

(10) Zhang, G.; Zhao, J.; Chow, P. C. Y.; Jiang, K.; Zhang, J.; Zhu, Z.; Zhang, J.; Huang, F.; Yan, H. Nonfullerene Acceptor Molecules for Bulk Heterojunction Organic Solar Cells. *Chem. Rev.* **2018**, *118* (7), 3447–3507.

(11) Coropceanu, V.; Chen, X.-K.; Wang, T.; Zheng, Z.; Brédas, J.-L. Charge-Transfer Electronic States in Organic Solar Cells. *Nat. Rev. Mater.* **2019**, *4* (11), 689–707.

(12) Qian, D.; Zheng, Z.; Yao, H.; Tress, W.; Hopper, T. R.; Chen, S.; Li, S.; Liu, J.; Chen, S.; Zhang, J.; Liu, X.-K.; Gao, B.; Ouyang, L.; Jin, Y.; Pozina, G.; Buyanova, I. A.; Chen, W. M.; Inganäs, O.; Coropceanu, V.; Brédas, J.-L.; Yan, H.; Hou, J.; Zhang, F.; Bakulin, A. A.; Gao, F. Design Rules for Minimizing Voltage Losses in High-Efficiency Organic Solar Cells.

Nat. Mater. **2018**, *17* (8), 703–709.

(13) Yan, C.; Barlow, S.; Wang, Z.; Yan, H.; Jen, A. K.-Y.; Marder, S. R.; Zhan, X. Non-Fullerene Acceptors for Organic Solar Cells. *Nat. Rev. Mater.* **2018**, *3*, 18003.

(14) Hou, J.; Inganäs, O.; Friend, R. H.; Gao, F. Organic Solar Cells Based on Non-Fullerene Acceptors. *Nat. Mater.* **2018**, *17*, 119.

(15) Liu, Q.; Jiang, Y.; Jin, K.; Qin, J.; Xu, J.; Li, W.; Xiong, J.; Liu, J.; Xiao, Z.; Sun, K.; Yang, S.; Zhang, X.; Ding, L. 18% Efficiency Organic Solar Cells. *Sci. Bull.* **2020**, *65* (4), 272–275.

(16) Karuthedath, S.; Gorenflot, J.; Firdaus, Y.; Chaturvedi, N.; De Castro, C. S. P.; Harrison, G. T.; Khan, J. I.; Markina, A.; Balawi, A. H.; Peña, T. A. Dela; Liu, W.; Liang, R.-Z.; Sharma, A.; Paleti, S. H. K.; Zhang, W.; Lin, Y.; Alarousu, E.; Anjum, D. H.; Beaujuge, P. M.; De Wolf, S.; McCulloch, I.; Anthopoulos, T. D.; Baran, D.; Andrienko, D.; Laquai, F. Intrinsic Efficiency Limits in Low-Bandgap Non-Fullerene Acceptor Organic Solar Cells. *Nat. Mater.* **2020**.

(17) Zhang, G.; Chen, X.-K.; Xiao, J.; Chow, P. C. Y.; Ren, M.; Kupgan, G.; Jiao, X.; Chan, C. C. S.; Du, X.; Xia, R.; Chen, Z.; Yuan, J.; Zhang, Y.; Zhang, S.; Liu, Y.; Zou, Y.; Yan, H.; Wong, K. S.; Coropceanu, V.; Li, N.; Brabec, C. J.; Brédas, J.-L.; Yip, H.-L.; Cao, Y. Delocalization of Exciton and Electron Wavefunction in Non-Fullerene Acceptor Molecules Enables Efficient Organic Solar Cells. *Nat. Commun.* **2020**, *11* (1), 3943.

(18) Köhler, A.; Beljonne, D. The Singlet–Triplet Exchange Energy in Conjugated Polymers. *Adv. Funct. Mater.* **2004**, *14* (1), 11–18.

(19) Zhang, J.; Tan, H. S.; Guo, X.; Facchetti, A.; Yan, H. Material Insights and Challenges for Non-Fullerene Organic Solar Cells Based on Small Molecular Acceptors. *Nat. Energy* **2018**, *3* (9), 720–731.

(20) Ran, N. A.; Roland, S.; Love, J. A.; Savikhin, V.; Takacs, C. J.; Fu, Y.-T.; Li, H.; Coropceanu, V.; Liu, X.; Brédas, J.-L.; Bazan, G. C.; Toney, M. F.; Neher, D.; Nguyen, T.-Q. Impact of Interfacial Molecular Orientation on Radiative Recombination and Charge Generation Efficiency. *Nat. Commun.* **2017**, *8* (1), 79.

(21) Mondelli, P.; Boschetto, G.; Horton, P. N.; Tiwana, P.; Skylaris, C.-K.; Coles, S. J.; Krompiec, M.; Morse, G. Meta-Analysis: The Molecular Organization of Non-Fullerene Acceptors. *Mater. Horizons* **2020**, *7* (4), 1062–1072.

(22) D'Avino, G.; Olivier, Y.; Muccioli, L.; Beljonne, D. Do Charges Delocalize over Multiple Molecules in Fullerene Derivatives? *J. Mater. Chem. C* **2016**, *4* (17), 3747–3756.

(23) Vandewal, K.; Benduhn, J.; Nikolis, V. C. How to Determine Optical Gaps and Voltage Losses in Organic Photovoltaic Materials. *Sustain. Energy Fuels* **2018**, *2* (3), 538–544.

(24) Terao, Y.; Sasabe, H.; Adachi, C. Correlation of Hole Mobility, Exciton Diffusion Length,

and Solar Cell Characteristics in Phthalocyanine/Fullerene Organic Solar Cells. *Appl. Phys. Lett.* **2007**, *90* (10), 103515.

(25) Menke, S. M.; Luhman, W. A.; Holmes, R. J. Tailored Exciton Diffusion in Organic Photovoltaic Cells for Enhanced Power Conversion Efficiency. *Nat. Mater.* **2013**, *12* (2), 152–157.

(26) Dong, Y.; Nikolis, V. C. V. C.; Talnack, F.; Chin, Y.-C.; Benduhn, J.; Londi, G.; Kublitski, J.; Zheng, X.; Mannsfeld, S. C. B. S. C. B.; Spoltore, D.; Muccioli, L.; Li, J.; Blase, X.; Beljonne, D.; Kim, J.-S.; Bakulin, A. A. A.; D'Avino, G.; Durrant, J. R. J. R.; Vandewal, K. Orientation Dependent Molecular Electrostatics Drives Efficient Charge Generation in Homojunction Organic Solar Cells. *Nat. Commun.* **2020**, *11* (1), 4617.

(27) Lüssem, B.; Riede, M.; Leo, K. Doping of Organic Semiconductors. *Phys. status solidi* **2013**, *210* (1), 9–43.

(28) Méndez, H.; Heimel, G.; Opitz, A.; Sauer, K.; Barkowski, P.; Oehzelt, M.; Soeda, J.; Okamoto, T.; Takeya, J.; Arlin, J.-B.; Balandier, J.-Y.; Geerts, Y.; Koch, N.; Salzmann, I. Doping of Organic Semiconductors: Impact of Dopant Strength and Electronic Coupling. *Angew. Chemie Int. Ed.* **2013**, *52* (30), 7751–7755.

(29) Tietze, M. L.; Pahner, P.; Schmidt, K.; Leo, K.; Lüssem, B. Doped Organic Semiconductors: Trap-Filling, Impurity Saturation, and Reserve Regimes. *Adv. Funct. Mater.* **2015**, *25* (18), 2701–2707.

(30) Méndez, H.; Heimel, G.; Winkler, S.; Frisch, J.; Opitz, A.; Sauer, K.; Wegner, B.; Oehzelt, M.; Röthel, C.; Duhm, S.; Többens, D.; Koch, N.; Salzmann, I. Charge-Transfer Crystallites as Molecular Electrical Dopants. *Nat. Commun.* **2015**, *6* (1), 8560.

(31) Salzmann, I.; Heimel, G.; Oehzelt, M.; Winkler, S.; Koch, N. Molecular Electrical Doping of Organic Semiconductors: Fundamental Mechanisms and Emerging Dopant Design Rules. *Acc. Chem. Res.* **2016**, *49* (3), 370–378.

(32) Yurash, B.; Cao, D. X.; Brus, V. V.; Leifert, D.; Wang, M.; Dixon, A.; Seifrid, M.; Mansour, A. E.; Lungwitz, D.; Liu, T.; Santiago, P. J.; Graham, K. R.; Koch, N.; Bazan, G. C.; Nguyen, T. Q. Towards Understanding the Doping Mechanism of Organic Semiconductors by Lewis Acids. *Nat. Mater.* **2019**, *18* (12), 1327–1334.

(33) Arvind, M.; Tait, C. E.; Guerrini, M.; Krumland, J.; Valencia, A. M.; Cocchi, C.; Mansour, A. E.; Koch, N.; Barlow, S.; Marder, S. R.; Behrends, J.; Neher, D. Quantitative Analysis of Doping-Induced Polarons and Charge-Transfer Complexes of Poly(3-Hexylthiophene) in Solution. *J. Phys. Chem. B* **2020**, *124* (35), 7694–7708.

Acknowledgements

What an experience! These last four years have been very tough, a lot of up and down moments, and yet full of personal satisfactions. I have acquired a lot of knowledge from the people I have met during the PhD, either in the CMN group and from co-workers. Therefore, I will dedicate this last page to express my gratitude.

In primis, I would like to deeply thank Prof. David Beljonne, my supervisor in this journey. He has immediately believed in my potential and he has given me his trust, since the very beginning. He has been able to fully understand me, knowing when I was willing to push and when pull the break. Actually, I have never felt the boredom with him!

Moreover, I have been very lucky to work with people as Prof. Yoann Olivier, Dr. Vincent Lemaur, Dr. Gabriele D'Avino and Dr. Luca Muccioli. Without their lead, experience and (most of all) patience, the PhD probably would have been more complicated. Then, few words also for the people in the CMN laboratory. I would thank Prof. Roberto Lazzaroni and Prof. Jérôme Cornil; our retired secretary Agnès and our technician Sébastien. A special thank goes to the old and present members of B157 and to my lunch teammates.

I would like to acknowledge the European Union's Horizon 2020 research and innovation program under Marie Skłodowska Curie Grant agreement No. 722651 (SEPOMO) for funding, but above all the students I have met in this programme. With some of them I have built a friendship (besides a working) relationship that I hope it will last long. And talking about friendship, how to forget my friends in Florence: "True friends are always free to separate, but they never do so".

Truly, I would have never achieved such a goal without the everlasting support of my family and, in particular, that of my parents, which this thesis is dedicated to. I owe you everything: the person I am today and what I am going to be is the result of the education you taught me and of all your sacrifices, done to allow me to study and grow as a scientist, but also as an adult.

At last, I must thank the person who saved me, for there was a period in which I was drowning in my personal ocean of uncertainty. That person is Elisa, my girlfriend: she is the light for me in dark places, when all other lights go out. I cannot be more grateful to have met you, here, in Mons.

Once a wise man told that there is no victory without sacrifice. I think (but I will softly say it) I have won. Nevertheless, this is not over: the best has yet to come!